Imperial College London

Department of Materials

Atomic Iron in Nitrogen-doped Carbon Electrocatalysts for Proton Exchange Membrane Fuel Cells

Angus Nils Pedersen

A thesis submitted in partial fulfilment of the requirements for the degree of Doctor of Philosophy at Imperial College London

February 2024

Declaration

I hereby declare that the work presented in this thesis has not been submitted for any other degree or professional qualification, and that it is the result of my own independent work. Information derived from the published and unpublished work of collaborators has been acknowledged in the "Contribution to Chapters" section, and references are given in the "List of Publications" section.

Angus Pedersen

16th February 2024

The copyright of this thesis rests with the author. Unless otherwise indicated, its contents are licensed under a Creative Commons Attribution-Non Commercial 4.0 International Licence (CC BY-NC). Under this licence, you may copy and redistribute the material in any medium or format. You may also create and distribute modified versions of the work. This is on the condition that: you credit the author and do not use it, or any derivative works, for a commercial purpose. When reusing or sharing this work, ensure you make the licence terms clear to others by naming the licence and linking to the licence text. Where a work has been adapted, you should indicate that the work has been changed and describe those changes. Please seek permission from the copyright holder for uses of this work that are not included in this licence or permitted under UK Copyright Law.

Abstract

Atomic Fe in Nitrogen-doped Carbon (Fe-N-C) is investigated for the O_2 reduction reaction in proton exchange membrane fuel cells (PEMFCs). Chapter 1 introduces the research motivation. Chapter 2 provides a literature review, scoping out gaps in the literature and thus the aims and objectives for the thesis. Chapter 3 covers the methods and characterisation techniques used in this thesis.

Chapter 4 focusses on the development and characterisation of a novel Fe-N-C with high surface area and porosity, produced by an Mg-templating approach. It is found this synthesis leads to record *in situ* electrochemical active site (FeN_x) utilisation in a rotating disc electrode. The FeN_x sites exhibit an axial coordination with low turnover frequency . Therefore, the impact of axial and N-coordination is investigated via DFT.

Chapter 5 investigates the *operando* Fe dissolution mechanism under inert (Ar) and active (O_2) conditions of the Fe-N-C developed in Chapter 4, using both flow-cell and gas diffusion electrode (GDE) coupled to an online ICP-MS. During O_2 reduction at 20^{o}C in GDE, a mechanism of Fe dissolution and reprecipitation into Fe_xO_y occurs due to pH increasing in the catalyst layer. This is supported by post-mortem characterization and kinetic modelling.

Chapter 6 examines the impacts of increasing the ionomer to catalyst ratio in H_2-O_2 fed PEMFCs. The Fe-N-C optimisation is probed using *in situ* electrochemical techniques. A uniquely high ionomer:Fe-N-C content is required for maximum performance due to the Fe-N-C's high mesoporosity.

Chapter 7 investigates the life cycle and techno-economic analysis of Fe-N-C versus Pt/C for PEMFCs. Fe-N-C production leads to lower predicted endpoint environmental impacts. Monetized environmental impacts are found to provide higher cost than the catalyst production. Based on the techno-economic analysis, the power density for Fe-N-C to compete with Pt/C is calculated.

Chapter 8 provides conclusions and research directions.

Acknowledgements

"No man is an island" – John Donne.

I must begin by thanking my extremely supportive supervisors, Professor Magda Titirici, and Professor Ifan Stephens. Magda and Ifan have taught me key skills for a scientist both inside, and perhaps more importantly, outside of the laboratory. Magda and Ifan's different research styles, knowledge and perspectives has been incredibly insightful and beneficial to my development. From their guidance, encouragement, and trust, I have been able to grow in confidence over my PhD into an independent researcher. I am extremely glad and grateful to have undertaken this journey under their supervision. I must also thank my co-supervisors at UCL, Professor Dan Brett and Dr. Rhodri Jervis, have provided important insights and access to fuel cell testing to their facilities.

With the support of Ifan and Magda, I was fortunate enough to spend two research placements abroad, one with Dr. Frederic Maillard at Grenoble University and, one with Professor Lior Elbaz at Bar-Ilan University. Both placements have helped shape my PhD journey and provided fruitful discussion. Fred and Lior's personal and group research environments have provided me with newfound friends and collaborators (Keyla, Kavita, Laetitia, Antoine, Rafi, Yan, Alisa), experiences, and perspectives. Thanks to Vincent Martin for conducting nearly fifty flow cell ICP-MS measurements during my time in Grenoble! Also, through collaboration with Fred, I met Dr. Serhiy Cherevko and Yu-Ping Ku, who I must thank for beneficial discussion and conducting GDE ICP-MS measurements. For fundings these trips I must thank the British Council/Wohl Clean Growth Alliance and Imperial Global Fellows Fund. Additionally, the funding provided by the generous Society of Chemical Industry Messel Scholarship is greatly appreciated. I was able to conduct my PhD and work with all these amazing researchers through the Advanced Characterisation of Materials Centre for Doctoral Training (ACM CDT), funded by the EPSRC. The ACM CDT provided a great cohort of friends (Tigran, Tiarnan, Alex, Toby, Claudia, Victoria, Alex, Samia) to undertake the PhD journey together, as well as providing excellent access to various unique training opportunities.

I think I have spent more time with my colleague, but more importantly, friend, Dr. Jesus Barrio, than anyone else the past 4 years. Jesus has helped guide my research and pushed my research productivity. I think was able to return the favour on the badminton court! Dr. Alain

Li helped guide my material synthesis at the start of my PhD and was extremely supportive throughout, as well as being a great friend. Dr. Alexander Bagger was only briefly at Imperial, but during this short time Alexander gave a different viewpoint towards my research and has been a sounding board for ideas, and successful collaborations. Also, Dr. Saurav Sarma seemed to know anything and everything, which was incredibly useful to have by my side. There are also the battery experts, Dr. Maria Crespo, and Dr. Heather Au, who have always been incredibly supportive and knowledgeable.

There is also the amazing team of Research Facility Managers in the Department of Materials - Sarah Fearn, Gwilherm Kerherve, Irena Nevjestic, Andrey Berenov. They are all excellent scientists who have always provided me with overwhelming support from their expert knowledge. There are also the Facility Managers in the Chemical Engineering analysis lab, Kaho Chueng and Patricia Carry, who have always been very helpful.

The research groups of Magda and Ifan are full of so many amazing and support researchers, creating a great work environment for the past four years. In no order I thank: Jingyu, Hui, Richard, Helen, Simon, Mengnan, Silvia, Olly, Romain, Craig, James, Zamaan, Sara, Andrea, Ken, Rob, and Han. To my exceptional UROP students, Sid, and Jason, I am excited to see their PhD journey just beginning and I am grateful for your help. Also, my amazing Master's student, Jinil Pandya, who has unwavering patience and commitment on the LCA project, thank you. Here I must also thank Professor Camille Petit, Dr. Andrea Bernardi, Dr. Grazia Leonzio, Dr. Alexey Serov and Professor Benoit Chachuat for supporting this project.

Outside of research, I must thank my partner, Rachel Fenner, who has been understanding and supportive when things were not going well and a great sounding board for my problems. Rachel has also been there to celebrate my achievements and enjoy life beyond the PhD. In this respect I also gratefully thank my family, Ralph, Mum, and Dad. After four years I think they may not still be quite sure what I do, but that has provided me with a nice grounding and escape from research. During my formative years I must also thank my parents for instilling the important values of community, hard work, rigour, and integrity, which have been critical over my PhD and will continue to be for the rest of my scientific career.

For setting me on this path towards the PhD, I must thank my school science teachers, who's fun and engaging lessons helped inspire me towards a career in science.

List of Publications

Publications contributing to thesis chapters are as follows:

Chapters 1 and Chapter 2

[1] **A. Pedersen**, J. Barrio, A. Li, R. Jervis, D. J. L. Brett, M.-M. Titirici, I. E. L. Stephens,* Adv. Energy Mater. 2022, 12, 2102715.

[2] J. Barrio, **A. Pedersen**, S. Favero, H. Luo, M. Wang, S. Ch. Sarma, J. Feng, L. T. T. Ngoc, S. Kellner, A. Y. Li, A. B. Jorge Sobrido, M.-M. Titirici,* Chem. Rev. 2022, 123, 5, 2311-2348.

[3] **A. Pedersen**,* A. Bagger, J. Barrio, F. Maillard, I. Stephens, M.-M. Titirici,* J. Mater. Chem. A 2023, 11, 23211-23222.

Chapter 3

[1] J. Barrio,[+] **A. Pedersen**,[+] S. Ch Sarma, A. Bagger, M. Gong, S. Favero, C.-X. Zhao, R. Garcia Serres, A. Y. Li, Q. Zhang, F. Jaouen, F. Maillard, A. Kucernak, I. E. L Stephens,* M.-M. Titirici,* Adv. Mater. 2023, 35, 2211022.

Chapter 4

[1] J. Barrio,[+] **A. Pedersen**,[+] S. Ch Sarma, A. Bagger, M. Gong, S. Favero, C.-X. Zhao, R. Garcia Serres, A. Y. Li, Q. Zhang, F. Jaouen, F. Maillard, A. Kucernak, I. E. L Stephens,* M.-M. Titirici,* Adv. Mater. 2023, 35, 2211022.

Chapter 5

[1] **A. Pedersen**,[+] K. Kumar,[+] Y Ping-Ku, V. Martin, L. Dubau, K. Teixeira Santos, J. Barrio, V. A. Saveleva, P. Glatzel, X. Li, A. Hutzler, A. Bonnefont, M.-M. Titirici, S. Cherevko, I. E. L. Stephens, F. Maillard.* *Manuscript under review*.

Chapter 6

[1] **A. Pedersen**,* R. Snitkoff-Sol, Y. Yurko, J. Barrio, R. Cai, T. Suter, G. Yang, S. Haigh, D. Brett, R. Jervis, M.-M. Titirici, I. E. L. Stephens, L. Elbaz.* *Manuscript under review*.

Chapter 7

[1] **A. Pedersen**,[+] J. Pandya,[+] G. Leonzio, A. Serov, A. Bernardi, I. Stephens, M.-M. Titirici, C. Petit, B. Chachuat,* Green Chem. 2023.

Chapter 8

[1] **A. Pedersen**,* A. Bagger, J. Barrio, F. Maillard, I. Stephens, M.-M. Titirici,* J. Mater. Chem. A 2023, 11, 23211-23222.

[+] Indicates equal contribution of authors.

* Corresponding author(s).

The individual contributions to the results chapters are detailed on the next part.

Publications not contributing to this thesis:

[1] Q. Li, Y. Xu, **A. Pedersen**, M. Wang, M. Zhang, J. Feng, H. Luo, M.-M. Titirici,* C. R. Jones,* Adv. Funct. Mater. 2024

[2] N. Hongrutai, S. Ch. Sarma Y. Zhou, S. Kellner, **A. Pedersen**, K. Adourian, H. Tyrrell, M. Ryan, J. Panpranot, J. Barrio,* J. Phys. Mater., 2024

[3] S. Ch Sarma,[+] J. Barrio,[+] M. Gong, **A. Pedersen,** A. Kucernak, M.-M. Titirici, I. E. L Stephens, Electrochimica Acta. 2023, 463, 142855.

[4] S. Ch Sarma,[+] J. Barrio,[+] A. Bagger, **A. Pedersen,** M. Gong, H. Luo, M. Wang, S. Favero, C.-X. Zhao, Q. Zhang, A. Kucernak, M.-M. Titirici, I. E. L Stephens, Adv. Funct. Mater. 2023, 2302468.

[5] Z. Mukadam,[+] S. Liu,[+] **A. Pedersen**, J. Barrio, S. Fearn, S. Ch. Sarma, M. M. Titirici, S. B. Scott, I. E. L. Stephens, K. Chan, S. Mezzavilla, Energy Environ. Sci. 2023, 16, 2934-2944

[6] A. Y. Li, **A. Pedersen**, J. Feng, H. Luo, J. Barrio, J. Roman, K. K. (Mimi) Hii, M.-M. Titirici, Green Chem. 2022, 24, 7574.

[7] J. Barrio,[+] **A. Pedersen**,[+] J. Feng, S. Sarma. M. Wang, A. Y. Li, H. Yadegari, H. Luo, M. P. Ryan, M.-M. Titirici, I. E. L. Stephens, J. Mater. Chem. A 2022, 10, 6023-6030.

[8] J. Feng, R. Cai, E. Magliocca, H. Luo, L. Higgins, G. L. F. Romario, X. Liang, **A. Pedersen**, Z. Xu, Z. Guo, A. Periasamy, D. Brett, T. S. Miller, S. J. Haigh, B. Mishra, M.-M. Titirici, Adv. Funct. Mater. 2021, 2102974.

Contributions to Chapters

Chapters 4-7 include results from collaborators. Personal contributions and those of collaborators are highlighted below:

Chapter 4: I carried out (R)RDE, EPR, N_2 sorption, Raman, XRD, EPR, and ICP-MS measurements and their analysis and discussion. I assisted with material preparation of Fe-N-C and synthesized the ^{57}Fe-N-C. The published manuscript was drafted with Jesús Barrio, with equal contributions.

Contributors: XPS was performed and analysed by Jesus Barrio. XAS analysed and TEM measured by Saurav Sarma. DFT calculated by Alexander Bagger. HAADF-STEM and EDX performed by Qiang Zhang and Chang-Xin Zhao. Mossbauer spectroscopy performed and analysed by Ricardo Garcia-Serres. Nitrite stripping performed by Mengjun Gong. TGA-MS performed by Silvia Favero. NMR performed by Alain Li. Supervision and support was provided by Ifan Stephens, Magda Titirici, Frederic Maillard, Frederic Jaouen and Anthony Kucernak.

Chapter 5: I conducted Material preparation/synthesis, RDE, on-line flow cell ICP-MS (with support of Vincent Martin), Raman, XRD measurements and XPS analysis. I led the investigation and the analysis and discussion of all results.

Contributors: On-line GDE ICP-MS performed by Kavita Kumar and Yu-Ping Ku. TEM performed by Laetitia Dubau. Some RDE measurements and XAS measurement by Keyla Teixeira Santos. XAS analysis by Viktoriia Saveleva. EELS performed by Xiaoyan Li. XPS performed by Jesús Barrio. HAADF-STEM performed by Andreas Hutzler. Kinetic modelling was calculated by Antoine Bonnefont. Supervision and support were provided by Ifan Stephens, Magda Titirici and Frederic Maillard.

Chapter 6: I carried out RDE, N_2 sorption, Raman, XRD, ICP-MS, material synthesis/preparation, fuel cell preparation and testing including electrochemical impedance and Fourier transform alternating current voltammetry. Led the investigation and the analysis and discussion of all results.

Contributors: Theo Suter provided initial fuel cell training and discussions. Guangmeimei Yang performed four probe electronic conductivity. Yan Yurko performed SEM measurements and DRT analysis. Rafi Snitkof-Sol helped analyse FTacV. Rongsheng Cai performed HAADF-STEM and EDX. Supervision and support were provided by Magda Titirici, Ifan Stephens, Dan Brett, Rhodri Jervis, Sarah Haigh and Lior Elbaz.

Chapter 7: I devised the project, life cycle inputs and scenarios with Jinil Pandya, I carried out the techno-economic analysis and Pt consumption scenarios. I conducted the analysis and discussion of results in the published work.

Contributors: Jinil Pandya carried out the preliminary LCA and TEA simulations and analysis. Grazia Leonzio carried out global sensitivity analysis and helped carry out LCA scenarios. Andrea Bernardi helped carry out LCA scenarios. Alexey Serov provided experimental information. Benoit Chachuat assisted with discussion of LCA results. Supervision and support were provided by: Magda Titirici, Camille Petit, and Benoit Chachuat.

List of Acronyms

BET	Brunauer-Emmett-Teller
CcO	Cytochrome c Oxidase
CV	Cyclic Voltammetry
DI	De-Ionized
DFT	Density Functional Theory
DRT	Distribution of Relaxation Times
EDX	Energy Dispersive X-ray Spectroscopy
EELS	Electron Energy Loss Spectroscopy
EIS	Electrochemical Impedance Spectroscopy
EPR	Electron Paramagnetic Resonance
EXAFS	Extended X-ray Absorption Fine Structure
FTacV	Fourier Transform alternating current Voltammetry
GDE	Gas Diffusion Electrode
HAADF-STEM	High-angle Annular Dark-Field Scanning Transmission Electron Microscopy
HFR	High Frequency Resistance
ICP-MS	Inductively Coupled Plasma Mass Spectroscopy
IEA	International Energy Agency
LCA	Life Cycle Analysis
NLDFT	Non-Linear Density Functional Theory
PEMFC	Proton Exchange Membrane Fuel Cell
PGM	Precious Group Metal
RDE	Rotating Disc Electrode
RRDE	Rotating Ring Disc Electrode
SEM	Scanning Electron Microscopy
TEA	Techno-economic Analysis
TEM	Transmission Electron Microscopy
TGA	Thermal Gravimetric Analysis
TOF	Turnover Frequency
US DOE	United States Department of Energy
XANES	X-ray Adsorption Near Edge Spectroscopy
XAS	X-ray Absorption Spectroscopy
XPS	X-ray Photoelectron Spectroscopy
XRD	X-ray Diffraction
ZIF	Zeolitic Imidazolate Framework

Table of contents

Declaration **1**
Abstract **2**
Acknowledgements **3**
List of Publications **5**
Contributions to Chapters **7**
List of Acronyms **9**
Table of contents **10**
Thesis Outline **14**
Chapter 1: Introduction and Motivation **15**
1.1 The Case for Renewable Energy 15
1.2 Electrochemical Energy Conversion and Proton Exchange Membrane Fuel Cells 16
1.2.1 Platinum-based Cathodes - The Crux of PEMFCs 17
1.2.2 An Alternative? 18
Chapter 2: Literature review **20**
2.1 PEMFCs 20
2.2 O_2 Reduction Theory 21
2.2.1 Density Functional Theory 22
2.3 Single metal atoms catalysts and Bio-Inspiration 23
2.4 Synthesis 25
2.4.1 N-C Support 25
2.4.2 Metal Precursors 27
2.4.3 Template 27
2.4.4 Processing Methods 27
2.4.5 Decoupled Processing and Active Metal Loading 30
2.4.6 Acid leaching 33
2.4.7 Ball Milling and Ultra Sonication 33
2.4.8 Environmental Impact 34
2.5 Active Site Quantification 34
2.5.1 Active Site Density and Site Utilisation 36
2.6 Degradation 37
2.6.1 Degradation Mechanisms 37
2.6.2 Methods to Reduce Degradation 39
2.7 Translating RDE to PEMFC 40
2.7.1 Activity 40
2.7.2 Stability 41
2.7.3 Gas Diffusion Electrode 41
2.7.4 Microenvironment and pH 41
2.7.5 PEMFC Device Considerations 42
2.8 Commercialisation and Techno-economics 43
2.9 Novelty, Thesis Aims and Objectives 45
References 47
Chapter 3: Materials and Methodology **56**
3.1 Catalyst Preparation 56
3.1.1 TAP X 56
3.1.2 TAP X@Fe 56

3.2 Characterisation Techniques 57
3.2.1 XPS 57
3.2.2 XAS 58
3.2.3 Raman Spectroscopy 59
3.2.4 N_2 sorption 59
3.2.5 XRD 61
3.2.6 ICP-MS 62
3.2.7 TGA-MS 63
3.2.8 EPR 63
3.2.9 Mössbauer Spectroscopy 65
3.2.10 Electron Microscopy 65
3.2.11 DFT 67
3.3 Electrochemical Techniques 67
3.3.1 RDE 67
3.3.2 GDE 72
3.3.3 PEMFC 73
3.3.4 EIS 73
3.3.5 FTacV 74
3.4 Life Cycle Analysis 75
References 76
Chapter 4: Synthesis of a Porous and High Active Site Utilisation Fe-N-C with Penta Coordination via Mg templating 79
4.1 Introduction 79
4.2 Experimental 80
4.2.1 Catalyst Preparation 80
4.2.2 RDE O_2 reduction 81
4.2.3 *In situ* Nitrite Stripping 81
4.2.4 Bulk Site Density and Utilisation 83
4.2.5 DFT Simulations 83
4.2.6 Characterisation 84
4.3 Results and Discussion 85
4.3.1 N-C Structural Evolution with Pyrolysis 85
4.3.2 Fe-N-C Characterisation 91
4.3.3 RDE O_2 Reduction Performance and Activity Descriptors 96
4.3.4 DFT 99
4.4 Conclusion 101
References 102
Chapter 5: Fe Dissolution in Fe-N-C Electrocatalysts during Acidic Oxygen Reduction: Impact of Local pH 105
5.1 Introduction 105
5.2 Experimental 108
5.2.1 Catalyst Preparation 108
5.2.2 RDE Electrode Preparation 108
5.2.3 Online Flow Cell ICP-MS 108
5.2.4 80^{o}C RDE Accelerated Stress Test 110
5.2.5 GDE 111
5.2.6 Kinetic Modelling Simulations 114

5.2.7 Characterisation 114
5.3 Results 116
5.3.1 Comparing TAP 900@Fe and TAP 900@^{57}Fe RDE O_2 Reduction Activity 116
5.3.2 Online Flow Cell ICP-MS 116
5.3.3 80^{o}C RDE AST 120
5.3.4 GDE O_2 Reduction and Degradation 121
5.3.5 Pre- and Post- GDE Protocol Characterisation 122
5.3.6 Online GDE ICP-MS 124
5.4 Discussion 127
5.4.1 Flow Cell ICP-MS and RDE 127
5.4.2 GDE ICP-MS 129
5.4.3 Kinetic Modelling 131
5.5 Conclusion 133
References 134
Chapter 6: Fe-N-C PEMFC Optimisation: The Effect of Ionomer Loading 137
6.1 Introduction 137
6.2 Experimental 139
6.2.1 Catalyst Preparation 139
6.2.2 RDE 139
6.2.3 PEMFC 139
6.2.4 Characterisation 142
6.3 Results and Discussion 144
6.3.1 Catalyst Powder Characterisation 144
6.3.2 I/C Ratio 147
6.3.3 SEM and Catalyst Layer Thickness 147
6.3.4 Void Volume and Carbon Structure 148
6.3.5 Electronic Conductivity 149
6.3.6 Site Density, Specific Capacitance and Active Site Utilisation 150
6.3.7 PEMFC Performance 152
6.3.8 EIS 154
6.3.9 DRT 156
6.4 Conclusion 158
References 159
Chapter 7: Comparative techno-economic and life-cycle analysis of Pt/C versus Fe-N-C 163
7.1 Introduction 163
7.2 Experimental 166
7.2.1 Life Cycle Analysis 166
7.2.2 Goal and Scope 167
7.2.3 Life Cycle Inventory 168
7.2.4 Impact Assessment 171
7.2.5 Interpretation 173
7.2.6 Techno-economic Analysis 174
7.2.7 Pt demand Forecasting 176
7.3 Results 177
7.3.1 Life Cycle Assessment 177
7.3.2 Techno-economic Analysis 181
7.4 Discussion 186

7.5 Conclusion 189
References 190
Chapter 8: Concluding Remarks 193
8.1 Conclusion 193
8.2 Future Work and Perspectives 195
8.2.1 Stability 195
8.2.2 Synthesis 197
8.2.3 Characterisation 197
8.2.4 Optimising PEMFC Performance 198
8.2.5 M-N-C: Beyond PEMFCs and electrocatalysis 198
References 200

Thesis Outline

The chapters of this thesis are summarized below:

Chapter 1 provides the motivation and requirements for sustainable electrochemical energy conversion technologies.

Chapter 2 explores the non-precious metal-based oxygen reduction literature and identifies possible research gaps and directions.

Chapter 3 covers the materials and methods used in this thesis and discusses principles and operation of characterisation techniques personally carried out.

Chapter 4 reports the synthesis and characterisation of a highly porous Fe-N-C based on Mg templating, highlighting active site utilisation and impact of penta-coordination.

Chapter 5 investigates the degradation and impact of Fe demetallation in a highly porous Fe-N-C using on-line flow cell and GDE ICP-MS. With microkinetic modelling results the degradation mechanism in GDE is elucidated.

Chapter 6 studies the impact of ionomer content on PEMFC performance of a highly porous Fe-N-C using a combination of electrochemical and ex-situ techniques.

Chapter 7 carries out a comparative LCA and TEA of Fe-N-C and Pt/C-based cathodes in PEMFCs based on several scenarios.

Chapter 8 provides conclusions of this PhD and perspectives for future work and research directions

Chapter 1: Introduction and Motivation

1.1 The Case for Renewable Energy

Since the mid-20th century, is there compelling evidence of essential alterations in the condition and operation of the Earth that surpass the scope of variability observed during the Holocene, and are primarily influenced by human activities.[1] In this new epoch, known as the Anthropocene, there is unequivocal evidence the sixth great mass extinction event in the history of life on Earth is underway.[2] This is in part caused by the rising anthropogenic global warming emissions such as CO_2, as shown by the Keeling curve (**Figure 1.1**).

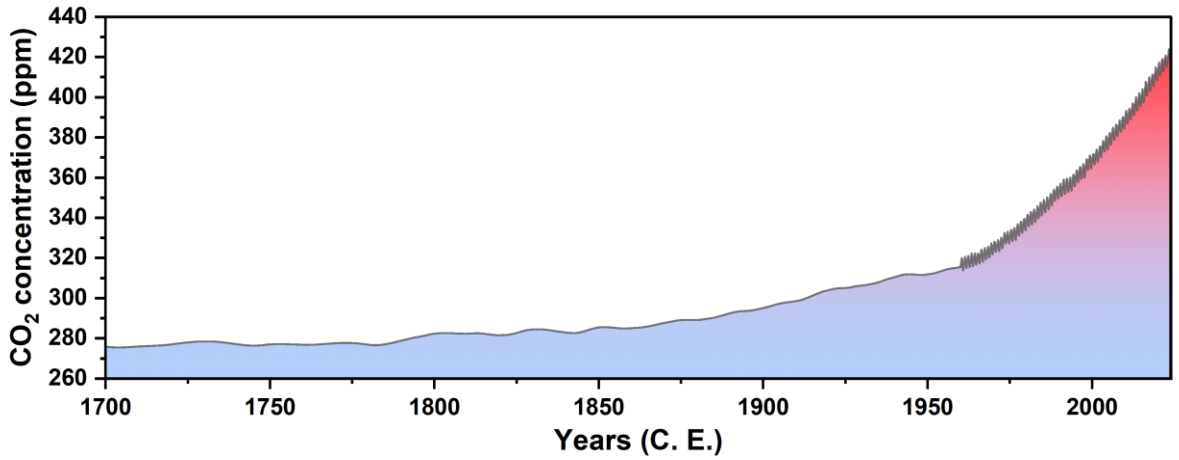


Figure 1.1. CO_2 concentration measured at Law Dome Ice Core (1700-1958) and Mauna Loa Observatory, Hawaii (1958-Present). Data obtained from refs.[3–5]

To prevent the global mean temperature rise exceeding 2°C compared to pre-industrial levels, under the 2015 Paris Agreement,[6] countries worldwide have established commitments for significant emission reductions, ultimately targeting net zero greenhouse gas emissions. Notably, in 2019, the UK government was the first major economy to enshrine in law a commitment to reduce greenhouse gas emissions to net zero by 2050. Accomplishing these commitments, particularly with the persistent growth in energy demands and populations, necessitates the substitution of unsustainable fossil fuel-based processes and precursors with renewable, clean energy methods and resources.[7] Currently, transport relies on 91% of its final energy coming from oil products, which is only 3.5% less than in the early 1970s.[8] Positively, according to the 2023 World Energy Outlook from the International Energy Agency (IEA), the world is currently on track to see fossil fuel consumption peak before 2030.[9] To realise this scenario in hard to abate industries, where direct electrification is not feasible (steel, petrochemical, long distance and heavy transport), requires significant ramp up of

Power-to-X, where X is an energy carrier, such as hydrogen, which can be derived and subsequently converted by electrochemical technologies (**Figure 1.2**).[10]

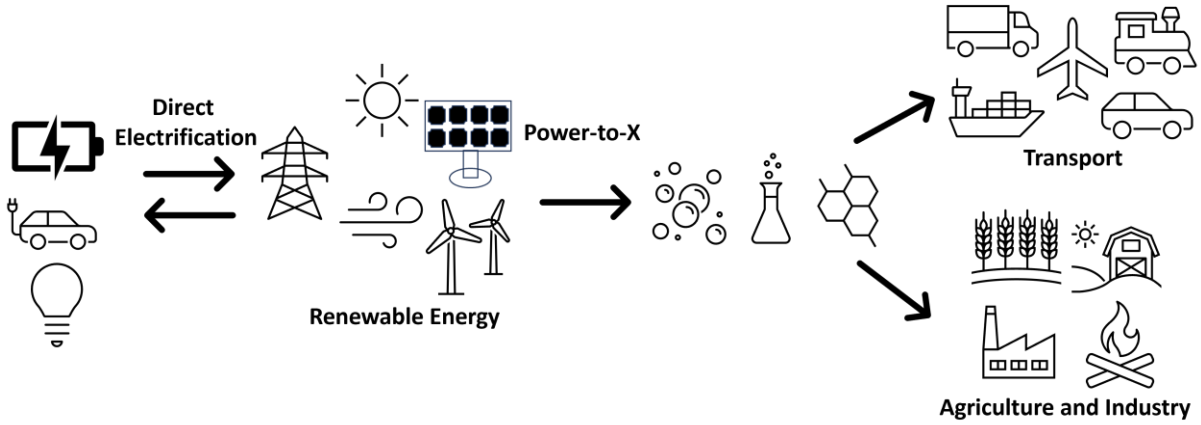


Figure 1.2. Simplified representation of future energy model.

1.2 Electrochemical Energy Conversion and Proton Exchange Membrane Fuel Cells

To achieve a fully sustainable approach in the case of H_2, its production must stem from water splitting in electrolyzers, encompassing H_2 and O_2 evolution processes, as opposed to relying on methane reforming (referred to as grey hydrogen production).[11,12] Subsequently, the generated green H_2 can be employed in commodity chemical production, or as a fuel along with an oxidant (O_2) to generate electricity within fuel cells.[13,14]

The IEA has projected that in order to achieve a global scenario of net zero emissions by 2050, approximately 60 Mt of H_2 will be utilized for electricity generation.[9] In the 2030 net zero scenario, almost 8 Mt of H_2 will be used directly in transport (50% road and 45% shipping).[15] Hydrogen-powered fuel cells, specifically low-temperature (80°C) polymer electrolyte membrane fuel cells (PEMFCs), represent a highly promising technology with a high technology readiness level for achieving zero CO_2 emissions in certain sectors of power generation.[16] This is primarily attributed to the adaptability and broad range of applications that PEMFCs offer in stationary and portable power generation, particularly in the field of transportation.[16] The increasing prominence of PEMFCs in transportation applications is supported, for instance, by the ambitious targets set by governments worldwide, aiming for the deployment of 2.5 million fuel cell electric vehicles (FCEVs) on the roads by 2030.[17]

1.2.1 Platinum-based Cathodes - The Crux of PEMFCs

PEMFCs typically employ nanoparticle platinum group metals (PGM), such as Pt, as catalysts for these reactions.[18] PEMFCs reactions can be broken into the anodic H_2 oxidation reaction, which is kinetically facile, being five-six times faster than the cathodic O_2 reduction reaction. Consequently, significantly higher amounts of Pt nanoparticle-based catalyst are required for cathodic O_2 reduction (historically 0.4 mg_{Pt} cm^{-2} at cathode versus 0.05 mg_{Pt} cm^{-2} at anode).[19] Additionally, breaking down the components and processes contributing to inefficiencies in PEMFCs, the most significant loss occurs from the large overpotential of the O_2 reduction reaction, labelled as η_{ORR} in **Figure 1.3a**. This clearly signifies the importance of developing efficient O_2 reduction electrocatalysts for PEMFCs.

Considering the economics, the estimated cost of PEMFCs in light-duty vehicles was approximately \$42.80/kW_{net} in 2020, considering a production volume of 500,000 units per year.[20] The US DOE has targeted a cost of \$30/kW_{net} at the same production rate for PEMFCs to be economically competitive.[21] This objective can be realized through significant reduction, or the complete elimination of PGM catalysts at the cathode, which are predicted by US DOE to account for nearly half of the cost of a PEMFC stack in light duty FCEVs (**Figure 1.3b**).[22] Significant reduction or elimination of Pt at PEMFC cathode has also been concluded as essential by the UK Advanced Propulsion Centre.[23]

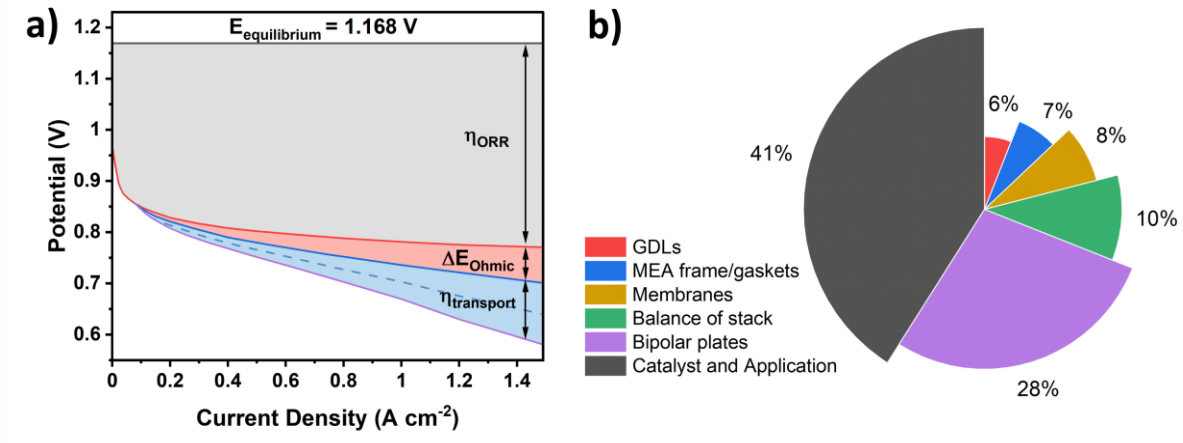


Figure 1.3. H_2/Air feed 80°C and 50 cm^2 PEMFC polarisation curve of Pt-based catalysts, with breakdown of losses highlighted and labelled. η_{ORR} represents the O_2 reduction overpotential, ΔE_{ohmic} represents ohmic losses and $\eta_{transport}$ represents transport losses. The purple line represents the measured cell potential. Figure adapted from references, with experimental measurement details provided therein.[19,24] b.) Calculated breakdown of component costs in 2017 of Pt-based PEMFC stack at 500,000 stacks $year^{-1}$. Values from ref.[25]

1.2.2 An Alternative?

A transition to PGM-free materials with lower costs, as well as greater accessibility, and higher production capacity is necessary, which can be facilitated by the utilization of Earth-abundant metals (**Figure 1.4a**).[26] However, the widespread adoption of such devices faces challenges related to the growing global demand for PGMs, limited recycling efforts, and the high costs associated with PGMs.[27] PGM-free consisting of atomically dispersed transition metal atoms coordinated to N-doped C (M-N-C, where M = Fe, Cu, Ni, Co, Mn[28] and recently Sn[29]) present a possibly cheaper[27] and more environmentally alternative to Pt-based PEMFC cathodes. However, the escalating demand for Co and Ni in energy applications may diminish their appeal in catalyst applications.[30] Fortunately, Fe-N-C has been shown to exhibit the greatest performance of M-N-C to date, rivaling that of Pt/C (**Figure 1.4b**).[31–33]

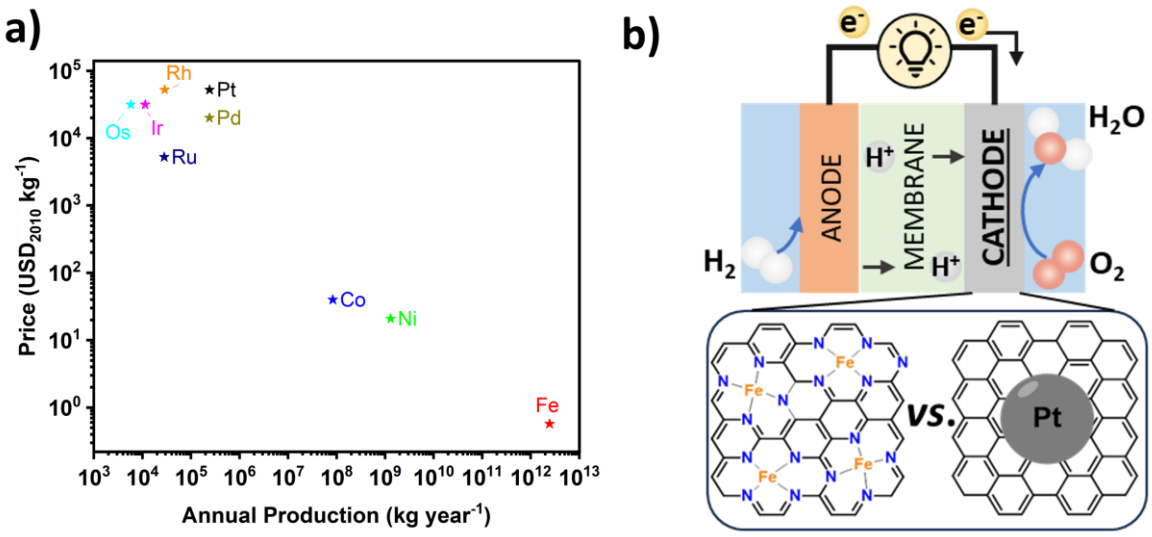


Figure 1.4. a.) Annual kg production and USD price per kg (in 2010) of Group VIII metals. Adapted from refs.[34,35] b.) Basic illustration of PEMFC operation with catalyst candidates at cathode depicted.

There has been tremendous progress in the performance of Fe-N-C-based catalysts over the past 15 years,[36–38] and particularly over the duration of my PhD, driven in part by consortium projects in the US DOE (Electrocat[39]) and EU (PEGASUS[40] and CRESCENDO[41]). The status of Fe-N-C and 2025 US DOE targets for PGM-free catalysts is provided in **Figure 1.5a**. There has recently been a significant leap in stability of Fe-N-C by Liu *et al.*, reaching the durability target of 30 mV loss in performance at 0.8 A cm^{-2} after 30,000 cycles (H_2-air).[33] Although, the same target at 1.5 A cm^{-2} remains distant. The activity target at 0.9 $V_{iR\text{-}free}$ (H_2-O_2, 1 bar O_2) has been met, granted with high loadings of Fe-N-C (~4 mg_{FeNC} cm^{-2}). Meanwhile, the performance of PEMFC operating under practical conditions for transportation applications (H_2–air at 1 bar)

still needs to double (151 vs. 300 mA cm^{-2} at 0.8 V). Ultimately, power density needs to improve to >1000 mW cm^{-2} to compete with Pt-based catalysts.

Increasing electrochemical performance of a catalyst generally entails two approaches: either increasing the quantity of available catalytic sites or increasing the inherent reactivity of these catalytic sites.[42] These two approaches can be deconvoluted by considering reactivity descriptor plots. To the best of my knowledge, these have so far been based on gravimetric or areal site density,[31,43,44] although these plots do not account for varying catalyst densities and the limited catalyst thickness available before PEMFC performance would become debilitated by mass transport.[19] Instead, it is worth considering the volumetric site density, as initially proposed in the seminal work by Gasteiger *et al.*[19] Here, Gasteiger concluded that a *cost-less* catalyst could compete with 47 wt.% Pt/C in PEMFCs if it displayed an activity of 130 A cm_{cat}^{-3} at 0.8 $V_{iR\text{-}free}$ (**Figure 1.5b**). One can see that state-of-the-art Fe-N-Cs show volumetric activity of 21-45 A cm_{cat}^{-3} (0.8 $V_{iR\text{-}free}$, 1 bar H_2-O_2),[31–33] signaling there is still a way to go to compete with Pt.

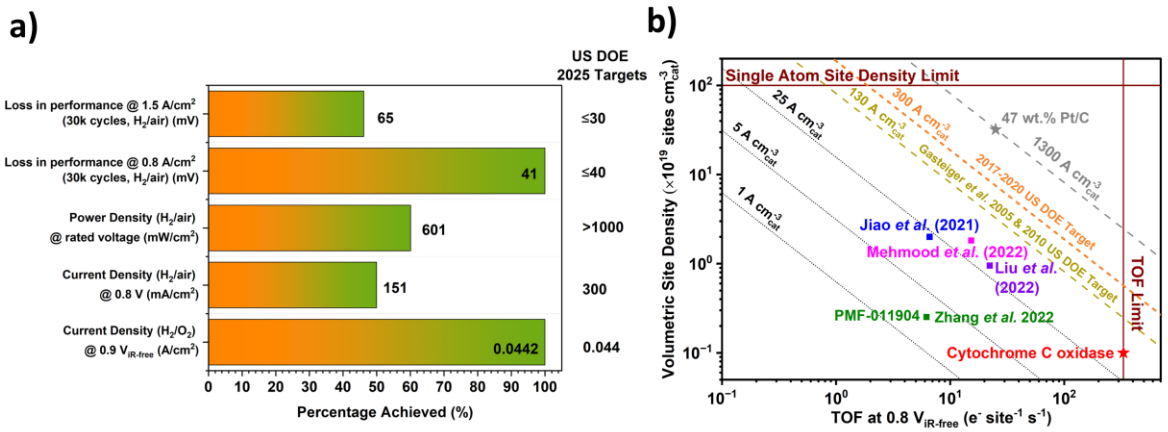


Figure 1.5 a.) Current performance status of state-of-the art Fe-N-C catalyst[33] and US DOE 2025 PEMFC Targets operating at 80°C.[27] b.) Volumetric site density and TOF of state-of-the-art Fe-N-C (Jiao et al.,[32] Liu et al.[33] and Mehmood et al.[31]) and commercial (PMF-011904)[45] Fe-N-C compared to enzyme Cytochrome c oxidase (based in values calculated in refs[46,47]), 47 wt.% Pt/C[19] and US DOE targets. Site density was based on nitrite stripping results. For PMF-011904, nitrite stripping values were obtained from Primbs et al.[44] while PEMFC performance obtained from Zhang et al.[45] The density (mg cm^{-3}) of plotted Fe-N-Cs was obtained from loading and thickness of catalyst layer in MEAs from refs. Fe-N-C performance based on H_2-O_2 1 bar. US DOE 2010 target derived from cost-less catalyst in Gasteiger et al.[19] and 2017-2020 Target from ref.[48] Single atom site density limit based on calculations by Mehmood et al.,[31] with assumed 100 µm thick cathode catalyst layer. The TOF limit is assumed to be equivalent to that of cytochrome c oxidase.

Chapter 2: Literature review

This chapter describes the operation of PEMFCs and the theory of O_2 reduction in acid environments. This is proceeded by synthesis strategies of M-N-Cs, and their activity and degradation mechanisms. Finally, considerations of translating performance from RDE to PEMFC are discussed.

2.1 PEMFCs

2.1.1.1 Design and Operation

Fuel Cells are electrochemical devices that can convert the chemical energy of fuel directly into DC electricity.[49] PEMFCs are equipped with a membrane electrode assembly (MEA), which includes a polymer electrolyte membrane situated between the anode and cathode, as illustrated in **Figure 2.1**. H_2 is oxidised at the anode to H^+ (**Equation 2.1**), with the membrane facilitating the flow of H^+ to react with O_2 at the cathode (**Equation 2.2**). The membrane obstructs the passage of electrons and unreacted fuel. This compels electrons to follow an alternative pathway through the external circuit, thereby providing power for an external load.[50]

$$\text{Anode: } H_2 \rightleftharpoons 2H^+ + 2e^- \qquad \textbf{Equation 2.1}$$

$$\text{Cathode: } O_2 + 4H^+ + 4e^- \rightleftharpoons 2H_2O \qquad \textbf{Equation 2.2}$$

The on both the cathode and anode side the MEA typically contains a gas diffusion and microporous layer, with the catalyst situated between the microporous layer and membrane. Meanwhile the single cell also contains gaskets, flow field plates and current collectors. A fuel cell stack is then simply made up of single cells sandwiched between cooling plates.

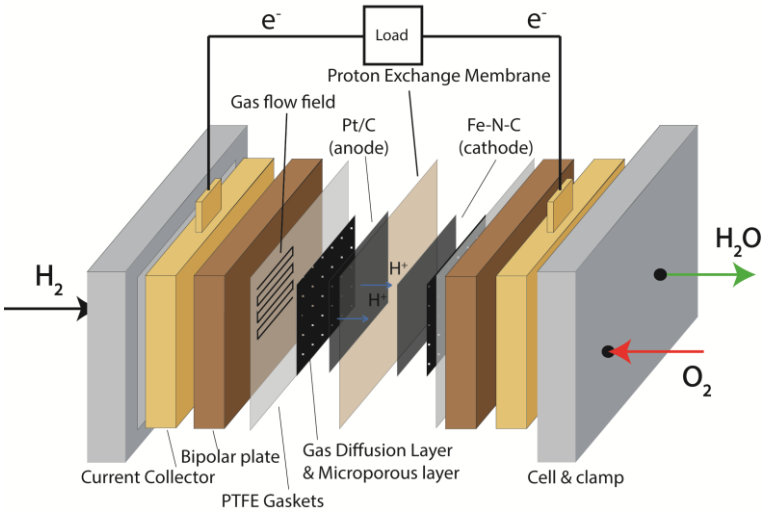


Figure 2.1 Illustration of PEMFC and its components.

2.1.1.2 History and Applications

Due to their fast response and high power density, PEMFCs are most suited to transport applications and backup power supplies.[21] Fuel Cells piqued scientific interest since their inception in 1839.[51] In terms of practical applications, notably they were initially used by NASA in space missions in the 1960s,[52] however it was not until the 1990s that fuel cells began to garner greater industrial attention, particularly in the transportation and back-up applications. This attention was especially prominent within the automotive industry with the advent of electrically driven vehicles.[53] Several commercial PEMFC-based cars have since been developed by BMW (iX5 Hydrogen),[54] and Hyundai (All-New Nexo),[55] and most notably by Toyota (Mirai).[56] PEMFC have also been employed in buses, trains and boats, among others.[57]

2.2 O_2 Reduction Theory

The standard potential of O_2 electrocatalyst is 1.23 V_{RHE} under standard conditions (25°C and 1 bar H_2 or O_2, **Table 2.1**) and 1.168 V_{RHE} at the typical operational temperature of PEMFCs (80°C).[58] The O_2 reduction can also proceed via two-electron pathway to H_2O_2 at 0.67 V_{RHE}; however, this is undesired in fuel cells since it halves the power density that can be delivered compared to the four-electron pathway to H_2O and can lead to generation of radicals when in contact with Fe. Still, H_2O_2 is an important industrial commodity chemical for industry.[59]

Table 2.1. Thermodynamic electrode potentials of O_2 reduction in acidic environment.[60,61]

Pathway	Thermodynamic electrode potential at standard conditions, E^0 (V_{SHE})	Equation
$O_2 + 2H^+ + 2e^- \rightarrow H_2O_2$	0.67	**Equation 2.3**
$H_2O_2 + 2H^+ + 2e^- \rightarrow 2H_2O$	1.77	**Equation 2.4**
$O_2 + 4H^+ + 4e^- \rightarrow 2H_2O$	1.23	**Equation 2.5**

The direct four-electron process for the O_2 reduction reaction in an acidic environment can take on either a dissociative or associative pathway. This distinction hinges on the energy barrier associated with oxygen activation on the catalyst surface, a barrier that arises due to the relatively weak bonding of atomic oxygen.[62] On multiple catalyst surfaces, the dissociative pathway for O_2 reduction has been deemed unlikely, primarily due to the elevated dissociative barrier associated with the O–O bond.[62,63] The associative mechanism, in which O_2 does not undergo dissociation prior to hydrogenation, is shown by **Equation 2.6**-**Equation 2.10**, along with the free energies pertinent to Pt(111) displayed in Figure 4b.[62] This mechanism entails the sequential addition of an electron and

proton in each step, and the activity is contingent on the transfer of a proton and electron to O_2*. During this process, the O-O bond within OOH* is broken by the active site.

$$O_2 + {}^* \rightarrow {O_2}^* \quad \textbf{Equation 2.6}$$

$${O_2}^* + H^+ + e^- \rightarrow OOH^* \quad \textbf{Equation 2.7}$$

$$OOH^* + H^+ + e^- \rightarrow O^* + H_2O \quad \textbf{Equation 2.8}$$

$$O^* + H^+ + e^- \rightarrow OH^* \quad \textbf{Equation 2.9}$$

$$OH^* + H^+ + e^- \rightarrow H_2O + {}^* \quad \textbf{Equation 2.10}$$

In acidic environments it has been proposed that O_2 reduction occurs through an "inner-sphere" mechanism, where reaction intermediates are adsorbed on the active site throughout the entire reaction.[64]

2.2.1 Density Functional Theory

Numerous metals have been subject to investigation regarding their O_2 reduction activity, employing density functional theory (DFT) calculations to construct volcano plots that correlate ORR activity with the adsorption energies of critical intermediates. Among the metal surfaces explored, the Pt metal surface exhibits the highest catalytic performance in ORR. This heightened catalytic activity arises from the intermediate adsorption of O* and HO*, aligning with the predictions of the Sabatier principle, which states that an ideal catalyst does not bind too weakly or strongly to reaction intermediates.[65] Utilising DFT, Nørskov, Rossmeisl and co-workers unveiled the correlation between catalytic performance and O_2 reduction reaction intermediate binding affinity to a catalyst, yielding the characteristic "volcano" plot.[66] This relationships has since been experimentally proven for O_2 reduction on both molecular catalysts[67] and platinum single crystals.[68–70] Additionally, DFT calculations reveal a robust linear scaling relationship among the adsorption energies of key intermediates in O_2 reduction, preventing their independent variation.[71] This scaling relationship is primarily attributed to the comparable binding energy of the oxygen atom within these intermediates.

These scaling relationships limit metal surfaces like Pt(111) and single atom catalysts to exhibit a required overpotential of approximately 0.3 to 0.4 V at a minimum, as shown by the free energy diagrams in **Figure 2.2**. Various approaches have been suggested to break scaling relations [72] and decrease overpotential, including inducing tensile lattice strain on the catalyst surface, introducing transient conditions through resonance oscillations, employing confinement and three-dimensional catalytic sites. Some of these strategies are analogous to the mechanisms utilized by the naturally occurring enzyme cytochrome c oxidase.[63,73–76]

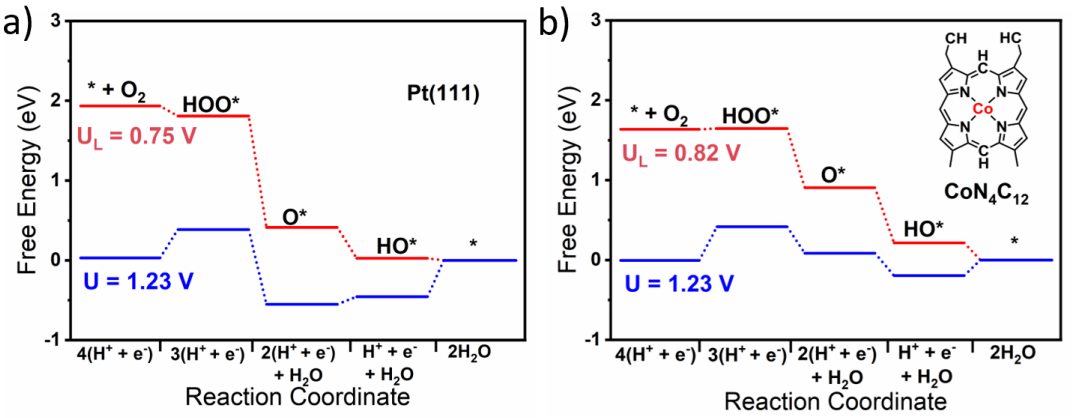


Figure 2.2 Free energy diagrams for O_2 reduction are shown at both limiting potential (UL, red lines) and equilibrium potential (U, blue lines), with "*" indicating the active site. a.) Associative mechanism on Pt(111). Adapted from reference.[66] b.) Associative mechanism on CoN_4C_{12} porphyrin. c.) Dissociative mechanism on in-plane adjacent Co_2N_5/graphene, with O adsorbed behind the dual metal atom site (Ob) reacting with O_2. The grey dashed line represents the surrounding graphene sheet. Values for CoN_4C_{12} and Co_2N_5/graphene were calculated using the VASP solvent model. Figure originally adapted from reference.[77] Reproduced from reference[47] with permission.

The use of DFT allows for the modelling of the binding energy of reaction intermediates to Pt nanoparticles with a degree of precision, owing to their crystalline nature, which can be replicated in single crystal studies. Presently, the most effective model M-N-C systems comprise of macrocycles, such as metal phthalocyanines or metal porphyrins, as they possess a well-defined structure in experiments and can be precisely imitated atom by atom in quantum chemistry simulations.[78] Although, these macrocycles typically exhibit rapid degradation or deactivation when exposed to acidic electrolytes, rendering them unsuitable as model M-N-C systems. Furthermore, the conventional pyrolysis techniques employed in the production of M-N-C catalysts generate a range of potential active sites characterized by diverse local carbon structures (defects, edges, oxygen groups), thereby altering the electron density. An approach is to acknowledge the variety of sites in a pyrolyzed catalyst and instead establish trends using a single model, such as an M-N_4-C site.

2.3 Single metal atoms catalysts and Bio-Inspiration

As catalyst metal clusters diminish in size to just a few metal atoms, discrete energy band structures become intricately linked with the number of metal atoms in the cluster. Consequently, the addition or removal of a single metal atom at this stage can significantly influence the electronic configuration and, consequently, the catalytic characteristics.[79] By reducing catalytic sites to the level of well-dispersed single-metal atom catalysts, it effectively boosts the fraction of metal centres with minimal coordination, thereby enabling utilisation of each individual metal atom.[80] When these

single atom catalysts are precisely defined, they can be fine-tuned to selectively drive specific chemical reactions by changing the metal atom or local ligand environment.

Jasinski first reported in 1964 O_2 reduction activity of macrocycles containing an M-N_4 core,[81] and in the 1970s Jahnke *et al.* discovered serendipitously that thermal decomposition of macrocycles to M-N-C led to improved activity.[82] O_2 reduction activity of transition metal M-N-C is ranked from highest to lowest in the following order: Fe > Co > Cu > Mn > Ni.[28] Recently, Sn-N-C has been discovered an active P-block catalyst, with equivalent TOF to Fe.[29]

Single atom M-N-C present remarkable similarity to active sites in biological systems.[46] In terms of Fe-N-C, the FeN_x active site in Fe-N-C resemble the Fe site in hemoglobin (**Figure 2.3a**), used for transporting binding and transporting Oxygen around the body.[83] Hemoglobin can even be used as a precursor to synthesise Fe-N-C catalysts, as we have previously reported.[84] Other single metal atom centres coordinated to nitrogen within a carbon framework exist in nature, such as Vitamin B12 with Co-N_5 centre (**Figure 2.3b**) and chlorophyll a with Mg-N_4 centre (**Figure 2.3c**), with the former being used successfully as a catalyst for O_2 reduction in PEMFCs, following pyrolysis.[85]

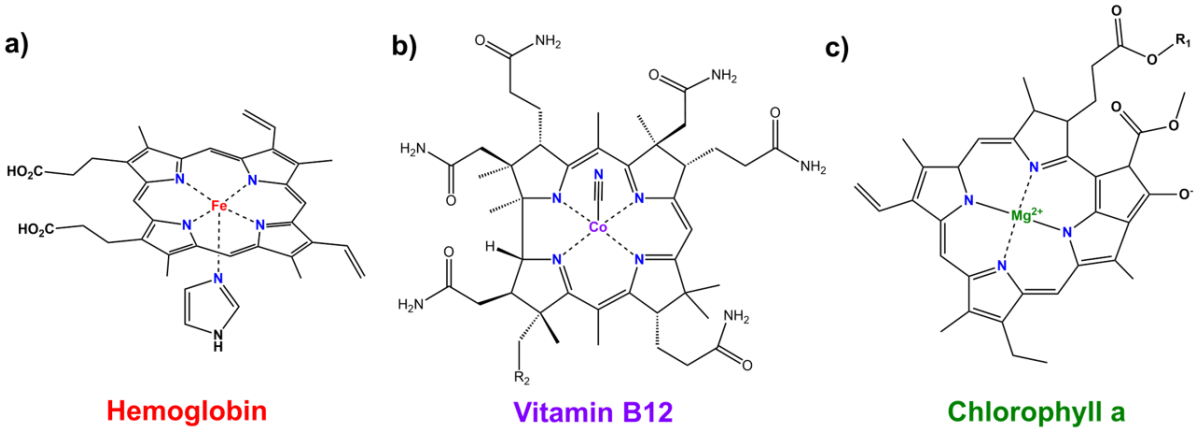


Figure 2.3. Structure of metal centres in a.) Hemoglobin. b.) Vitamin B12 c.) Chlorophyll a.

In the quest for inspiration from nature, some of the most challenging multi-electron reactions entail the involvement of two readily available metal atoms at the active site.[86] For instance, in the case of cytochrome c oxidase (CcO), a single CuB is positioned above the heme a3 site, as depicted in **Figure 2.4a**. This enzyme facilitates an exceptionally efficient and specific four-electron reduction of dioxygen to water, all the while preventing the generation of hydrogen peroxide.[74,87,88] The comparison in TOF of CcO to a commercial single atom Fe-N-C (PMF-011904) is provided in **Figure 2.4b**, where CcO present well over an order of magnitude higher TOF than PMF-011904, and comparable TOF to Pt(111) based on extension of the Tafel slope. Interestingly, back in the 1979-1980, Collman *et al.* synthesized a macrocyclic cofacial dicobalt porphyrin (Co_2FTF, for structure see

inset **Figure 2.4b**), which almost exclusively formed water, unlike its single site analogue.[89,90] Co_2FTF also presented an impressively high TOF, exceeding that of Pt(111) (**Figure 2.4b**).

While enzymes and macrocycles can be affixed to electrodes to facilitate effective electrocatalytic reactions,[91] their stability poses a significant challenge in harsh fuel cell environments (enzyme activity declines within hours).[92] Additionally, their extensive preparation and purification, and enzymes large electrode surface area/volumetric site density contribute to their limitations.[93]

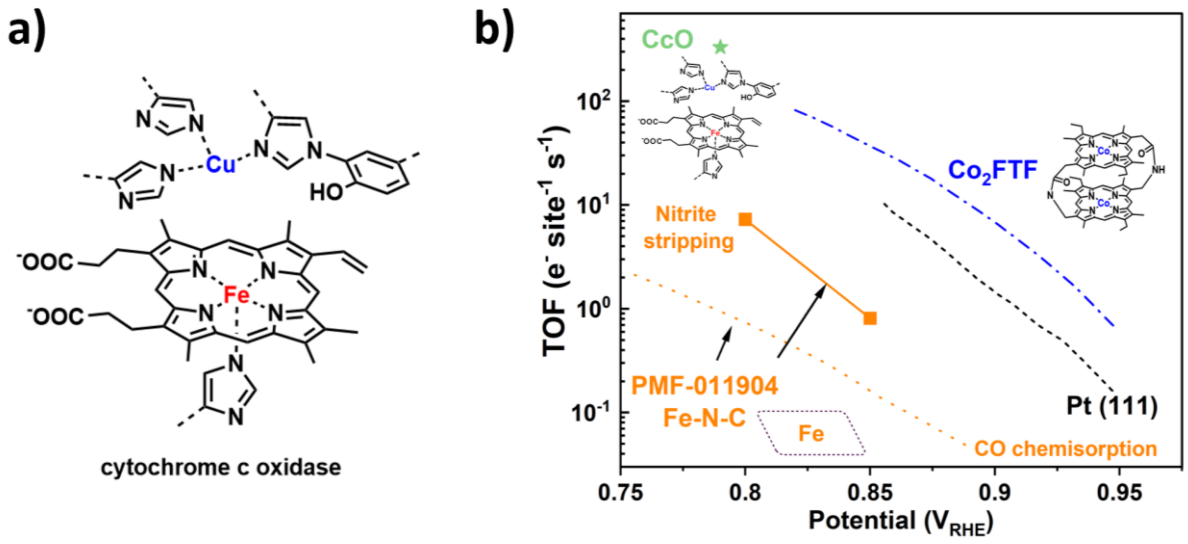


Figure 2.4. a.) Structure of in cytochrome c oxidase (CcO) where Cu_B site sites heme a_3. Adapted from reference.[94] b.) Calculated TOF at varying potentials for dual-metal atom active site in molecular (Co_2FTF), enzyme (CcO), plus Pt(111), a commercial single atom electrocatalyst (PMF-011904, Pajarito Powder LLC). Co_2FTF (blue dash-dot line) in 0.5 M CF_3CO_2H at 250 rpm.[89] CcO (green star): A. ferrooxidans CcO with ferrocenecarboxylic acid redox mediator.[91] Pajarito: PMF-011904 catalyst in 0.5 M H_2SO_4 at 1600 rpm. Orange dotted line represents ex-situ cryo CO chemisorption, orange squares represent in-situ electrochemical nitrite$^-$ stripping results.[95] Pt(111): black dashed line in 0.1 M $HClO_4$ at 1600 rpm.[70] Figure reproduced with permission.[47] Copyright 2021, Wiley-VCH. See ref [47] for calculations on TOF of catalysts.

To the best of my knowledge, there has not been experimentally rigorously confirmed heterogeneous dual metal atom active site with O_2 reduction activity superior to single atom M-N-C active site in acidic environment. This may be due to the unfavourable formation energy for many types of dual metal atom catalysts, as we [96] and Karmodak and Nørskov [97] have recently shown via DFT. For this reason, the next Section (Synthesis) and the remainder of this thesis focuses on the development of Fe-N-C.

2.4 Synthesis

2.4.1 N-C Support

Optimising the N-C support is critical to providing sufficient surface area and porosity, electrical conductivity, resistance to corrosion, and N sites.[98] [99] To produce a high density of $M\text{-}N_x$ sites, a

carbon material consisting of high numbers of nitrogen sites with vacancies is required, along too high N content would lead to semi-conductor behaviour. Meanwhile, porosity is critical to mass transport and high micropore volume is essential to host Fe-Nx sites.[44,100]

The N-C support can be obtained from a variety of precursors, such as organic monomers (e.g. aniline and cyanamide),[101] aerogels,[102,103] nitrogen-doped carbon nanotubes and graphene,[98,104] biomass (e.g. chitosan),[105,106] and metal organic frameworks (most commonly zeolitic imidazolate frameworks (ZIFs)),[107,108] as illustrated in **Figure 2.5a**. A huge library of organic building blocks is available for selection with varying types and quantity of N sites and properties (melting and boiling points). Biomass serves as a more sustainable approaches, although its properties are harder to tune and there is a limited number of biomasses containing N moieties.[46] Carbonaceous aerogels are a rising class of substrates for preparation of Fe-N-C due to their high specific surface area, tuneable pore size distribution and high electrical conductivity.[109] ZIFs are easy to prepare and can serve as sacrificial templates, molecular-scale cages, or porous metal-containing N-doped carbon materials, although most are not stable at relevant pyrolysis temperature which are required to obtain conductivity.[110]

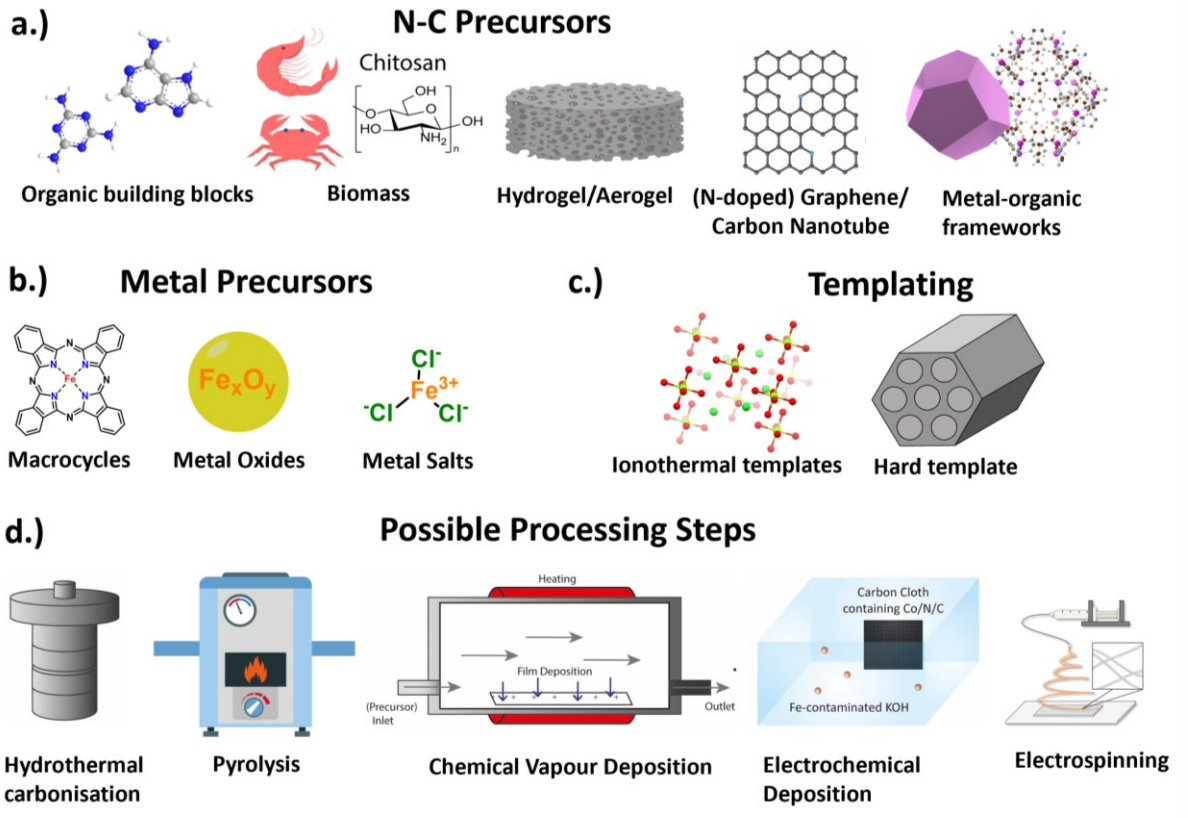


Figure 2.5. Representation of some of the options for a.) N-C precursors b.) Metal Precursors c.) Templates d.) Processing steps used to produce Fe-N-C catalysts. Figure adapted and reproduced from ref with permission.[47]

2.4.2 Metal Precursors

A very of Fe metal precursors can be used. Pre-defined Fe-N_4 macrocyclic precursors such as porphyrins, phthalocyanines, and corroles (**Figure 2.5b**) can be used.[111] These cannot be directly used for O_2 reduction in acidic medium due to their rapid degradation, and instead require a pyrolysis step, which causes disintegration of most Fe-N_x sites.[112]

Anhydrous and hydrated Fe salts (e.g., $FeCl_2$, $FeCl_3$, $FeCl_2{\cdot}4H_2O$) can be used.[32,113] It has been found some of these Fe salt precursors transform to Fe oxides during pyrolysis (discussed further in Section 2.4.4.1 and 2.4.4.4).[113] To avoid pyrolysis, eutectics of two metal salts at specified ratios can also be used to substantially lower the melting point of the constituent metal salts (e.g., $FeCl_3$:LiCl), enabling their direct use for loading into N-C.[114]

2.4.3 Template

Templates are often used to assist creating increased surface area and hierarchal structure for improved mass transport and active site accessbility of single atom sites. Ordered mesoporous carbon (**Figure 2.5c**) has been used to produce FeCo-N-C based on SBA-15 templates and Fe/Co macrocycles (FeTMPP, CoTMPP).[115] Silica templating is also commonly used.[116,117] However, these hard templating methods typically require harsh HF treatment for the silica template removal, which has environmental and safety concerns. Although there have been recent developments in removal of Silica via more environmentally benign and safer means.[118] Instead, ionothermal templates can be used which are more facile to remove since they typically based mixtures organic precursors with inorganic salt melts containing Lewis-acid metal cations. The Lewis-acid metal cations are suspected to help enable the beneficial formation of N_x sites during carbonisation($2 \leq x \leq 4$).[119] The salt template can be easily washed out after carbonisation with mild acid washing to generate a hierarchal pore structure with high surface area.[119,120]

2.4.4 Processing Methods

2.4.4.1 Deposition

Chemical vapour deposition (CVD) is commonly used for the industrial production of carbon nanotubes, by heating carbonaceous gases (e.g., acetylene) over metal catalyst nanoparticles such as Fe, Co, or Ni, depositing graphitic carbon on the surface of the catalyst.[121] For M-N-C it has been developed as a non-contact pyrolysis method to deposit active metals[113] or coatings from the gas phase.[33] Considering the Fe-O phase diagram at oxygen-deficient concentrations, as present during pyrolysis (**Figure 2.6a**), some Fe precursors, such as $FeCl_2{\cdot}4H_2O$ form iron oxides at intermediate temperatures (300-600°C), and Fe at >600°C, which has been experimentally confirmed.[113] Wu and

coworkers demonstrated the ability of CVD to produce different M-N-C (where M = Fe, Co, Ni or Mn) for O_2 reduction.[122] Improved O_2 reduction activity with Fe-N-C was subsequently achieved by Jiao *et al* with CVD.[32] CVD has most recently been used to improve stability by depositing an atomically thin N layer[33] and scalable processes are being developed based on fluidised bed reactors.[123]

Another non-contact method is atomic layer deposition (ALD), which facilitates the precise and reproducible formation of atomic layers on materials with high surface areas. The deposition in ALD occurs via sequential self-limiting surface reactions, interspersed with inert gas purging to ensure layer separation. ALD methodology finds applicability in high surface area substrates. Drawbacks of ALD include its high equipment costs, slow deposition rates, and restrictions on reagents for self-limiting reactions, often involving highly toxic precursors (e.g., H_2S). Nevertheless, efforts to broaden the range of more sustainable and cost-effective precursors, including base metals, are ongoing.[124–128] These limitations contribute to the limited adoption of ALD in typical chemistry laboratories and hinder its transition from laboratory-scale research to industrial use in catalysis. Additionally, ALD is notably temperature-sensitive, often necessitating a trial-and-error approach for successful synthesis.

Other deposition methods also exist such as electrochemical deposition. Hu and colleagues serendipitously observed that iron impurities in their KOH electrolyte underwent electrochemical deposition on their Co-N/C single (**Figure 2.5d**), leading to the formation of a Fe-Co-N/C dual metal atom catalyst, where oxygen atoms bridged the Fe-Co.[129] This approach outlines a straightforward method for generating well-defined and electrochemically active dual metal atom sites, which could potentially be extended to other elements of interest, similar to achievements in other types of catalytic sites.[130] Moreover, precise control during synthesis can be achieved by optimizing the concentration of the metal precursor and the deposition time. The work conducted by Hu and coworkers emphasizes the significance of employing high-purity electrolytes and rigorous electrochemical testing protocols [131] to prevent the potential contamination of catalytic sites.

2.4.4.2 Wet Chemical

Wet chemical approaches are accessible for common chemistry laboratories, typically employing low temperatures and solvents (e.g., water, ethanol, methanol), enabling flexible, quick and large scale synthesis of a library of single atoms catalysts.[132,133] Although, the use of large volumes of non-aqueous solvents can be economically problematic for scale-up if recycling of solvents cannot be easily implemented. Also, pyrolysis of precursors is still required if using non-conductive precursors.

2.4.4.3 Other methods

Electrospinning is a versatile and scalable method to produce nano-structure fibres with controlled morphology, enabling a hierarchal structure for electrocatalysts with efficient mass transport for PEMFCs.[134–136] Although, preparation of the electrospinning solution needs to be carefully fine-tuned and is restricted in properties (viscosity) to ensure facile and smooth spraying. Additionally, if used to prepare M-N-Cs, a significant portion of the catalyst layer would consist of fibres which are inactive to O2 reduction, thereby reducing the maximum achievable volumetric active site density.

3D printing can be used to create structures in a controlled manor, having recently been demonstrated as an approach that can produce single atom catalysts.[137] However, controllably introducing nano-porosity during printing is beyond the capability of such a technique.

Hydrothermal carbonisation is an environmentally benign, cheap, and scalable way to prepare M-N-C derived from waste or bio-derived precursors,[138,139] or graphene oxide.[140] However, these M-N-C particles are bulky and still require a pyrolysis step to become active towards O_2 reduction. Additionally, they have not led to state-of-the-art performance to date.[138,139]

2.4.4.4 Pyrolysis

A high temperature pyrolysis step is necessary to generate activity towards O_2 reduction, by creating a delocalised pi-electrons with the carbon support creating an electron withdrawing environment.[141] Naturally, the pyrolysis step is also required to create sufficient conductivity (discussed further in Section 2.7.5.1). The pyrolysis temperatures usually range from ~700-1,000°C, with selection of atmosphere (N_2, Ar, H_2, NH_3 or mixtures), being crucial in controlling the catalyst composition and morphology and therefore its activity and stability.[142] For instance, NH_3 pyrolysis leads to very active but unstable Fe-N-C in acid due to the basicity of the N groups created.[142] The pyrolysis step has often been considered as a “black box”, although recent work has begun to understand Fe-N_x formation in situ.[143–145] The production is often a mixture of species, such as N-doped carbon defects or edges, Fe-Nx sites, and inorganic metal particles, metal oxides and carbides.[146] Having such a mixture makes it difficult to deconvolute catalyst properties with activity, although it is still possible with a combination of techniques including ^{57}Fe Mössbauer spectroscopy.[147]

Around 650°C, the formation of iron carbide (**Equation 2.11**) is experimentally known to become dominant.[148] This is unsurprising since on the Fe-C phase diagram, beyond 6.7 wt.% Carbon, Fe_3C is the stable Fe phase[149] and from the Fe-N-C phase diagram at 580°C, a mix of Fe_3C and iron carbo-

nitrides ($Fe_3(C,N)_{1-x}$) is expected (**Figure 2.6b**). It has been previously established that iron carbide and iron nitride phases exhibit much lower or no appreciable direct O_2 reduction activity compared to Fe-N_x sites.[147,150] However, Fe_3C has been shown to enhance TOF of nearby FeN_x sites,[95,151] although excessive Fe_3C formation causes reduction in the number of FeN_x active sites.[148] Dopants such as S can be used to suppress Fe carbide formation.[148]

$$3FeO + C \rightarrow Fe_3C + \frac{2}{3}O_2 \qquad \textbf{Equation 2.11}$$

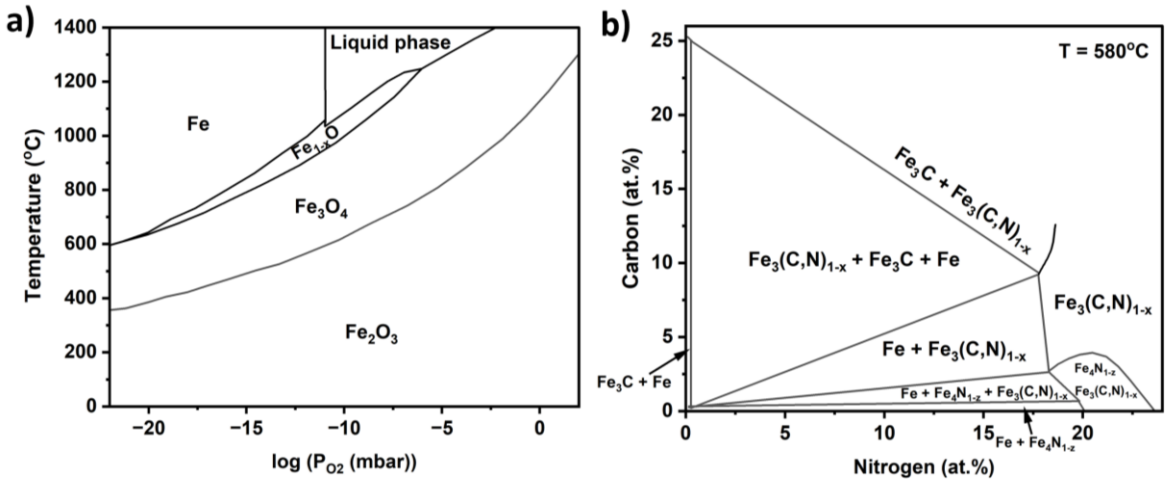


Figure 2.6. Phase diagrams of a.) binary Fe-O system at low O pressure/concentration. Data plotted from ref.[152] b.) Ternary Fe-N-C system at 580°C. Data plotted from ref.[153]

2.4.5 Decoupled Processing and Active Metal Loading

The difficulties of forming undesirable side phases during direct pyrolysis of Fe, N and C precursors directly has been discussed above and can be summarized by the lefthand side of **Figure 2.7**. Alternatively, the N-C precursor could be directly pyrolysed and the Fe precursor loaded at low temperatures (middle scheme in **Figure 2.7**), however this still leads to a distribution of active sites with poor performance. Instead, an active site templating method, using a metal that does not undergo carbothermal reduction reactions during pyrolysis, can coordinated to N_x sites, and be replaced by Fe at low temperature, would solve these pertinent problems. This process is depicted by the right-hand scheme of **Figure 2.7**. The idea of a decoupled pyrolysis and active metal loading was already floated by Yeager and coworkers in 1989 [154] and recently developed by Fellinger and colleagues.[32,114,119,155] It should be noted that this approach may not be applicable to all metals. For instance, coordination of Sn after formation of N-C does not appear to lead to atomically dispersed Sn-N-C.[156]

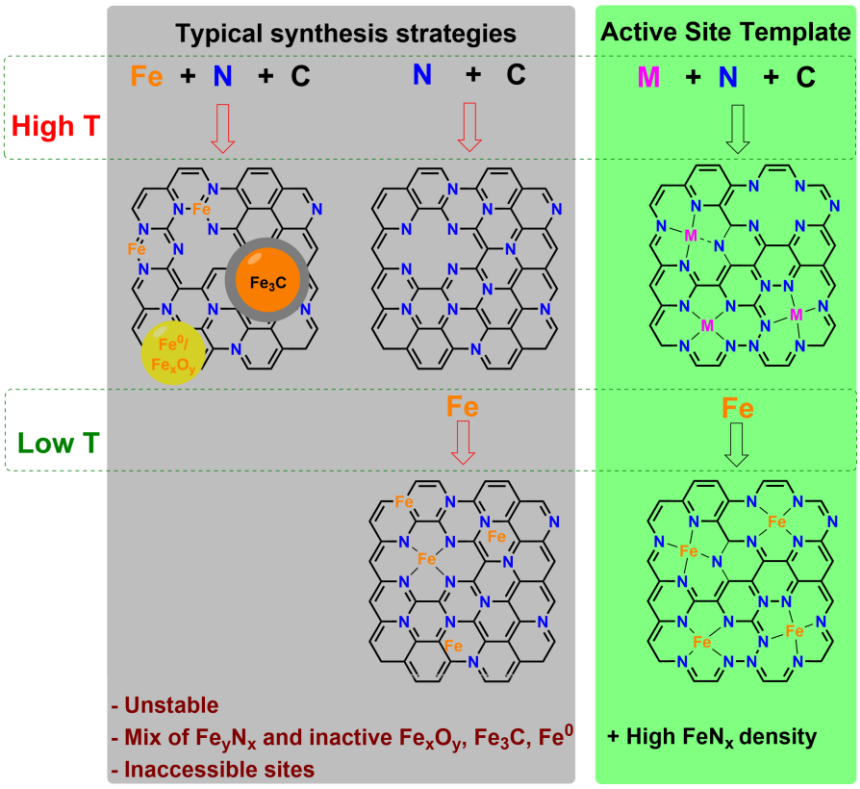


Figure 2.7. Schematic representation of typical synthetic approaches employed. **Left**: One pot pyrolysis with Fe, N and C precursors. **Right**: Active site templating.

To determine potential suitable candidates as an active site template it is worth consulting Ellingham diagrams of metal oxides (**Figure 2.8**). These depict a species stability with temperature (under varying conditions), based on thermodynamics, using the change in Gibbs Free Energy (Δ*G,* **Equation 2.14**-**Equation 2.15**). A reaction will proceed if the total free energy is negative, although the reaction can be very slow if the activation energy is high.

$$\Delta G = H - T\Delta S \qquad \textbf{Equation 2.12}$$

$$\Delta G = RTlnk_{eq} \qquad \textbf{Equation 2.13}$$

Where Δ*S* is the change in entropy and *H* is the enthalpy of the system. k_{eq} is the equilibrium constant.

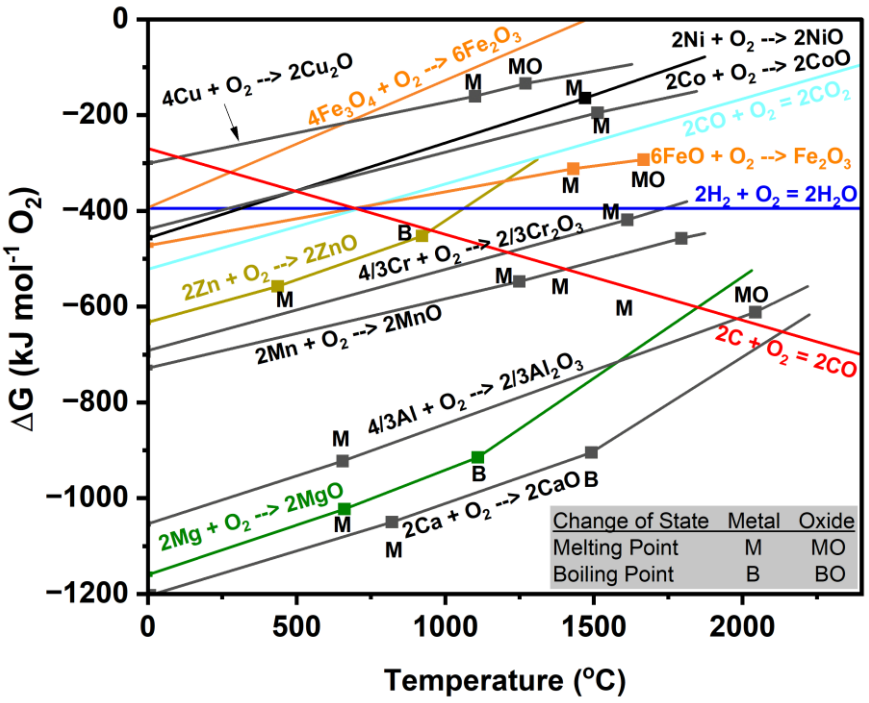


Figure 2.8. Ellingham diagram for different metal oxides. Replotted from ref.[157]

From Ellingham diagrams (**Figure 2.8**) it is clear C can act as a sufficient reductant for metal oxides, which is problematic for M-N-C synthesis. Zn ions undergo carbothermal reduction at higher temperature compared to Fe ions and begin evaporating at 907°C.[157] Additionally, metallic Zn does not catalyse graphitization.[158] Tetrahedral ZnN_4 sites can be found in Zeolitic framework-8 (ZIF-8), which has proven to be an excellent template for creating catalysts with high-density active sites with state-of-the-art activity [31–33] due to its stable structure (**Figure 2.9**). One issue with ZIF-8 is its inherent purely microporous structure, which could lead to issues of mass transport and active site accessibility, discussed further in Section 2.5.1.

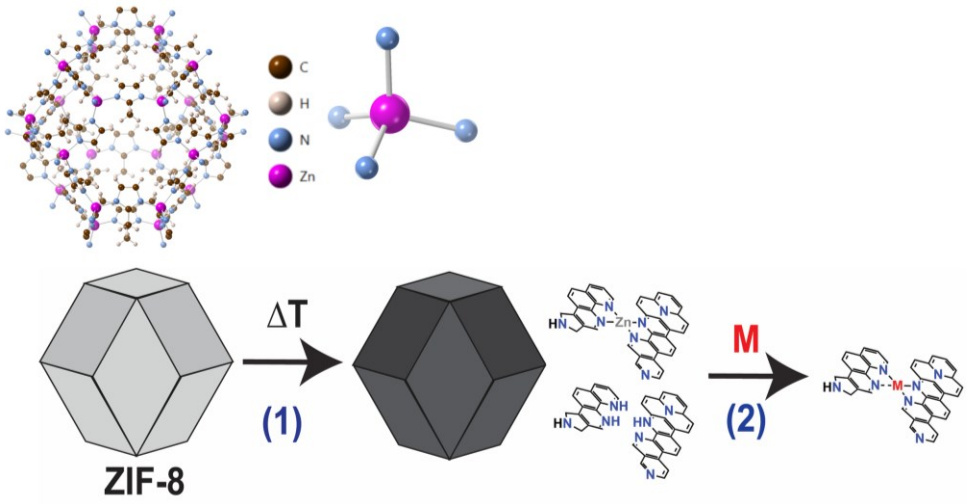


Figure 2.9. (Top) atomic structure of ZIF-8 with (produced from CrystalMaker software). Bottom – schematic representation of ZIF-8 decoupled pyrolysis (1) and metal loading (2). Reproduced from reference [96] under Creative Commons CC BY 3.0.

Mg can also serve as a suitable MgN_4 active site template, known to exist in chlorophyll, as mentioned earlier (**Figure 2.3c**). Additionally, based on Ellingham diagrams (**Figure 2.8**), Mg would not undergo carbothermal reduction until exceedingly high temperatures (1,800^{o}C). Mg also possesses the added benefit of Mg decomposing into solid MgO during the carbonisation process, which can generate high micro and mesoporosity.[119,120] Mg-based ZIF with high micro and mesoporosity to ZIF-8 can even be synthesized, although under more strictly controlled conditions.[159] Other metals such as Ca can also be candidates for active site templates since they form stable phthalocyanines[120] and do not undergo carbothermal reduction within relevant pyrolysis temperatures (**Figure 2.8**).

2.4.6 Acid leaching

Acid leaching steps are commonly carried out to remove templates and/or undesirable Fe phases, with the removal of the latter improving the durability of the Fe-N-C.[160,161] This typically comes at a cost of reduced activity, owing to the increase in surface oxygen groups which reduces TOF by modulating electron delocalisation.[162–164] Jaouen and coworkers determined that acid washing steps could be avoided with purely atomic Fe-N_x sites by adopting a purely dry synthetic procedure.[142]

2.4.7 Ball Milling and Ultra Sonication

Ball milling involves rotating a jar and jar (typically ZrO) between 100-800 rpm. It can be used to prepare N-C carbons[165] and ZIFs[166,167] without the need for solvents, presenting an environmental benign and scalable approach. Ball milling is also used to break down M-N-C particles for improved mass transport and improved O_2 reduction performance, with reduced H_2O_2 production (three times less than wet-phase synthesis).[168,169]

Ultrasonication is another method to break down particles within catalyst inks. Direction sonication from probe/horn tips should be avoided where possible due to contamination from erosion of the tip.[170] Ice-water baths should be used to prevent heating of the catalyst ink which can degrade the catalyst prior to electrochemical testing.[171]

Pt-based catalyst show significant decrease in PEMFC performance when prepared by sonication rather than ball milling or cavitation due to Pt agglomeration and dissolution.[172] Differences between the Fe-N-C electrocatalyst powder and its electrode due to ink processing steps has been recently been investigated.[173]

2.4.8 Environmental Impact

As can be seen from above, M-N-Cs can be prepared from a variety of different routes, each with their own environmental impacts. M-N-Cs have been suggested to have a low environmental footprint compared to Pt-based catalysts,[174] despite lacking demonstrated or quantified evidence via life cycle assessments. The intricacies of the synthesis process for advanced M-N-C catalysts, involving multiple steps (as discussed above), might contribute to increased waste generation. Also, at the device level, the larger quantity of PEMFC components required by Fe-N-C compared to Pt/C for equivalent performance would create increased environmental impacts, in particular Nafion, which is known for its environmental implications.[175] The environmental impact of critical materials, including Pt, in PEMFCs has been conducted via life cycle analysis.[176] A life cycle analysis as part of the PEGASUS research programme comparing Fe-N-C and Pt/C found that Fe-N-C could potentially exhibit higher impacts on global warming potential, human toxicity, abiotic depletion, and eutrophication.[175] Although, the Fe-N-C in this case was based on carbon nanotubes which were poorly performing in PEMFC and did not consider the current lifetime of the catalyst, where advanced M-N-C catalysts remains notably inferior to that of Pt-based counterparts, with replacement of catalyst and membrane creating a larger environmental impact.

2.5 Active Site Quantification

A range of techniques, both ex situ and in situ, have been developed for quantifying active sites in M-N-Cs (**Figure 2.10**). Established ex situ methods include CO cryo adsorption[177] and acid leaching.[178] In half cells, in situ techniques include cyanide[179] and nitrite stripping,[180] while in PEMFCs, Fourier-transform alternating current voltammetry (FTacV) has been employed.[181] These methods collectively allow for the quantification of active sites within M-N-Cs. By applying these techniques, researchers have been able to compare turnover frequencies (TOF) and establish reactivity descriptors among various reported catalysts from cross laboratory studies.[43,44] This enables a deeper understanding of catalyst performance and facilitates the identification of catalysts with superior active sites from specific synthesis methods.

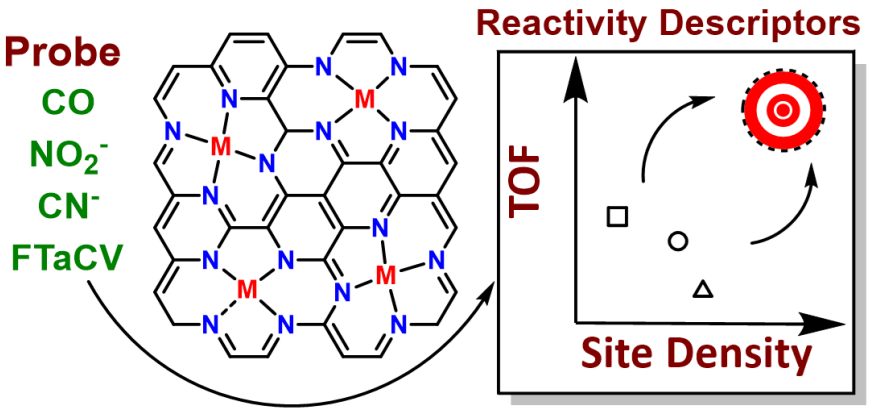


Figure 2.10. Establishment of reactivity descriptors (TOF vs Site Density) in M-N-Cs based on ex situ and/or in situ probes. Reproduced from reference[96] under Creative Commons CC BY 3.0.

The most established and commonly implemented techniques are ex situ CO cryo adsorption, developed by Strasser and coworkers,[177] and in situ nitrite stripping, developed by Kucernak and coworkers.[180] Both techniques possess benefits and drawbacks. CO cryo adsorption only provides quantification of gas accessible active sites under ex-situ conditions. In the case of in situ nitrite stripping, there have been conflicting claims regarding the number of electrons transferred during the electrochemical process, with reports ranging from 3 to 5 electrons transferred (**Figure 2.11**).[180,182] Recently, an Fe-N-C was found to exhibit 100% faradaic efficiency of nitrite reduction to ammonia.[183] This variability could be attributed to the presence of different M-N_x sites within the catalyst, which may produce different reaction products (such as hydroxylamine or ammonium) and consequently involve a varying number of electrons in the process. Further research is needed to investigate this variation and understand the specific mechanisms at play. Also worth noting is that nitrite stripping has been reported to probe not only single metal atom species, but also other components, such as the N/C framework[184] and Fe_xO_y.[185] Fe_xO_y commonly forms during accelerated stress tests of Fe-N-Cs, which can make post-mortem active site quantification using probe molecules more complex and challenging to interpret. Recently, Bae *et al*. developed an acid washing technique, which could be used to quantify the amount of iron oxides over a stability test, therefore enabling quantification of active sites via nitrite stripping over the same test.[186]

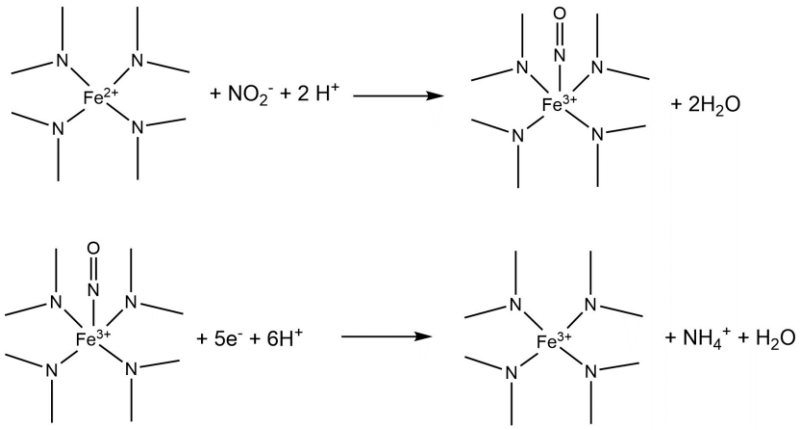


Figure 2.11. Proposed five electron reaction scheme of NO_2^- to NH_4^+ by Malko *et al.*[180] Reproduced under Creative Commons CC BY 4.0.

The reversible redox couple identified in certain Fe-N-C catalysts, occurring at approximately 0.76 V_{RHE} in an acidic environment, has been extensively verified as the transition between Fe^{II} and Fe^{III} states originating from Fe-N_x sites,[187–189] in particular those high spin $Fe^{III}N_x$ sites.[188] This Fe^{II}/Fe^{III} redox can therefore be used to quantify the number of FeN_x active sites, although over time this redox becomes convoluted with broad redox from quinone/hydroquinone species and the low $Fe^{III}N_x$ site density can be difficult to accurately determine directly from the redox peak. To solve this issue, FTacV has been recently developed which allows precise quantification of Fe^{II}/Fe^{III} by deconvoluting faradaic and non-faradaic processes.[181]

2.5.1 Active Site Density and Site Utilisation

The ideal configuration of high-density active sites necessitates accessibility to reactants to enhance overall performance. The concept of M-Nx active site utilisation was first introduced by Strasser and coworkers.[190] Several studies have reported achieving 100% active site utilization based on ex situ CO cryo adsorption;[32] however, quantifications from electrochemical methods reveal lower site numbers, typically below 10%.[44]

Wan et al. emphasized that electrochemically active utilization, based on nitrite stripping, in ZIF-8 derived Fe-N-C could reach 40% at the minimum site density of 1.3×10^{19} sites $g_{M\text{-}N\text{-}C}^{-1}$, facilitated by silica templating. Notably, the utilization declined with increasing site density.[191] Recent research efforts have focused on augmenting the electrochemically active site utilization and mass transport properties while maintaining a high site density, achieved by introducing more mesoporosity within the electrocatalyst, as demonstrated in our recent work and that of others.[192,193] Alternative metal-organic frameworks (MOFs) like MIL-101 and MOF-5 have also exhibited improved mesoporosity compared to ZIF-8 after pyrolysis, leading to the creation of active M-N-Cs.[194,195]

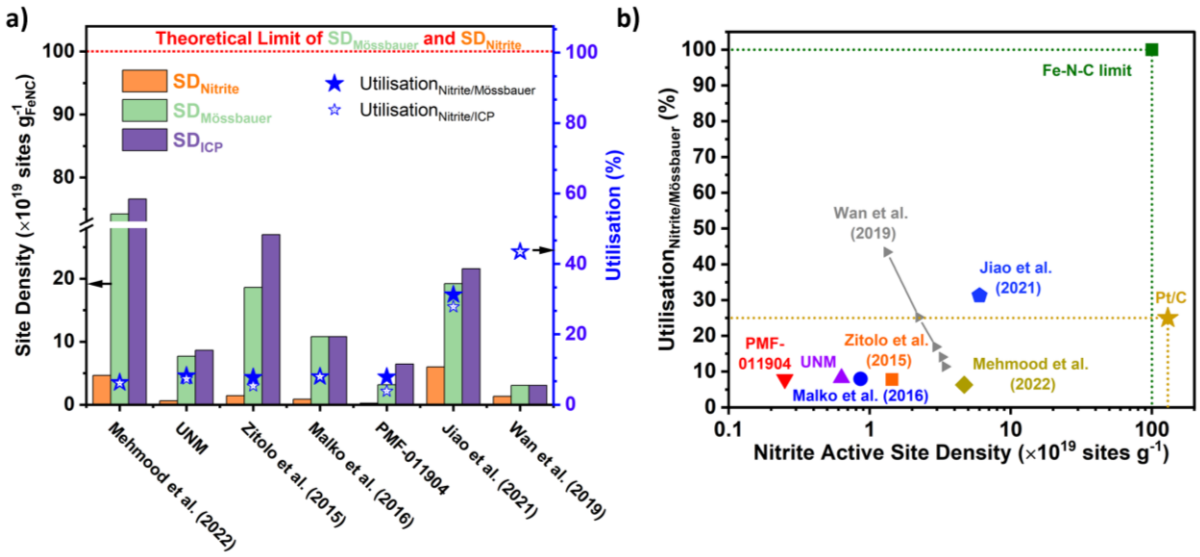


Figure 2.12. a.) Site density and utilisation determined from nitrite stripping and Mössbauer (D1+D2 sites) for benchmark single atom FeNC catalysts of; Zitolo et al. (zeolitic imidazolate framework-8 (ZIF-8) derived),[160] Malko et al.,[196] University New Mexico (UNM) and Pajarito Powder Inc. commercial catalyst PMF-011904,[197] Mehmood et al.,[31] and Jiao et al..[32] All Fe-N-C nitrite site density electrochemical measurements with assumed 5 e^- nitrite stripping process in 0.5 M sodium acetate buffer (pH 5.2) in a rotating disk electrode with 0.2 mg_{FeNC} cm^{-2} loading except Wan et al. who used 0.27 mg_{FeNC} cm^{-2}. b.) Utilisation of Fe-N-C for their site density with the theoretical active site density limit represented by the green dashed lines, as calculated by Mehmood et al. [31] Pt/C utilisation limit guided by gold dashed line. Pt/C SD based on 100 m^2 g_{Pt}^{-1} electrochemical surface area in a fuel cell, as calculated by Mehmood et al.,[31] while Pt utilisation assume 3 nm particles with 25% electrochemical utilisation. Figures reproduced from ref [192] under Creative Commons CC BY 3.0.

2.6 Degradation

2.6.1 Degradation Mechanisms

While "volcano" type relationships are effective for optimizing catalyst activity within a group of materials by identifying activity descriptors, they are not suitable for evaluating other crucial factors, such as stability.[72]

A thorough review on the degradation of M-N-Cs for O_2 reduction has recently been provided by Kumar *et al.*[198] and Bae *et al.*[199] Here, a summary of these different pathways is represented in **Figure 2.13.** These processes include demetallation,[200] protonation of N-groups, [201] [202] electrochemical carbon corrosion [203] [204] and chemical carbon oxidation via hydrogen peroxide,[201] which is generated in situ.

Decoupling of degradation mechanisms has recently been attempted.[205] The main initial degradation mechanism of Fe-N-C has been identified as Fe active site dissolution.[206–208] This has been identified from operando techniques such as flow cell and recently GDE coupled to ICP-MS.[161,186,209] Although, the GDE ICP-MS only displayed a maximum current density of 10 mA cm^{-2},[186] which is not comparable or relevant to PEMFCs, therefore warranting further investigation. The

change in active site density and rate constant in situ can be easily monitored in PEMFCs with FTacV,[188] although this method does not reveal the fate of demetallized Fe. The mechanism has also been deconvoluted using in situ distribution of relation times (DRT).[206,207]

While carbon corrosion thermodynamic potentials occur within the O_2 reduction potential window (**Equation 2.14**-**Equation 2.15**), in reality a large overpotential is required, with carbon corrosion only beginning between 0.8-1.0 V_{RHE}.[208,209] These potentials can occur in PEMFCs during start-up and shutdown or fuel starvation, therefore leading to carbon corrosion.[161] Although high voltages (>0.9 V_{RHE}) are avoided in commercialised FCEVs such as the Toyota Mirai.[210]

$$C + 2H_2O \rightarrow CO_2 + 4H^+ + 4e^- \quad E^o = 0.207\ V_{SHE} \qquad \textbf{Equation 2.14}$$

$$C + H_2O \rightarrow CO + 2H^+ + 2e^- \quad E^o = 0.518\ V_{SHE} \qquad \textbf{Equation 2.15}$$

Where E^o is the thermodynamic potential.

The reaction kinetics of carbon oxidation are increased with increasing temperature,[204,209] which impacts electron delocalization, subsequently affecting the turnover frequency of M-N-Cs.[162–164]

A particular concern of long-term Fe-N-C stability is their potential degradation through the Fenton reaction, where Fe^{2+} reacts with the hydrogen peroxide, generating hydroxide and hydroperoxyl radicals:

$$Fe^{2+} + H_2O_2 \rightarrow Fe^{3+} + HO^{\bullet} + HO^{-} \qquad \textbf{Equation 2.16}$$

These radicals are known for their highly corrosive nature towards various materials, including Nafion, commonly employed as the membrane in PEMFCs. Other transition metals such as Co presents the potential for a more stable catalyst, owing to its less harmful Fenton effect when compared to catalysts containing Fe.[201,211]

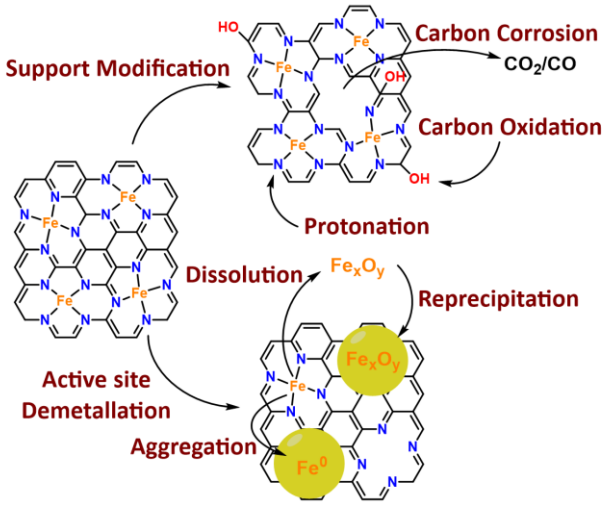


Figure 2.13. Illustration of different degradation mechanisms identified and proposed to date. Reproduced from reference [96] under Creative Commons CC BY 3.0.

2.6.2 Methods to Reduce Degradation

Fe-N-C catalysts derived from poly-aniline have shown no clear degradation for 500 h operation in PEMFC under potentiostatic conditions (at 0.3 A cm^{-2}),[212] however these catalyst could not deliver high power density. Notably, a recent breakthrough has resulted in enhancing the stability of a highly active Fe-N-C catalyst in PEMFCs, extending its operational lifetime to over 300 hours, a performance on par with Pt/C. This advancement was achieved by applying an atomically thin layer of N-C onto the highly active Fe-N-C.[33] Additionally, the incorporation of well-dispersed nanoparticles (CeO_x, TaO_x) and single-atom radical scavengers has proven effective in mitigating the degradation of Fe-N-C caused by reactive oxygen species.[213–215] Atomically dispersed Pt has also been shown to improve Fe-N-C stability, which can serve as inspiration to explore other stabilisers.[186]

Furthermore, the reactivation of Fe-N-C to prolong its catalyst lifespan has been successfully demonstrated through in situ electrochemical reduction, which effectively reduces the concentration of O species, resulting in a transient yet improved turnover frequency.[162,163]

Following Fe-N-C, the next most active M-N-C candidates are Co-N-C and Mn-N-C, and they have an advantage in terms of lower reactivity towards Fenton's reaction compared to Fe-N-C. This reduced reactivity means they experience less deactivation when exposed to H_2O_2. Consequently, Co-N-C and Mn-N-C show 30-56% less degradation over stability tests in PEMFCs lasting from 16 to 100 hours, compared to equivalently synthesized Fe-N-C. [174,216]

For instance, the degradation rate of Co-N-C from Chen et al. is 0.23 mA cm^{-2} h^{-1} after 100 hours at 0.7 V, whereas equivalently synthesized Fe-N-C exhibits a degradation rate of 0.60 mA cm^{-2} h^{-1} under the same conditions (**Figure 2.14**). However, it is important to note that the degradation rate of Co-N-C and Mn-N-C is still higher than the recent state-of-the-art Fe-N-C developed by Liu et al., which exhibited a degradation rate of 0.13 mA cm^{-2} h^{-1} after 300 hours at 0.67 V.

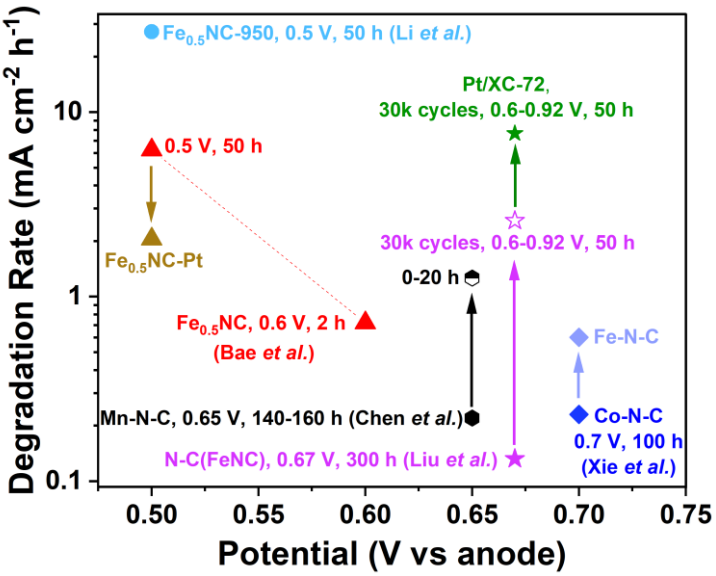


Figure 2.14. Degradation rate at different PEMFC potentials (vs anode), time intervals and accelerated stress test protocols for Fe-N-Cs and Pt/XC-72 (all PEMFC at 80°C). Liu et al.[33] N-C(FeNC) 300 h at 0.67 V (H_2/air 200 cm^3 min^{-1}) and 0.6 to ~0.92 V with 3 s holds (30k cycles (50 h), H_2/air 200 cm^3 min^{-1}, 1 bar_a). Bae et al.[186] $Fe_{0.5}NC$ 2 h potential hold at 0.6 $V_{vs\ anode}$ and 50 h at 0.5 $V_{vs\ anode}$. Li et al.[188] $Fe_{0.5}NC$-950 (H_2/O_2 60 cm^3 min^{-1}, 1 bar_g). Chen et al.[174] Mn-N-C degradation rate between 140-160 h and 0-20 h holds at 0.65 $V_{vs\ anode}$ (H_2/air, 200 cm^3 min^{-1}, 1 bar_g). Xie et al.[216] Co-N-C and Fe-N-C (H_2/air, 1 bar_g). Reproduced from reference [96] under Creative Commons CC BY 3.0

2.7 Translating RDE to PEMFC

2.7.1 Activity

Various studies have underscored the remarkable activity of different Pt nanoparticle shapes in RDE testing. However, this heightened activity has not translated effectively to enhanced performance in PEMFCs.[217] Notably, with regard to Fe-N-C catalysts, some investigations have indicated elevated RDE activity compared to that in PEMFCs, taking into consideration the influence of temperature.[169,218] Contrarily, Jaouen et al. demonstrated a nearly fivefold increase in activity for a specific Fe-N-C catalyst in PEMFCs relative to RDE, with temperature effects taken into account.[219] Conversely, a distinct Fe-N-C synthesized via an alternate method did not exhibit such disparities. This dissimilarity was attributed to anion adsorption on to protonated N from the H_2SO_4 electrolyte in RDE.[219]

Moreover, their research emphasized the critical nature of optimizing the catalyst ink formulation to achieve comparable O_2 reduction activities between RDE and PEMFCs.[219] Methods for optimizing the catalyst layer in PEMFCs have been developed for M-N-Cs,[220] although the optimization process remains time-consuming and reliant on trial-and-error methods. It is pertinent to note that the electrode preparation step can influence the properties of M-N-C and subsequent structure-activity-stability relationships.[173] The transition from a double to a triple phase boundary from half-cell to

PEMFC can also affect properties such as active site utilization and limitations in mass transport. Microenvironmental changes significantly influence the reaction kinetics as well.[221]

2.7.2 Stability

RDEs do not accurately represent degradation rates or conditions in PEMFCs. This is due to the completely different operating conditions and principles of each device. Of note is the fact that the mass activity and hence charge passed, is at least an order of magnitude lower in PEMFC compared to RDE. To demonstrate, a high-performance M-N-C on an RDE at 0.6 V_{RHE} in O_2-saturated 0.1 M $HClO_4$ with 1600 rpm can expect a current density around 5 mA cm^{-2}, equivalent to a mass activity of 25 A $g^{-1}_{M\text{-}N\text{-}C}$ at 0.2 $mg_{M\text{-}N\text{-}C}$ cm^{-2}. Meanwhile, the same M-N-C under H_2-O_2 operation in PEMFC can show (assuming sufficient catalyst properties) current density of 1 A cm^{-2}, equal to 250 A $g^{-1}_{M\text{-}N\text{-}C}$ for a loading of 4 $mg_{M\text{-}N\text{-}C}$ cm^{-2}. Another key parameter is temperature, where RDE studies typically operate at 25°C, rather than 80°C, which is used in PEMFCs.[222]

2.7.3 Gas Diffusion Electrode

Various gas diffusion electrode (GDE) structures have been designed, enabling the examination of catalyst performance and stability under high current conditions relevant to device operations, with lower system complexities compared to PEMFCs. It is noteworthy that there has been an increasing trend in studies employing GDEs with M-N-Cs in alkaline conditions, yet relatively few studies have integrated M-N-Cs into acidic GDE environments. Anticipatedly, the more frequent adoption of GDE tests will expedite the development of electrocatalysts and aid in traversing the "valley of death" in research and development.[223] Nonetheless, the utilization of electrolyte in GDEs still presents challenges in accurately simulating the behaviour of PEMFCs. The presence of electrolyte may lead to pH variations across the catalyst layer, necessitating further investigation through modelling approaches which has not been considered to date.

2.7.4 Microenvironment and pH

Although PEMFCs function within a strongly acidic bulk environment, it has been modelled that the pH increases along small mesopore channels, which remain isolated from direct contact with Nafion and are instead filled with water.[224] The active sites of M-N-Cs are believed to reside within micropores,[44,100,225] inaccessible to direct Nafion contact, and instead occupied by water during PEMFC operation (**Figure 2.15a**). It is pertinent to note that high surface area microporous M-N-C materials contain 10-20 wt.% water under standard atmospheric conditions.[226]

Consequently, the consumption of protons and O_2 at high current densities could potentially induce local pH variations at active sites, as recently examined during O_2 reduction down to pH 2 in RDE

tests.[227] If local pH changes do occur, it could have implications for the O_2 reduction pathway, activity, and degradation process. M-N-C are known to be more active under alkaline O_2 reduction.[184] Considering degradation pathway, it is essential to acknowledge Pourbaix diagrams.[228,229] Pourbaix diagrams have been developed for metal surfaces (at specific temperatures and concentrations) rather than single atoms species, however they may still broadly describe stable regions. For Fe surfaces (**Figure 2.15a**), at certain potentials with increased pH, Fe^{3+} and Fe^{2+} may form Fe_2O_3 species, commonly observed following stability assessments.[185,188] Moreover, concerning activity, at pH 7, the concentration of H^+ is 10^{-7} M, exerting a detrimental effect on kinetics.[116]

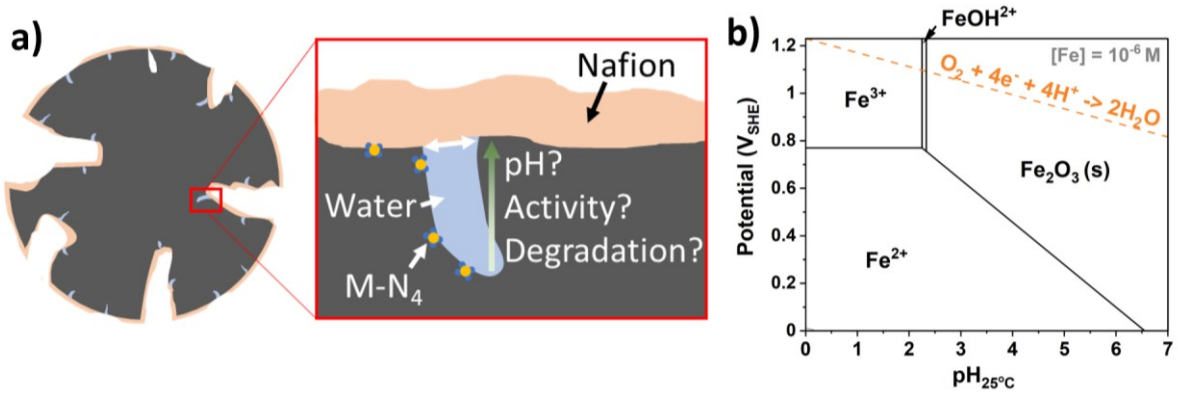


Figure 2.15. a.) Schematic representation of Fe-N-C particle with inset showing possible microenvironments around M-N_4 active site. b.) Pourbaix diagram of Fe metal at 25°C at concentration of 10^{-6} M. Figure a.) reproduced from reference [96] under Creative Commons CC BY 3.0. Fe pourbaix adapted from ref.[230]

2.7.5 PEMFC Device Considerations

2.7.5.1 Electronic Conductivity

Despite the acknowledged significance of electrical conductivity in electrocatalysis, only a limited number of studies have focused on measuring the conductivity of electrocatalysts in their prepared state or when integrated into electrodes. Boettcher and colleagues have extensively explored the impact of conductivity on the performance of oxygen evolution catalysts derived from abundant earth materials.[231] However, there remains a notable dearth of research specifically addressing the conductivity of M-N-Cs.[232–234] Notably, experimental measurements have indicated through-plane electron conductivity to be approximately three orders of magnitude lower than in-plane conductivity.[235] Moreover, given that the thickness of M-N-Cs is typically around ten times greater than that of Pt/C, the influence of electrical conductivity becomes more pronounced. For example, with a carbon support electron conductivity of 20 S m^{-1} and a catalyst layer thickness of 100 µm, a loss of 50 mV has been observed, as highlighted by Kulikovsky.[232] Similarly, Jaouen *et al*. modelled various proton and electron conductivity values, finding an 80 mV loss for an electron conductivity

of 20 S m^{-1} under the same catalyst thickness.[212] Their findings underscored the necessity of an electronic conductivity of 100 S m^{-1} to mitigate losses at high current densities.[212]

Jaouen and colleagues have referenced the potential influence of surface and local active site conductivity in other work.[164] They proposed that the generation of H_2O_2 in situ, leading to the exfoliation of graphene sheets or the oxidation of edges, might result in reduced conductivity specifically at the edges of graphene sheets. As these edges are typically the preferred locations for active sites, this phenomenon could significantly affect the turnover frequency, according to their findings.[164]

2.7.5.2 Ionomer and Protonic Conductivity

In RDE ionomer serves as a binder for the catalyst to adhere to the electrode, with protons supplied by the electrolyte. Meanwhile, in PEMFC the amount and distribution of the ionomer becomes pivotal to facilitating the O_2 reduction reaction. For instance the catalyst/ionomer interaction is dependent on catalyst properties (e.g. amount and type of O and N groups).[236] While PEMFC performance is dependent on many factors (preparation route e.g. hot pressing, electrode morphology, electrical conductivity), commonly one of the most crucial influences for optimum performance is the ionomer:Fe-N-C ratio.[220,237,238] Modelling from Jaouen and coworkers identified that proton conductivity of 5 S m^{-1} is required to prevent restriction of proton supply (and losses) at high current density in Fe-N-C based PEMFC.[212]

2.7.5.3 Hydrophobicity

The surface hydrophobic characteristics of the carbon support at M-N_x sites significantly impact water management and subsequently influence the performance of PEMFCs. Nevertheless, there is a notable lack of water vapor physisorption measurements within the M-N-C field, with some limited exploration observed for electrochemical CO_2 reduction by Strasser and co-workers.[239]

2.8 Commercialisation and Techno-economics

In 2015 James *et al.* conducted a techno-economic analysis of a polyaniline-based Fe-N-C, finding a low material production cost of 74-129 USD kg^{-1}, compared to ~41,000 USD kg^{-1} for a Pt-based alloys.[240] They further found that a power density of 475 mW cm^{-2} at 0.5 V was required to compete with the Pt cathode in PEMFCs. Since then, to the best of my knowledge, no other Fe-N-C techno-economic assessment has been publicly undertaken. Additionally, there has not been a consideration of how the technoeconomic assessment would be affected by the different monetized environmental impacts of Fe-N-C and Pt/C systems.

PGM-free cathodes in PEMFCs were first commercially demonstrated in 2017 by Ballard Power and Nisshinbo Holders.[241] This commercialised M-N-C has been reported to operate >500 h in PEMFC,[242] although the reported activity was not comparable to Pt-based catalysts. Here, they suggested that the M-N-C-based cathodes would be suitable for a low power emergency backup. This application is well-suited to the benefits of M-N-C which are remarkably poison tolerant to impurities and contaminants when compared to Pt-based catalysts.[196] Poor air quality and contamination can be likely scenarios in an emergency situation such as fires or volcanic eruptions. Since Nisshinbo's efforts, commercialisation efforts of M-N-Cs for fuel cells has been undertaken by Pajarito Powder, LLC (USA)[243,244] and lately Celcibus AB (Sweden).[245]

2.9 Novelty, Thesis Aims and Objectives

Based on the introduction, motivation and literature review, the novelty and aims of this thesis can be broken down into three parts. The objectives then proceed, detailing how these aims will be achieved.

Novelty and Aim: 1. Fe-N-C catalysts to date have typically possessed a mixture of active (FeN_x) and in-active sites (e.g. Fe_xO_y, Fe_3C), with electrochemical active site utilisation <10% (based on five electron nitrite stripping). Therefore, this thesis aims to synthesise and characterise a novel Fe-N-C containing purely Fe-N_x sites, with >>10% electrochemical active site utilisation. The Fe-N-C will be tested and optimised for O_2 reduction performance from RDE to PEMFC.

> **Objectives 1.** The Fe-N-C will be synthesized based on a decoupled pyrolysis and low temperature Fe loading method which will prevent formation of Fe_3C and other undesirable side phase from direct Fe-N-C pyrolysis. Confirmation of purely FeN_x will be provided by a combination of characterisation techniques (HAADF-STEM, XAS and Mossbauer). The accessibility and utilisation of FeN_x sites and high site density will be granted by using Mg as an active site template and porogen. These electrochemical metrics and the catalyst TOF will be evaluated based on in situ electrochemical techniques of nitrite stripping and FTacV. Optimisation of PEMFC testing will be based on electrochemical techniques including EIS, DRT and FTacV.

Novelty and Aim: 2. Previous *operando* and post-mortem ICP-MS studies have only considered low active site utilisation Fe-N-C under low current density conditions (<50 mA cm^{-2}). Additionally, kinetic degradation models of Fe-N-C have only been based on electrochemical data in PEMFC. Consequently, this thesis aims to monitor and kinetically model Fe dissolution of a high utilisation Fe-N-C under different operating regimes, including testing under device relevant operation (>50 mA cm^{-2}).

> **Objectives 2.** The Fe-N-C developed from Aim 1. will serve as a model catalyst to understand degradation due to its high active utilisation. Operation of online flow cell and GDE coupled to ICP-MS will enable *operando* tracking of Fe dissolution from FeN_x under active (O_2) and inert (Ar) conditions. RDE and GDE will run at both 25°C and close to 80°C to mimic real PEMFC operation. GDE O_2 reduction will exceed >50 mA cm^{-2} to represent PEMFC current densities. The pH/microenvironment and catalyst layer properties will be evaluated based on kinetic modelling with parameters based on experimental results. Post-mortem

characterisation will identify the fate of Fe (TEM, HAADF-STEM, XAS) and the contribution of Fe dissolution to performance degradation.

Novelty and Aim: 3. It has been assumed in the literature that Fe-N-C possess lower environmental impacts and manufacturing costs compared to Pt-based cathodes in PEMFCs. This assumption will be tested for the first time in this thesis via a comparative life cycle and techno-economic analysis of Fe-N-C versus Pt/C in PEMFCs. The techno-economic results will be used to determine the required performance of Fe-N-C to compete with Pt/C in PEMFCs.

Objectives 3. The analysis will be based on the amount of catalyst required to produce 80 kW (without considering durability). The Fe-N-C economic and environmental assessment will be based on commercial performance and synthesis to ensure the assessment is based on a scalable and commercially relevant production method. Pt/C values will be based on US DOE targets and inputs material and energy inputs obtained from literature. The environmental impact will be explored using different future scenarios. The environmental impacts will be monetized to understand the environmental cost compared to the direct production cost. Costs of material inputs will be obtained from quotes from industrial manufacturers. The techno-economic assessment will use dynamic learning curves to estimate PEMFC production costs at different scales.

References

1 Steffen, Will, Broadgate, Wendy, Deutsch, Lisa, Gaffney, Owen, and Ludwig, Cornelia, *Anthr. Rev.*, 2015, **2**, 81–98.
2 G. Ceballos, P. R. Ehrlich, A. D. Barnosky, A. García, R. M. Pringle and T. M. Palmer, *Sci. Adv.*, 2015, **1**, e1400253.
3 D. M. Etheridge, L. P. Steele, R. L. Langenfelds, R. J. Francey, J.-M. Barnola and V. I. Morgan, *J. Geophys. Res. Atmospheres*, 1996, **101**, 4115–4128.
4 C. MacFarling Meure, D. Etheridge, C. Trudinger, P. Steele, R. Langenfelds, T. van Ommen, A. Smith and J. Elkins, *Geophys. Res. Lett.*, 2006, **33**, 1–4.
5 C. D. Keeling, S. C. Piper, R. B. Bacastow, M. Wahlen, T. P. Whorf, M. Heimann and H. A. Meijer, *Exchanges of Atmospheric CO2 and 13CO2 with the Terrestrial Biosphere and Oceans from 1978 to 2000. I. Global Aspects*, Scripps Institution of Oceanography, San Diego, 2001.
6 United Nations Framework Convention on Climate Change, *Adoption of the Paris Agreement*, 2015.
7 R. C. Armstrong, C. Wolfram, K. P. de Jong, R. Gross, N. S. Lewis, B. Boardman, A. J. Ragauskas, K. Ehrhardt-Martinez, G. Crabtree and M. V. Ramana, *Nat. Energy*, 2016, **1**, 1–8.
8 International Energy Authority, Transport - Energy System, https://www.iea.org/energy-system/transport, (accessed November 7, 2023).
9 International Energy Agency, *World Energy Outlook*, 2022.
10 J. K. Nørskov, A. Latimer and C. F. Dickens, *Energy X: Research needs towards sustainable production of fuels and chemicals*, EU Horizon 2020, 2019.
11 A. Grimaud, J. Rossmeisl and P. Strasser, *Research needs towards sustainable production of fuels and chemicals*, Belgium, 2019.
12 K. Ayers, N. Danilovic, R. Ouimet, M. Carmo, B. Pivovar and M. Bornstein, *Annu. Rev. Chem. Biomol. Eng.*, 2019, 10, 219–239.
13 X. X. Wang, M. T. Swihart and G. Wu, *Nat. Catal.*, 2019, **2**, 578–589.
14 X. Tian, X. F. Lu, B. Y. Xia and X. W. Lou, *Joule*, 2020, **4**, 45–68.
15 International Energy Agency, *Global Hydrogen Review*, 2023.
16 International Energy Agency, *Global Hydrogen Review*, 2022.
17 International Energy Agency, *The Future of Hydrogen*, 2019.
18 B. Lu, Q. Liu and S. Chen, *ACS Catal.*, 2020, **10**, 7584–7618.
19 H. A. Gasteiger, S. S. Kocha, B. Sompalli and F. T. Wagner, *Appl. Catal. B Environ.*, 2005, **56**, 9–35.
20 B. James, *2018 Cost Projections of PEM Fuel Cell Systems for Automobiles and Medium-Duty Vehicles*, Strategic Analysis, Inc, Arlington, VA, 2018.
21 Office of Energy Efficiency and Renewable Energy, *Fuel Cell Technologies Office: Multi-Year Research, Development, and Demonstration Plan: 3.4 Fuel Cells*, Washington, 2016.
22 B. D. James, J. M. Huya-Kouadio, C. Houchins and D. A. DeSantis, *Final Report: Mass Production Cost Estimation of Direct H2 PEM Fuel Cell Systems for Transportation Applications (2012-2016)*, Strategic Analysis Inc., Golden, CO (United States), 2016.
23 Advanced Propulsion Centre UK, *Fuel Cell Industry Challenges 2020-2035+*, 2021.
24 C. Wei, R. R. Rao, J. Peng, B. Huang, I. E. L. Stephens, M. Risch, Z. J. Xu and Y. Shao-Horn, *Adv. Mater.*, 2019, **31**, 1806296.
25 S. T. Thompson, B. D. James, J. M. Huya-Kouadio, C. Houchins, D. A. DeSantis, R. Ahluwalia, A. R. Wilson, G. Kleen and D. Papageorgopoulos, *J. Power Sources*, 2018, **399**, 304–313.
26 W. Xia, A. Mahmood, Z. Liang, R. Zou and S. Guo, *Angew. Chem. Int. Ed.*, 2016, **55**, 2650–2676.
27 S. T. Thompson and D. Papageorgopoulos, *Nat. Catal.*, 2019, 2, 558–561.
28 H. Peng, F. Liu, X. Liu, S. Liao, C. You, X. Tian, H. Nan, F. Luo, H. Song, Z. Fu and P. Huang, *ACS Catal.*, 2014, **4**, 3797–3805.

29 F. Luo, A. Roy, L. Silvioli, D. A. Cullen, A. Zitolo, M. T. Sougrati, I. C. Oguz, T. Mineva, D. Teschner, S. Wagner, J. Wen, F. Dionigi, U. I. Kramm, J. Rossmeisl, F. Jaouen and P. Strasser, *Nat. Mater.*, 2020, **19**, 1215–1223.

30 R. Bellabarba, P. Johnston, S. Moss, C. Sievers, B. Subramaniam, C. Tway, Z. Wang and H. Zhu, *ACS Catal.*, 2023, **13**, 7917–7928.

31 A. Mehmood, M. Gong, F. Jaouen, A. Roy, A. Zitolo, A. Khan, M. Sougrati, M. Primbs, A. M. Bonastre, D. Fongalland, G. Drazic, P. Strasser and A. Kucernak, *Nat. Catal.*, 2022, **5**, 311–323.

32 L. Jiao, J. Li, L. L. Richard, Q. Sun, T. Stracensky, E. Liu, M. T. Sougrati, Z. Zhao, F. Yang, S. Zhong, H. Xu, S. Mukerjee, Y. Huang, D. A. Cullen, J. H. Park, M. Ferrandon, D. J. Myers, F. Jaouen and Q. Jia, *Nat. Mater.*, 2021, **20**, 1385–1391.

33 S. Liu, C. Li, M. J. Zachman, Y. Zeng, H. Yu, B. Li, M. Wang, J. Braaten, J. Liu, H. M. Meyer, M. Lucero, A. J. Kropf, E. E. Alp, Q. Gong, Q. Shi, Z. Feng, H. Xu, G. Wang, D. J. Myers, J. Xie, D. A. Cullen, S. Litster and G. Wu, *Nat. Energy*, 2022, **7**, 652–663.

34 H. Shen, T. Thomas, S. A. Rasaki, A. Saad, C. Hu, J. Wang and M. Yang, *Electrochem. Energy Rev.*, 2019, **2**, 252–276.

35 P. C. K. Vesborg and T. F. Jaramillo, *RSC Adv.*, 2012, **2**, 7933–7947.

36 E. Proietti, F. Jaouen, M. Lefèvre, N. Larouche, J. Tian, J. Herranz and J.-P. Dodelet, *Nat. Commun.*, 2011, **2**, 1–9.

37 M. Lefèvre, E. Proietti, F. Jaouen and J. P. Dodelet, *Science*, 2009, **324**, 71–74.

38 G. Wu, K. L. More, C. M. Johnston and P. Zelenay, *Science*, 2011, **332**, 443–447.

39 S. T. Thompson, A. R. Wilson, P. Zelenay, D. J. Myers, K. L. More, K. C. Neyerlin and D. Papageorgopoulos, *Solid State Ion.*, 2018, **319**, 68–76.

40 PEMFC based on platinum Group metAl free StrUctured cathodeS (PEGASUS), https://cordis.europa.eu/project/id/779550, (accessed January 27, 2022).

41 Critical Raw material ElectrocatalystS replacement ENabling Designed pOst-2020 PEMFC (CRESCENDO), https://cordis.europa.eu/project/id/779366, (accessed September 10, 2021).

42 J. D. Benck, T. R. Hellstern, J. Kibsgaard, P. Chakthranont and T. F. Jaramillo, *ACS Catal.*, 2014, **4**, 3957–3971.

43 F. Luo, S. Wagner, W. Ju, M. Primbs, S. Li, H. Wang, U. I. Kramm and P. Strasser, *J. Am. Chem. Soc.*, 2022, **144**, 13487–13498.

44 M. Primbs, Y. Sun, A. Roy, D. Malko, A. Mehmood, M.-T. Sougrati, P.-Y. Blanchard, G. Granozzi, T. Kosmala, G. Daniel, P. Atanassov, J. Sharman, C. Durante, A. Kucernak, D. Jones, F. Jaouen and P. Strasser, *Energy Environ. Sci.*, 2020, **13**, 2480–2500.

45 H. Zhang, L. Osmieri, J. H. Park, H. T. Chung, D. A. Cullen, K. C. Neyerlin, D. J. Myers and P. Zelenay, *Nat. Catal.*, 2022, 571–592.

46 J. Barrio, A. Pedersen, S. Favero, H. Luo, M. Wang, S. Ch. Sarma, J. Feng, L. T. T. Ngoc, S. Kellner, A. Y. Li, A. B. Jorge Sobrido and M.-M. Titirici, *Chem. Rev.*, 2023, **123**, 2311–2348.

47 A. Pedersen, J. Barrio, A. Li, R. Jervis, D. J. L. Brett, M. M. Titirici and I. E. L. Stephens, *Adv. Energy Mater.*, 2022, **12**, 2102715.

48 US DOE, *Technical Plan - Fuel Cells*, 2012.

49 N. M. Markovic and P. N. Ross, *CATTECH*, 2000, **4**, 110–126.

50 X.-Z. Yuan and H. Wang, in *PEM fuel cell electrocatalysts and catalyst layers: fundamentals and applications*, ed. J. Zhang, Springer, London, 2008, pp. 1–88.

51 W. R. Grove, *Lond. Edinb. Dublin Philos. Mag. J. Sci.*, 1839, **14**, 127–130.

52 G. Halpert, H. Frank and S. Surampudi, *Electrochem. Soc. Interface*, 1999, **8**, 25.

53 F. Barbir, in *PEM Fuel Cells: Theory and Practice*, Amsterdam ; London : Academic Press, 2005, pp. 1–16.

54 BMW, Step inside the new BMW iX5 Hydrogen, https://discover.bmw.co.uk/article/step-inside-the-new-bmw-ix5-hydrogen, (accessed November 1, 2023).

55 Hyundai, NEXO, https://www.hyundai.com/uk/en/models/nexo.html, (accessed November 1, 2023).
56 T. Yoshizumi, H. Kubo and M. Okumura, *SAE Tech. Pap.*, 2021, **2021-01–0740**, 1–6.
57 J.-H. Wee, *Renew. Sustain. Energy Rev.*, 2007, **11**, 1720–1738.
58 P. Vanýsek, *CRC Handbook of Chemistry and Physics*, CRC Press, Boca Raton, USA, 92nd edn., 2011.
59 S. Yang, A. Verdaguer-Casadevall, L. Arnarson, L. Silvioli, V. Čolić, R. Frydendal, J. Rossmeisl, I. Chorkendorff and I. E. L. Stephens, *ACS Catal.*, 2018, **8**, 4064–4081.
60 E. Yeager, *J. Mol. Catal.*, 1986, **38**, 5–25.
61 A. Bard and L. Faulkner, *Electrochemical Methods: Fundamentals and Applications*, John Wiley & Sons, New York, 2001.
62 J. K. Nørskov, J. Rossmeisl, A. Logadottir, L. Lindqvist, J. R. Kitchin, T. Bligaard and H. Jónsson, *J. Phys. Chem. B*, 2004, **108**, 17886–17892.
63 A. Kulkarni, S. Siahrostami, A. Patel and J. K. Nørskov, *Chem. Rev.*, 2018, **118**, 2302–2312.
64 N. Ramaswamy and S. Mukerjee, *Adv. Phys. Chem.*, 2012, **2012**, 1–17.
65 P. Sabatier, *Berichte Dtsch. Chem. Ges.*, 1911, **44**, 1984–2001.
66 J. K. Nørskov, J. Rossmeisl, A. Logadottir, L. Lindqvist, J. R. Kitchin, T. Bligaard and H. Jónsson, *J. Phys. Chem. B*, 2004, **108**, 17886–17892.
67 J. H. Zagal and M. T. M. Koper, *Angew. Chem. - Int. Ed.*, 2016, 55, 14510–14521.
68 A. S. Bandarenka, H. A. Hansen, J. Rossmeisl and I. E. L. Stephens, *Phys. Chem. Chem. Phys.*, 2014, **16**, 13625–13629.
69 I. E. L. Stephens, A. S. Bondarenko, F. J. Perez-Alonso, F. Calle-Vallejo, L. Bech, T. P. Johansson, A. K. Jepsen, R. Frydendal, B. P. Knudsen, J. Rossmeisl and I. Chorkendorff, *J. Am. Chem. Soc.*, 2011, **133**, 5485–5491.
70 K. D. Jensen, J. Tymoczko, J. Rossmeisl, A. S. Bandarenka, I. Chorkendorff, M. Escudero-Escribano and I. E. L. Stephens, *Angew. Chem. Int. Ed.*, 2018, **57**, 2800–2805.
71 H. Wan, A. Jensen, M. Escudero-Escribano and J. Rossmeisl, *ACS Catal.*, 2020, **10**, 5979–5989.
72 J. Pérez-Ramírez and N. López, *Nat. Catal.*, 2019, 2, 971–976.
73 Z. W. Seh, J. Kibsgaard, C. F. Dickens, I. Chorkendorff, J. K. Nørskov and T. F. Jaramillo, *Science*, 2017, **355**, eaad4998.
74 C. H. Kjaergaard, J. Rossmeisl and J. K. Nørskov, *Inorg. Chem.*, 2010, **49**, 3567–3572.
75 Z. F. Huang, J. Song, S. Dou, X. Li, J. Wang and X. Wang, *Matter*, 2019, **1**, 1494–1518.
76 J. Gopeesingh, M. A. Ardagh, M. Shetty, S. T. Burke, P. J. Dauenhauer and O. A. Abdelrahman, *ACS Catal.*, 2020, **10**, 9932–9942.
77 K. L. Svane, H. A. Hansen and T. Vegge, *J. Catal.*, 2021, **393**, 230–237.
78 J. H. Zagal and M. T. M. Koper, *Angew. Chem. - Int. Ed.*, 2016, **55**, 14510–14521.
79 H. Yan, Y. Lin, H. Wu, W. Zhang, Z. Sun, H. Cheng, W. Liu, C. Wang, J. Li, X. Huang, T. Yao, J. Yang, S. Wei and J. Lu, *Nat. Commun.*, 2017, **8**, 1–10.
80 J. Zhang, Q. Huang, J. Wang, J. Wang, J. Zhang and Y. Zhao, *Chin. J. Catal.*, 2020, **41**, 783–798.
81 R. Jasinski, *Nature*, 1964, **201**, 1212–1213.
82 H. Jahnke, M. Schönborn and G. Zimmermann, *Top. Curr. Chem.*, 1976, **61**, 133–181.
83 T. L. Poulos, *Chem. Rev.*, 2014, **114**, 3919–3962.
84 A. Y. Li, A. Pedersen, J. Feng, H. Luo, J. Barrio, J. Roman, K. K. (Mimi) Hii and M.-M. Titirici, *Green Chem.*, 2022, **24**, 7574–7583.
85 S.-T. Chang, C.-H. Wang, H.-Y. Du, H.-C. Hsu, C.-M. Kang, C.-C. Chen, J. C. S. Wu, S.-C. Yen, W.-F. Huang, L.-C. Chen, M. C. Lin and K.-H. Chen, *Energy Environ. Sci.*, 2012, **5**, 5305–5314.
86 R. M. Bullock, J. G. Chen, L. Gagliardi, P. J. Chirik, O. K. Farha, C. H. Hendon, C. W. Jones, J. A. Keith, J. Klosin, S. D. Minteer, R. H. Morris, A. T. Radosevich, T. B. Rauchfuss, N. A. Strotman, A. Vojvodic, T. R. Ward, J. Y. Yang and Y. Surendranath, *Science*, 2020, **369**, eabc3183.

87 M. Wikström, K. Krab and V. Sharma, *Chem. Rev.*, 2018, **118**, 2469–2490.
88 P. E. M. Siegbahn and M. R. A. Blomberg, *Chem. Rev.*, 2010, **110**, 7040–7061.
89 J. P. Collman, P. Denisevich, Y. Konai, M. Marrocco, C. Koval and F. C. Anson, *J. Am. Chem. Soc.*, 1980, **102**, 6027–6036.
90 J. P. Collman, M. Marrocco, P. Denisevich, C. Koval and F. C. Anson, *J. Electroanal. Chem.*, 1979, **101**, 117–122.
91 X. Wang, R. Clément, M. Roger, M. Bauzan, I. Mazurenko, A. De Poulpiquet, M. Ilbert and E. Lojou, *J. Am. Chem. Soc.*, 2019, **141**, 11093–11102.
92 H. Chen, O. Simoska, K. Lim, M. Grattieri, M. Yuan, F. Dong, Y. S. Lee, K. Beaver, S. Weliwatte, E. M. Gaffney and S. D. Minteer, *Chem. Rev.*, 2020, 120, 12903–12993.
93 J. A. Cracknell, K. A. Vincent and F. A. Armstrong, *Chem. Rev.*, 2008, **108**, 2439–2461.
94 Y. Liu, G. Zhou, Z. Zhang, H. Lei, Z. Yao, J. Li, J. Lin and R. Cao, *Chem. Sci.*, 2020, **11**, 87–96.
95 M. Primbs, Y. Sun, A. Roy, D. Malko, A. Mehmood, M.-T. Sougrati, P.-Y. Blanchard, G. Granozzi, T. Kosmala, G. Daniel, P. Atanassov, J. Sharman, C. Durante, A. Kucernak, D. Jones, F. Jaouen and P. Strasser, *Energy Environ. Sci.*, 2020, **13**, 2480–2500.
96 A. Pedersen, A. Bagger, J. Barrio, F. Maillard, I. Stephens and M.-M. Titirici, *J. Mater. Chem. A*, 2023, **11**, 23211–23222.
97 N. Karmodak, S. Vijay, G. Kastlunger and K. Chan, *ACS Catal.*, 2022, **12**, 4818–4824.
98 J. Shui, M. Wang, F. Du and L. Dai, *Sci. Adv.*, 2015, **1**, 1–8.
99 S. Liao, B. Li and Y. Li, in *PEM fuel cell electrocatalysts and catalyst layers: fundamentals and applications*, ed. J. Zhang, Springer, London, 2008, pp. 487–546.
100 F. Jaouen, M. Lefèvre, J.-P. Dodelet and M. Cai, *J. Phys. Chem. B*, 2006, **110**, 5553–5558.
101 H. T. Chung, D. A. Cullen, D. Higgins, B. T. Sneed, E. F. Holby, K. L. More and P. Zelenay, *Science*, 2017, **357**, 479–484.
102 L. Peles-Strahl, Y. Persky and L. Elbaz, *SusMat*, 2023, **3**, 44–57.
103 H. Ge, N. Bibent, K. Teixeira Santos, K. Kumar, J. Jaxel, M.-T. Sougrati, A. Zitolo, M. Dupont, F. Lecoeur, M. Mermoux, V. Martin, L. Dubau, F. Jaouen, F. Maillard and S. Berthon-Fabry, *ACS Catal.*, 2023, **13**, 1149–1163.
104 C. H. Choi, M. W. Chung, H. C. Kwon, J. H. Chung and S. I. Woo, *Appl. Catal. B Environ.*, 2014, **144**, 760–766.
105 X. Peng, L. Zhang, Z. Chen, L. Zhong, D. Zhao, X. Chi, X. Zhao, L. Li, X. Lu, K. Leng, C. Liu, W. Liu, W. Tang and K. P. Loh, *Adv. Mater.*, 2019, **31**, 1–7.
106 R. Ma, G. Lin, Q. Ju, W. Tang, G. Chen, Z. Chen, Q. Liu, M. Yang, Y. Lu and J. Wang, *Appl. Catal. B Environ.*, 2020, **265**, 118593.
107 Q. Lai, L. Zheng, Y. Liang, J. He, J. Zhao and J. Chen, *ACS Catal.*, 2017, **7**, 1655–1663.
108 L. Jiao, G. Wan, R. Zhang, H. Zhou, S. H. Yu and H. L. Jiang, *Angew. Chem. - Int. Ed.*, 2018, **57**, 8525–8529.
109 B. Nagy, S. Villar-Rodil, J. M. D. Tascón, I. Bakos and K. László, *Microporous Mesoporous Mater.*, 2016, **230**, 135–144.
110 S. Gong, C. Wang, P. Jiang, L. Hu, H. Lei and Q. Chen, *J. Mater. Chem. A*, 2018, **6**, 13254–13262.
111 Y. Zhao, J. Wan, H. Yao, L. Zhang, K. Lin, L. Wang, N. Yang, D. Liu, L. Song, J. Zhu, L. Gu, L. Liu, H. Zhao, Y. Li and D. Wang, *Nat. Chem.*, 2018, **10**, 924–931.
112 G. Lalande, G. Faubert, D. Guay, J. P. Dodelet and L. T. Weng, *J. Power Sources*, 1996, **61**, 227–237.
113 J. Li, L. Jiao, E. Wegener, L. L. Richard, E. Liu, A. Zitolo, M. T. Sougrati, S. Mukerjee, Z. Zhao, Y. Huang, F. Yang, S. Zhong, H. Xu, A. J. Kropf, F. Jaouen, D. J. Myers and Q. Jia, *J. Am. Chem. Soc.*, 2020, **142**, 1417–1423.
114 D. Menga, F. Ruiz-Zepeda, L. Moriau, M. Šala, F. Wagner, B. Koyutürk, M. Bele, U. Petek, N. Hodnik, M. Gaberšček and T. Fellinger, *Adv. Energy Mater.*, 2019, **9**, 1902412.

115 J. Y. Cheon, T. Kim, Y. Choi, H. Y. Jeong, M. G. Kim, Y. J. Sa, J. Kim, Z. Lee, T.-H. Yang, K. Kwon, O. Terasaki, G.-G. Park, R. R. Adzic and S. H. Joo, *Sci. Rep.*, 2013, **3**, 2715.
116 S. Rojas-Carbonell, C. Santoro, A. Serov and P. Atanassov, *Electrochem. Commun.*, 2017, **75**, 38–42.
117 A. Serov, K. Artyushkova, N. I. Andersen, S. Stariha and P. Atanassov, *Electrochimica Acta*, 2015, **179**, 154–160.
118 A. Cosenza, L. Delafontaine, A. Ly, H. Wang, E. Murphy, Y. Liu, S. Specchia and P. Atanassov, *J. Power Sources*, 2023, **556**, 1–10.
119 A. Mehmood, J. Pampel, G. Ali, H. Y. Ha, F. Ruiz-Zepeda and T.-P. Fellinger, *Adv. Energy Mater.*, 2018, **8**, 1701771.
120 J. Pampel, A. Mehmood, M. Antonietti and T.-P. Fellinger, *Mater. Horiz.*, 2017, **4**, 493–501.
121 J. Kong, A. M. Cassell and H. Dai, *Chem. Phys. Lett.*, 1998, **292**, 567–574.
122 S. Liu, M. Wang, X. Yang, Q. Shi, Z. Qiao, M. Lucero, Q. Ma, K. L. More, D. A. Cullen, Z. Feng and G. Wu, *Angew. Chem. Int. Ed.*, 2020, **59**, 21698–21705.
123 M. Primbs, E. Hornberger, P. Schroeer, S. Selve and P. Strasser, ECS, 2023.
124 L. Du, W. Huang, Y. Zhang, X. Liu and Y. Ding, *Chem. Commun.*, 2019, **55**, 1943–1946.
125 Y. Shao, Z. Guo, H. Li, Y. Su and X. Wang, *Angew. Chem. Int. Ed.*, 2017, **129**, 3274–3279.
126 A. L. Johnson and J. D. Parish, *ACS Symp. Ser.*, 2018, **1311**, 1–53.
127 B. C. Mallick, C. Hsieh, K. Huang, K. Yin and Y. A. Gandomi, *ECS J. Solid State Sci. Technol.*, 2019, **8**, N55–N78.
128 B. S. Lim, A. Rahtu and R. O. Y. G. Gordon, *Nat. Mater.*, 2003, **2**, 749–754.
129 L. Bai, C.-S. Hsu, D. T. L. Alexander, H. M. Chen and X. Hu, *J. Am. Chem. Soc.*, 2019, **141**, 14190–14199.
130 J. Zhang, J. Liu, L. Xi, Y. Yu, N. Chen, S. Sun, W. Wang, K. M. Lange and B. Zhang, *J. Am. Chem. Soc.*, 2018, **140**, 3876–3879.
131 C. Wei, R. R. Rao, J. Peng, B. Huang, I. E. L. Stephens, M. Risch, Z. J. Xu and Y. Shao-Horn, *Adv. Mater.*, 2019, **31**, 1–24.
132 J. Lu, X. Hai, S. Mitchell, E. Zurich, K. Harrath, H. Xu, D. Akl, D. Kong, J. Li, Z. Li, H. Yang, Y. Cui, C. Su, X. Zhao, J. Li and J. Pérez-Ramírez, *Nat. Nanotechnol.*, 2022, **17**, 174–181.
133 H. Yang, L. Shang, Q. Zhang, R. Shi, G. I. N. Waterhouse, L. Gu and T. Zhang, *Nat. Commun.*, 2019, **10**, 4585.
134 Y. Wen, M. D. R. Kok, J. P. V. Tafoya, A. B. J. Sobrido, E. Bell, J. T. Gostick, S. Herou, P. Schlee, M.-M. Titirici, D. J. L. Brett, P. R. Shearing and R. Jervis, *J. Energy Chem.*, 2021, **59**, 492–529.
135 C. Liu, J. Wang, J. Li, J. Liu, C. Wang, X. Sun, J. Shen, W. Han and L. Wang, *J. Mater. Chem. A*, 2017, **5**, 1211–1220.
136 J. Li, S. Brüller, D. C. Sabarirajan, N. Ranjbar-Sahraie, M. T. Sougrati, S. Cavaliere, D. Jones, I. V. Zenyuk, A. Zitolo and F. Jaouen, *ACS Appl. Energy Mater.*, 2019, **2**, 7211–7222.
137 F. Xie, X. Cui, X. Zhi, D. Yao, B. Johannessen, T. Lin, J. Tang, T. B. F. Woodfield, L. Gu and S.-Z. Qiao, *Nat. Synth.*, 2023, **2**, 129–139.
138 L. T. Song, Z. Y. Wu, F. Zhou, H. W. Liang, Z. Y. Yu and S. H. Yu, *Small*, 2016, **12**, 6398–6406.
139 J. Feng, R. Cai, E. Magliocca, H. Luo, L. Higgins, G. L. F. Romario, X. Liang, A. Pedersen, Z. Xu, Z. Guo, A. Periasamy, D. Brett, T. S. Miller, S. J. Haigh, B. Mishra and M.-M. Titirici, *Adv. Funct. Mater.*, 2021, **31**, 2102974.
140 H. Fei, J. Dong, Y. Feng, C. S. Allen, C. Wan, B. Volosskiy, M. Li, Z. Zhao, Y. Wang, H. Sun, P. An, W. Chen, Z. Guo, C. Lee, D. Chen, I. Shakir, M. Liu, T. Hu, Y. Li, A. I. Kirkland, X. Duan and Y. Huang, *Nat. Catal.*, 2018, **1**, 63–72.
141 N. Ramaswamy, U. Tylus, Q. Jia and S. Mukerjee, *J. Am. Chem. Soc.*, 2013, **135**, 15443–15449.
142 P. G. Santori, F. D. Speck, J. Li, A. Zitolo, Q. Jia, S. Mukerjee, S. Cherevko and F. Jaouen, *J. Electrochem. Soc.*, 2019, **166**, F3311–F3320.

143 Y. Chen, Y. Huang, M. Xu, T. Asset, X. Yan, K. Artyushkova, M. Kodali, E. Murphy, A. Ly, X. Pan, I. V. Zenyuk and P. Atanassov, *Mater. Today*, 2022, **53**, 58–70.
144 Y. Huang, Y. Chen, M. Xu, T. Asset, P. Tieu, A. Gili, D. Kulkarni, V. De Andrade, F. De Carlo, H. S. Barnard, A. Doran, D. Y. Parkinson, X. Pan, P. Atanassov and I. V. Zenyuk, *Mater. Today*, 2021, **47**, 53–68.
145 Y. Huang, Y. Chen, M. Xu, A. Ly, A. Gili, E. Murphy, T. Asset, Y. Liu, V. De Andrade, C. U. Segre, A. L. Deriy, F. De Carlo, M. Kunz, A. Gurlo, X. Pan, P. Atanassov and I. V. Zenyuk, *Mater. Today*, 2023, **69**, 66–78.
146 A. Serov, K. Artyushkova, E. Niangar, C. Wang, N. Dale, F. Jaouen, M.-T. Sougrati, Q. Jia, S. Mukerjee and P. Atanassov, *Nano Energy*, 2015, **16**, 293–300.
147 N. Larouche, D. Schmeisser, J. Dodelet and C. Senftenberg, *J. Am. Chem. Soc.*, 2014, **136**, 978–985.
148 U. I. Kramm, I. Herrmann-Geppert, S. Fiechter, G. Zehl, I. Zizak, I. Dorbandt, D. Schmeißer and P. Bogdanoff, *J. Mater. Chem. A*, 2014, **2**, 2663–2670.
149 G. J. Long and H. P. Leighty, *J. Chem. Educ.*, 1982, **59**, 948.
150 T. Sun, Y. Jiang, Q. Wu, L. Du, Z. Zhang, L. Yang, X. Wang and Z. Hu, *Catal. Sci. Technol.*, 2017, **7**, 51–55.
151 W.-J. Jiang, L. Gu, L. Li, Y. Zhang, X. Zhang, L.-J. Zhang, J.-Q. Wang, J.-S. Hu, Z. Wei and L.-J. Wan, *J. Am. Chem. Soc.*, 2016, **138**, 3570–3578.
152 G. Ketteler, W. Weiss, W. Ranke and R. Schlögl, *Phys. Chem. Chem. Phys.*, 2001, **3**, 1114–1122.
153 T. Woehrle, A. Leineweber and E. J. Mittemeijer, *HTM J. Heat Treat. Mater.*, 2010, **65**, 243–248.
154 S. Gupta, D. Tryk, I. Bae, W. Aldred and E. Yeager, *J. Appl. Electrochem.*, 1989, **19**, 19–27.
155 A. Mehmood, M. Gong, F. Jaouen, A. Roy, A. Zitolo, A. Khan, M. Sougrati, M. Primbs, A. M. Bonastre, D. Fongalland, G. Drazic, P. Strasser and A. Kucernak, *Nat. Catal.*, 2022, **5**, 311–323.
156 H. M. Fruehwald, I. I. Ebralidze, O. V. Zenkina and E. B. Easton, *ChemElectroChem*, 2021, **8**, 53–61.
157 Ellingham, H. J. T., *J. Soc. Chem. Ind.*, 1944, **63**, 125–160.
158 D. Menga, J. L. Low, Y.-S. Li, I. Arčon, B. Koyutürk, F. Wagner, F. Ruiz-Zepeda, M. Gaberšček, B. Paulus and T.-P. Fellinger, *J. Am. Chem. Soc.*, 2021, **143**, 18010–18019.
159 S. Horike, K. Kadota, T. Itakura, M. Inukai and S. Kitagawa, *Dalton Trans.*, 2015, **44**, 15107–15110.
160 A. Zitolo, V. Goellner, V. Armel, M. T. Sougrati, T. Mineva, L. Stievano, E. Fonda and F. Jaouen, *Nat. Mater.*, 2015, **14**, 937–942.
161 C. H. Choi, C. Baldizzone, G. Polymeros, E. Pizzutilo, O. Kasian, A. K. Schuppert, N. Ranjbar Sahraie, M.-T. Sougrati, K. J. J. Mayrhofer and F. Jaouen, *ACS Catal.*, 2016, **6**, 3136–3146.
162 P. Boldrin, D. Malko, A. Mehmood, U. I. Kramm, S. Wagner, S. Paul, N. Weidler and A. Kucernak, *Appl. Catal. B Environ.*, 2021, **292**, 120169.
163 C. H. Choi, H. K. Lim, M. W. Chung, G. Chon, N. Ranjbar Sahraie, A. Altin, M. T. Sougrati, L. Stievano, H. S. Oh, E. S. Park, F. Luo, P. Strasser, G. Dražić, K. J. J. Mayrhofer, H. Kim and F. Jaouen, *Energy Environ. Sci.*, 2018, **11**, 3176–3182.
164 V. Goellner, V. Armel, A. Zitolo, E. Fonda and F. Jaouen, *J. Electrochem. Soc.*, 2015, **162**, H403–H414.
165 R. Sibul, E. Kibena-Põldsepp, S. Ratso, M. Kook, M. Käärik, M. Merisalu, P. Paiste, J. Leis, V. Sammelselg and K. Tammeveski, *Electrochem. Commun.*, 2018, **93**, 39–43.
166 T. D. Bennett, S. Cao, J. C. Tan, D. A. Keen, E. G. Bithell, P. J. Beldon, T. Friscic and A. K. Cheetham, *J. Am. Chem. Soc.*, 2011, **133**, 14546–14549.
167 V. Armel, S. Hindocha, F. Salles, S. Bennett, D. Jones and F. Jaouen, *J. Am. Chem. Soc.*, 2017, **139**, 453–464.
168 S. Ratso, M. T. Sougrati, M. Käärik, M. Merisalu, M. Rähn, V. Kisand, A. Kikas, P. Paiste, J. Leis, V. Sammelselg, F. Jaouen and K. Tammeveski, *ACS Appl. Energy Mater.*, 2019, **2**, 7952–7962.

169 S. Ünsal, M. Bozzetti, Y.-C. Chen, R. Girod, A. Berger, J. S. Diercks, S. Gialamoidou, J. Lyu, M. Medarde, H. A. Gasteiger, V. Tileli, T. J. Schmidt and J. Herranz, *J. Electrochem. Soc.*, 2023, **170**, 074502.
170 B. G. Pollet and S. S. Kocha, *Johns. Matthey Technol. Rev.*, 2022, **66**, 61–76.
171 K. Shinozaki, J. W. Zack, R. M. Richards, B. S. Pivovar and S. S. Kocha, *J. Electrochem. Soc.*, 2015, **162**, F1144–F1158.
172 H. Kuroki, K. Onishi, K. Asami and T. Yamaguchi, *Ind. Eng. Chem. Res.*, 2019, **58**, 19545–19550.
173 V. A. Saveleva, K. Kumar, P. Theis, N. S. Salas, U. I. Kramm, F. Jaouen, F. Maillard and P. Glatzel, *ACS Appl. Energy Mater.*, 2023, **6**, 611–616.
174 M. Chen, X. Li, F. Yang, B. Li, T. Stracensky, S. Karakalos, S. Mukerjee, Q. Jia, D. Su, G. Wang, G. Wu and H. Xu, *ACS Catal.*, 2020, **10**, 10523–10534.
175 J. Cren, J. A. Jacques, C. Paulus, R. Couturier and B. Andre, *PEGASUS: D4.1-Life Cycle Assessment*, 2021.
176 R. Stropnik, A. Lotrič, A. Bernad Montenegro, M. Sekavčnik and M. Mori, *Energy Sci. Eng.*, 2019, **7**, 2519–2539.
177 F. Luo, C. H. Choi, M. J. M. Primbs, W. Ju, S. Li, N. D. Leonard, A. Thomas, F. Jaouen and P. Strasser, *ACS Catal.*, 2019, **9**, 4841–4852.
178 T.-P. Fellinger, D. Menga, A. G. Buzanich and F. Wagner, *Angew. Chem. Int. Ed.*, 2022, **61**, 1–5.
179 G. Bae, H. Kim, H. Choi, P. Jeong, D. H. Kim, H. C. Kwon, K.-S. Lee, M. Choi, H.-S. Oh, F. Jaouen and C. H. Choi, *JACS Au*, 2021, **1**, 586–597.
180 D. Malko, A. Kucernak and T. Lopes, *Nat. Commun.*, 2016, **7**, 13285.
181 R. Z. Snitkoff-Sol, A. Friedman, H. C. Honig, Y. Yurko, A. Kozhushner, M. J. Zachman, P. Zelenay, A. M. Bond and L. Elbaz, *Nat. Catal.*, 2022, **5**, 163–170.
182 D. H. Kim, S. Ringe, H. Kim, S. Kim, B. Kim, G. Bae, H.-S. Oh, F. Jaouen, W. Kim, H. Kim and C. H. Choi, *Nat. Commun.*, 2021, **12**, 1856.
183 E. Murphy, Y. Liu, I. Matanovic, M. Rüscher, Y. Huang, A. Ly, S. Guo, W. Zang, X. Yan, A. Martini, J. Timoshenko, B. R. Cuenya, I. V. Zenyuk, X. Pan, E. D. Spoerke and P. Atanassov, *Nat. Commun.*, 2023, **14**, 4554.
184 M. Gong, A. Mehmood, B. Ali, K.-W. Nam and A. Kucernak, *ACS Catal.*, 2023, **13**, 6661–6674.
185 K. Kumar, L. Dubau, M. Mermoux, J. Li, A. Zitolo, J. Nelayah, F. Jaouen and F. Maillard, *Angew. Chem. Int. Ed.*, 2020, **59**, 3235–3243.
186 G. Bae, M. M. Kim, M. H. Han, J. Cho, D. H. Kim, M.-T. Sougrati, J. Kim, K.-S. Lee, S. H. Joo, W. A. Goddard, H.-S. Oh, H. Kim, F. Jaouen and C. H. Choi, *Nat. Catal.*, 2023, 1–11.
187 Q. Jia, N. Ramaswamy, H. Hafiz, U. Tylus, K. Strickland, G. Wu, B. Barbiellini, A. Bansil, E. F. Holby, P. Zelenay and S. Mukerjee, *ACS Nano*, 2015, **9**, 12496–12505.
188 J. Li, M. T. Sougrati, A. Zitolo, J. M. Ablett, I. C. Oğuz, T. Mineva, I. Matanovic, P. Atanassov, Y. Huang, I. Zenyuk, A. Di Cicco, K. Kumar, L. Dubau, F. Maillard, G. Dražić and F. Jaouen, *Nat. Catal.*, 2021, **4**, 10–19.
189 L. Osmieri, R. K. Ahluwalia, X. Wang, H. T. Chung, X. Yin, A. J. Kropf, J. Park, D. A. Cullen, K. L. More, P. Zelenay, D. J. Myers and K. C. Neyerlin, *Appl. Catal. B Environ.*, 2019, **257**, 117929.
190 N. R. Sahraie, U. I. Kramm, J. Steinberg, Y. Zhang, A. Thomas, T. Reier, J. P. Paraknowitsch and P. Strasser, *Nat. Commun.*, 2015, **6**, 1–9.
191 X. Wan, X. Liu, Y. Li, R. Yu, L. Zheng, W. Yan, H. Wang, M. Xu and J. Shui, *Nat. Catal.*, 2019, **2**, 259–268.
192 J. Barrio, A. Pedersen, S. Ch. Sarma, A. Bagger, M. Gong, S. Favero, C. Zhao, R. Garcia-Serres, A. Y. Li, Q. Zhang, F. Jaouen, F. Maillard, A. Kucernak, I. E. L. Stephens and M. Titirici, *Adv. Mater.*, 2023, **35**, 2211022.
193 Y. Wang, M. J. Larsen, S. Rojas, M.-T. Sougrati, F. Jaouen, P. Ferrer, D. Gianolio and S. Berthon-Fabry, *J. Power Sources*, 2021, **514**, 230561.

194 X. Xie, L. Peng, H. Yang, G. I. N. Waterhouse, L. Shang and T. Zhang, *Adv. Mater.*, 2021, **33**, 2101038.
195 X. Xie, L. Shang, X. Xiong, R. Shi and T. Zhang, *Adv. Energy Mater.*, 2022, **12**, 2102688.
196 D. Malko, T. Lopes, E. Symianakis and A. R. Kucernak, *J. Mater. Chem. A*, 2015, **4**, 142–152.
197 M. Primbs, Y. Sun, A. Roy, D. Malko, A. Mehmood, M.-T. Sougrati, P.-Y. Blanchard, G. Granozzi, T. Kosmala, G. Daniel, P. Atanassov, J. Sharman, C. Durante, A. Kucernak, D. Jones, F. Jaouen and P. Strasser, *Energy Environ. Sci.*, 2020, **13**, 2480–2500.
198 K. Kumar, L. Dubau, F. Jaouen and F. Maillard, *Chem. Rev.*, 2023, **123**, 9265–9326.
199 T. Asset, F. Maillard and F. Jaouen, in *Supported Metal Single Atom Catalysis*, eds. P. Serp and D. P. Minh, Wiley, 2022, pp. 531–582.
200 M. Lefèvre and J. P. Dodelet, *Electrochimica Acta*, 2003, **48**, 2749–2760.
201 D. Banham, S. Ye, K. Pei, J. I. Ozaki, T. Kishimoto and Y. Imashiro, *J. Power Sources*, 2015, **285**, 334–348.
202 J. Herranz, F. Jaouen, M. Lefèvre, U. I. Kramm, E. Proietti, J. P. Dodelet, P. Bogdanoff, S. Fiechter, I. Abs-Wurmbach, P. Bertrand, T. M. Arruda and S. Mukerjee, *J. Phys. Chem. C*, 2011, **115**, 16087–16097.
203 U. I. Kramm, M. Lefèvre, P. Bogdanoff, D. Schmeißer and J. P. Dodelet, *J. Phys. Chem. Lett.*, 2014, **5**, 3750–3756.
204 V. Goellner, C. Baldizzone, A. Schuppert, M. T. Sougrati, K. Mayrhofer and F. Jaouen, *Phys. Chem. Chem. Phys.*, 2014, **16**, 18454–18462.
205 S. Ünsal, R. Girod, C. Appel, D. Karpov, M. Mermoux, F. Maillard, V. A. Saveleva, V. Tileli, T. J. Schmidt and J. Herranz, *J. Am. Chem. Soc.*, 2023, **145**, 7845–7858.
206 Q. Meyer, S. Liu, Y. Li and C. Zhao, *J. Power Sources*, 2022, **533**, 231058.
207 S. Liu, Q. Meyer, C. Jia, S. Wang, C. Rong, Y. Nie and C. Zhao, *Energy Environ. Sci.*, 2023, **16**, 3792–3802.
208 R. Chenitz, U. I. Kramm, M. Lefèvre, V. Glibin, G. Zhang, S. Sun and J.-P. Dodelet, *Energy Environ. Sci.*, 2018, **11**, 365–382.
209 C. H. Choi, C. Baldizzone, J.-P. Grote, A. K. Schuppert, F. Jaouen and K. J. J. Mayrhofer, *Angew. Chem. Int. Ed.*, 2015, **54**, 12753–12757.
210 T. Takahashi, T. Ikeda, K. Murata, O. Hotaka, Shigeki Hasegawa, Y. Tachikawa, M. Nishihara, J. Matsuda, T. Kitahara, S. M. Lyth, A. Hayashi and K. Sasaki, *J. Electrochem. Soc.*, 2022, **169**, 044523.
211 J. Zagal, M. Páez, A. A. Tanaka, J. R. dos Santos and C. A. Linkous, *J. Electroanal. Chem.*, 1992, **339**, 13–30.
212 F. Jaouen, E. Proietti, M. Lefèvre, R. Chenitz, J.-P. Dodelet, G. Wu, H. Taek Chung, C. Marie Johnston and P. Zelenay, *Energy Environ. Sci.*, 2011, **4**, 114–130.
213 H. Xie, X. Xie, G. Hu, V. Prabhakaran, S. Saha, L. Gonzalez-Lopez, A. H. Phakatkar, M. Hong, M. Wu, R. Shahbazian-Yassar, V. Ramani, M. I. Al-Sheikhly, D. Jiang, Y. Shao and L. Hu, *Nat. Energy*, 2022, **7**, 281–289.
214 Y. Chu, E. Luo, Y. Wei, S. Zhu, X. Wang, L. Yang, N. Gao, Y. Wang, Z. Jiang, C. Liu, J. Ge and W. Xing, *Chem Catal.*, 2023, **3**, 100532.
215 D. Shin, S. Bhandari, M. F. Tesch, S. A. Bonke, F. Jaouen, S. Chabbra, C. Pratsch, A. Schnegg and A. K. Mechler, *J. Energy Chem.*, 2022, **65**, 433–438.
216 X. Xie, C. He, B. Li, Y. He, D. A. Cullen, E. C. Wegener, A. J. Kropf, U. Martinez, Y. Cheng, M. H. Engelhard, M. E. Bowden, M. Song, T. Lemmon, X. S. Li, Z. Nie, J. Liu, D. J. Myers, P. Zelenay, G. Wang, G. Wu, V. Ramani and Y. Shao, *Nat. Catal.*, 2020, **3**, 1044–1054.
217 I. E. L. Stephens, J. Rossmeisl and I. Chorkendorff, *Science*, 2016, **354**, 1378–1379.
218 A. M. Damjanović, B. Koyutürk, Y.-S. Li, D. Menga, C. Eickes, H. A. El-Sayed, H. A. Gasteiger, T.-P. Fellinger and M. Piana, *J. Electrochem. Soc.*, 2021, **168**, 114518.

219 F. Jaouen, V. Goellner, M. Lefèvre, J. Herranz, E. Proietti and J. P. Dodelet, *Electrochimica Acta*, 2013, **87**, 619–628.
220 D. Malko, T. Lopes, E. A. Ticianelli and A. Kucernak, *J. Power Sources*, 2016, **323**, 189–200.
221 J.-Q. Zhong, K.-J. Yan, J. Yang, W.-H. Yang and X.-D. Yang, *ACS Catal.*, 2022, **12**, 9003–9010.
222 K. Kumar, T. Asset, X. Li, Y. Liu, X. Yan, Y. Chen, M. Mermoux, X. Pan, P. Atanassov, F. Maillard and L. Dubau, *ACS Catal.*, 2021, **11**, 484–494.
223 D. Siegmund, S. Metz, V. Peinecke, T. E. Warner, C. Cremers, A. Grevé, T. Smolinka, D. Segets and U.-P. Apfel, *JACS Au*, 2021, **1**, 527–535.
224 I. V. Zenyuk and S. Litster, *ECS Trans.*, 2013, **58**, 27–35.
225 U. I. Kramm, J. Herranz, N. Larouche, T. M. Arruda, M. Lefèvre, F. Jaouen, P. Bogdanoff, S. Fiechter, I. Abs-Wurmbach, S. Mukerjee and J. P. Dodelet, *Phys. Chem. Chem. Phys.*, 2012, **14**, 11673–11688.
226 A. Mehmood, J. Pampel, G. Ali, H. Y. Ha, F. Ruiz-Zepeda and T.-P. Fellinger, *Adv. Energy Mater.*, 2018, **8**, 1701771.
227 B. N. Ruggiero, K. M. Sanroman Gutierrez, J. D. George, N. M. Mangan, J. M. Notestein and L. C. Seitz, *J. Catal.*, 2022, **414**, 33–43.
228 M. J. N. Pourbaix, Delft, 1945.
229 M. Pourbaix, *Atlas of Electrochemical Equilibria in Aqueous Solutions*, National Association of Corrosion Engineers, 1974.
230 B. Beverskog and I. Puigdomenech, *Corros. Sci.*, 1996, **38**, 2121–2135.
231 D. Xu, M. B. Stevens, M. R. Cosby, S. Z. Oener, A. M. Smith, L. J. Enman, K. E. Ayers, C. B. Capuano, J. N. Renner, N. Danilovic, Y. Li, H. Wang, Q. Zhang and S. W. Boettcher, *ACS Catal.*, 2019, **9**, 7–15.
232 T. Reshetenko, A. Serov, M. Odgaard, G. Randolf, L. Osmieri and A. Kulikovsky, *Electrochem. Commun.*, 2020, **118**, 106795.
233 A. Kulikovsky, *Electrochem. Sci. Adv.*, 2021, **1**, e2000023.
234 Y.-S. Li, D. Menga, H. A. Gasteiger and B. Suthar, *J. Electrochem. Soc.*, 2023, **170**, 094503.
235 M. Ahadi, M. Tam, J. Stumper and M. Bahrami, *Int. J. Hydrog. Energy*, 2019, **44**, 3603–3614.
236 K. Artyushkova, M. J. Workman, I. Matanovic, M. J. Dzara, C. Ngo, S. Pylypenko, A. Serov and P. Atanassov, *ACS Appl. Energy Mater.*, 2018, **1**, 68–77.
237 G. Wang, L. Osmieri, A. G. Star, J. Pfeilsticker and K. C. Neyerlin, *J. Electrochem. Soc.*, 2020, **167**, 044519.
238 X. Yin, L. Lin, H. T. Chung, S. Komini Babu, U. Martinez, G. M. Purdy and P. Zelenay, *ECS Trans.*, 2017, **77**, 1273–1281.
239 W. Ju, A. Bagger, G.-P. Hao, A. S. Varela, I. Sinev, V. Bon, B. Roldan Cuenya, S. Kaskel, J. Rossmeisl and P. Strasser, *Nat. Commun.*, 2017, **8**, 1–9.
240 B. D. James, *DOE Hydrogen and Fuel Cells Program Review Fuel Cell Vehicle and Bus Cost Analysis*, 2015.
241 *Fuel Cells Bull.*, 2017, **2017**, 1.
242 D. Banham, J. Y. Choi, T. Kishimoto and S. Ye, *Adv. Mater.*, 2019, **31**, 1–6.
243 Pajarito Powder LLC, *Active and Durable PGM-free Cathodic Electrocatalysts for Fuel Cell Application*, 2021.
244 Pajarito Powder, https://pajaritopowder.com/, (accessed September 10, 2021).
245 Celcibus AB, https://celcibus.com/, (accessed September 30, 2023).

Chapter 3: Materials and Methodology

In this chapter I outline the protocols used to produce the materials which are studied hereafter. Brief and relevant background theory and experimental techniques which are used are then presented and discussed. Preparation, measurement, and equipment details are provided where the conditions and protocol remain consistent in subsequent chapters. Otherwise, the details are provided within the relevant chapter.

3.1 Catalyst Preparation

Chapters 3, 4 and 5 in this thesis entail the preparation of novel Fe-N-Cs, which are detailed below.

3.1.1 TAP X

The N-C precursor was formed from 2,4,6-triaminopyrimidine (97% Sigma Aldrich), denoted as TAP. TAP and magnesium chloride hexahydrate (99% Sigma Aldrich) in a weight ratio of 1:8 using a mortar and pestle. The resulting mixture was pyrolyzed in a ceramic crucible, filled to one-third of its capacity with the material, at temperatures ranging from 800 to 1000^{o}C for one hour under a N_2 atmosphere with a flow rate of 300 mL min^{-1} and a heating rate of 5^{o}C min^{-1}. The resulting materials were then collected, ground to a fine powder with a pestle and mortar and subjected to an overnight wash with 2 M HCl (prepared by diluting fuming 37% HCl, Merck) to eliminate any remaining $MgCl_2$ and MgO species. Following the washing process, the powders were filtered thoroughly with distilled water, dried at 80^{o}C under vacuum, and labelled as TAP X (where X represents the pyrolysis temperature).

3.1.2 TAP X@Fe

Fe was incorporated into the nitrogen moieties of the prepared TAP materials using a low-temperature wet impregnation method in methanol reflux. In this procedure, 60 mg of TAP X material was placed in a 250 mL round-bottom flask along with 75 mL of methanol (VWR, AnalaR NORMAPUR Reag. Ph. Eur., ACS) and stirred vigorously until a uniform dispersion was achieved. Subsequently, 75 mL of a methanol solution containing FeCl2 (98% purity, Sigma Aldrich) at a concentration of 25×10^{-3} M was added to the mixture, which was then refluxed at 90°C for 24 hours. Following Fe coordination, the resulting product was filtered, rinsed with methanol, and washed with 0.5 M H2SO4 (Sigma Aldrich, 95-98%) overnight to eliminate any

aggregated Fe species. Lastly, the obtained TAP X@Fe materials were filtered, thoroughly rinsed with distilled water, and dried under vacuum at 80°C.

3.1.2.1 TAP 900@^{57}Fe

The iron precursor, $^{57}FeCl_2$, was prepared through several steps, as reported by Kramm and coworkers.[1] First, ^{57}Fe (250 mg, Iron-57, 99.9% purity with 95.5% ^{57}Fe, Cambridge Isotope Laboratories) was added to a solution containing 1:1 ratio of 37% HCl (Fisher Chemical, analytical reagent grade) and H_2O (50 mL). The solution was then subjected to reflux at 115°C for 3 hours until complete dissolution. Subsequently, $^{57}FeCl_2$ was obtained by allowing the solution to evaporate under vacuum at 60°C for 3 hours, followed by overnight drying at 80°C and freeze drying overnight. TAP 900@^{57}Fe was then prepared in the same manner as TAP 900@Fe, but with $^{57}FeCl_2$ precursor.

3.2 Characterisation Techniques

The probing region of these techniques and others are summarised in **Figure 3.1**.

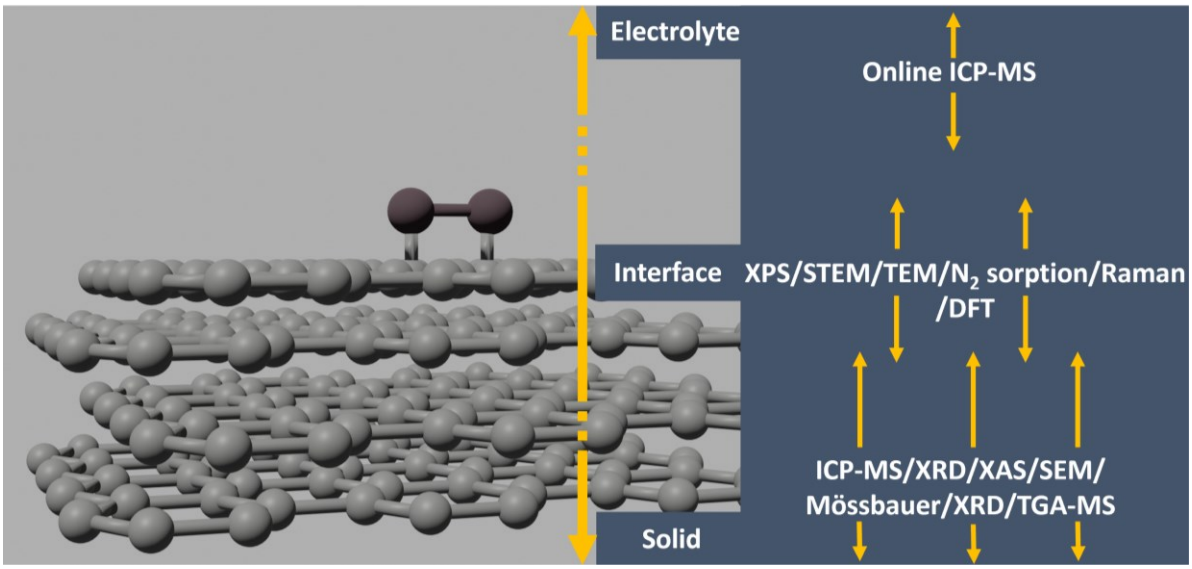


Figure 3.1. Different regions probed by characterisation techniques. Adapted from reference.[2]

3.2.1 XPS

XPS is a surface sensitive technique based on the principle of the photoelectric effect to determine elemental composition and their chemical states, which is critical for catalysis. Samples under analysis are irradiated with a monochromatic X-ray beam of specific energy, with the kinetic energy of the emitted secondary photoelectron (E_k) measured.[3] There is also the work function of the spectrometer (φ), which can be determined from calibration, e.g.,

with the binding energy of C 1s (284.8 eV).[3] The difference between the measured incident photon energy (*hv*) and the sum E_k and $\boldsymbol{\varphi}$ provides the binding energy, E_B:[3]

$$\boldsymbol{E_B = hv - E_K - \varphi} \qquad \textbf{Equation 3.1}$$

Where *hv* represents the energy of the x-ray beam, E_k is the kinetic energy of the secondary photoelectron, represents the work function of the detector.

The type of local coordination of the analysed atom can result in a shift in the binding energy, which can then be resolved with fitting based on known values. For example, N1s spectra can displays a distribution of different N environments (e.g., pyridinic, pyrrolic, graphitic, M-N). XPS peak intensity is related to the concentration of the analysed element, thus also providing quantitative information.

3.2.1.1 XPS Measurements

XPS was carried out using the Thermo Fisher K-Alpha XPS system, and subsequent spectral analysis was performed using the Avantage software. To account for charging effects, all spectra were calibrated using the carbon C1s peak at 284.8 eV as a reference point.

3.2.2 XAS

X-ray Absorption Spectroscopy (XAS) is a bulk method which is typically conducted at synchrotron facilities, offering insights into the electronic structure of materials.[4] As is the case in XPS, every element has a unique specific energy to excite core electrons, however, with XAS bulk information is obtained, rather than surface. Specifically, it can provide details about the oxidation states of catalyst atoms, the occupancy of d-orbitals, and the local symmetry through X-ray Absorption Near-Edge Spectroscopy (XANES).[4] Meanwhile, Extended X-ray Absorption Fine Structure (EXAFS) analysis, which usually involved Fourier transformed data, allows for the determination of coordination numbers and atomic bond distances within the material, based on fitting.[4] In the case of M-N-C, this information is critical to confirming atomically dispersed transition metals with N-coordination. It should be noted structures determined from XAS data are defined by a best-fit model, with the presented best-fit model not always having physical grounding. It is also difficult to resolve between certain elements such as N and O. Additionally, XAS provides sample-averaged information and from its nature as a bulk method, recognizes both electrochemically accessible and inaccessible sites. This implies that the identified sites may not necessarily contribute to the electrochemical activity.

3.2.3 Raman Spectroscopy

Raman spectroscopy is based on the principle of non-destructive Raman scattering phenomena,[5] which entails a laser (monochromatic light) interacting with a sample, causing some photons to be inelastically scattered at higher or lower wavelengths, known as Stokes or anti-Stokes, respectively. This is owing to the interaction of the light with molecular vibrations in the sample, where the energy shift to proportional to the sample's vibrational frequency. For the vibration to be Raman active it must induce a change in polarizability in the probed molecule. Raman spectroscopy can probe the hybridization of carbon on the sample surface, which can then determine the degree of graphitisation. In graphitic samples, prominent peaks include the G band (around 1580 cm^{-1}), which corresponds to carbon atoms in-plane vibrations (sp2 carbon atoms).[6] The D band (around 1355 cm^{-1}) arises from out-of-plane breathing mode from disordered carbon atoms.[6] Meanwhile, the 2D band (around 2700 cm^{-1}) indicates graphene layer stacking. A common approach to interpretating Raman spectra in carbon is comparing the intensity ratio of the D to G bands (I_d/I_g) based on either the peak height or peak area, where an increase in I_d/I_g demonstrates an increase in defects in the carbon surface.

3.2.3.1 Raman Spectroscopy Measurement Details

Raman spectra were acquired utilizing an inVia Renishaw confocal Raman microscope, where a LASER (Light Amplification by Stimulated Emission of Radiation) beam with a wavelength of 532 nm was employed. This LASER beam was focused through a 50× objective lens from Leica. To prevent any damage or burning of the samples, the intensity of the LASER was kept at 2.5 mW.

3.2.4 N_2 sorption

N_2 sorption is another non-destructive technique which can determine the pore volume and specific surface area based on N_2 interactions. Quantities of N_2 gas are dosed which adsorb on the sample surface, causing an increase in the relative pressure P/P_0 up until the saturation pressure. Desorption follows the reverse with removal of N_2 gas from the sample. The International Union of Pure and Applied Chemistry (IUPAC) defined six general classifications of isotherms, which result from certain material properties.[7]

The Brunauer-Emmett-Teller (BET) is a commonly applied method to determine the specific surface area of a sample, based on a monolayer of N_2 physisorption. It is based on the

assumptions that: (1) Gaseous molecules adsorb physically on a solid infinitely. (2) Gaseous molecules interact only with the neighbouring layer. (3) All adsorption sites are energetically identical. (4) Only adsorbate-adsorbent interactions are considered, with no lateral adsorbate-adsorbate interactions with the same layer. (5) Langmuir theory is applicable to each layer. (6) Adsorption enthalpy for the first layer of adsorption is constant and higher than subsequent layers. (7) Adsorption enthalpy for the second layer and above is equivalent to the enthalpy of liquefaction.

The specific surface area is calculated based on transforming the isotherm into a linear plot using Equation *3.2* and deriving a monolayer capacity value, n_m:

$$\frac{\boldsymbol{P/P_0}}{\boldsymbol{n(1-(P/P_0)}} = \frac{\boldsymbol{1}}{\boldsymbol{n_m C}} + \frac{\boldsymbol{C-1}}{\boldsymbol{n_m C}}\left(\frac{\boldsymbol{P}}{\boldsymbol{P_0}}\right) \qquad \textbf{Equation 3.2}$$

Where *C* is a constant and *n* is the specific amount of adsorbed gas at the relative pressure.

The BET surface area, S_{BET}, can then be found using molecular cross-sectional area of the gas molecule, σ, e.g., 0.162 nm^2 for N_2 at 77 K.

$$\boldsymbol{S_{BET}} = \frac{\boldsymbol{n_m\, \sigma N_A}}{\boldsymbol{m_{sample}}} \qquad \textbf{Equation 3.3}$$

Where N_A is Avogadro's number and m_{sample} is the sample mass.

Rouquerol developed a procedure to reduce the subjectivity in the monolayer capacity assessment in microporous materials, based on two criteria:[8]

1. C must be positive. A negative value is non-physical.
2. The range selection of P/P_0 should increase linearly with $V(1-P/P_0)$, up to a maximum point.

To reduce human error, this process has recently been automated with BET Surface Identification software.[9] However, error from N_2 sorption still arises due to the quadrupole moments of nitrogen, which makes its orientation dependent on the adsorbents surface chemistry. Another method from Barrett, Joyner and Halenda (BJH), based on the Kelvin model of pore filling, can accurately calculate values for purely meso- and macro-porous material, however it cannot be applied to microporous materials. This is due to the BJH not accounting for interactions between the pore surface and sorption fluid, which are significant in the micropore region. This can leads to underestimate between 20-30% for <10 nm pore

size.[7] These limitations can be avoided by applying methods based on DFT. Non-local density functional theory (NLDFT) models have been developed to determine the pore size and distribution based on the gas adsorption isotherms and its fluid density under the conditions. Based on the model used, the results can generate theoretical isotherms which an account for porosity across the entire micro-, meso- and macropore distribution.[10] For graphene-like carbon, the heterogeneous surface carbon 2D NLDFT method incorporates appropriate energetical heterogeneity and geometrical corrugation of the carbon surface, thus avoiding artefacts.[11]

3.2.4.1 N_2 Sorption Measurement Details

Isotherms were obtained at a temperature of -196°C within a pressure range spanning from 10^{-5} to 0.99, utilizing a Micromeritics 3Flex system. The samples were subjected to a degassing process, lasting for a duration of 16 hours, at a temperature of 200°C. The BET specific surface area was determined using BET Surface Identification software.[9] This calculation was based on the adsorption isotherm within the relative pressure range of <0.3, employing the optimal region for a linear fit comprising 10 data points (with an R-squared value exceeding 0.995), based on the Rouquerol method.[10] The pore size distribution was derived from the adsorption isotherm using a heterogeneous surface carbon 2D-non-local density functional theory (NLDFT) approach. The resulting pore size distribution was plotted over a range spanning from 0.3 to 50.0 nm, utilising SAIEUS software version 3.06.

3.2.5 XRD

During X-ray diffraction (XRD) measurements, X-rays are directed towards the sample, and depending on the crystalline structure of the sample, X-ray will be diffracted at certain angles, according to the spacing between atomic planes, as described by Bragg's law:

$$n\lambda = 2dsin\theta \qquad \textbf{Equation 3.4}$$

Where *d* Is the interplanar spacing, 2θ is the diffracted angle of the beam relative to the incident x-ray beam, λ represents the wavelength of the incident x-rays and *n* is an integer.

When measuring powder samples all diffraction directions need to be measured to the random orientation. The intensity of specific peak depends on the number of moieties with that particular crystallographic phase, and if the concentration of a particular crystalline domain is too low it a diffraction peak will not appear. The width is inversely proportional to

the crystal size. A broad peak is indicative of a small crystal domain or an amorphous phase such as carbon.

3.2.5.1 XRD Measurement Details

XRD patterns were acquired utilizing a PANanalytical X'PERT PRO powder X-ray diffractometer, employing a Cu Kα source, which was operated at 45 kV and 30 mA, with a scan step size of 0.033°.

3.2.6 ICP-MS

ICP-MS is a sensitive technique which can quantitatively detect (dissolved) metals and some non-metals down to parts-per-trillion, 10^{-12}.[12] The main components of an ICP-MS system include the torch assembly, nebulizer, spray chamber, ion deflector, mass filter and finally detector (**Figure 3.2**). First the nebulizer creates a fine aerosol from the sample solution with Ar gas, for introduction into the plasma. However, before that, the spray chamber filters droplets to <10 μm diameter. The plasma is created by an intense magnetic field tangential to the flow of gas, causing the gas to ionise, which forms a high temperature (around 10^3 K) plasma after introduction of a high voltage spark. The plasma torch generates positively charged ions which are then guided to the mass spectrometer interface under 1-2 torr vacuum via a sampler and skimmer cone. Ions then pass into the mass spectrometer analyser with a vacuum pressure of 10^{-6} torr. Mass separation is based on allowing ions of interest with a particular mass to charge ratio (m/z) to pass through the detector, typically using a quadrupole separator. Finally, ions are converted to an electric signal by a detector.[12]

In 2011, the first successful demonstration of coupling electrochemical measurements to on-line ICP-MS was conducted by Mayrhofer and coworkers.[13] This allowed measurements of metals, typically the active centre, under dynamic conditions, providing a wealth of information on degradation mechanisms.[14]

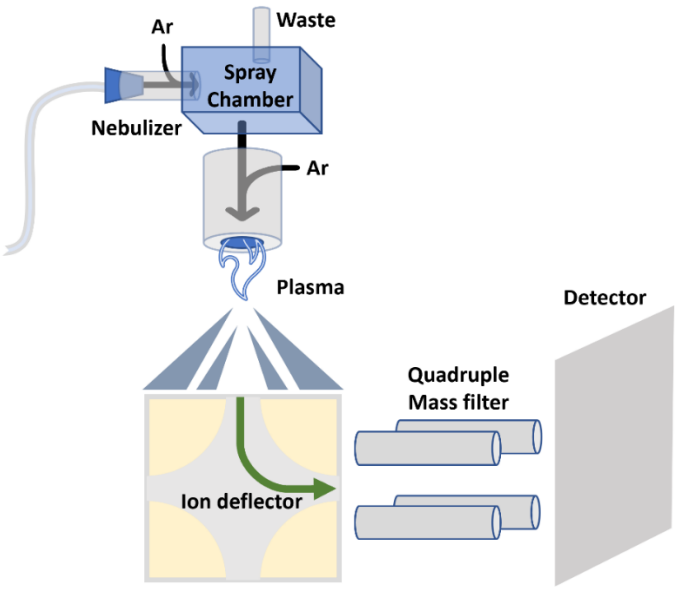


Figure 3.2 Simplified illustration of ICP-MS operation.

3.2.6.1 Ex-Situ ICP-MS Measurement Details

ICP-MS data were obtained using an Agilent 7900 spectrometer manufactured by Agilent Technologies. To prepare the samples for ICP-MS analysis, material was initially digested in aqua regia. Aqua regia was made up of 25% volume/volume (v/v%) nitric acid (HNO3, 70%, Certified AR, Eur.Ph., Fisher Chemical, Fisher Scientific) and 75% v/v% hydrochloric acid (HCl, 37%, Certified AR, Eur.Ph., Fisher Chemical, Fisher Scientific). The digestion process was carried out using a MARS 6 microwave at a power level of 1,500 watts for a duration of 15 minutes at a temperature of 215°C. Subsequently, the resulting solutions were diluted and analysed. The analysis was performed against calibration standards, specifically containing concentrations of 0, 2, 50, 100, 200, and 500 parts ppb.

3.2.7 TGA-MS

Thermal gravimetric analysis coupled to mass spectrometry (TGA-MS) is a powerful technique to determine rection pathways during pyrolysis.[15] In this setup, the mass of the sample is monitored while being heated and evolved gases are detected by MS.

3.2.8 EPR

Electron Paramagnetic Resonance (EPR) spectroscopy probes unpaired electrons within materials, such as radicals or transition metal ions, using a magnetic field. Paramagnetic species in samples under a magnetic field and with microwave radiation will experience a

change in the energy level of the electrons at certain frequencies. X-band EPR uses a microwave frequency around 9.5 GHz and an applied magnetic field of around 0.3 T.[16] Continuous wave EPR involves sample irradiation from low intensity monochromatic microwaves. Absorption occurs when the energy of the electromagnetic wave (*hv*) equals the energy difference of the two energy states of the electron. The interaction between the unpaired electron(s) and the magnetic field is described by *g* values according to the following:

$$\Delta \boldsymbol{E} = \boldsymbol{hv} = \boldsymbol{g}\, \boldsymbol{\mu_B} \boldsymbol{B_0} \qquad \textbf{Equation 3.5}$$

Where *h* is Planck's Constant (6.63×10^{-34} J s^{-1}), *v* is the microwave frequency, μ_B is the Bohr Magneton (9.27×10^{-24} J T^{-1}) and B_o is the magnetic field strength (T).

The *g* value depends on the molecular environment and the spin-orbit interaction, which scales with the atomic number. Therefore, the *g* value provides a fingerprint for identifying compounds. From this, information on the oxidation and spin state can be obtained, as well as possible quantitative information. The fast relaxation times of transition metal complexes can lead to extensive broadening of EPR spectrum. To combat this, cryogenic temperature (e.g. 5 K) can be used slow the relaxation times.[16] For Fe, the most common oxidation states are Fe^{II} or Fe^{III}, which have 6 and 5 e^- in their d-orbitals. Fe^{III} can contain unpaired electrons in any of its spin states with half integer spin (S=1/2, 3/2 or 5/2), which are all detectable by EPR. However, X-band EPR is not sensitive towards Fe^{II} (states of S=1 and S=2) due to large field splitting only has unpaired electrons in spin

3.2.8.1 EPR Measurement Details

Continuous-wave electron paramagnetic resonance (EPR) measurements using an X-band CW ELEXSYS E500 EPR spectrometer manufactured by Bruker. The spectrometer was equipped with a cryogen-free variable temperature cryostat from Oxford Instruments. Materials were placed in a 3 mm Wilmad quartz (CFQ) EPR tube obtained from Sigma Aldrich. The EPR spectra were recorded at a temperature of 5 K and a frequency of 9.71 GHz. The experimental setup utilized 20 milliwatts (mW) of incident microwave power, a modulation frequency of 100 kilohertz (kHz), a modulation amplitude of 1 Gauss (G), a power attenuation of 10 decibels (dB), and a magnetic field sweeping increment of 0.5 Gauss, ranging from 50 to 7000 Gauss.

3.2.9 Mössbauer Spectroscopy

Mössbauer spectroscopy is based on the recoilless nuclear resonance absorption of gamma rays in solid samples and relies on detection of isotopes of elements. For Fe-N-C, it can offer characterisation of ^{57}Fe sites oxidation and spin states through fingerprints on their local electronic configuration and coordination.[17,18] There are three parameters, composed of three separated interactions: isomer shift, quadrupole splitting and magnetic interaction. Isomer shift depends on electric monopole interaction. [19] Quadrupole splitting is caused by an electric field gradient at the iron nucleus and defines the deviation from cubic symmetry.[19] Magnetic interactions are based on selection rules, which for Fe can lead to six different transitions (for ferro-, ferri-, and antiferromagnetic moieties), which form sextets in Mössbauer spectra.[19] To resolve between superparamagnetic species (e.g., nanometric Fe_xO_y) and atomic FeN_x sites, cryogenic conditions are required.[20,19] This is because the probability of recoilless nuclear resonance increases with decreasing temperature.[19]

3.2.9.1 Mössbauer Spectroscopy Measurement Details

Mössbauer spectra were recorded at a temperature of 5 K using a strong-field Mössbauer spectrometer that featured an Oxford Instruments Spectromag 4000 cryostat housing an 8 T split-pair superconducting magnet. The spectrometer operated in a constant acceleration mode and utilized a transmission geometry setup. To reference the isomer shifts, a room-temperature metallic Fe foil was employed as the standard. Data analysis was carried out using the Python software package easyMoss previously developed by Garcia-Serres.[21]

3.2.10 Electron Microscopy

3.2.10.1 SEM

Scanning electron microscopy (SEM) is useful for imaging the bulk structure and morphology of conductive catalyst particles and layers, based on an electron beam interacting with the sample, causing secondary electrons, and backscattered to be emitted, which are detected for imaging.[22]

3.2.10.2 TEM

Transmission electron microscopy (TEM) operates in a different fashion to SEM. In TEM the electron beam transmits through the sample to form an image on the detector, thus requiring atomically thin (~100 nm) samples.[23] The benefit to this operation is the higher resolution

that can be achieved, providing information on crystalline, although information on the 3D structure and samples is restricted.

3.2.10.3 HAADF-STEM

Aberration-corrected Scanning Transmission Electron Microscopy (STEM) is a technique capable of producing images with atomic resolution, by using a convergent beam on the sample (unlike TEM which uses a parallel beam). This technique is particularly useful for visualizing the distribution and arrangement of transition metal atoms in the catalyst.

Various imaging modes are available, depending on the angle at which the detector is placed. High-Angle Annular Dark-Field (HAADF)-STEM is a specific imaging mode where the detector is placed at a high angle (>50 mrads) relative to the incident beam. In HAADF-STEM, transition metal atoms in catalytic sites appear brighter in the images due to their higher atomic numbers compared to the catalyst support (N and C).[24] HAADF-STEM has conclusively shown the atomic structure in Fe-N_4 sites.[25] Although beam damage needs to be considered when imaging metallic single atoms, which can be unstable.[26]

3.2.10.4 EELS

Electron Energy-Loss Spectroscopy (EELS) measures the loss of energy an electron experiences as it interacts with a sample.[27] It can be combined with microscopy techniques to, however beam damage is even more problematic in STEM-EELS owing to inefficiencies in inelastic core-loss scattering, but can be reduced by advanced data collection and analysis methods.[28]

3.2.10.5 EDX

Energy dispersive X-ray spectroscopy (EDX) can also be coupled to the microscopy techniques above, enabling elemental mapping of samples. Here, a primary high energy electron beam causes electrons in the sample to reach a higher energy level excited state. This electron eventually relaxes to its ground state, emitting an x-ray. The energy of this x-ray is characteristic of each element and transition, allowing its identification and quantification.[22] The drawbacks to EDX is the lower reduced sensitivity and spatial resolution compared to STEM-EELS.[27]

3.2.11 DFT

DFT is a mathematical method which can be used to determine an approximate solution of the Schrödinger equation for a multi-bodied system. This solution is a probability function, known as a wave function, describing the likelihood of locating an electron at a certain energy level. Consequently, solving Schrödinger's equation with relatively low computational costs can provide properties and structure of solids, liquids, and gases. DFT can be used to identify trends and explain help predict or explain experimental results.

3.3 Electrochemical Techniques

3.3.1 RDE

Membrane Electrode Assemblies (MEAs) offer the most accurate representation of catalyst performance in PEMFCs. However, utilizing MEAs involves relatively high catalyst quantities and materials and a time-consuming measurement process for screening catalysts.[29] Instead, RDEs are the most commonly used initial screening tool due to their rapid testing, low catalyst amounts and wealth of information they can provide. Initial electrochemical activity assessments evaluate cyclic voltammetry and electrochemical impedance spectroscopy (EIS). RDE tests can determine critical electrochemical properties such as the kinetic current density and mass activity, reaction mechanism, product selectivity and the turnover frequency (TOF) of catalysts. Trends in activity between RDE and fuel cells have been shown, demonstrating RDEs as a sufficient screening tool.[29]

RDEs can function either in a stationary or rotating mode. In the rotating mode, forced convection is introduced to the system, significantly enhancing mass transport by drawing reactants toward the electrode surface and expelling reacted species outward in a laminar flow pattern. Even in the rotating mode, a small stagnant diffusion layer exists on the electrode surface. In contrast, stationary RDE operation primarily relies on mass transport via diffusion.[30]

An illustration of a typical three-electrode cell used for O_2 reduction is shown in **Figure 3.3a**, with labels indicating the working electrode (5 mm glassy carbon where catalyst is deposited), counter electrode (graphite rod), reference electrode (Ag/AgCl), gas inlet and electrolyte. Perchloric acid ($HClO_4$) is selected as the electrolyte for RDE measurements since it is known ClO_4^- adsorbs weaker than SO_4^- which is the other commonly used anion.[31] The O_2 reduction current density in RDE is limited to ~6 mA cm^{-2} at 1,600 rpm due to the very low solubility of

O_2 in aqueous electrolyte solutions.[29] For instance, the solubility of O_2 is 1.1×10^{-3} mol dm^{-3} in 0.1 M H_2SO_4 at standard temperature and pressure.[32]

3.3.1.1 CV and LSV

Cyclic voltammetry (CV) and linear sweep voltammetry (LSV) are the common approaches to assess the electrochemical response and activity of catalysts. As the names suggest, CVs sweep the potential at a certain scan rate between two set potentials and the sweep is then conducted in the reverse direction, while LSV only sweeps the potential in one direction.[33] These measurements result in a voltammogram, which is a plot of current versus potential.

A typical O_2 reduction curve is depicted in **Figure 3.3b**, with the labelled regions of kinetic, mixed kinetic-diffusion and diffusion controlled.

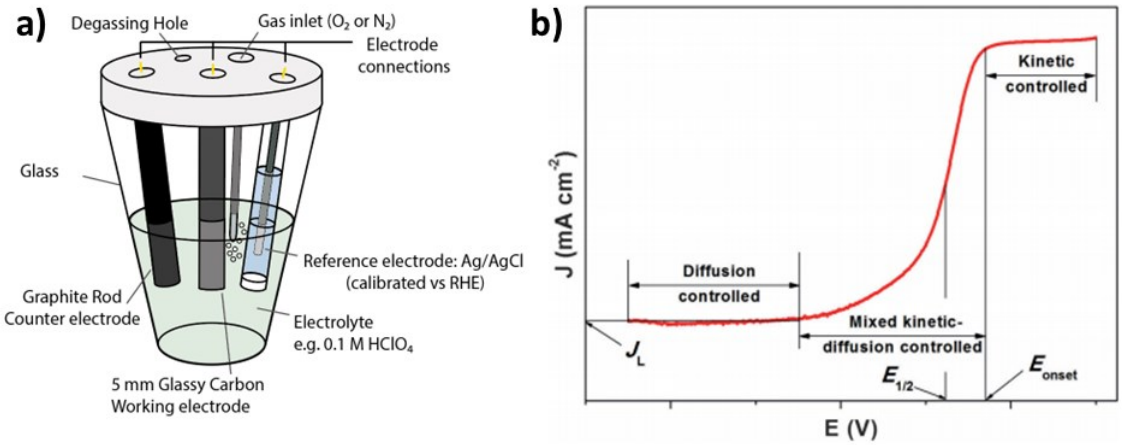


Figure 3.3. a.) Illustration of three-electrode cell used in this thesis with labelled components. b.) RDE O_2 reduction linear sweep voltammetry. Figure b.) Reproduced from reference [34] with permission. Copyright 2016, Wiley-VCH.

3.3.1.2 iR-correction

The resistance of the electrolyte between the reference and working electrode (*R*) in RDE *i-V* measurements causes an ohmic potential drop (*iR*) which can be accounted for by **Equation 3.6**.

$$E_{RHE,iR-free} = E_{RHE} - iR \qquad \textbf{Equation 3.6}$$

Where E_{RHE} is potential versus RHE, i is measured current (A) and *R* is the electrolyte solution resistance (Ω).

The resistance mainly arises from the low electrolyte concentration and distance between the reference and working electrode. For 0.1 M $HClO_4$ at 293 K with a distance between the

working and reference electrode of 10-20 mm, the resistance will be around 20-30 Ω.[35] *R* in can be determined using the "current interrupt" technique or from electrochemical impedance spectroscopy (EIS – See Section 3.3.4).[36]

3.3.1.3 Capacitance Correction

When conducting O_2 reduction measurements, background capacitive current is observed from the electric double layer on the electrode and catalysts, which linearly depends on the scan rate:

$$j = C_{DL}\frac{dE}{dt} \qquad \textbf{Equation 3.7}$$

Where *j* is the current, C_{DL} is the double layer capacitance and *dE/dt* is the scan rate.

To minimize capacitive currents, it is advised to utilize scan rates of 20 mV s^{-1} or lower, with 5 mV s^{-1} removing the need for capacitive correction.[37] However, there is evidence suggesting that employing a scan rate of 20 mV s^{-1} enhances the reproducibility of CV outcomes and demonstrates greater stability, particularly in the presence of elevated contaminant concentrations.[38]

3.3.1.4 Reference Electrode Calibration

To convert between the potential of the reference electrode to that of the reference hydrogen electrode (RHE), the Nernst equation can be used:

$$E_{RHE} = E_{Ag/AgCl} + 0.059pH + E^{\circ}_{Ag/AgCl} \qquad \textbf{Equation 3.8}$$

Where $E_{Ag/AgCl}$ is the potential versus the Ag/AgCl reference and $E^{\circ}_{Ag/AgCl}$ = 0.21 V at 20 °C.

However, it is critical to calibrate non-RHE reference electrode regularly since the $E^{\circ}_{Ag/AgCl}$ of the reference electrode likely varies and also drifts over time due to change in the concentration of Ag/AgCl over time to check for drift and ensure correct potential are reported, rather than those calculated from Nernst-based equations.

Ag/AgCl calibration was carried out as reported by Wei *et al.*[39] Prior to each electrochemical test, the reference electrode was calibrated in a separate cell with 0.1 M $HClO_4$ purged with hydrogen (1 bar) for at least 10 minutes. During calibration, a 3 mm Pt RDE tip (Metrohm) working electrode was rotated at 1,600 rpm for 5 cyclic voltammograms at a scan rate of 10 mV s^{-1} between -0.26 to -0.28 $V_{Ag/AgCl}$, using a Pt rod (Metrohm) as the counter electrode and Ag/AgCl as the reference electrode. The conversion factor between Ag/AgCl and RHE was

determined from the average values obtained from the forward and backward scans at zero current.[39] An example of the reference electrode calibration is provided below in **Figure 3.4**, and the conversion is given below:

$$E_{RHE} = E_{Ag/AgCl} + E^{cal}_{Ag/AgCl} \quad \textbf{Equation 3.9}$$

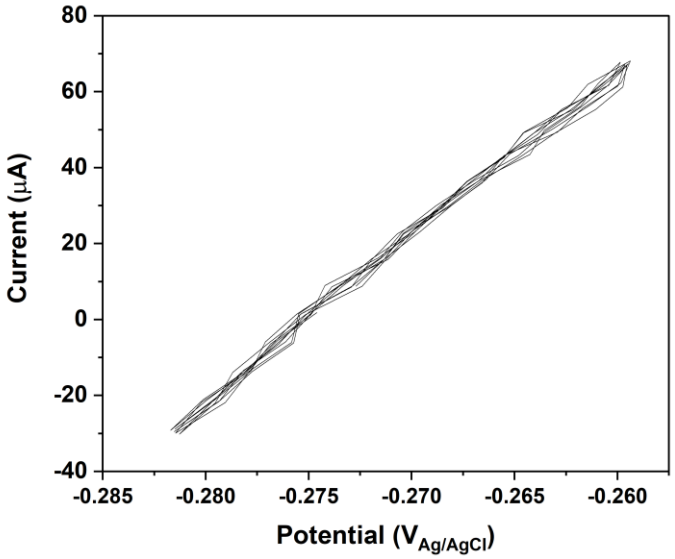


Figure 3.4. Example calibration of $Ag/AgCl_{sat}$ electrode in 0.1 M $HClO_4$. Cyclic voltammetry (10 mV s^{-1}) under 1 bar hydrogen purging with a 3 mm Pt RDE at 1600 rpm with Ag/AgCl (reference electrode) and Pt rod (counter electrode). Data adapted from reference.[40]

3.3.1.5 Koutecky-Levich Analysis and Mass Activity

The measured current density in RDE, *j*, can be determined using the Koutecky-Levich equation (**Equation 3.10**). It is important to mention that the Koutecky-Levich equation is applicable only to reactions that exhibit a first-order dependence on the reactant in the gas phase.[41] To find the diffusion-limited current, j_d, one can identify the plateau current, e.g. at 0.2 V_{RHE}, where the overpotential is sufficiently large to assume that the reaction rate is primarily influenced by mass transport alone. Subsequently, the kinetic current, j_k, can be derived from **Equation 3.11**. This calculation which removes transport limiting currents that come from differing oxygen concentrations between the bulk and electrode surface.

$$\frac{1}{j} = \frac{1}{j_k} + \frac{1}{j_d} \quad \textbf{Equation 3.10}$$

$$j_k = \frac{j_m j_d}{j_d - j_m} \quad \textbf{Equation 3.11}$$

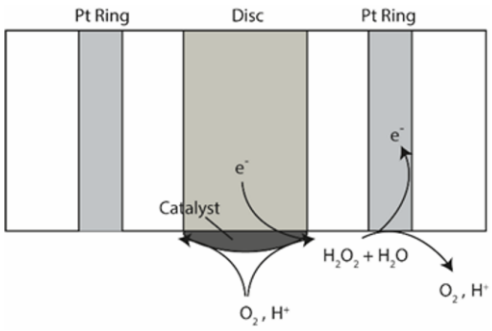
Subsequently, the kinetic mass activity, m_{kin}, at a particular potential can be found:

$$m_{kin} = \frac{j_{kin}}{L_{FeNC}}$$ **Equation 3.12**

Where m_{kin} is the kinetic mass activity at e.g. 0.80 or 0.85 V_{RHE} (A g_{FeNC}^{-1}) and L_{FeNC} is the catalyst loading on the RDE (mg_{FeNC} cm^{-2}).

3.3.1.6 RRDE

A rotating ring disc electrode (RRDE) operates similarly to an RDE, but with the inclusion of a ring electrode encircling the disk electrode on the working electrode. The presence of the ring electrode in an RRDE enables the determination of the reaction pathway and selectively in the O_2 reduction mechanism based on the number of electrons involved and the quantity of H_2O_2 generated.[42] This analysis is depicted in **Figure 3.5.** To achieve this, the voltage applied to the ring electrode is set sufficiently high to induce an immediate reaction of the product leaving the disk electrode, e.g., 1.27 V_{RHE}.[43]



Disc:

$O_2 + 4e^- + 4H^+ \rightarrow 2\ H_2O$

$O_2 + 2e^- + 2H^+ \rightarrow H_2O_2$

Ring:

$H_2O_2 \rightarrow O_2 + 2e^- + 2H^+$

Figure 3.5. Left: illustration of glass carbon disc and Pt ring in RRDE system and Right: reaction pathways at each electrode.

The number of electrons transferred (n) was calculated based on the disk and ring current using the subsequent equation:[43]

$$\boldsymbol{n = 4 \times \frac{j_d}{j_d + \frac{j_r}{N_c}}}$$ **Equation 3.13**

Where j_r is the ring current and N_c is the measured collection efficiency (21.67%). N_c calibration was obtained according to the protocol of Zhou et al.[43] Briefly, chronoamperometric measurement over 60 s in the same conditions as above under N_2 saturated conditions, with additional 0.004 M $K_3Fe(CN)_6$ (EMSURE® ACS, Reag. Ph Eur, Sigma Aldrich) and the disk and ring set to 0.1 V and 1.27 V_{RHE}, respectively. The last 10 s of chronoamperometry were averaged to obtain j_r and j_d and N_c calculated via the following:

$$N_c = \frac{j_r - j_{r0}}{j_d}$$ **Equation 3.14**

Where j_{r0} includes anodic current not arising from reduced $Fe(CN)_6^{4-}$ on the disk.

Additionally, the H_2O_2% was obtained from:

$$H_2O_2\ \% = 2 \times \frac{\frac{j_r}{N_c}}{j_d + \frac{j_r}{N_c}} \times 100$$ **Equation 3.15**

3.3.1.7 Electrode Preparation and Measurement Protocol

A 5 mm glassy carbon rotating disk electrode (RDE, Metrohm) was prepared by polishing with a micropolish cloth and 0.05 µm alumina suspension (Buehler) in a figure of eight pattern.[33] The catalysts derived from TAP were drop-casted onto the freshly polished RDE using an ink comprising 4 mg of the catalyst, 480 µL of 18.2 MΩ cm deionized water, 480 µL of isopropanol (≥99.5% Honeywell, Fisher Scientific), and 40 µL of 5wt% Nafion® D-521 (5% w/w in water and 1-propanol, Alfa Aesar). This ink was freshly sonicated for 30 minutes in an ice-cooled bath sonicator (132 kHz ultrasonic cleaner, VWR). The drop-cast ink was dried at 700 rpm for 30 minutes under ambient air conditions, resulting in a catalyst loading of 0.26 mg_{FeNC} cm^{-2}.

Cyclic voltammograms were recorded after purging the electrolyte with the analyte gas (N_2 or O_2) for at least 15 minutes. For N_2-saturated conditions (measurements at the 10th cycle displayed), scans were conducted at a scan rate of 50 mV s^{-1} at 0 rpm. In the case of O_2 or N_2-saturated electrolytes (measurements at the 3rd cycle displayed), scans were performed at a scan rate of 10 mV s^{-1} at 1,600 rpm. To correct for pseudocapacitance, N_2-saturated measurements were subtracted from the O_2-saturated results (for the same scan rate).

3.3.2 GDE

Several alternative electrochemical screening methods have been developed to circumvent the oxygen mass transport constraints associated RDEs, enabling device relevant current densities. These include innovations such as the floating electrode [44] and the gas diffusion electrode.[45] One issue of GDE operation is correctly and precisely compensating for *iR*, since the large R of the electrolyte causes significant *iR* drop at high current densities in polarisation curves.[46] This can be done by a recommended combination of in situ and post-mortem correction.[46]

3.3.3 PEMFC

Real catalyst performance ultimately needs to be evaluated in MEA configuration in a PEMFC. However, due to the time and material consuming nature of PEMFC testing, only the most promising electrocatalysts from RDE and GDE level are typically tested. The amount of material used can be minimized by minimising the surface area of the MEA. The general operation and setup of PEMFCs has been discussed in **Section 2.1.1.1**. The setup used for PEMFC testing in this Thesis is depicted in **Figure 3.6**, with components labelled.

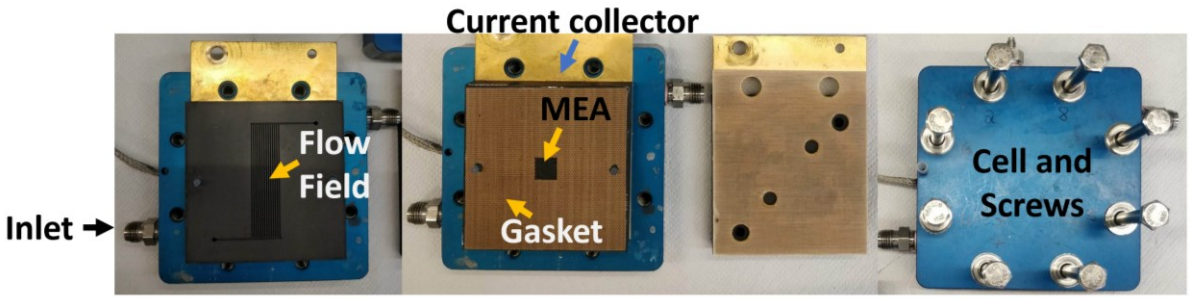


Figure 3.6. Images of PEMFC cell and components with 1 cm^2 working area of MEA.

3.3.4 EIS

Electrochemical Impedance Spectroscopy (EIS) is a potent yet frequently misconstrued method for assessing processes (mass transport, kinetic, charge transfer) within electrochemical cells. EIS is an alternating current technique which involves applying a small amplitude sinusoidal wave to the working electrode (voltage or current) and measuring the resulting wave perturbation as a function of the frequency. Impedance signifies the overall resistance to the flow of current in an electrical circuit encompassing resistors, capacitors, and inductors. EIS data can thus be analysed by employing these components to construct equivalent circuits, as illustrated in **Figure 3.7a**. Resistance offered by the electrolyte to ion flow can be straightforwardly represented as a resistor. Additionally, the electrical double layer formed by ion adsorption on electrode surfaces can be modelled as a capacitor. Another form of resistance encountered in electrochemical systems is the charge transfer resistance, influenced by factors like catalyst properties, applied potential, interfacial oxygen concentration, and temperature.

EIS data can be presented using Nyquist plots, which represent impedance as a vector with Z' (real impedance) and Z'' (imaginary impedance) on the x- and y-axis, respectively, at each excitation frequency (as shown in **Figure 3.7b**). The first intercept of the real axis is the ohmic

resistance, which in an RDE system can arise from the solution resistance. The distance of a data point from the origin corresponds to the magnitude of the vector, denoted as |Z|, while the angle from the x-axis signifies the phase shift. Nyquist plots, however, do not enable sufficient interpretation of the high frequency data as the axes scale is determined by low frequency data.[47] Plus, direct matching of frequency-impedance is not possible. Instead Bode plots can be used which show log|Z| = *f*(log*f*) and -phase = *f*(log*f*), making impedance data clear over a wide frequency range and matching of excitation frequency with modulus of impedance. The validity of EIS data to an equivalent circuit can be tested by the Kramers-Kronig test which evaluates the linearity, causality, stability and finiteness.[48]

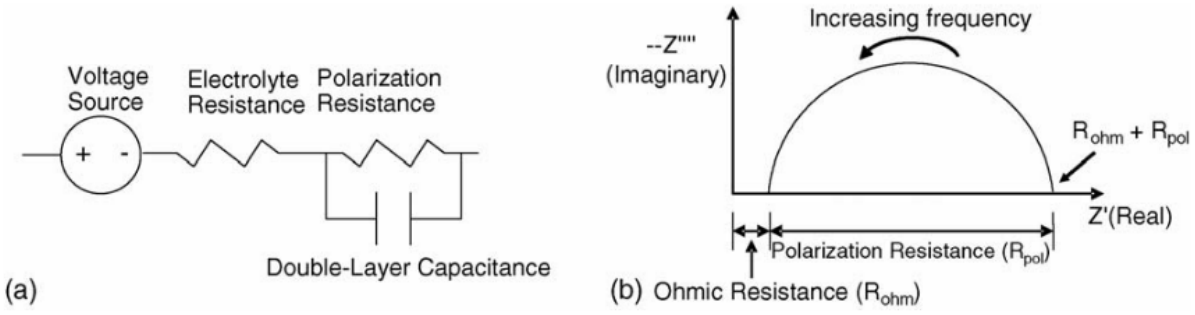


Figure 3.7 a.) Example of an equivalence circuit. b.) Example Nyquist plot with labelled system properties. Reproduced from reference with perimision.[49] Copyright 2001, Wiley.

3.3.5 FTacV

Alternating current voltammetry can be used to deconvolute the faradaic and non-faradaic processes with exceptionally high quantitative precision.[49] This non-linear Faradaic current enables study of electron transfer in Faradaic processes, such as the Fe^{II}/Fe^{III} redox couple present in some Fe-N-C. Faradaic signals are intrinsically non-linear and thus produce harmonic components at *f*, 2*f*, 3*f*, …, n*f*. Each harmonic can be detected using lock-in amplifiers tuned to the frequency of interest. Fast Fourier transforms can convert from time to frequency domain. This allows higher-order harmonics to be filtered with relative ease (**Figure 3.8b**). Harmonics greater or equal to four are typically composed of purely Faradaic process, with the non-Faradaic contribution removed.[50] These harmonics are sensitive to reaction kinetics on the surface of the electrode, which can represent Fe sites in Fe-N-C. An inverse of the fast Fourier Transform can select individual harmonics in the time domain (**Figure 3.8c**). From here the number of redox species can be extracted using a representative model based on the Nernst equation.

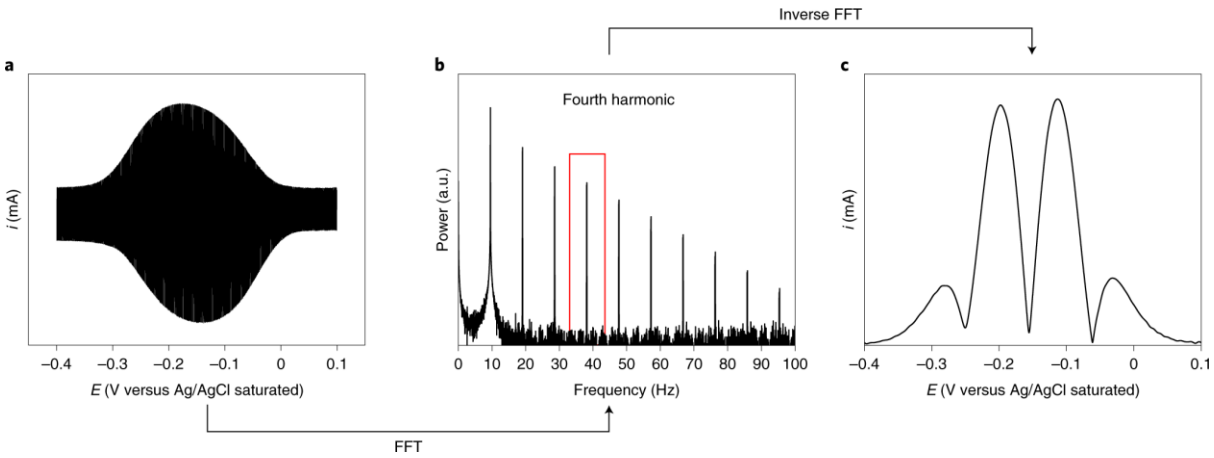


Figure 3.8. Process of FTacV data treatment for fourth harmonic. a.) Raw FTacV measurements. b.) fast Fourier transform converts the current from time to frequency domain, producing a power spectrum. Reproduced from ref [51] with permission. Copyright 2024, Nature Research.

3.4 Life Cycle Analysis

LCA stands as a notable approach for assessing the environmental impacts linked with goods, procedures, or actions throughout their entire life cycle, spanning from the acquisition and processing of basic materials to recycling and ultimate disposal.[52] By consolidating the environmental pressures into a range of impact groups and benchmarks, the outcomes of LCA can be comprehensively interpreted and employed to steer the development of eco-friendly products and procedures. LCA has been broadly utilized to contrast the manufacturing methods of chemicals and fuels, encompassing initial technologies,[53] yet its usage in the production of catalysts has been limited.[54]

LCA comprise of four phases:[55]

1. Goal and Scope Definition
2. Inventory Analysis
3. Impact Assessment
4. Interpretation

References

1 L. Ni, C. Gallenkamp, S. Paul, M. Kübler, P. Theis, S. Chabbra, K. Hofmann, E. Bill, A. Schnegg, B. Albert, V. Krewald and U. I. Kramm, *Adv. Energy Sustain. Res.*, 2021, **2**, 2000064.

2 A. Pedersen, J. Barrio, A. Li, R. Jervis, D. J. L. Brett, M. M. Titirici and I. E. L. Stephens, *Adv. Energy Mater.*, 2022, **12**, 2102715.

3 P. Van der Heide, *X-Ray Photoelectron Spectroscopy: An Introduction to Principles and Practices*, John Wiley & Sons, Ltd, 2011.

4 Cramer, Stephen, *X-ray Spectroscopy with Synchrotron Radiation: Fundamentals and Applications*, Springer, 2020.

5 Chandrasekhara Venkata Raman, *Indian J. Phys.*, 1928, **2**, 387–398.

6 A. C. Ferrari and J. Robertson, *Phys. Rev. B*, 2000, **61**, 14095–14107.

7 M. Thommes, K. Kaneko, A. V. Neimark, J. P. Olivier, F. Rodriguez-Reinoso, J. Rouquerol and K. S. W. Sing, *Pure Appl. Chem.*, 2015, **87**, 1051–1069.

8 J. Rouquerol, P. Llewellyn and F. Rouquerol, in *Studies in Surface Science and Catalysis*, Elsevier, 2007, vol. 160, pp. 49–56.

9 J. W. M. Osterrieth, J. Rampersad, D. Madden, N. Rampal, L. Skoric, B. Connolly, M. D. Allendorf, V. Stavila, J. L. Snider, R. Ameloot, J. Marreiros, C. Ania, D. Azevedo, E. Vilarrasa-Garcia, B. F. Santos, X.-H. Bu, Z. Chang, H. Bunzen, N. R. Champness, S. L. Griffin, B. Chen, R.-B. Lin, B. Coasne, S. Cohen, J. C. Moreton, Y. J. Colón, L. Chen, R. Clowes, F.-X. Coudert, Y. Cui, B. Hou, D. M. D'Alessandro, P. W. Doheny, M. Dincă, C. Sun, C. Doonan, M. T. Huxley, J. D. Evans, P. Falcaro, R. Ricco, O. Farha, K. B. Idrees, T. Islamoglu, P. Feng, H. Yang, R. S. Forgan, D. Bara, S. Furukawa, E. Sanchez, J. Gascon, S. Telalović, S. K. Ghosh, S. Mukherjee, M. R. Hill, M. M. Sadiq, P. Horcajada, P. Salcedo-Abraira, K. Kaneko, R. Kukobat, J. Kenvin, S. Keskin, S. Kitagawa, K. Otake, R. P. Lively, S. J. A. DeWitt, P. Llewellyn, B. V. Lotsch, S. T. Emmerling, A. M. Pütz, C. Martí-Gastaldo, N. M. Padial, J. García-Martínez, N. Linares, D. Maspoch, J. A. Suárez del Pino, P. Moghadam, R. Oktavian, R. E. Morris, P. S. Wheatley, J. Navarro, C. Petit, D. Danaci, M. J. Rosseinsky, A. P. Katsoulidis, M. Schröder, X. Han, S. Yang, C. Serre, G. Mouchaham, D. S. Sholl, R. Thyagarajan, D. Siderius, R. Q. Snurr, R. B. Goncalves, S. Telfer, S. J. Lee, V. P. Ting, J. L. Rowlandson, T. Uemura, T. Iiyuka, M. A. Veen, D. Rega, V. Van Speybroeck, S. M. J. Rogge, A. Lamaire, K. S. Walton, L. W. Bingel, S. Wuttke, J. Andreo, O. Yaghi, B. Zhang, C. T. Yavuz, T. S. Nguyen, F. Zamora, C. Montoro, H.-C. Zhou, A. Kirchon and D. Fairen-Jimenez, *Adv. Mater.*, 2022, 2201502.

10 J. Rouquerol, F. Rouquerol, P. Llewellyn, G. Maurin and K. S. W. Sing, *Adsorption by powders and porous solids: principles, methodology and applications*, Academic press, 2013.

11 J. Jagiello and J. P. Olivier, *Adsorption*, 2013, **19**, 777–783.

12 R. Thomas, *Practical Guide to ICP-MS: A Tutorial for Beginners, Third Edition*, CRC Press, 2013.

13 S. O. Klemm, A. A. Topalov, C. A. Laska and K. J. J. Mayrhofer, *Electrochem. Commun.*, 2011, **13**, 1533–1535.

14 O. Kasian, S. Geiger, K. J. J. Mayrhofer and S. Cherevko, *Chem. Rec.*, 2019, **19**, 2130–2142.

15 D. Menga, J. L. Low, Y.-S. Li, I. Arčon, B. Koyutürk, F. Wagner, F. Ruiz-Zepeda, M. Gaberšček, B. Paulus and T.-P. Fellinger, *J. Am. Chem. Soc.*, 2021, **143**, 18010–18019.

16 M. M. Roessler and E. Salvadori, *Chem. Soc. Rev.*, 2018, **47**, 2534–2553.

17 T. Mineva, I. Matanovic, P. Atanassov, M. T. Sougrati, L. Stievano, M. Clémancey, A. Kochem, J. M. Latour and F. Jaouen, *ACS Catal.*, 2019, **9**, 9359–9371.

18 U. I. Kramm, J. Herranz, N. Larouche, T. M. Arruda, M. Lefèvre, F. Jaouen, P. Bogdanoff, S. Fiechter, I. Abs-Wurmbach, S. Mukerjee and J. P. Dodelet, *Phys. Chem. Chem. Phys.*, 2012, **14**, 11673–11688.

19 U. I. Kramm, L. Ni and S. Wagner, *Adv. Mater.*, 2019, **31**, 1805623.

20 L. Ni, C. Gallenkamp, S. Paul, M. Kübler, P. Theis, S. Chabbra, K. Hofmann, E. Bill, A. Schnegg, B. Albert, V. Krewald and U. I. Kramm, *Adv. Energy Sustain. Res.*, 2021, 2000064.
21 Garcia-Serres, Ricardo, *Zenodo*, , DOI:10.5281/zenodo.5634948.
22 J. I. Goldstein, D. E. Newbury, J. R. Michael, N. W. M. Ritchie, J. H. J. Scott and D. C. Joy, *Scanning Electron Microscopy and X-Ray Microanalysis*, Springer, New York, NY, 2018.
23 D. Williams and Carter, Barry, *Transmission Electron Microscopy*, Springer-Verlag, US, Second., 2009.
24 S. J. Pennycook and P. D. Nellist, *Scanning Transmission Electron Microscopy: Imaging and Analysis*, Springer Science & Business Media, 2011.
25 M. Zachman, D. Chung, E. Holby, M. Chi and D. Cullen, *Microsc. Microanal.*, 2020, **26**, 162–163.
26 H. Yan, Y. Lin, H. Wu, W. Zhang, Z. Sun, H. Cheng, W. Liu, C. Wang, J. Li, X. Huang, T. Yao, J. Yang, S. Wei and J. Lu, *Nat. Commun.*, 2017, **8**, 1–10.
27 R. F. Egerton, *Electron Energy-Loss Spectroscopy in the Electron Microscope*, Springer Science & Business Media, 2011.
28 E. Guan, J. Ciston, S. R. Bare, R. C. Runnebaum, A. Katz, A. Kulkarni, C. X. Kronawitter and B. C. Gates, *ACS Catal.*, 2020, **10**, 9065–9085.
29 S. Martens, L. Asen, G. Ercolano, F. Dionigi, C. Zalitis, A. Hawkins, A. Martinez, L. Seidl, A. C. Knoll, J. Sharman, P. Strasser, D. Jones and O. Schneider, *J. Power Sources*, 2018, **392**, 274–284.
30 J. Zhang, *PEM fuel cell electrocatalysts and catalyst layers: Fundamentals and applications*, Springer, London, 2008.
31 K. Shinozaki, J. W. Zack, S. Pylypenko, B. S. Pivovar and S. S. Kocha, *J. Electrochem. Soc.*, 2015, **162**, F1384–F1396.
32 W. Xing, M. Yin, Q. Lv, Y. Hu, C. Liu and J. Zhang, in *Rotating Electrode Methods and Oxygen Reduction Electrocatalysts*, eds. W. Xing, G. Yin and J. Zhang, Elsevier, Amsterdam, 2014, pp. 1–31.
33 N. Elgrishi, K. J. Rountree, B. D. McCarthy, E. S. Rountree, T. T. Eisenhart and J. L. Dempsey, *J. Chem. Educ.*, 2018, **95**, 197–206.
34 W. Xia, A. Mahmood, Z. Liang, R. Zou and S. Guo, *Angew. Chem. - Int. Ed.*, 2016, **55**, 2650–2676.
35 D. Van Der Vliet, D. S. Strmcnik, C. Wang, V. R. Stamenkovic, N. M. Markovic and M. T. M. Koper, *J. Electroanal. Chem.*, 2010, **647**, 29–34.
36 K. R. Cooper and M. Smith, *J. Power Sources*, 2006, **160**, 1088–1095.
37 C. M. Pedersen, M. Escudero-Escribano, A. Velázquez-Palenzuela, L. H. Christensen, I. Chorkendorff and I. E. L. Stephens, *Electrochimica Acta*, 2015, **179**, 647–657.
38 H. A. Gasteiger, S. S. Kocha, B. Sompalli and F. T. Wagner, *Appl. Catal. B Environ.*, 2005, **56**, 9–35.
39 C. Wei, R. R. Rao, J. Peng, B. Huang, I. E. L. Stephens, M. Risch, Z. J. Xu and Y. Shao-Horn, *Adv. Mater.*, 2019, **31**, 1806296.
40 J. Barrio, A. Pedersen, J. Feng, S. Ch. Sarma, M. Wang, A. Y. Li, H. Yadegari, H. Luo, M. P. Ryan, M.-M. Titirici and Ifan. E. L. Stephens, *J. Mater. Chem. A*, 2022, **10**, 6023–6030.
41 P. J. Rheinländer, J. Herranz, J. Durst and H. A. Gasteiger, *J. Electrochem. Soc.*, 2014, **161**, F1448–F1457.
42 U. A. Paulus, T. J. Schmidt, H. A. Gasteiger and R. J. Behm, *J. Electroanal. Chem.*, 2001, **495**, 134–145.
43 R. Zhou, Y. Zheng, M. Jaroniec and S.-Z. Qiao, *ACS Catal.*, 2016, **6**, 4720–4728.
44 C. M. Zalitis, D. Kramer and A. R. Kucernak, *Phys. Chem. Chem. Phys.*, 2013, **15**, 4329–4340.
45 L. Pan, S. Ott, F. Dionigi and P. Strasser, *Curr. Opin. Electrochem.*, 2019, **18**, 61–71.
46 K. Ehelebe, N. Schmitt, G. Sievers, A. W. Jensen, A. Hrnjić, P. Collantes Jiménez, P. Kaiser, M. Geuß, Y. P. Ku, P. Jovanovič, K. J. J. Mayrhofer, B. Etzold, N. Hodnik, M. Escudero-Escribano, M. Arenz and S. Cherevko, *ACS Energy Lett.*, 2022, **7**, 816–826.
47 A. Ch. Lazanas and M. I. Prodromidis, *ACS Meas. Sci. Au*, 2023, **3**, 162–193.

48 M. Schönleber, D. Klotz and E. Ivers-Tiffée, *Electrochimica Acta*, 2014, **131**, 20–27.
49 A. Bard and L. Faulkner, *Electrochemical Methods: Fundamentals and Applications*, John Wiley & Sons, New York, 2001.
50 S.-X. Guo, A. M. Bond and J. Zhang, *Rev. Polarogr.*, 2015, **61**, 21–32.
51 R. Z. Snitkoff-Sol, A. Friedman, H. C. Honig, Y. Yurko, A. Kozhushner, M. J. Zachman, P. Zelenay, A. M. Bond and L. Elbaz, *Nat. Catal.*, 2022, **5**, 163–170.
52 J. Guinée and R. Heijungs, in *Sustainable Supply Chains*, Springer, 2017, vol. 4, pp. 15–41.
53 J. Kleinekorte, L. Fleitmann, M. Bachmann, A. Kätelhön, A. Barbosa-Póvoa, N. Von Der Assen and A. Bardow, *Annu Rev Chem Biomol Eng 2020*, 2020, **11**, 203–233.
54 S. Evangelisti, C. Tagliaferri, D. Brett and P. Lettieri, in *Modern Developments in Catalysis*, World Scientific, 2017, pp. 289–312.
55 ISO 14040, *Environmental management—life cycle assessment—principles and framework*, 2006.

Chapter 4: Synthesis of a Porous and High Active Site Utilisation Fe-N-C with Penta Coordination via Mg templating

4.1 Introduction

One common approach to enhance the catalytic performance of Fe-N-C materials involves the modulation of their intrinsic activity, through the manipulation of the local coordination environment. This can be achieved through techniques such as the creation of dual metal atom catalysts[1,2] or the introduction of axial ligands.[3,4] The selection of appropriate axial ligands has been guided by insights obtained from various analytical techniques, including in situ Mössbauer spectroscopy, x-ray absorption spectroscopy, nuclear inelastic scattering, and electron paramagnetic resonance.[5,6] Notably, some of these axial ligands bear a striking resemblance to biological systems,[7] with N axially coordinated FeN_4 sites resembling the well-known heme structure.[8] However, it is important to note that the spectroscopic discernibility of these axial ligands is often challenging in the typically heterogeneous Fe-N-C catalysts,[9] making it difficult to draw conclusive experimental structure-activity correlations. To overcome these experimental limitations, computational methods, particularly density functional theory, have been employed to investigate the effects of axial ligands on model Fe-N-C systems.[10,11] Nevertheless, a comprehensive exploration of the impact of various possible axial ligands on different Fe sites, including pyridinic and pyrrolic configurations, remains an open research question.[12]

An alternative avenue for improving the catalytic performance of Fe-N-C materials involves increasing the number of active sites. Mehmood *et al*. have notably demonstrated substantial progress in this regard. Their work has showcased the achievement of a bulk FeN_x site density ($SD_{Mössbauer}$, **Equation 4.3**) reaching an impressive 7.4×10^{20} sites $g_{Fe\text{-}N\text{-}C}^{-1}$. Furthermore, they reported a high in situ nitrite stripping site density ($SD_{nitrite}$, according to **Equation 4.4**) of 4.67×10^{19} sites $g_{Fe\text{-}N\text{-}C}^{-1}$. However, it is noteworthy that the electrochemical utilization of FeN_x compared to the bulk Fe and FeNx, stood at a modest 6% ($Utilisation_{Nitrite/ICP}$, **Equation 4.6**, and $Utilisation_{Nitrite/Mössbauer}$, **Equation 4.5**).[13] This implies there remains ample room for enhancing the surface, accessible, FeN_x site density.[13]

To provide a meaningful perspective, it is worth noting that 3 nm diameter Pt nanoparticles, which are representative of commercial Pt/C catalysts, are geometrically constrained,

resulting in only approximately 35% of the Pt atoms being exposed on the nanoparticle surface.[14] Furthermore, in the cathodes of PEMFCs, the ratio of specific Pt surface area (m^2 g_{Pt}^{-1}) to that of the Pt catalyst (m^2 g_{Pt}^{-1}) is typically in the range of approximately 70-90%, depending on the preparation method. As a result, the electrochemical utilization of the total Pt content at the PEMFC cathode is anticipated to be approximately 25-32% for 3 nm Pt nanoparticles.[15] This utilization corresponds to a Pt surface site density of 1.31×10^{21} sites g_{Ft}^{-1}, assuming electrochemical surface areas of 100 m^2 g_{Pt}^{-1} in PEMFCs employing 2.8 nm Pt nanoparticles.[13]

This comparison underscores the need for significant enhancements in the accessibility and surface density of FeN_x active sites to compete with the site densities achieved by Pt/C catalysts. While it is noteworthy that the gas accessibility of FeN_x sites has reached 100%, as evidenced by *ex situ* cryo CO sorption measurements,[16] In terms of in situ electrochemical FeN_x utilisation, Wan *et al*. found that mesoporous structures play a critical role in achieving record $Utilisation_{Nitrite/ICP}$ and $Utilisation_{Nitrite/Mössbauer}$ values, reaching an impressive 43%, albeit at a relatively low $SD_{nitrite}$ of 1.32×10^{19} sites $g_{Fe\text{-}N\text{-}C}^{-1}$. Notably, their study also revealed a notable decrease in utilisation as the $SD_{nitrite}$ increased.[17] Furthermore, *in situ* nitrite stripping have frequently reported utilisation values below 10%.[18]

In this chapter, I present a method for the preparation of Fe-N-C materials that exhibit a high level of electrochemical utilization of FeN_x active sites. The approach leverages the unique properties of a Mg salt, which serves as both an active site template and a porogen, along with an alternative organic precursor, 2,4,6-Triaminopyrimidine (TAP). This combination allows the creation of a highly porous, nitrogen-doped carbon host that is well-suited for coordinating Fe. DFT is then employed to examine the impact of axial ligands on model FeN_4 pyridinic and pyrrolic sites, providing insights into their influence on O_2 reduction activity.

4.2 Experimental

4.2.1 Catalyst Preparation

N-C, Fe-N-C and ^{57}Fe-N-C catalysts were prepared according to Chapters 3.2.1-3.2.3.

To summarise, the N-C precursor is prepared by grinding together 2,4,6-triaminopyrimidine (TAP) with $MgCl_2{\cdot}6H_2O$ in a 1:8 weight ratio. The N-C is TAP X (where X denotes the 1 h pyrolysis temperature of 800, 900, or 1000°C, with 5°C/min heating rate), which is washed

with 2 M HCl. The Fe-N-C is TAP X@Fe, where @Fe represents the catalyst loaded with Fe through a 24 h low temperature (90°C) methanol reflux method, and subsequent acid wash with 0.5 M H_2SO_4.

4.2.2 RDE O_2 reduction

Electrochemical tests for oxygen reduction were conducted using an AUTOLAB PGSTAT302N in an electrolyte comprising 0.1 M $HClO_4$ (Suprapur®, Merck) saturated with N_2 (≥99.99998% BIP® Plus, Air Products) and O_2 (≥99.9998% Ultrapure Plus, Air Products). These tests were carried out in a glass cell featuring a three-electrode configuration. The reference electrode used was $Ag/AgCl_{sat}$ (3M KCl), while a glassy carbon rod served as the counter electrode. To account for the solution ohmic drop (R = 23 Ω), iR correction was applied post-electrochemistry. R was determined from the intercept of the real impedance axis in the Nyquist plot, obtained via electrochemical impedance measurement in the frequency range of 10^{-5} – 10 Hz while at open circuit potential.

For the best-performing material (observed in the cathodic scans of the cyclic voltammograms under O_2 at 1600 rpm), electrochemical measurements were repeated five times.

The kinetic current density (j_{kin}) at potentials of 0.80 and 0.85 V_{RHE} was determined using the Koutecký–Levich (**Equation 3.11**). Subsequently, the kinetic mass activity can be found from **Equation 3.12**.

Electrochemical measurements were conducted in a Rotating Ring-Disk Electrode (RRDE) setup to determine the number of electrons transferred. The platinum (Pt) ring electrode was set at 1.27 V_{RHE}. The ink composition, preparation, and catalyst loading matched those employed in the RDE measurements. The number of electrons transferred and H_2O_2 % was calculated according to **Equation 3.13** and **Equation 3.15**.

Accelerated stress test cyclic voltammetry cycles were conducted between 0.8-0.4 V_{RHE} at 100 mV s^{-1} under O_2-saturation, with Pt ring applied at 1.27 V_{RHE} throughout.

4.2.3 *In situ* Nitrite Stripping

Following an updated protocol,[13] in situ nitrite stripping was conducted to assess site density and turnover frequency (TOF). To prepare the catalyst ink, 5 mg of Fe-N-C was mixed with 519

µL of isopropanol, 519 µL of H2O, and 54 µL of Nafion® (5wt% solution, Sigma-Aldrich). After 30 minutes of bath sonication, the catalyst ink was drop-casted onto a 5 mm glassy carbon disk of a rotating disk electrode (Pine Instruments, model AFE6R1AU, and rotator model AFMSRCE) and left to air-dry at room temperature, while rotating at approximately 200-300 rpm. This was repeated until achieving a catalyst loading of 0.2 $mg_{Fe\text{-}N\text{-}C}$ cm^{-2}. All electrochemical measurements were conducted in a 0.5 M sodium acetate buffer (comprising sodium acetate (99% purity Sigma-Aldrich), glacial acetic acid, and ultrapure water (18.2 MΩ cm, MilliQ) as the electrolyte (pH 5.2). The catalyst cleaning protocol consisted of the following steps: two cyclic voltammetry cycles were performed in an O_2-saturated electrolyte at a scan rate of 5 mV s^{-1} within the potential range of 1.0-0.3 V_{RHE}, followed by ten cyclic voltammetry cycles in an N_2-saturated electrolyte at a scan rate of 100 mV s^{-1} within the same potential range. Subsequently, five cyclic voltammetry cycles were performed at a scan rate of 10 mV s^{-1}. This entire cleaning sequence was repeated twice. For precise determination of the stripping charge during the nitrite stripping cyclic voltammetry scans, a current integrator was utilized.

The catalyst poisoning step, measurement conditions for O_2 reduction activities, and nitrite stripping cyclic voltammetry scans at fresh, poisoned, and recovered stages were consistent with previous protocols.[19] Notably, a second nitrite poisoning step was introduced during the recovered catalyst phase to minimize potential variations in the baseline cyclic voltammetry current due to O_2 reduction steps. It is worth mentioning that O_2 reduction measurements were not taken between the fresh, poisoned, and recovered stages during the second poisoning measurements.

TOF values were determined from *in situ* nitrite stripping in the range of 0.80-0.85 V_{RHE} based on the following equation:

$$TOF = \frac{(j_{k(unpoisoned)} - j_{k(poisoned)}) \times N_A}{SD_{Nitrite} \times F} \qquad \textbf{Equation 4.1}$$

Where $j_{k(unpoisoned)}$ is the unpoisoned kinetic mass activity and $j_{k(unpoisoned)}$ is the poisoned kinetic mass activity.

4.2.4 Bulk Site Density and Utilisation

The total Fe site density of the bulk catalyst can be found from the Fe content based on ICP-MS measurement, SD_{ICP} (sites $g_{Fe\text{-}N\text{-}C}^{-1}$), according to:

$$\boldsymbol{SD_{ICP} = \frac{(Fe_{ICP}/100)\times N_A}{M_{Fe}}} \qquad \textbf{Equation 4.2}$$

Fe_{ICP} is Fe wt.% determined by ICP-MS and M_{Fe} is the molar mass of Fe (55.845 g mol^{-1}).

The FeN_x site density of the bulk catalyst based on cryo Mössbauer spectroscopy, $SD_{Mössbauer}$ (sites $g_{Fe\text{-}N\text{-}C}^{-1}$) can be found from the percentage of doublet species assigned to FeN_x sites, $FeN_{x\,(Mössbauer)}$ (%):

$$\boldsymbol{SD_{Mössbauer} = (FeN_{x(Mössbauer)}/100) \times SD_{ICP}} \qquad \textbf{Equation 4.3}$$

In situ nitrite stripping site density was determined using the following equation:

$$\boldsymbol{SD_{Nitrite} = \frac{Q_{strip} \times N_A}{F \times n_{strip}}} \qquad \textbf{Equation 4.4}$$

Where $SD_{Nitrite}$ is the site density according to nitrite stripping (sites $g_{Fe\text{-}N\text{-}C}^{-1}$), Q_{strip} (C $g_{Fe\text{-}N\text{-}C}^{-1}$) is the nitrite reductive stripping charge determined from the stripping peak, n_{strip} is the number of electrons associated with the reduction of one adsorbed nitrosyl per site and its value is assumed as five, N_A is Avogadro's constant (6.023×10^{23} mol^{-1}) and F is Faraday's constant (96,485 C mol^{-1}).

Two utilisation percentages of FeN_x sites can be calculated according to the following:

$$\boldsymbol{Utilisation_{Nitrite/(Mössbauer)} = \frac{SD_{Nitrite}}{SD_{(Mössbauer)}} \times 100(\%)} \qquad \textbf{Equation 4.5}$$

$$\boldsymbol{Utilisation_{Nitrite/ICP} = \frac{SD_{Nitrite}}{SD_{ICP}} \times 100(\%)} \qquad \textbf{Equation 4.6}$$

Where $Utilisation_{Nitrite/(Mössbauer)}$ is the number of electrochemically accessible FeN_x sites to number of bulk FeN_x sites and $Utilisation_{Nitrite/ICP}$ is the number of electrochemically accessible FeN_x sites to number of bulk Fe atoms.

4.2.5 DFT Simulations

The atomic structures used in this chapter were generated employing the Atomic Simulation Environment package.[20] Ground state DFT calculations were conducted at the Generalized Gradient Approximation level, utilizing the Grid-based Projected Augmented Wave

program.[21] Calculations employed a finite difference approach with the BEEF-vdW exchange and correlation functional.[22] Brillouin zone was sampled using a 2 × 2 × 1 Monkhorst-Pack k-point set and a grid spacing of h = 0.18 Å. For structural optimization, all configurations underwent relaxation until the forces on the atoms were reduced to less than 0.05 eV per Ångström. It is important to note that the unit cell used for all structures is periodic in the x and y directions, and appropriate vacuum regions were included on each side of the catalyst plane along the z-axis to avoid artificial interactions between periodic images. To determine the Gibbs free energy contributions, entropy and zero-point energy corrections were accounted for, which were added to the DFT energies.[23]

4.2.6 Characterisation

4.2.6.1 HAADF-STEM and EDX

HAADF-STEM images, with aberrations effectively corrected, were captured using a FEI Titan Cubic Themis G2 300 transmission electron microscope. This microscope was outfitted with double spherical aberration correctors and a HAADF detector, featuring a convergence angle of 24 mrad and a collection angle spanning from 90 to 240 mrad. The operating voltage employed was 300 kV. Elemental mapping through EDX was performed using an Oxford Instruments X-ray spectrometer.

4.2.6.2 NMR

Solid-state 13C nuclear magnetic resonance (NMR) spectroscopy was conducted using a Bruker Avance III HD 600MHz spectrometer. The sample was placed in a 3.2 mm rotor and spun at a rate of 15,000 revolutions per second (Hz). The NMR sequence utilized was hpdec (1-dimensional 13C NMR with decoupling).

4.2.6.3 TGA-MS

TGA was conducted using a Perkin-Elmer TGA8000 instrument. These tests were carried out in a N_2 atmosphere with a flow rate of 40 mL min^{-1} (standard temperature and pressure). The temperature range for these tests spanned from 30°C to 1000°C, with a gradual heating rate of 5°C min^{-1}.

For TGA-MS (Thermogravimetric Analysis coupled with Mass Spectrometry) measurements, a Netzsch thermal analyzer (TG 209 F1 Libra) was employed, along with a Netzsch quadrupole mass spectrometer (QMS 403 D Aeolos). In all experiments, a nitrogen flow rate of 40 mL min^{-1} was maintained. The samples were heated from an initial temperature of 25°C to a final

temperature of 800°C, with a controlled heating rate of 2°C min^{-1}. Approximately 15 milligrams of the sample material were used for each measurement. The choice of a low heating rate and sample quantity was deliberate, aimed at preventing heat transfer limitations and minimizing the sublimation of TAP. The mass spectrometry data were acquired within a mass-to-charge ratio (m/z) range spanning from 2 to 100.

4.2.6.4 DSC

Differential scanning calorimetry (DSC) was employed to ascertain the melting point of TAP. The sample was placed within an aluminium pan, cooled to -100°C, allowed to reach thermal equilibrium for a duration of 10 minutes, and then heated up to 400°C. This heating process was conducted at a rate of 5°C min^{-1}, all under 40 mL min^{-1} N_2 flowrate.

4.2.6.5 XAS

XAS measurements were conducted at beamline I20 of Diamond Light Source under fluorescence mode. The acquired data underwent normalization to the incident intensity and were processed using Athena.[24] A standard Fe foil served as the reference to calibrate the beam energy, yielding a derivative (E_0) value of 7112.0 eV, corresponding to the first inflection point of the absorption K-edge. For the XAS analysis, approximately 7 mg of the sample were mixed with 10 milligrams of cellulose and compacted into a pellet measuring 5 mm in diameter with a thickness ranging from 0.5 to 1 mm. XANES spectra were generated after background corrections were applied both before and after the edge region, and then they were normalized with respect to the edge step. EXAFS data for the catalyst materials were Fourier transformed within the range of 3 to 10.5 $Å^{-1}$. These transformed data were subsequently plotted in R-space and subjected to analysis.

4.3 Results and Discussion

4.3.1 N-C Structural Evolution with Pyrolysis

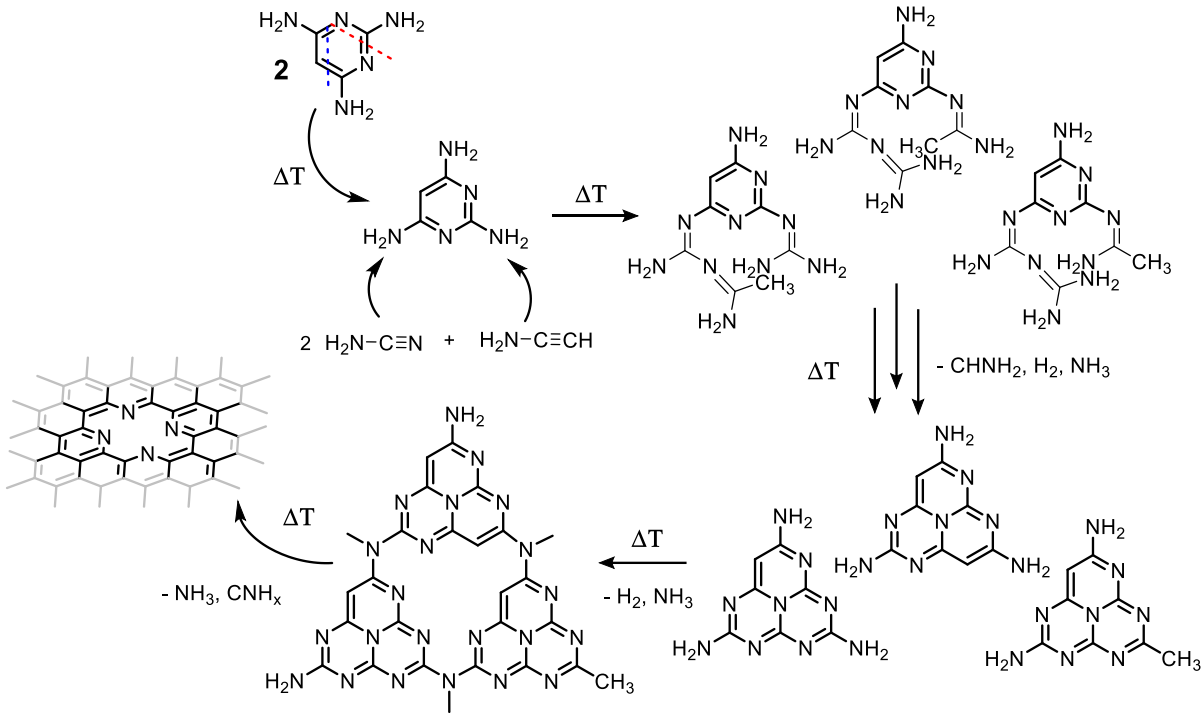
Nitrogen-doped carbon materials were synthesized by subjecting TAP to pyrolysis in the presence of $MgCl_2 \cdot 6H_2O$ at temperatures ranging from 800 to 1000°C. TAP has previously been recognized for its utility as a carbon dopant in polymeric semiconductors and covalent organic materials, where it enhances electronic conductivity and photocatalytic performance.[25,26] However, its application as a foundational building block for the creation of conductive carbon-based electrocatalysts has remained relatively unexplored.[27]

Furthermore, the precise mechanism governing the polymerization pathway of TAP during pyrolysis has, until now, eluded comprehensive elucidation.

The choice of TAP as the precursor is motivated by its structural resemblance to melamine (**Figure A1**). Melamine serves as a precursor to the polymeric semiconductor known as graphitic carbon nitride,[28] a material that has gained considerable attention as a platform for single and dual atom catalysts.[1,29,30] However, graphitic carbon nitride presents inherent limitations, notably its wide band gap of 2.7 eV and its susceptibility to decomposition at elevated temperatures (above 700°C), rendering it unsuitable for serving as a conductive scaffold for electrochemical devices.[31] In contrast, TAP can act as a versatile building block, enabling the creation of a conductive, nitrogen-doped carbon material that offers an advantageous coordination environment for metallic ions.

The hypothesis revolves around the thermal condensation of TAP, leading to the liberation of NH_3 and the formation of reaction intermediates akin to melem, which resembles a heptazine-like unit. Such intermediates have been identified in the pyrolysis of melamine and other triazine-based compounds.[32] As temperatures rise, within the range of 400-500°C, it is likely that a polymeric material similar to graphitic carbon nitride begins to take shape. Subsequently, this material undergoes decomposition, releasing C-N based radicals and ultimately yielding a nitrogen-doped carbon material (**Scheme 4.1**).

Moreover, the incorporation of $MgCl_2{\cdot}6H_2O$ as a porogen in the synthesis methodology facilitates the self-assembly of TAP via N-H···O hydrogen bonds with water molecules. This is followed by polymerization in a completely molten state (**Figure 4.1a**). It is noteworthy that TAP exhibits a melting point at 235°C. The use of a molten intermediate in the pyrolysis of triazine-based molecules has consistently proven highly effective for the synthesis of carbon-based materials.[33] This approach not only offers a homogeneous environment for polymerization, but also facilitates the optimal dispersion of Mg. This results in the creation of materials characterized by exceptional levels of porosity at elevated temperatures.[34,35]



Scheme 4.1. Suggested polymerization pathway of 2,4,6-Triaminopyrimidine. Reproduced from ref [36] under Creative Commons CC BY 3.0.

The conversion of TAP into a conductive carbon framework was comprehensively studied using thermogravimetric analysis coupled to mass spectrometry (TGA-MS). The TGA curves reveal distinct thermal decomposition stages that shed light on the transformation of TAP into a conductive carbon material. Between 200 and 320°C, a significant mass loss of approximately 66% is observed. This mass loss is primarily attributed to the release of ammonia (NH_3) as evidenced by the mass spectrometry data (m/z = 17). Additionally, low molecular weight molecules such as ethynamine (C_2H_3N, m/z = 41) and cyanamide (CN_2H_2, m/z = 42), among others, are detected (**Figure 4.1b** and **Figure A2**). The liberation of ammonia, cyanamide, and ethynamine suggests the formation of reaction intermediates during this temperature range. These intermediates contribute to the creation of a carbon nitride-like polymer structure, akin to the proposed structure by May (**Scheme 4.1**).[37] Notably, while melamine decomposes into three cyanamide fragments, TAP exhibits a different decomposition pattern, yielding a mixture of cyanamide and ethynamine. These compounds are involved in reactions with pristine TAP, resulting in the formation of conductive melem-like scaffolds characterized by direct C-C bonds.

Subsequently, in the temperature range from 320 to 700°C, there is a much more gradual decrease in mass, accounting for only a 14% loss (**Figure 4.1b**). The mass spectrometry data

in this range indicate the presence of heavier species compared to those detected at lower temperatures. Notable species include cyanogen $(CN)_2$ (m/z = 52), ammonium cyanide CH_4N_2 (m/z = 44), isocyanoethene C_3H_2N (m/z = 52), and others. This observation suggests that tertiary amine bonds, which connect heptazine-like units in the polymeric material, undergo decomposition through the release of radicals. This decomposition process ultimately leads to the formation of a nitrogen-doped carbon material, with a yield of approximately 12% achieved at 800°C.[38]

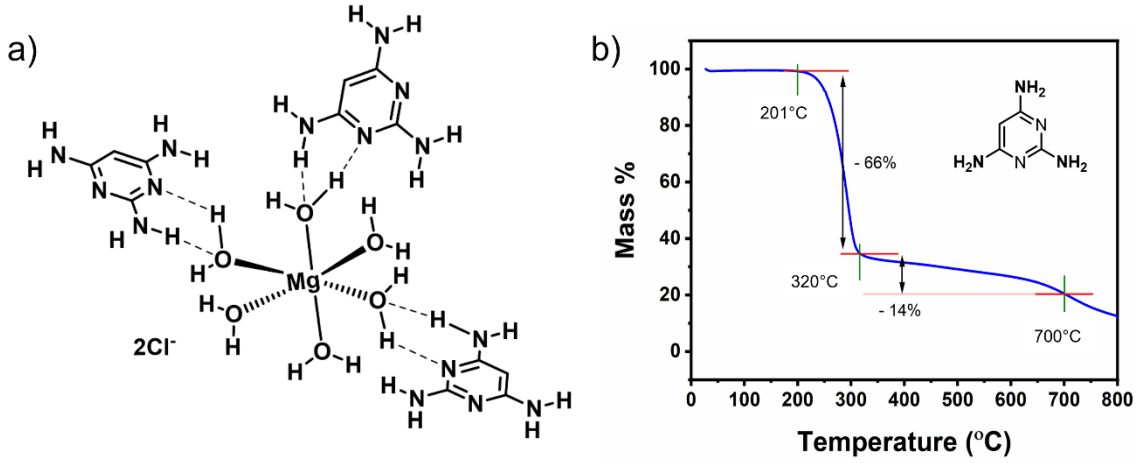


Figure 4.1. a.) Representation of the self-assembly between 2,4,6-Triaminopyrimidine and $MgCl_2{\cdot}6H_2O$ b.) TGA curve of TAP. Reproduced from ref [36] under Creative Commons CC BY 3.0.

In pursuit of optimizing the nitrogen content, conductivity, and porosity of TAP-based materials, pyrolysis experiments in the presence of $MgCl_2{\cdot}6H_2O$ at elevated temperatures (800-1000°C) were performed. TGA-MS unveiled a consistent polymerization pathway when $MgCl_2$ was introduced (**Figure A3-4**). The TGA curve displayed a stepwise mass loss occurring below 250°C, coinciding with the gradual removal of crystal water from MgCl2·6H2O, resulting in the formation of $MgCl_2{\cdot}4H_2O$ (at 65°C-120°C), $MgCl_2{\cdot}2H_2O$ (at 120°C-160°C), $MgCl_2{\cdot}H_2O$ (at 160°C-195°C), and eventually $MgCl_2$ (at 195°C-245°C) (**Figure A3**). TGA-MS data demonstrates the release of water ((m/z) = 18) at each dehydration step, along with the liberation of HCl ((m/z) = 36) during the final dehydration and above 450°C, indicative of the transformation of $MgCl_2$ to MgOHCl, as suggested in a previous study.[34] Importantly, the onset temperature for TAP decomposition was higher in the presence of $MgCl_2{\cdot}6H_2O$ compared to the absence of this compound. Nonetheless, the decomposition products of TAP remained consistent, encompassing ammonia, amine-based molecules, and low-molecular-

weight cyanides. This indicates that the presence of $MgCl_2 \cdot 6H_2O$ did not alter the polymerization pathway of TAP.

Subsequent to pyrolysis at temperatures ranging from 800 to 1000°C, the resulting materials exhibited a highly amorphous structure, attributed to the increased surface area in comparison to pyrolysis without a porogen (**Figure A5**). A faint diffraction peak at 2θ = 26.4°, corresponding to the (002) interlayer stacking peak, was observed in TAP 800. Notably, N2 sorption measurements revealed specific surface areas reaching up to 3,293 $m^2\ g^{-1}$ for TAP 900, as determined by Brunauer-Emmett-Teller (BET) analysis (**Figure 4.2a**, **Figure A6**). These materials exhibited micro- and mesoporous characteristics, consistent with previous findings in analogous materials prepared via ionothermal methods.[34,39]

The pore size distribution in all pyrolyzed TAP materials displayed a bimodal pore size distribution. The smaller pores, centered around 0.7-1 nm, indicated the presence of suitable micropores for the coordination of metal-based species (**Figure 4.2b**). Moreover, larger micropores to small mesopores (1-4 nm) were evident, accompanied by a minor fraction of large mesopores around 40 nm, contributing to the overall pore volume (**Figure 4.2b**). The total micropore volume exhibited a gradual decrease from TAP 800 (0.91 $cm^3\ g^{-1}$) to TAP 1000 (0.58 $cm^3\ g^{-1}$), possibly attributed to micropore collapse at higher pyrolysis temperatures. Conversely, total mesopore volumes displayed a significant increase from 0.90 $cm^3\ g^{-1}$ to 1.95 $cm^3\ g^{-1}$ as the pyrolysis temperature elevated from 800°C to 900°C (**Figure A7**).

Notably, TEM images of TAP 900 confirmed the formation of a highly porous amorphous material (**Figure A8**). Raman spectroscopy revealed a lower D/G band intensity ratio (I_D/I_G) at higher pyrolysis temperatures, indicating a higher degree of dopants and defects in TAP 800. At 1000°C, a graphene-like material with low nitrogen content and a higher degree of graphitization was evident (**Figure A9**).

In summary, the remarkable porosity observed in the materials derived from TAP can be attributed to a combination of two effects. Firstly, the bubble templating effect arises from the release of C/N fragments, including ammonia, amine-based molecules, and low-molecular-weight cyanides, during the pyrolysis process. Secondly, the hard templating effect is induced by MgO. A notable distinction in surface area compared to prior studies employing $MgCl_2 \cdot 6H_2O$ as a porogen can be attributed to two key factors. Firstly, TAP possesses a higher

number of hydrogen bond donors, primarily in the form of amine moieties (3 amines versus 1 in the case of adenine, a previously employed precursor[34,35,40]). This increased presence of hydrogen bond donors enables a more significant release of ammonia and other nitrogen-based fragments during pyrolysis. Secondly, TAP exhibits a lower melting point than adenine, a previously used precursor. This lower melting point facilitates the complete dissolution of unreacted, pristine TAP molecules within the ionothermal medium, consequently promoting its polymerization process. These factors collectively contribute to the distinctive characteristics observed in TAP-derived materials, further enhancing their porosity, and rendering them promising candidates for various applications in materials science and beyond.

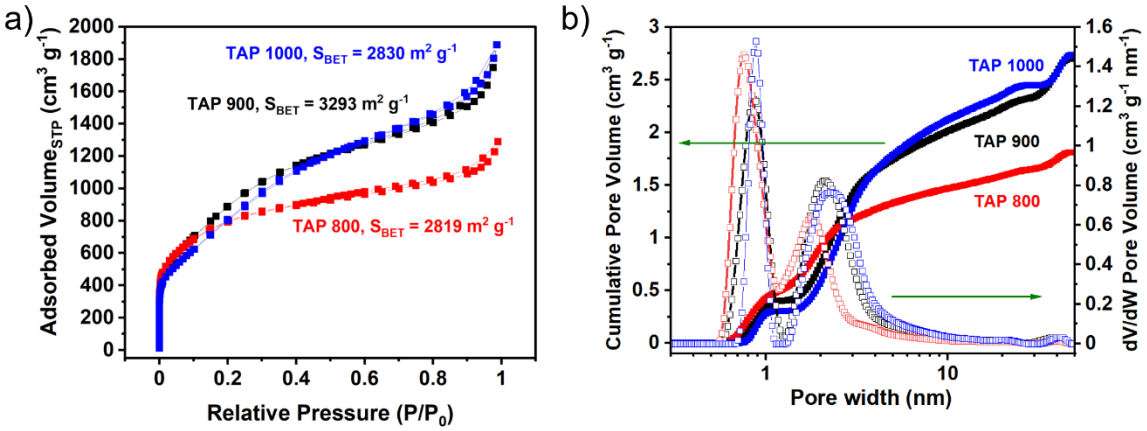


Figure 4.2. TAP-derived materials a.) N_2 sorption isotherms with BET specific surface areas and b.) Corresponding pore size distributions and cumulative pore volumes, determined by 2D-NLDFT heterogeneous surface carbon model. Reproduced from ref [36] under Creative Commons CC BY 3.0.

The decline in nitrogen content at elevated pyrolysis temperatures was substantiated through XPS measurements (**Figure 4.3b** and **Table A1**). TAP 800 exhibited a nitrogen content of 23.5 atomic percent (at.%), which potentially hampers its electrical conductivity. In contrast, TAP 900 and TAP 1000 displayed lower nitrogen contents of 4.5 at.% and 1.8 at.%, respectively. These reduced nitrogen contents are deemed suitable as they still provide a significant amount of N with lone electron pairs that can coordinate with Fe species, thus enabling the formation of single-atom catalysts, without compromising the material's conductivity, as previously reported.[28]

Both the C1s and N1s spectra of the TAP-derived materials exhibited highly similar profiles. The C1s spectrum featured chemical binding energies indicative of C-C, C-N, and C=O bonds (**Figure A10**), while the N1s spectrum presented three primary contributions representing

pyridinic, pyrrolic, and graphitic nitrogen. Intriguingly, in TAP 900, a new contribution emerged, suggesting coordination with residual Mg species. The persistence of small quantities of Mg was verified by inductively coupled plasma mass spectrometry (ICP-MS) (**Figure A11**). While some Mg may also be coordinated in TAP 800, the low nitrogen content and signal-to-noise ratio in TAP 900 allowed for the detection of minority nitrogen chemical states. Furthermore, at 1000°C, the band corresponding to pyrrolic nitrogen (at 401.2 eV) became predominant, indicating either the degradation of pyridine-like moieties or their conversion into pyrrolic motifs.[41]

4.3.2 Fe-N-C Characterisation

To introduce Fe coordination into TAP 800-1000, a low-temperature methanol reflux method with $FeCl_2$ was employed(**Figure 4.3a**).[40] XPS and ICP-MS confirmed the successful incorporation of Fe into TAP 900@Fe, with Fe content measured at 0.70 wt.% and 0.52 wt.%, respectively. According to ICP-MS, TAP 900 contained 0.39 wt.% Mg and 0.18 wt.% Fe (with Fe likely originating from contaminants in the TAP precursor), whereas only 0.02 wt.% Mg remained in TAP 900@Fe (**Figure A11**). The increase of 0.34 wt.% (0.073 at.%) in Fe and the decrease of 0.37 wt.% (0.183 at.%) in Mg from TAP 900 to TAP 900@Fe suggest that low-temperature Fe coordination facilitates the transmetalation of Mg for Fe. Similar trends were observed for TAP 1000 to TAP 1000@Fe, though not for TAP 800 to TAP 800@Fe (**Figure A11**).

For further detailed characterization, focus is made on TAP 900@Fe due to its superior electrocatalytic activity, as shown later. In the N1s XPS spectra of TAP 900@Fe, a peak at 399.5 eV emerged, which could be attributed to N-Fe coordination, constituting 34.5 at.% (**Figure A12**). In comparison to TAP 900, the overall contribution of pyridinic moieties decreased from 29.2% to 16.9%, while the contribution related to nitrogen coordinated to metals (Mg in the case of TAP 900 and Fe in the case of TAP 900@Fe) increased from 18% to 34.5%. The pyrrolic components remained relatively consistent (**Figure 4.3c** and **Table A2**). These observations suggest that Fe coordinates primarily via pyridinic nitrogen rather than pyrrolic nitrogen. XRD patterns indicated the absence of large, aggregated Fe-based nanoparticles, as no diffraction peaks corresponding to Fe oxides, nitrides, carbides, or metallic Fe were observed (**Figure A13**). Such species have been shown to exhibit considerably lower electrochemical activity for O_2 reduction compared to Fe-N-C

materials,[42,43] and their presence could hinder the electrochemical accessibility of FeN_x active sites.

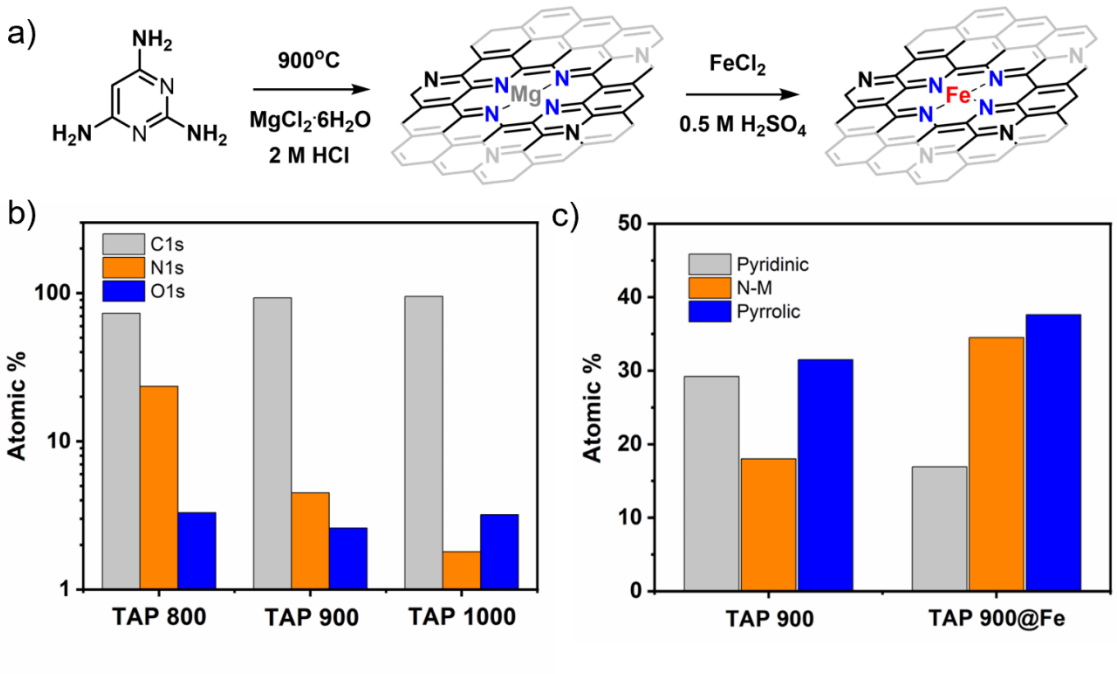


Figure 4.3. a.) Diagram illustrating proposed Fe coordination within TAP 900. B.) Elemental surface composition of TAP 800-1000 according to XPS. c.) Breakdown of contributions of XPS N1s species identified in TAP 900 and TAP 900@Fe. Reproduced from ref [36] under Creative Commons CC BY 3.0.

Examination of the Fe within TAP 900@Fe at the atomic level was probed using high angle annular dark field scanning transmission electron microscopy (HAADF-STEM). HAADF-STEM images show distinct luminous spots embedded within an amorphous matrix. These luminous spots correspond to isolated Fe sites within nitrogen-doped carbon (**Figure 4.4a-c**). Notably, the images revealed the complete absence of clustered or aggregated Fe species (**Figure A14**). Moreover, from atomic resolution energy dispersive X-ray spectroscopy (EDX) mapping (**Figure 4.4d-f**, **Figure A15**), the homogenesis and uniform dispersion of C, N, Fe, and O throughout the material is confirmed. The presence of O originates from surface functionalities, which aligns with earlier findings from XPS (**Table A1**).

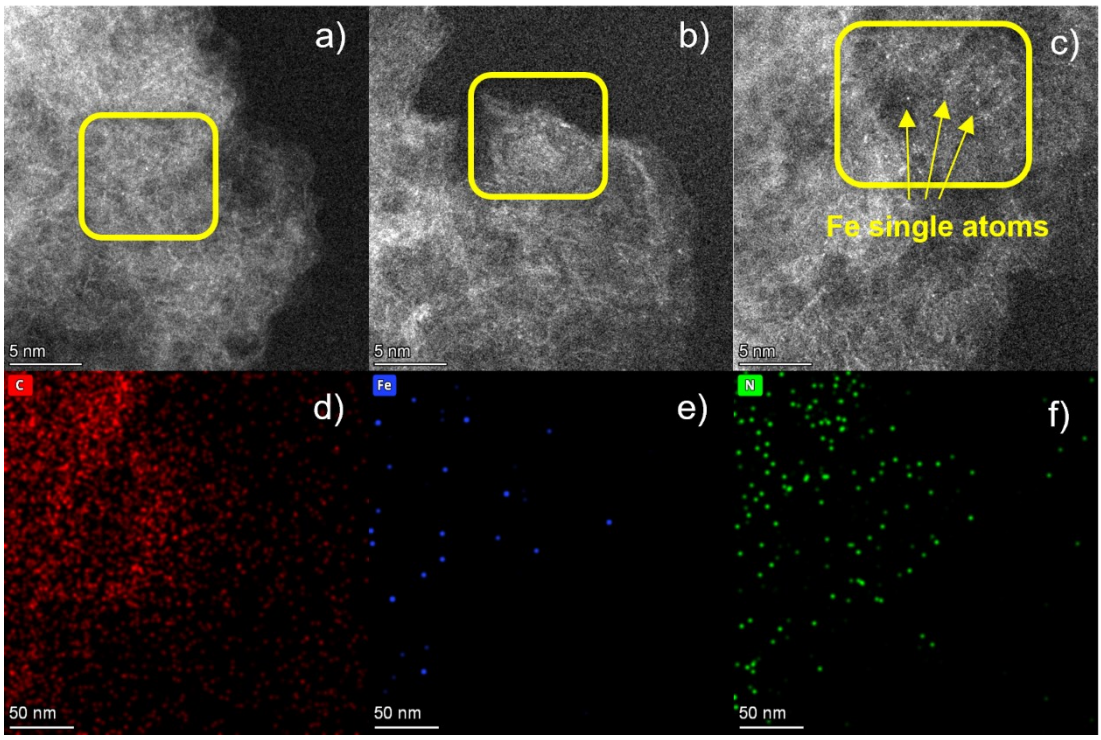


Figure 4.4. TAP 900@Fe a-c.) HAADF-STEM in different location with single atoms distributed homogeneously, as highlighted. EDX elemental mapping for d.) C e.) Fe and f.) N. Reproduced from ref [36] under Creative Commons CC BY 3.0.

Through the use of *ex situ* X-ray absorption spectroscopy, an in-depth assessment of the oxidation state and coordination environment of Fe in TAP 900@Fe is conducted. **Figure 4.5a** illustrates the comparison of Fe-K edge X-ray absorption near-edge structure (XANES) spectra for TAP 900@Fe in relation to reference samples (Fe foil, Fe_2O_3, $Fe^{II}Pc$, and Cl-$Fe^{III}Pc$). Notably, the absorption edge for TAP 900@Fe is the highest, slightly exceeding that of Fe_2O_3, which suggests an average Fe oxidation state of +3. Significant alterations are also observed in the pre-edge region. In the case of $Fe^{II}Pc$, a characteristic peak at 7118 eV corresponds to the FeN_4 moiety, displaying preserved D4h symmetry around Fe and resulting from a 1s → 4pz electronic transition. However, TAP 900@Fe exhibits a peak at 7113 eV instead of 7118 eV, indicating a distorted square planar geometry. This distortion likely arises from axial coordination involving -N/-O or Cl^- originating from the Mg templating agent. **Figure 4.5b** presents a Fourier-transformed extended X-ray absorption fine structure (EXAFS) comparison, demonstrating the absence of a Fe-Fe peak and confirming the presence of single Fe atoms within TAP 900@Fe, consistent with the HAADF-STEM findings (**Figure 4.4a-c**).

To explore unpaired electrons within TAP 900 and TAP900@Fe, *ex situ* cryogenic electron paramagnetic resonance (EPR) spectroscopy at 5 K (**Figure 4.5c**). The small, sharp signal at g ~2 in TAP 900@Fe is attributed to background signals from the EPR resonator or the empty EPR tube. Conversely, the substantial and sharp g ~2 signal in TAP 900 likely originates from organic radicals associated with defects in the carbon matrix, which appear to have been eliminated during subsequent metalation or acid washing processes. Interestingly, the signal observed in TAP 900@Fe closely resembles EPR results from a Fe-doped $CaBi_2Nb_2O_9$ material.[44] The g ~ 4.3 value is assigned to high-spin Fe^{3+} with rhombic zero-field splitting (E/D = 1/3),[5,44] while the weak shoulder at g ~ 9.6 has been previously linked to Fe^{3+} exhibiting lower rhombicity (E/D ≤ 1/3).[44] Furthermore, a broad axial signal spanning from g = 6 to g = 2 is observed in TAP 900@Fe, which has previously been characterized as high-spin Fe^{III} with significant axial zero-field splitting due to a square pyramidal or quasi-octahedral coordination environment.[5,45]

To gain a better understanding of the Fe sites, Mössbauer spectroscopy was conducted at low temperature (5.3 K) under both low (60 mT) and high (7 T) external magnetic fields on TAP 900@^{57}Fe. The spectral data were analysed through fitting simulations, resulting in the identification of five distinct Fe assignments (**Figure 4.5d** and **Table A3**). It is worth noting that the low-field spectrum revealed a small percentage (≤10%) of slow-relaxing paramagnetic entities, which were attributed to aggregates of ferric oxide, which have also been observed in low temperature methanol reflux.[13] These aggregates were not detected during characterisation (XRD, HAADF-STEM, XANES) of TAP 900@Fe, indicating the bulk sensitivity of Mössbauer to these nanometric Fe aggregates. While they do introduce some distortion to the spectral baseline, their contribution was too minor to generate discernible features above the noise level. As such, these oxide phases were excluded from both spectra, allowing the baseline to shift accordingly.

Among the identified species, a distinct Fe^{III} high-spin (HS) component labelled D1 (comprising 41% of the total) was prominent, coinciding with the broad axial signal observed in EPR spectroscopy (g = 2 and g = 6). Minority species D2 (17%), D3 (13%), D4 (18%), and D5 (11%) were also discerned and are further elaborated on in **Supplementary Note A1**. The primary focus in the discussion centres on the signal corresponding to D1, primarily due to its prevalence and its typically inferred higher reactivity.[6]

Component D1 exhibits an isomer shift of 0.47 mm s^{-1} and a quadrupole splitting of 1.05 mm s^{-1}. These values closely align with those of a penta-coordinated FeN_4 configuration featuring an axial nitrogen ligand, closely resembling a heme moiety.[8] This arrangement was previously identified using nuclear inelastic scattering and EPR.[8] Additionally, a similar D1 component has been ascribed to a penta-coordinated $Fe^{III}N_4C_{12}$ configuration with an axial oxygen ligand, based on DFT calculations and Mössbauer spectroscopy.[6,46]

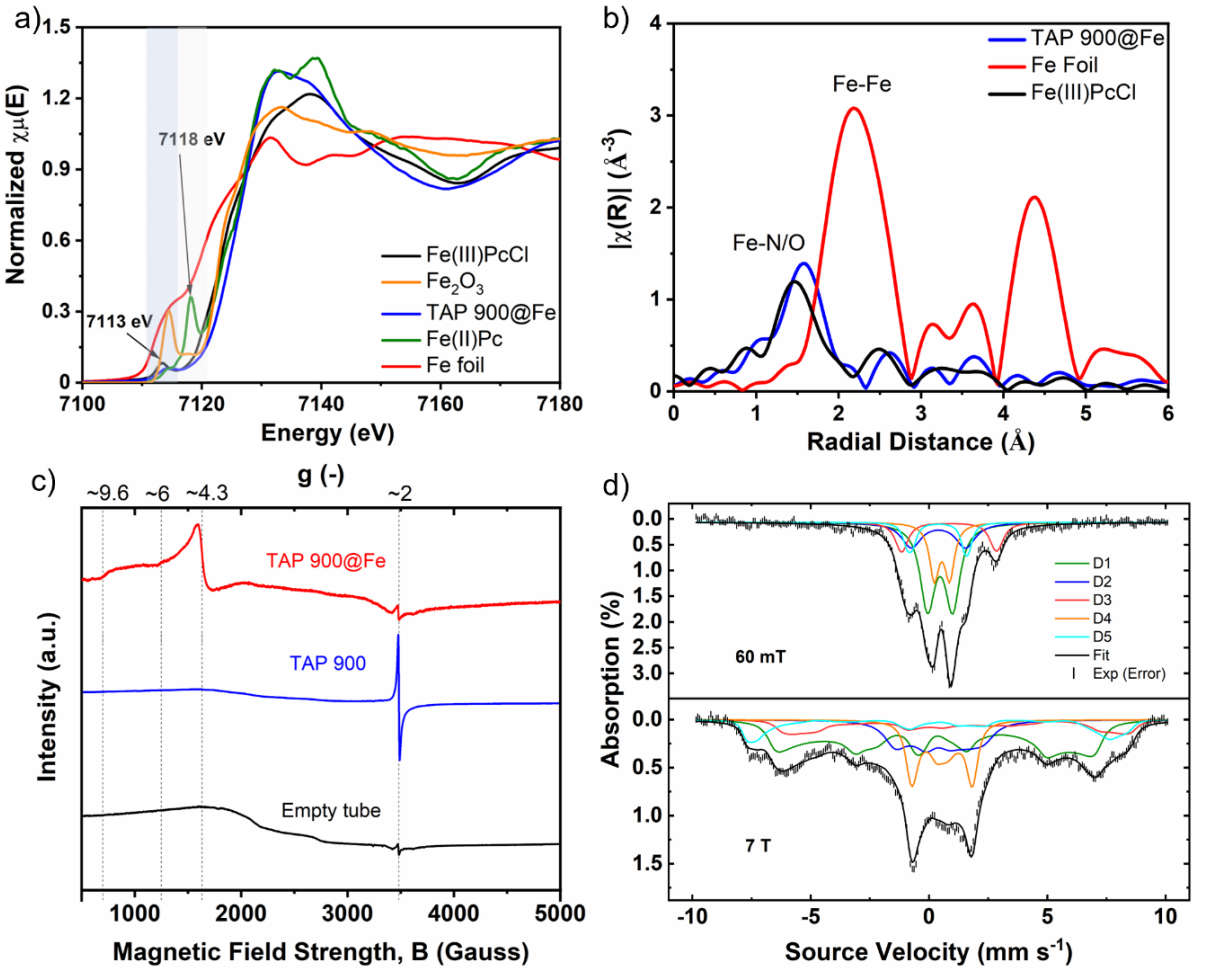


Figure 4.5. a.) Fe K-edge XANES spectra of the freshly prepared TAP 900@Fe compared with Fe foil, Fe_2O_3, $Fe^{II}Pc$ and $Fe^{III}PcCl$, confirming average Fe oxidation state in the synthesized sample is +3. b.) Fourier Transform of TAP 900@Fe, Fe foil and $Fe^{III}PcCl$ demonstrating the lack ofFe-Fe bond in TAP 900@Fe. c.) Low-temperature (5 K) X-band EPR signals of TAP 900, TAP 900@Fe and empty quartz EPR tube. d.) Low-temperature (5.3 K) Mössbauer spectrum of TAP 900@^{57}Fe in a weak (60 mT, upper) or a strong magnetic field (7 T, lower) applied parallel to the gamma rays. Five distinct Fe components identified as Fe^{III} HS (D1, green), Fe^{II} IS (D2, blue), Fe^{II} HS (D3, red), Fe^{II} LS (D4, orange) and Fe^{III} HS (D5, turquoise). The solid black line represents the composite spectrum, while the vertical black lines indicate the error bars associated with the measured spectrum. Reproduced from ref [36] under Creative Commons CC BY 3.0.

4.3.3 RDE O_2 Reduction Performance and Activity Descriptors

To assess the electrochemical oxygen reduction activity of the prepared materials, a three-electrode RDE system with O_2-saturated 0.1 M $HClO_4$ electrolyte was employed. The metal-free TAP materials displayed no activity for O_2 reduction (**Figure 4.6a** and **Figure A16**). After the addition of Fe, TAP 900@Fe exhibited the highest activity, with a kinetic current density (J_{kin}) of -1.04 ± 0.12 mA cm^{-2} at 0.8 V_{RHE} and a corresponding kinetic mass activity (m_{kin}) of 4.0 ± 0.46 A $g_{Fe\text{-}N\text{-}C}^{-1}$. In contrast, TAP 800@Fe remained inactive, possibly due to its high nitrogen content, which limited its conductivity. Meanwhile, TAP 1000@Fe displayed only slightly lower mass activity than TAP 900@Fe, reaching J_{kin} = -0.76 mA cm^{-2} at 0.8 V_{RHE} and a corresponding mass activity of 2.9 A $g_{Fe\text{-}N\text{-}C}^{-1}$. A comparison of the kinetic mass activity of TAP 900@Fe with reported high-performing Fe-N-C oxygen reduction electrocatalysts in the literature can be found in **Figure A17**.

Initially, the selectivity for 2-electron H_2O_2 formation was negligible across the potential range (<3%, **Figure 4.6b**, **Figure A18a, b**). To assess the stability and performance of TAP 900@Fe, an accelerated stress test was conducted under O_2-saturation in a narrow cyclic voltammetry potential window of 0.4-0.8 V_{RHE} at 100 mV s^{-1}. This allowed us to focus on the carbon oxidation effect associated with local H_2O_2 production[47] and Fe demetallation on TAP 900@Fe performance, while avoiding direct carbon oxidation at high potentials (>1.0-1.1 V_{RHE} at room temperature) on FeN_x sites.[48] During the accelerated stress test, the Pt ring was held at 1.27 V_{RHE} to minimize H_2O_2 accumulation in the electrolyte.

Even after 8,000 cycles, TAP 900@Fe remained selective for the 4-electron process, with H_2O_2 production increasing only slightly but remaining below 10% between 0.2-0.75 V_{RHE} (**Figure 4.6b**, **Figure A18a, b**). Under O_2-saturated accelerated stress test conditions, TAP 900@Fe experienced a 15% drop of kinetic mass activity at 0.8 V_{RHE} after 1,500 cycles (3.40 A $g_{Fe\text{-}N\text{-}C}^{-1}$). The relatively low H_2O_2 production, even after 1,500 cycles, may explain the high relative stability of TAP 900@Fe. However, the initial kinetic mass activity decreased by 46% after 8,000 cycles (2.15 A $g_{Fe\text{-}N\text{-}C}^{-1}$, **Figure A19**), possibly due to ongoing carbon oxidation by local H_2O_2.[47]

Post-electrochemistry assessments using HAADF-STEM after 8,000 accelerated stress testing cycles revealed that Fe single atoms remained within the material, with no Fe aggregation

observed (**Figure A20**). Elemental mapping through EDX also confirmed the distribution of nitrogen (N) and Fe within the TAP 900@Fe (**Figure A21**).

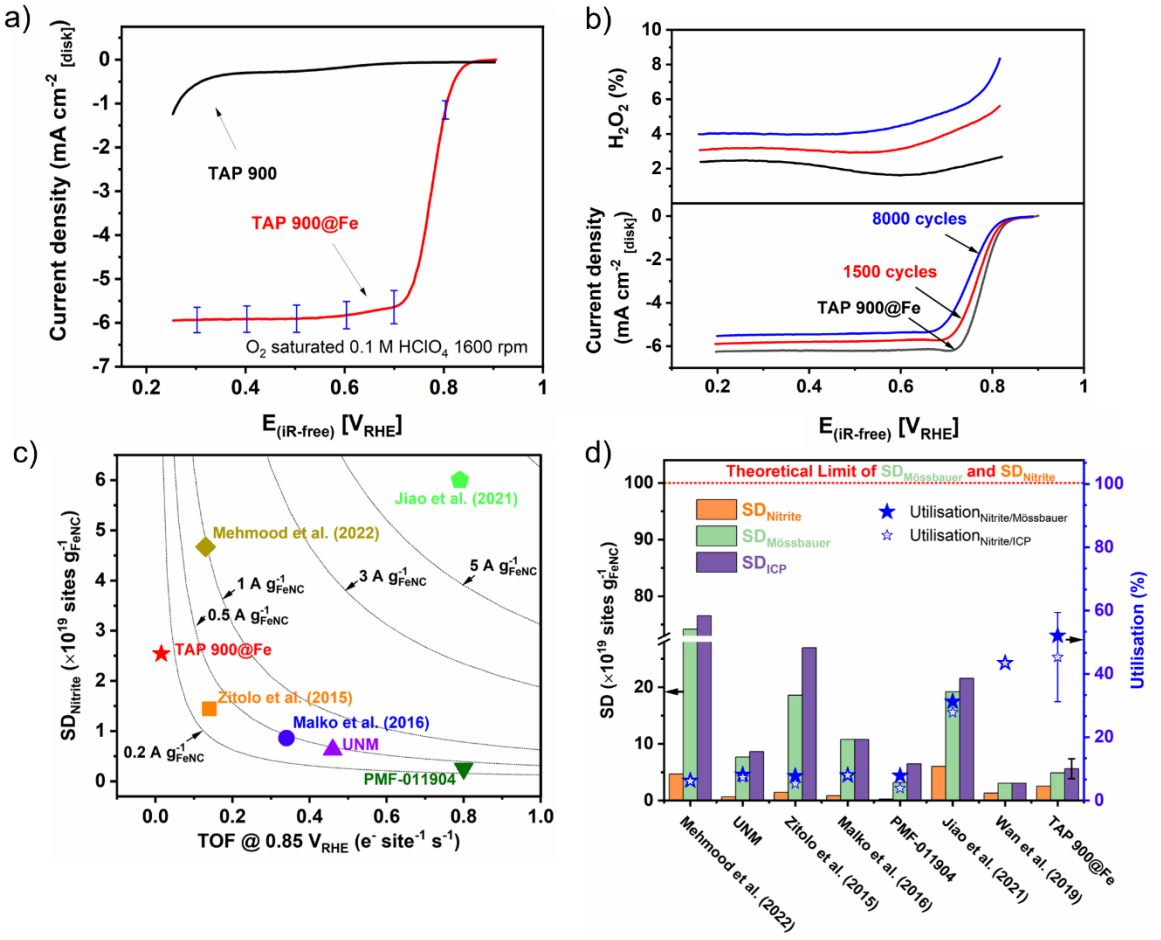


Figure 4.6. a.) Cathodic scan of the cyclic voltammogram in room temperature O_2-saturated 0.1 M $HClO_4$ at 1600 rpm and 10 mV s^{-1} with 0.26 $mg_{Fe\text{-}N\text{-}C}$ cm^{-2}. Capacitance correction applied by subtracting N_2-saturated measurement. *iR* correction applied (*R* = 23 Ω). For TAP 900@Fe, five independent measurements were carried out with the average value plotted with error bars representing the standard deviation. b.) H_2O_2 % and O_2 reduction current density from cathodic scan RRDE measurements for fresh TAP 900@Fe and post 1,500 and 8,000 accelerated stress test cyclic voltammetry cycles (0.8-0.4 V_{RHE} at 100 mV s^{-1} under O_2-saturation with Pt ring applied at 1.27 V_{RHE} throughout). c.) Comparison of $SD_{nitrite}$ and TOF with corresponding mass isoactivity at 0.85 V_{RHE} of benchmark Fe-N-C of; Zitolo *et al*. (zeolitic imidazolate framework-8 (ZIF-8) derived),[49] Malko *et al*. (polymerized di-amino naphthalene based),[50] University New Mexico and Pajarito Powder Inc. commercial catalyst PMF-011904 (both silica-templating-based),[51] Mehmood *et al*. (ZIF-8 derived),[13] and Jiao *et al*. (ZIF-8 derived).[16] Part of data obtained is replotted from ref.[52] All $SD_{Nitrite}$ electrochemical measurements with assumed 5 e^- nitrite stripping process in 0.5 M sodium acetate buffer (pH 5.2) in a RDE with 0.2 $mg_{Fe\text{-}N\text{-}C}$ cm^{-2}, except Wan *et al.* who used 0.27 $mg_{Fe\text{-}N\text{-}C}$ cm^{-2} and did not present data at 0.85 V_{RHE} (see Fig A23e for 0.80 V_{RHE} data). d.) Different *SD* and *Utilisation* metrics for Fe-N-Cs, with the theoretical active *SD* limit represented by the red dashed line, as calculated by Mehmood *et al.*[13] Reproduced from ref [36] under Creative Commons CC BY 3.0.

Active site density ($SD_{nitrite}$) for TAP 900@Fe was probed using *in situ* nitrite stripping, assuming a complete five-electron reduction of NO to NH_{4+}. This provides a lower-bound estimate of the active site density compared to CO cryo-chemisorption, which can probe sites that are electrochemically inaccessible and can also yield another utilization factor.

TAP 900@Fe exhibits a high initial $SD_{nitrite}$ of 2.54×10^{19} sites $g_{Fe\text{-}N\text{-}C}^{-1}$ (**Figure 4.6c**). Kumar *et al*. recently found *in situ* nitrite stripping also probes iron oxides that formed *in situ* as a result of degradation of FeN_x sites.[53,54] No Fe oxides (or other phases) were detected in TAP900@Fe pre- and post-electrochemical testing from HAADF-STEM and elemental mapping EDX (**Figure A20, A25**), while pre-electrochemical testing low-temperature Mössbauer measurements suggested Fe oxides could exist in a small minority of ≤10% (**Figure 4.5d**). It should also be noted, Gong *et al.* recently found nitrite stripping also probes N-C sites.[55]

The $SD_{nitrite}$ for TAP 900@Fe surpasses previous benchmark Fe-N-C catalysts;[18] however recent progress with zeolitic imidazolate framework-8 derived catalysts have achieved remarkable $SD_{Nitrite}$ values of 4.7 and 6.0×10^{19} sites $g_{Fe\text{-}N\text{-}C}^{-1}$.[13,16] Still, it is important to consider that even in high $SD_{nitrite}$ catalysts, the vast majority (>70%) of the loaded FeN_x is not utilized (**Figure 4.6d**). This raises questions about the electrochemical utilization of FeN_x in fuel cells, particularly when thick Fe-N-C layers (around 100 µm) are used, and achieving uniform ionomer distribution is challenging.

It is noteworthy that some reports have claimed exceptionally high $SD_{nitrite}$ values, but with lower SDICP values, suggesting potential artifacts in nitrite or ICP measurements. The $Utilisation_{Nitrite/ICP}$ and $Utilisation_{Nitrite/Mössbauer}$ values for TAP 900@Fe are remarkably high at 45% and 52%, respectively, surpassing previous records. It's worth mentioning that recent studies have proposed a 3-electron pathway for nitrite stripping, which would imply even higher utilization values (75% and 87%) if considered.

In summary, the high electrocatalytic activity of TAP 900@Fe can be attributed to its high FeN_x active site density and utilization, which is likely influenced by its high mesoporosity. The interaction between TAP and Mg salt during pyrolysis plays a crucial role in enabling this mesoporosity, as TAP self-assembles around the water molecules in the Mg salt through hydrogen bonding, leading to a homogeneous liquid-state polymerization without grain boundaries and, consequently, sufficient porosity after acid washing.

In comparing the Fe-N-C catalyst to Pt/C (**Figure A23f**), it becomes apparent that even with significant advancements in achieving a 100% FeNx utilization rate, the theoretical limit for accessible active sites SD in FeN_x falls short of that observed in Pt sites within Pt/C. Consequently, based solely on site density considerations, the catalytic activity of Fe-N-C appears inadequate to compete with Pt/C. Therefore, it becomes imperative to consider the TOF of FeN_x sites.

Although the TAP 900@Fe catalyst exhibits a high FeN_x utilization, it yields relatively low TOF values, specifically 0.087 and 0.015 $e^-\ sites^{-1}\ s^{-1}$ at electrode potentials of 0.80 and 0.85 V_{RHE}, respectively (**Figure 4.6c** and **Figure A23e**). Analysis of low-temperature Mössbauer spectroscopy (**Figure 4.5d**) reveals that the dominant component in the catalyst is D1 Fe^{III} high-spin (HS). Notably, it has been previously associated with penta-coordinated $Fe^{III}N_4C_{12}$ sites with axial oxygen (O) ligands, which have exhibited high TOF values.[6]

For example, Jiao et al. reported a catalyst that was predominantly composed of $Fe^{III}N_4C_{12}$ sites with axial O ligands (D1 = 90%) and demonstrated state-of-the-art catalytic activity with a TOF of 0.8 $e^-\ site^{-1}\ s^{-1}$ at 0.80 and 0.85 V_{RHE}. In contrast, a catalyst containing D1 sites with a penta-coordinated $Fe^{III}N_4$ configuration and N axial ligands (TOF approximately zero at 0.8 V_{RHE}) displayed activity more comparable to that observed with TAP 900@Fe.[8] It is worth noting that the presence of an N ligand may induce an undesirable shift in the binding energy of Fe, thereby resulting in the observed lower TOF values. As observed in this study, determining the specific active site coordination environment ex situ in these materials is a challenging task. Fe-N-C catalysts, even those composed entirely of FeN_x sites, typically comprise a range of different active site configurations.

4.3.4 DFT

To gain a fundamental understanding of how different axial ligands influence electrocatalytic activity, DFT simulations were conducted, focusing on the *OH intermediate in the O_2 reduction reaction volcano (**Figure 4.7**). While TAP 900@Fe primarily contains pyridine moieties (as shown in **Figure 4.3c**), both pyridine and pyrrole motifs were employed in the DFT calculations (**Figure A24** and **Figure 4.7b**) to account for the varied activity of these two types of sites.

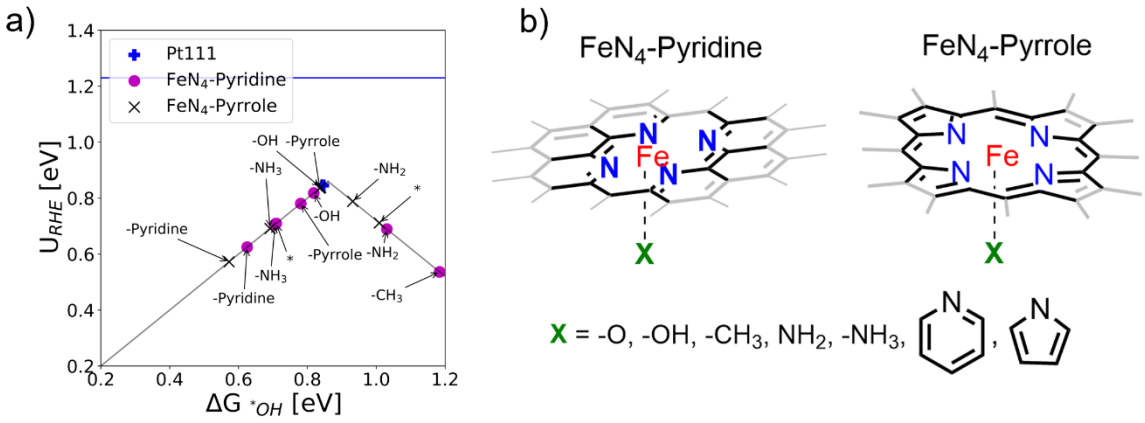


Figure 4.7. a.) ORR activity volcano represented by O_2 reduction potential (RHE), U_{RHE}, on y-axis and binding energy of *OH intermediate (ΔG_{*OH}) on the x-axis. This indicates how O_2 reduction activity varies across a series of FeN_4 pyridine and pyrrole sites with different axial ligands, and compared to Pt(111) as reference. b.) Schematic representations depict the axial coordination in FeN_4-Pyridine (left) and FeN_4-Pyrrole (right) configurations. "X" denotes the axial ligand and * denotes the pristine FeN_4 structure. Reproduced from ref [36] under Creative Commons CC BY 3.0.

From DFT, various axial ligands were systematically tested, including -Pyrrole, -Pyridine, $-NH_3$, $-NH_2$, $-CH_3$, -OH, -O, and the pristine structure (-*), through simulations of *OH binding energy on FeN_4 sites. These simulations allowed us to compare the binding energies with those observed on Pt(111), as illustrated in **Figure 4.7a-b**. These different axial ligands represent an exploration of how the *OH binding energy on FeN_4 sites changes when various axial ligands are introduced. For example, the presence of a nitrogen axial bond is represented by $-NH_2$, while an oxygen axial bond is represented by -OH, and so on. It is worth noting that there is not a widely accepted consensus in the literature on modelling metal-nitrogen-carbon (M-N-C) systems,[56,57] and as such, water solvation was not applied to the *OH binding energies on the FeN_4 sites. However, for Pt(111), -0.3 eV solvation stabilization was applied, as per previous literature.[23] In **Figure A25**, an ORR volcano with a -0.3 eV solvation stabilisation is applied to all binding energies. This demonstrates that while the DFT axial trend study remains robust in terms of the order of *OH binding, the absolute water solvation may cause the data points to shift up or down on the volcano. Unfortunately, the exact water solvation in M-N-C systems is not well-known, underscoring the challenge in precisely predicting these properties.

Figure 4.7a highlights an interesting trend for pyridine FeN_4 sites. The introduction of an axial -OH ligand weakens the *OH binding energy, pushing the pyridine FeN_4 site closer to the top of the volcano. Conversely, the axial $-NH_2$ ligand deactivates the pyridine FeN_4 site. In

contrast, pyrrolic FeN_4 sites exhibit a different trend. The -OH and -NH_2 ligands strengthen the *OH binding energy, positioning the pyrrolic FeN_4 site with an -NH_2 axial ligand close to the top of the volcano. Notably, recent research has suggested that pyrrolic Fe sites may exhibit low catalytic activity.[58] DFT results here suggests that the activity of pyrrolic sites could be enhanced through axial ligand coordination, such as pyrrole or -NH_2.

This represents a significant finding, as it reveals for the first time that the type or absence of axial ligands has a substantial impact on *OH binding energy for both pyridinic and pyrrolic sites. Consequently, discussions comparing pyridinic versus pyrrolic sites should consider the influential role of axial ligands in the catalytic activity of these sites.

4.4 Conclusion

In summary, a highly porous Fe-N-C material with exceptional Fe utilisation efficiency for O_2 reduction reaction in acidic environments was achieved, according to *in situ* nitrite stripping. This material was prepared using a two-step synthesis approach, involving the coordination of Fe within a highly porous nitrogen-doped carbon framework. The nitrogen-doped carbon framework was synthesized using 2,4,6-Triaminopyrimidine as the foundational C-N building block, with $MgCl_2{\cdot}6H_2O$ serving as a templating agent to create active site templates and porosity.

The substantial mesoporosity of the substrate facilitated the formation of electrochemically accessible FeNx sites. This was corroborated by achieving a remarkable electrochemical FeNx utilization rate of 52%, with a high density of electrochemically active sites amounting to 2.54×10^{19} sites $g_{Fe\text{-}N\text{-}C}^{-1}$, as determined through in situ nitrite stripping analysis. Further characterization using ex situ XAS and low-temperature Mössbauer spectroscopy revealed that the predominant active site configuration in TAP 900@^{57}Fe was a penta-coordinated FeN_x site with an axial ligand.

To gain deeper insights into the influence of axial ligands on pyridinic and pyrrolic FeN4 sites, DFT calculations were conducted. These computations unveiled the varying effects of axial ligands on the binding energy of the OH intermediate, highlighting that axial ligands can either enhance or diminish the catalytic activity of pyridinic and pyrrolic FeN_4 catalysts.

References

1 A. Pedersen, J. Barrio, A. Li, R. Jervis, D. J. L. Brett, M. M. Titirici and I. E. L. Stephens, *Adv. Energy Mater.*, 2022, **12**, 2102715.

2 J. Wang, Z. Huang, W. Liu, C. Chang, H. Tang, Z. Li, W. Chen, C. Jia, T. Yao, S. Wei, Y. Wu and Y. Li, *J. Am. Chem. Soc.*, 2017, **139**, 17281–17284.

3 C. Zúñiga Loyola and F. Tasca, *Curr. Opin. Electrochem.*, 2023, **40**, 101316.

4 L. Zhang, N. Jin, Y. Yang, X.-Y. Miao, H. Wang, J. Luo and L. Han, *Nano-Micro Lett.*, 2023, **15**, 228.

5 L. Ni, C. Gallenkamp, S. Paul, M. Kübler, P. Theis, S. Chabbra, K. Hofmann, E. Bill, A. Schnegg, B. Albert, V. Krewald and U. I. Kramm, *Adv. Energy Sustain. Res.*, 2021, **2**, 2000064.

6 J. Li, M. T. Sougrati, A. Zitolo, J. M. Ablett, I. C. Oğuz, T. Mineva, I. Matanovic, P. Atanassov, Y. Huang, I. Zenyuk, A. Di Cicco, K. Kumar, L. Dubau, F. Maillard, G. Dražić and F. Jaouen, *Nat. Catal.*, 2021, **4**, 10–19.

7 J. Barrio, A. Pedersen, S. Favero, H. Luo, M. Wang, S. Ch. Sarma, J. Feng, L. T. T. Ngoc, S. Kellner, A. Y. Li, A. B. Jorge Sobrido and M.-M. Titirici, *Chem. Rev.*, 2023, **123**, 2311–2348.

8 S. Wagner, H. Auerbach, C. E. Tait, I. Martinaiou, S. C. N. Kumar, C. Kübel, I. Sergeev, H.-C. Wille, J. Behrends, J. A. Wolny, V. Schünemann and U. I. Kramm, *Angew. Chem. Int. Ed.*, 2019, **58**, 10486–10492.

9 C. Gallenkamp, U. I. Kramm and V. Krewald, *Chem. Commun.*, 2021, **57**, 859–862.

10 P. Hutchison, P. S. Rice, R. E. Warburton, S. Raugei and S. Hammes-Schiffer, *J. Am. Chem. Soc.*, 2022, **144**, 16524–16534.

11 X. Yang, D. Xia, Y. Kang, H. Du, F. Kang, L. Gan and J. Li, *Adv. Sci.*, 2020, **7**, 2000176.

12 X. She, J. Gao, Y. Gao, H. Tang, K. Li, Y. Wang and Z. Wu, *New J. Chem.*, 2022, **46**, 16138–16150.

13 A. Mehmood, M. Gong, F. Jaouen, A. Roy, A. Zitolo, A. Khan, M. Sougrati, M. Primbs, A. M. Bonastre, D. Fongalland, G. Drazic, P. Strasser and A. Kucernak, *Nat. Catal.*, 2022, **5**, 311–323.

14 R. Van Hardeveld and F. Hartog, *Surf. Sci.*, 1969, **15**, 189–230.

15 F. Jaouen, D. Jones, N. Coutard, V. Artero, P. Strasser and A. Kucernak, *Johns. Matthey Technol. Rev.*, 2018, **62**, 231–255.

16 L. Jiao, J. Li, L. L. Richard, Q. Sun, T. Stracensky, E. Liu, M. T. Sougrati, Z. Zhao, F. Yang, S. Zhong, H. Xu, S. Mukerjee, Y. Huang, D. A. Cullen, J. H. Park, M. Ferrandon, D. J. Myers, F. Jaouen and Q. Jia, *Nat. Mater.*, 2021, **20**, 1385–1391.

17 X. Wan, X. Liu, Y. Li, R. Yu, L. Zheng, W. Yan, H. Wang, M. Xu and J. Shui, *Nat. Catal.*, 2019, **2**, 259–268.

18 M. Primbs, Y. Sun, A. Roy, D. Malko, A. Mehmood, M.-T. Sougrati, P.-Y. Blanchard, G. Granozzi, T. Kosmala, G. Daniel, P. Atanassov, J. Sharman, C. Durante, A. Kucernak, D. Jones, F. Jaouen and P. Strasser, *Energy Environ. Sci.*, 2020, **13**, 2480–2500.

19 D. Malko, A. Kucernak and T. Lopes, *Nat. Commun.*, 2016, **7**, 13285.

20 A. Hjorth Larsen, J. Jørgen Mortensen, J. Blomqvist, I. E. Castelli, R. Christensen, M. Dułak, J. Friis, M. N. Groves, B. Hammer, C. Hargus, E. D. Hermes, P. C. Jennings, P. Bjerre Jensen, J. Kermode, J. R. Kitchin, E. Leonhard Kolsbjerg, J. Kubal, K. Kaasbjerg, S. Lysgaard, J. Bergmann Maronsson, T. Maxson, T. Olsen, L. Pastewka, A. Peterson, C. Rostgaard, J. Schiøtz, O. Schütt, M. Strange, K. S. Thygesen, T. Vegge, L. Vilhelmsen, M. Walter, Z. Zeng and K. W. Jacobsen, *J. Phys. Condens. Matter*, 2017, **29**, 273002.

21 J. Enkovaara, C. Rostgaard, J. J. Mortensen, J. Chen, M. Dułak, L. Ferrighi, J. Gavnholt, C. Glinsvad, V. Haikola, H. A. Hansen, H. H. Kristoffersen, M. Kuisma, A. H. Larsen, L.

Lehtovaara, M. Ljungberg, O. Lopez-Acevedo, P. G. Moses, J. Ojanen, T. Olsen, V. Petzold, N. A. Romero, J. Stausholm-Møller, M. Strange, G. A. Tritsaris, M. Vanin, M. Walter, B. Hammer, H. Häkkinen, G. K. H. Madsen, R. M. Nieminen, J. K. Nørskov, M. Puska, T. T. Rantala, J. Schiøtz, K. S. Thygesen and K. W. Jacobsen, *J. Phys. Condens. Matter*, 2010, **22**, 253202.

22 J. Wellendorff, K. T. Lundgaard, A. Møgelhøj, V. Petzold, D. D. Landis, J. K. Nørskov, T. Bligaard and K. W. Jacobsen, *Phys. Rev. B*, 2012, **85**, 235149.

23 J. K. Nørskov, J. Rossmeisl, A. Logadottir, L. Lindqvist, J. R. Kitchin, T. Bligaard and H. Jónsson, *J. Phys. Chem. B*, 2004, **108**, 17886–17892.

24 B. Ravel and M. Newville, *J. Synchrotron Radiat.*, 2005, **12**, 537–541.

25 M. K. Bhunia, K. Yamauchi and K. Takanabe, *Angew. Chem. Int. Ed.*, 2014, **53**, 11001–11005.

26 M. Shunmughanathan, N. Madankumar and K. Pitchumani, *ChemistrySelect*, 2018, **3**, 13743–13750.

27 Z. Zhou, F. He, Y. Shen, X. Chen, Y. Yang, S. Liu, T. Mori and Y. Zhang, *Chem. Commun.*, 2017, **53**, 2044–2047.

28 J. Barrio, M. Volokh and M. Shalom, *J. Mater. Chem. A*, 2020, **8**, 11075–11116.

29 Z. Chen, S. Pronkin, T.-P. Fellinger, K. Kailasam, G. Vilé, D. Albani, F. Krumeich, R. Leary, J. Barnard, J. Meurig Thomas, J. Pérez-Ramírez, M. Antonietti and D. Dontsova, *ACS Nano*, 2016, **10**, 3166–3175.

30 S. K. Kaiser, Z. Chen, D. Faust Akl, S. Mitchell and J. Pérez-Ramírez, *Chem. Rev.*, 2020, **120**, 11703–11809.

31 F. K. Kessler, Y. Zheng, D. Schwarz, C. Merschjann, W. Schnick, X. Wang and M. J. Bojdys, *Nat. Rev. Mater.*, 2017, **2**, 17030.

32 B. Jürgens, E. Irran, J. Senker, P. Kroll, H. Müller and W. Schnick, *J. Am. Chem. Soc.*, 2003, **125**, 10288–10300.

33 W. Zhang, J. Barrio, C. Gervais, A. Kocjan, A. Yu, X. Wang and M. Shalom, *Angew. Chem. Int. Ed.*, 2018, **57**, 9764–9769.

34 J. Pampel, A. Mehmood, M. Antonietti and T.-P. Fellinger, *Mater. Horiz.*, 2017, **4**, 493–501.

35 J.-C. Li, Y. Meng, R. Ma, H. Hu, S. Zhao, Y. Zhu, P.-X. Hou and C. Liu, *ACS Appl. Mater. Interfaces*, 2021, **13**, 58576–58584.

36 J. Barrio, A. Pedersen, S. Ch. Sarma, A. Bagger, M. Gong, S. Favero, C.-X. Zhao, R. Garcia-Serres, A. Y. Li, Q. Zhang, F. Jaouen, F. Maillard, A. Kucernak, I. E. L. Stephens and M.-M. Titirici, *Adv. Mater.*, 2023, **35**, 2211022.

37 H. May, *J. Appl. Chem.*, 1959, **9**, 340–344.

38 S. C. Moldoveanu, *Pyrolysis of organic molecules: applications to health and environmental issues*, Elsevier, 2009.

39 M. Mazzucato, G. Daniel, A. Mehmood, T. Kosmala, G. Granozzi, A. Kucernak and C. Durante, *Appl. Catal. B Environ.*, 2021, **291**, 120068.

40 A. Mehmood, J. Pampel, G. Ali, H. Y. Ha, F. Ruiz-Zepeda and T.-P. Fellinger, *Adv. Energy Mater.*, 2018, **8**, 1701771.

41 D. Menga, J. L. Low, Y.-S. Li, I. Arčon, B. Koyutürk, F. Wagner, F. Ruiz-Zepeda, M. Gaberšček, B. Paulus and T.-P. Fellinger, *J. Am. Chem. Soc.*, 2021, **143**, 18010–18019.

42 T. Sun, Y. Jiang, Q. Wu, L. Du, Z. Zhang, L. Yang, X. Wang and Z. Hu, *Catal. Sci. Technol.*, 2017, **7**, 51–55.

43 U. I. Kramm, M. Lefèvre, N. Larouche, D. Schmeisser and J.-P. Dodelet, *J. Am. Chem. Soc.*, 2014, **136**, 978–985.

44 N. A. Zhuk, V. P. Lutoev, B. A. Makeev, S. V. Nekipelov, A. V. Koroleva, A. V. Fedorova, M. V. Yermolina, D. S. Beznosikov and L. O. Karlova, *J. Mater. Res. Technol.*, 2020, **9**, 4173–4182.

45 J. Nehrkorn, B. M. Martins, K. Holldack, S. Stoll, H. Dobbek, R. Bittl and A. Schnegg, *Mol. Phys.*, 2013, **111**, 2696–2707.

46 T. Mineva, I. Matanovic, P. Atanassov, M. T. Sougrati, L. Stievano, M. Clémancey, A. Kochem, J. M. Latour and F. Jaouen, *ACS Catal.*, 2019, **9**, 9359–9371.

47 C. H. Choi, H. K. Lim, M. W. Chung, G. Chon, N. Ranjbar Sahraie, A. Altin, M. T. Sougrati, L. Stievano, H. S. Oh, E. S. Park, F. Luo, P. Strasser, G. Dražić, K. J. J. Mayrhofer, H. Kim and F. Jaouen, *Energy Environ. Sci.*, 2018, **11**, 3176–3182.

48 C. H. Choi, C. Baldizzone, J.-P. Grote, A. K. Schuppert, F. Jaouen and K. J. J. Mayrhofer, *Angew. Chem. Int. Ed.*, 2015, **54**, 12753–12757.

49 A. Zitolo, V. Goellner, V. Armel, M. T. Sougrati, T. Mineva, L. Stievano, E. Fonda and F. Jaouen, *Nat. Mater.*, 2015, **14**, 937–942.

50 D. Malko, T. Lopes, E. Symianakis and A. R. Kucernak, *J. Mater. Chem. A*, 2015, **4**, 142–152.

51 M. Primbs, Y. Sun, A. Roy, D. Malko, A. Mehmood, M.-T. Sougrati, P.-Y. Blanchard, G. Granozzi, T. Kosmala, G. Daniel, P. Atanassov, J. Sharman, C. Durante, A. Kucernak, D. Jones, F. Jaouen and P. Strasser, *Energy Environ. Sci.*, 2020, **13**, 2480–2500.

52 A. Mehmood, M. Gong, F. Jaouen, A. Roy, A. Zitolo, A. Khan, M. Sougrati, M. Primbs, A. M. Bonastre, D. Fongalland, G. Drazic, P. Strasser and A. Kucernak, Dataset for the paper “High Loading of Single Atomic Iron Sites in Pyrolysed Fe-NC Oxygen Reduction Catalysts for Proton Exchange Membrane Fuel Cells.”

53 K. Kumar, T. Asset, X. Li, Y. Liu, X. Yan, Y. Chen, M. Mermoux, X. Pan, P. Atanassov, F. Maillard and L. Dubau, *ACS Catal.*, 2021, **11**, 484–494.

54 K. Kumar, L. Dubau, M. Mermoux, J. Li, A. Zitolo, J. Nelayah, F. Jaouen and F. Maillard, *Angew. Chem. Int. Ed.*, 2020, **59**, 3235–3243.

55 M. Gong, A. Mehmood, B. Ali, K.-W. Nam and A. Kucernak, *ACS Catal.*, 2023, **13**, 6661–6674.

56 F. Luo, A. Roy, L. Silvioli, D. A. Cullen, A. Zitolo, M. T. Sougrati, I. C. Oguz, T. Mineva, D. Teschner, S. Wagner, J. Wen, F. Dionigi, U. I. Kramm, J. Rossmeisl, F. Jaouen and P. Strasser, *Nat. Mater.*, 2020, **19**, 1215–1223.

57 F. Calle-Vallejo, A. Krabbe and J. M. García-Lastra, *Chem. Sci.*, 2017, **8**, 124–130.

58 D. Menga, A. Guilherme Buzanich, F. Wagner and T.-P. Fellinger, *Angew. Chem. Int. Ed.*, 2022, **61**, e202207089.

Chapter 5: Fe Dissolution in Fe-N-C Electrocatalysts during Acidic Oxygen Reduction: Impact of Local pH

5.1 Introduction

Fe-N-C durability is still far below commercial realization for transport applications (>5,000 h)[1], with demetallation of FeN_x active sites suggested as the primary irreversible performance degradation mechanism in PEMFCs [2–4] and the first step in aggregation scenario.[5] Inductively-coupled plasma mass spectrometry (ICP-MS) is a highly sensitive technique which can provide time- and potential-resolved Fe dissolution profiles from Fe-N-C catalysts. Monitoring Fe dissolution from *ex situ* ICP-MS, in tandem with other characterization techniques, in rotating disc electrode (RDE)[6] and PEMFC has revealed significant dissolution of Fe,[7] although probing the mechanism requires *operando* measurements. In the first online flow cell ICP-MS study, Choi *et al.* suggested formation of insoluble ferric (Fe^{III}) species, which dissolve under PEMFC operating conditions ($E_{cathode}$ < 0.7 V_{RHE}) due to *operando* reduction to soluble ferrous (Fe^{II}) cations.[8] This is in line with former *ex situ* ICP-MS findings of Zelenay and coworkers[6] who suggested higher solubility of Fe^{II} species in acid solutions compared to Fe^{III} species. Previous online flow cell ICP-MS studies also provided critical information on the effects of pyrolysis atmosphere, bulk electrolyte pH, and catalyst modification on the extent of Fe dissolution.[8–10]

Nonetheless, flow cell ICP-MS studies are limited to low current densities, and cannot reproduce all the practical conditions occurring in an operating PEMFC device (O_2 partial pressure and current density, lower relative humidity).[11] In this respect, online gas diffusion electrode (GDE) ICP-MS is an adequate tool to simulate the environment of a PEMFC cathode more realistically, and gain PEMFC-relevant durability trends. For instance, Ehelebe *et al*. first demonstrated significantly lower dissolution of Pt/C catalysts in GDE configuration compared to flow cell systems due to varying mass transport conditions of Pt species,[12] as previously proposed.[13] Very recently, Choi and coworkers[14] monitored *in situ* changes in active site density and *operando* Fe dissolution of a Fe-N-C under Ar and O_2 at different temperatures using GDE ICP-MS cell in acidic conditions. From site density monitoring, the reduced turnover frequency also confirmed the reactive oxygen species catalyzed carbon corrosion scenario.[15,16] However, despite using a GDE, Choi and coworkers current densities at 0.6 V chronoamperometric holds (<10 mA cm^{-2}) were comparable to values achievable in flow cell

(~1 mA cm^{-2}), and not practical PEMFCs. They observed from *post-mortem* transmission electron microscopy (TEM) and energy dispersive x-ray spectroscopy (EDX) elemental mapping that Fe deposited as Fe_xO_y nanoparticles after O_2 reduction in their Fe-N-C derived from microporous zeolitic imidazolate framework-8 (ZIF-8), confirming earlier findings from Kumar *et al*.[15] Evidence of Fe_xO_y nanoparticle formation in PEMFC-relevant conditions has previously been ascribed to highly active but unstable high-spin FeN_4C_{12} moieties, *via* Mössbauer spectroscopy.[17]

Temperature is also a critical parameter for durability of Fe-N-C catalysts. Goellner *et al*. first evidenced that the rate of corrosion of a N-C matrix (square wave cycling between 0.9-1.4 V_{RHE}) increases 14-fold when temperatures increase from 20 to 80 °C. This resulted in 18× larger O_2 reduction activity decay (at 0.8 V_{RHE}) due to increased Fe demetallation.[18] Carbon corrosion can be avoided at 25 °C in RDE by keeping potential <0.9 V_{RHE},[9] although some carbon corrosion (<7 mA cm^{-2}) is reported in PEMFC at 80 °C.[19] Kumar *et al.* reported Fe cluster formation under load cycling (Ar-saturated 0.1 M H_2SO_4, 0.6-1.0 V_{RHE}) at 80 °C, but did not observe Fe clusters at 60 °C, providing strong evidence of the effect of temperature on the fate of Fe species.[5] Finally, it is noted that Osmieri *et al*. reported greater performance loss under air-fed vs. N_2-fed PEMFC cathode (3 s holds at 0.95 and 0.6 $V_{vs\ anode}$, 80 ^{0}C), although with no nanoparticle formation.[20] There are thus conflicting results in literature, which is could be due to operation conditions, (temperature, gas atmosphere, Nafion content, current densities, potential etc.), storage conditions,[21] electrode preparation[22] and synthesized Fe-N-C properties.[17] Moreover, Fe-N-C catalysts studied by *operando* ICP-MS have consisted of low active site utilization Fe-N-C derived from ZIF-8. As I have highlighted in **Chapter 4**, such catalysts display a predominantly or purely microporous structure. This limits the mass transport and electrochemical active site utilization (number of electrochemically accessible FeN_x sites to the total number of FeN_x sites) to typically <10%.[23–25] This prompted me to revisit Fe dissolution and the fate of Fe in FeN_x active sites from the high FeN_x utilisation (>50%) TAP 900@Fe with high micro- and meso-porosity (**Figure 4.2**). This pore structure can facilitate mass transport of reactants for improved activity, while also enabling transport of dissolved Fe ions for *operando* ICP-MS detection.

The impact on Fe-N-C activity from changes in the (micro-) environment from RDE to GDE/PEMFC has been discussed.[26–28] Local pH is one value which could vary between

electrocatalysts and testing conditions, and is recognized to influence Fe-N-C activity.[29–31] Meanwhile, the influence of pH on degradation is beginning to receive greater attention in modelling reaction mechanisms and dissolution trends.[32] Local pH (at the interface between the working electrode and the bulk of the electrolyte) and its effects has been investigated and discussed quite extensively in electrochemical CO_2 reduction;[33,34] however, so far it has garnered limited experimental and theoretical evidence for ORR.[35–37] Meanwhile, kinetic modelling work by Zenyuk and Litster found increased pH deeper within Pt mesopore channels, which was not infiltrated with Nafion and instead filled with water.[38] It is worth considering that FeN_x active sites are proposed to be located within micropores,[19,24,39] which are expected to be filled with water.[19] Although, micropore flooding has been suggested to not be a critical mechanism contributing to PEMFC performance decay.[40] Instead, kinetic models of Fe-N-C activity decay under different potentiostatic conditions in PEMFCs have been previously proposed,[19,41,42] which has led to some debate.[43,44] Still, to date these kinetic models of Fe-N-C have not factored in pH change and conditions in GDEs have not been considered.

In this Chapter, I monitor Fe dissolution of the developed high electrochemical utilization Fe-N-C catalyst using *operando* flow cell and GDE ICP-MS. The fate of Fe-N-C catalysts is determined by combined Fe demetallation, reactive oxygen species action (magnifying Fe demetallation) and local pH changes caused by O_2 reduction. A suite of complimentary *pre-* and *post-mortem* characterization techniques (SEM, TEM, STEM, EDX, Raman spectroscopy, XRD, XPS, XANES) illustrate changes in structure and chemistry. Local pH change from O_2 reduction is supported by microkinetic modelling.

5.2 Experimental

5.2.1 Catalyst Preparation

Fe-N-C and ^{57}Fe-N-C catalysts were prepared according to Chapters 3.2.1-3.2.3.

5.2.2 RDE Electrode Preparation

a 5 mm glassy carbon disc enclosed in a custom polyether ether ketone (PEEK) shroud. To prepare the rotating disk electrode (RDE) tips, they were subjected to cleaning in caro acid, which was created by mixing 30% H_2O_2 with 96% H_2SO_4 in a 1:1 ratio for a minimum of 5 hours. Subsequently, the tips were boiled in milli-Q water twice and then dried in an oven at 60^{o}C to ensure the complete removal of any remaining water. The RDE tips were further polished using 3 µm and then 1 µm diamond paste on a polishing pad to achieve a polished and reflective surface. Due to the hydrophobic nature of the catalyst, a droplet of deionized (DI) water was placed over the RDE tip and transferred to a desiccator, which was then evacuated to create a vacuum. After removing the RDE tip from the desiccator, the catalyst was wetted, and any visible air bubbles were eliminated. With the droplet still present on the catalyst, the RDE tip was placed in the custom-made flow cell or RDE cell.

5.2.3 Online Flow Cell ICP-MS

The experimental setup employed a custom-made PEEK cell (**Figure 5.1**) featuring a three-electrode configuration. This configuration utilized a glassy carbon rod as the counter electrode (SIGRADUR, HTW GmbH) and an airtight Ag/AgCl (ET072, eDAQ) reference electrode. The Ag/AgCl electrode underwent calibration against the RHE using both a Hydroflex (Gaskatel) and a self-made Pt wire RHE. To prevent interference from ArO+, the online flow cell ICP-MS measurement utilized ^{57}Fe in TAP 900@^{57}Fe. The flow rate of the electrolyte was regularly monitored each day, typically ranging from 430 to 480 µL/min. Prior to and following the completion of the electrochemical measurement protocol, calibration of the inductively coupled plasma mass spectrometer (ICP-MS) was conducted. Calibration involved the use of a blank and five standard solutions of ^{56}Fe and ^{24}Mg at concentrations of 0, 5, 10, 20, and 50 ppb. The calibration factor for ^{57}Fe was adjusted to account for its natural abundance of 2.12%. Calibration curves were generated both before and after online ICP-MS measurements, and appropriate corrections were applied to account for any drift. Analysis of ^{57}Fe and ^{24}Mg was carried out using a PerkinElmer NexION 2000c spectrometer coupled with the custom-made electrochemical flow cell, and data was recorded using Syngistix software.

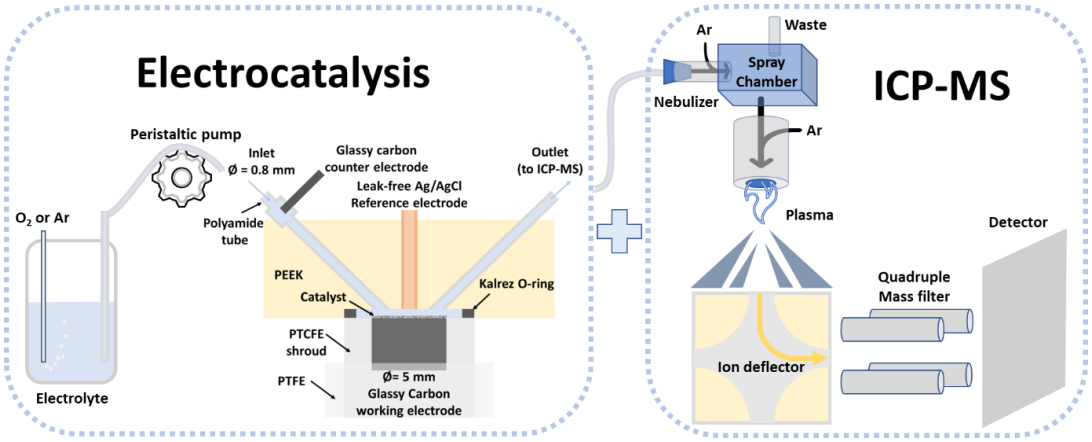


Figure 5.1. Schematic of flow cell setup with RDE disk electrode tip, Ag/AgCl reference electrode and glassy carbon counter electrode coupled to online ICP-MS.

Ar or O_2 was continuously passed through the feed electrolyte (0.1 M $HClO_4$ or 0.05 M H_2SO) for a minimum of 20 mins before initiating measurements. The potential was stabilized at 0.9 V_{RHE} for 200 seconds before and after each measurement to ensure a consistent background for the ICP-MS measurement. The Ohmic drop (*R*) in the cell was determined initially through electrochemical impedance measurements at open circuit potential (OCP), obtained from the intercept of the real impedance axis. R was observed to vary between 5 and 25 Ω, and if it exceeded 25 Ω, the cell was reinstalled after checking for any bubbles or leaks.

The experimental procedure began with 50 CV scans under Ar-saturation, ranging from 0.925 to 0.2 V_{RHE} at 50 mV s^{-1}, followed by 6 CVs under Ar-saturation within the same potential range at 10 mV s^{-1}. An additional 6 CVs were performed under O_2-saturation, following the same potential range and scan rate. Subsequently, either an AST under O_2-saturation was conducted for 1 hour, involving potential holds at 0.9 and 0.6 V_{RHE} for 3 s intervals, or chronoamperometry (CA) was performed at 0.2 or 0.6 V_{RHE} for 1 h under O_2-saturation. In instances where Ar AST was conducted, O_2-saturated measurements were omitted beforehand to prevent any residual O_2 from impacting the results. Finally, 6 CVs were recorded under O_2-saturation, covering the range from 0.925 to 0.2 V_{RHE} at 10 mV s^{-1}. At the conclusion of each measurement, a synchronization step from 0.9 to 0.2 to 0.9 V_{RHE} was implemented to align the ICP-MS and electrochemical data. An overview of the protocol is provided in **Figure 5.2**.

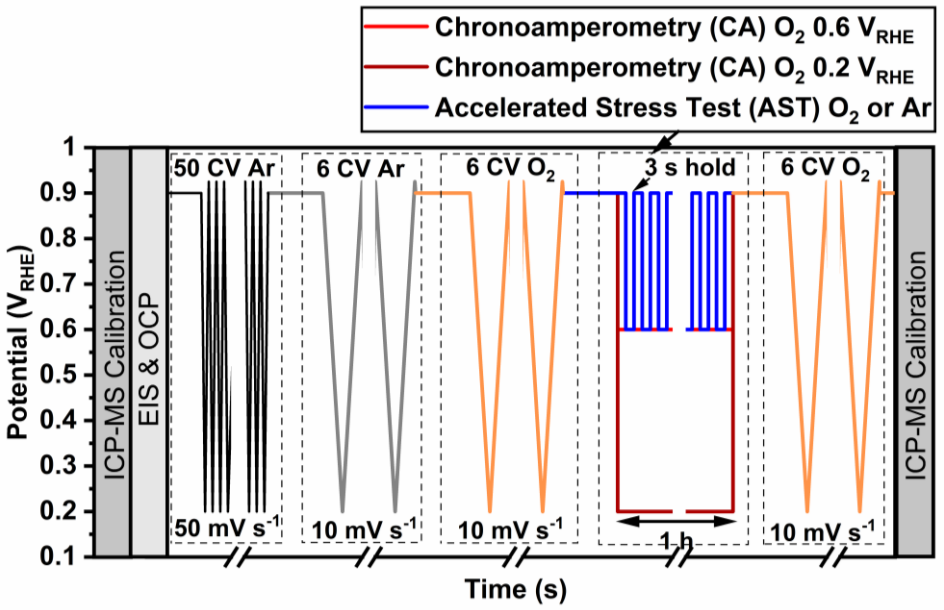


Figure 5.2. Protocol followed during flow cell ICP-MS electrochemical testing.

5.2.4 80°C RDE Accelerated Stress Test

The RDE measurements were performed in a three-electrode setup using an AUTOLAB PGSTAT302N in an electrolyte of 0.1 M $HClO_4$, which was saturated with either Ar (99.999%, Messer) or O_2 (99.999%, Messer). A custom-designed sealed RDE cell was utilized to prevent the evaporation of electrolyte, as previously documented. This cell design is known for its ability to retain the electrolyte within the system. The 80°C accelerated stress test (AST) was conducted without rotation due to limitations associated with the specialized high-temperature cell structure. The AST procedure included 3-second intervals at 0.9 and 0.6 V_{RHE} under both Ar and O_2-saturated conditions in 0.1 M $HClO_4$, maintained at 80°C (Suprapur, Carl Roth). Initial O_2 reduction performance (1,600 rpm, 10 mV s^{-1}) and Ar cyclic voltammetry (CV) (50 mV s^{-1}) were recorded, as well as subsequent measurements after 1,000 and 8,000 cycles. An 85% iR correction was implemented during the O_2 reduction measurement. The capacitance correction for O_2 reduction was carried out by subtracting the current under equivalent measurement conditions, under Ar saturation. Postmortem ICP-MS was conducted after 8,000 AST cycles at 80°C, involving the withdrawal of 10 mL of electrolyte from the cell immediately and after a 2 h hold at open circuit potential.

5.2.5 GDE

5.2.5.1 Electrode Manufacture

The gas diffusion electrodes (GDEs) were created by applying an Fe-N-C ink onto a gas diffusion layer (GDL) that included a microporous layer (Freudenberg, H23C8, 218±5 µm) using a doctor-blade coating method. During the doctor-blade coating, the temperature of the plate of the automated film applicator (Zehntner, ZAA 2300) was maintained at room temperature (25°C). The ink consisted of 12 wt.% solids in isopropanol (Supelco, EMSURE, ACS ISO), with the solid fraction comprising 41.3 wt. % of TAP 900@Fe material and 58.7 wt. % of Nafion (Fuel Cell Store, D2021). To ensure the effective utilization of the catalyst layer due to the high mesopore volume of TAP 900@Fe, a relatively high ionomer to FeNC weight ratio of 1.42:1 was employed. The ink was stirred for 30 minutes and sonicated for 1 hour (100 W VWR Ultrasonic Cleaner USC 500 THD) at a temperature below 30°C, followed by continuous stirring until deposition. After the ink was applied onto the GDL, the samples were dried at 60°C for 1 hour under atmospheric pressure and an additional hour under reduced pressure. The catalyst layer loading was determined to be 0.9±0.1 mg_{FeNC} cm^{-2} by weighing the GDE before and after the Fe-N-C coating. The catalyst layer thickness was measured to be 58±4 µm using a micrometer (Helios Preisser, 0912501).

5.2.5.2 Online GDE ICP-MS

The online Fe dissolution was measured using the previously reported GDE-ICP-MS setup, as illustrated in **Figure 5.3**. Before conducting electrochemical tests, the GDEs underwent a one-hour immersion in ultrapure water. The electrolyte, reference electrode, and counter electrodes used were 0.1 M $HClO_4$ (Suprapur, Sigma Aldrich), Ag/AgCl (Metrohm), and Ti/Ir mixed oxide grid (METAKEM), respectively. The Ag/AgCl electrode was calibrated daily at the specific temperature of interest ($E_{Ag/AgCl}$ = 0.316 ± 0.011 V_{RHE} at 20°C and $E_{Ag/AgCl}$ = 0.297 ± 0.013 V_{RHE} at 75°C). During O_2 measurements in the GDE, a 100% post iR correction was applied, while for Ar measurements, 50% was applied in-situ and 50% was applied post the Ar experiment.

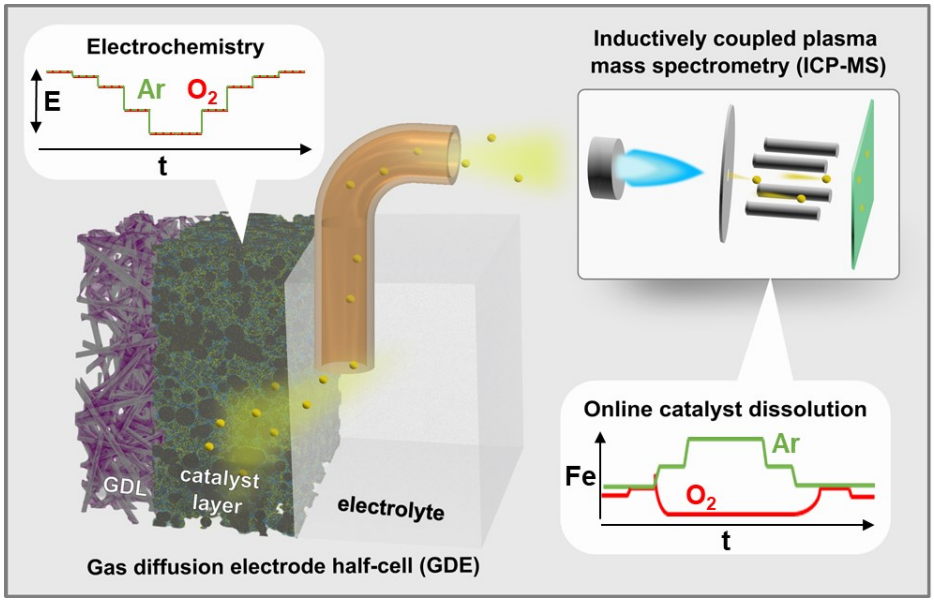


Figure 5.3. Schematic representing GDE coupled to ICP-MS. Adapted from ref. [12]

Depending on the gas atmosphere under examination, two distinct electrochemical techniques were utilized. Potentiostatic methods were employed in an Ar atmosphere, while galvanostatic techniques were applied in an O2 atmosphere. This decision was made because unpredictable uncompensated resistance was observed at varying current densities in the O2 atmosphere during potentiostatic holds, and the iR-compensated potential would not be directly comparable under the two different gas conditions.

To simulate the recently standardized PEMFC AST conditions under an O2 environment in the GDE, the current was held for 3-second intervals, repeated 200 times, at -0.05 and -50 mA cm^{-2}, corresponding to approximately 0.85 and 0.6 $V_{RHE,\ iR\text{-}free}$, respectively. In the case of an Ar atmosphere, the potential was held for 3-second intervals, 200 times, between 0.9 and 0.6 $V_{RHE,\ iR\text{-}free}$. Prior to and following the AST, 240 s of potentiostatic and galvanostatic holds were implemented between (-1 and -100 mA cm^{-2}) and (0.85 and 0.50 $V_{RHE,\ iR\text{-}free}$), respectively, as depicted in **Figure 5.4**.

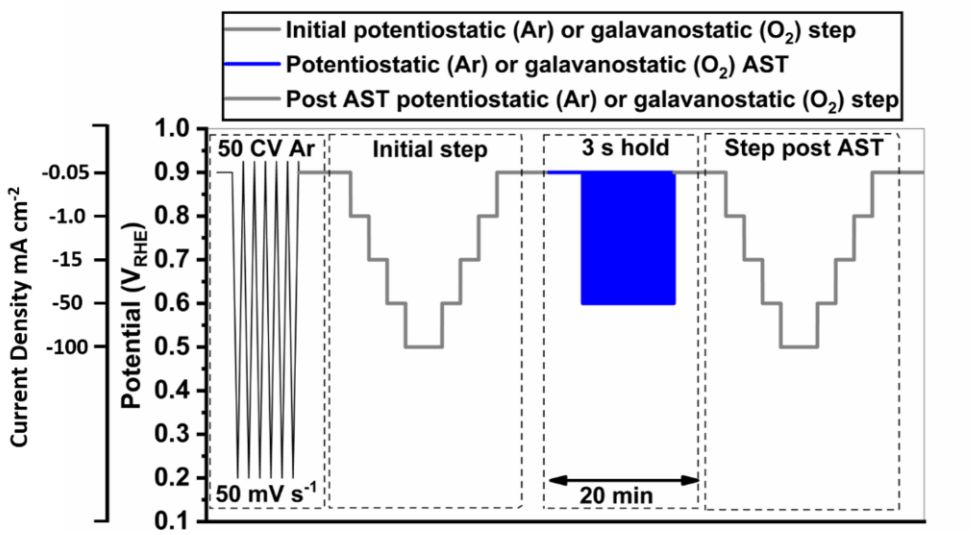


Figure 5.4. Protocol followed during GDE-ICP-MS testing.

An ICP-MS from Perkin Elmer (NexION 350 model) was utilized in dynamic reaction cell mode with methane (99.9995%, Air Liquide) to limit the potential impact of polyatomic interference between ^{56}Fe and $^{40}Ar^{16}O^{+}$. To account for any instrument drift during measurements, 2.5 ppb of Ge in 1 wt.% nitric acid HNO_3 was employed as an internal standard. For calibration purposes, four-point calibration curves were generated using a blank and three standard solutions of Fe, with concentrations of 0, 1, 5, and 25 ppb prepared daily.

To facilitate continuous extraction of the electrolyte to the ICP-MS, a flow rate of 0.203-0.226 mL min^{-1} was maintained via a capillary. The collection efficiency (CE) was determined using **Equation 5.1**:

$$CE = \frac{m_{Fe,ICP-MS}}{m_{Fe,bulk,end} - m_{Fe,bulk,start} + m_{Fe,ICP-MS}} \qquad \textbf{Equation 5.1}$$

Where $m_{Fe,ICP-MS}$ is the total Fe amount collected in the ICP-MS, $m_{Fe,bulk,start}$ and $m_{Fe,bulk,end}$ are the quantity of Fe in the bulk electrolyte before and after the analysis, respectively. The CE values obtained are presented in **Table 5.1**.

Before each measurement, 50 cycles at 50 mV s^{-1} in an Ar atmosphere were conducted between 0.20 and 0.925 V_{RHE}, as illustrated in **Figure 5.4**. The calculated Fe dissolution (based on catalyst loadings, flow rate, and collection efficiencies, as outlined in Table S1) was smoothed by employing adjacent averaging over 30 neighbouring data points.

The rate of Fe dissolution is given by **Equation 5.2**:[45]

$$\frac{dFe}{dt} = \frac{[Fe] \times Q}{m_{FeNC} \times A \times CE} \qquad \textbf{Equation 5.2}$$

Where dFe/dt is the rate of Fe dissolution normalised to catalyst loading ($ng_{Fe}\ s^{-1}\ g_{FeNC}^{-1}$), *[Fe]* is the concentration of Fe ($ng_{Fe}\ L^{-1}$), *Q* is flowrate ($L\ s^{-1}$), m_{FeNC} is catalyst loading of Fe-N-C on RDE or GDE ($g_{FeNC}\ cm^{-2}$), and *A* is the area of the RDE tip (0.19635 cm^2) or GDE electrode (2.01 cm^2). *CE* is the collection efficiency. *CE* is assumed 100% in flow cell ICP-MS and is calculated in GDE ICP-MS (see **Table 5.1** for values).

Table 5.1. Loading, flow rate and collection efficiency for GDE ICP-MS experiments.

Conditions	Loading ($mg_{FeNC}\ cm^{-2}$)	Flow rate ($mL\ min^{-1}$)	Collection efficiency (%)
Ar 20 °C	0.93	0.207	26.5
	0.93	0.207	35.5
O_2 20 °C	0.87	0.214	23.5
	1.03	0.203	28.7
O_2 75 °C	0.71	0.214	32.8
	0.82	0.226	29.4

5.2.6 Kinetic Modelling Simulations

5.2.7 Characterisation

5.2.7.1 HAADF-STEM and EDX

HAADF-STEM was performed with a Talos F200i (ThermoFisher Scientific) operated at an acceleration voltage of 200 kV, a beam current of ca 40 pA, and a convergence angle of 10.5 mrad. EDX employed a Dual Bruker XFlash 6T-100 EDS detector.

5.2.7.2 XANES

Fe Kβ high energy-resolution fluorescence-detected-XANES experiments were conducted at beamline ID26, European Synchrotron Radiation Facility (ESRF). The storage ring operated in 7/8 multibunch mode with an electron current of 200 mA. The pristine catalyst powder and thin films of catalytic suspensions were analyzed, utilizing three undulators (u35) to produce incoming photons. A pair of cryogenically cooled Si(111) crystals then monochromatized the radiation. To calibrate the incident beam energy, a reference metallic iron foil set the first inflection point of the Fe K edge at 7112 eV. In the experimental setup, Germanium (Ge) crystal analyzers (Ge(620) for Kβ and Ge(440) for Kα) in Rowland geometry were employed. Si avalanche photodiode (APD) with 200 µm thickness and 10 x 10 mm2 active area was used

as a detector. The dead time correction was performed using a nonparalyzable model with τ = 3.83 · 10-8. Kβ XANES spectra were collected in a continuous scan mode by varying the incident energy from 7090 to 7200 over Fe K edge with an energy step 0.1 eV and duration 50 seconds. The stability of the catalyst under the beam was controlled via short XANES spectra of 5 seconds collected at the same spot during at least 10 minutes.

The TAP 900@Fe powder was blended with BN3 (Aldrich®) at a mass ratio of 1:3 and subsequently compressed into pellets using a 1-ton force. This identical procedure was applied to both FeO (Aldrich®) and Fe_2O_3 (Aldrich®). These pellets, along with GDE and glassy carbon rods carrying fresh ink or post-mortem catalyst samples were positioned in a sample holder. XANES spectra were normalized by the incoming flux recorded by detecting the scattering from a Kapton foil with a photo diode and then were normalized in area using the full measured energy range. All the data treatment was performed in python-based scripts. The data were collected in the presence of air at room temperature.

5.3 Results

5.3.1 Comparing TAP 900@Fe and TAP 900@^{57}Fe RDE O_2 Reduction Activity

Considering O_2 reduction, reduced activity has previously been reported for ^{57}Fe enriched Fe-N-C samples compared to Fe-N-C prepared in the same manner but with natural abundance Fe precursor.[46] The RDE O_2 reduction activity for TAP 900@^{57}Fe and TAP 900@Fe can be found in **Figure B1a-b**. The kinetic region and mass activity at 0.8 $V_{RHE,\ iR\text{-}free}$ in O_2-saturated RDE is lower in TAP 900@^{57}Fe compared to previously reported TAP 900@Fe, with 3.77±0.54 and 5.01±0.79 A g_{FeNC}^{-1}, respectively (**Figure B1a**). The lower activity with ^{57}Fe enrichment follows the previous report.[46]

5.3.2 Online Flow Cell ICP-MS

Moving to *operando* flow cell ICP-MS measurements in 0.1 M $HClO_4$, TAP 900@^{57}Fe was used to avoid polyatomic interference from ArO^+ and maximize spectrometric signal. The setup and experimental protocol are depicted in **Figure 5.1** and **Figure 5.2**, respectively. First, ICP-MS calibration, electrochemical impedance spectroscopy and open circuit potential (OCP) were conducted to ensure correct installation and operation. Next, 50 fast (50 mV s^{-1}) cyclic voltammograms (CV) between 0.925-0.200 V_{RHE} were measured in Ar-saturated electrolyte to allow the catalyst to reach a stable electrochemical and dissolution measurement (**Figure 5.5a** a, 0.2 mg_{FeNC} cm^{-2}). Mg was also monitored during the initial 50 cycles due to its use as a template during synthesis, with 0.06 wt.% detected from *ex situ* ICP-MS (**Figure A11**). Mg dissolution did not vary with potential (**Figure 5.5a**) and so is not considered further. Meanwhile, the rate of Fe dissolution followed an exponential decay. It is also worth noting that there is a constant 130 ng_{Fe} g_{FeNC}^{-1} s^{-1} ^{57}Fe concentration observed when held at 0.9 V_{RHE} (**Figure 5.5a-c**), which was also the OCP of the catalyst.

Considering the effect of increased Fe-N-C loading, the amount of ^{57}Fe dissolution follows a linear trend over the initial 50 CVs (**Figure B2a**). The percentage of total ^{57}Fe detected increases from 7.5±2.9% to 15.2±3.3% as catalyst loading increases from 0.05 to 0.40 $mg_{Fe\text{-}N\text{-}C}$ cm^{-2}, with 11.3±5.6% at 0.20 $mg_{Fe\text{-}N\text{-}C}$ cm^{-2} (**Figure B2b**). This finding appears counterintuitive as one would expect either an equivalent percentage of Fe detected relative to the loading, or even a reduced percentage of detected Fe due to blocking of active sites with increasing thickness of the catalyst layer.

After the initial 50 CVs at 50 mV s^{-1}, six CVs were conducted at 10 mV s^{-1} under Ar and then O_2-saturation. With increasing TAP 900@^{57}Fe loading under O_2-saturation, the limiting current density (below 0.65 V_{RHE}) only incrementally increases. This slight increase can be explained by the increasing thickness of the catalyst layer with loading, which penetrates deeper into the flowing O_2-saturated electrolyte. Meanwhile, between 0.65-0.80 V_{RHE} there is an increasing O_2 reduction peak in the cathodic direction (**Figure B3a**). This is caused by a build-up of O_2 concentration locally in the catalyst layer while scanning the potential region of 0.80-0.925 V_{RHE}, where very little ORR is observed. Under Ar-saturated conditions the current density increases proportional to the catalyst loading, although an increasing O_2 reduction peak on the cathodic scan is noted (**Figure B3b**). This is thought to occur due to air ingress at the junction of the Kalrez O-ring and cell (or cavitation from the peristaltic pump), which leads to trace amounts of O_2 entering the flow cell system during most Ar-saturated measurements. Still, the amount of O_2 appears negligible. Normalizing the ^{57}Fe detected to charge passed and catalyst loading shows the amount of ^{57}Fe detected is constant under O_2 but increases with reduced catalyst loading under Ar (**Figure B3c-d**). Meanwhile, the amount of ^{57}Fe detected is equivalent under either gas saturation, with 1.3-2.0% of total ^{57}Fe detected, and linear dependence with Fe-N-C loading (**Figure B3e-f**). Focusing on the dissolution at 0.2 mg_{FeNC} cm^{-2}, similar profiles are observed under Ar and O_2-saturation (**Figure 5.5b**). To better distinguish the Fe dissolution features, slow CVs (1 mV s^{-1}) were conducted under O_2-saturation (**Figure 5.5c**). The slow scans show two onsets of ^{57}Fe dissolution above background levels on the cathodic scan at *ca.* 0.72 and 0.33 V_{RHE} (**Figure 5.5c**).

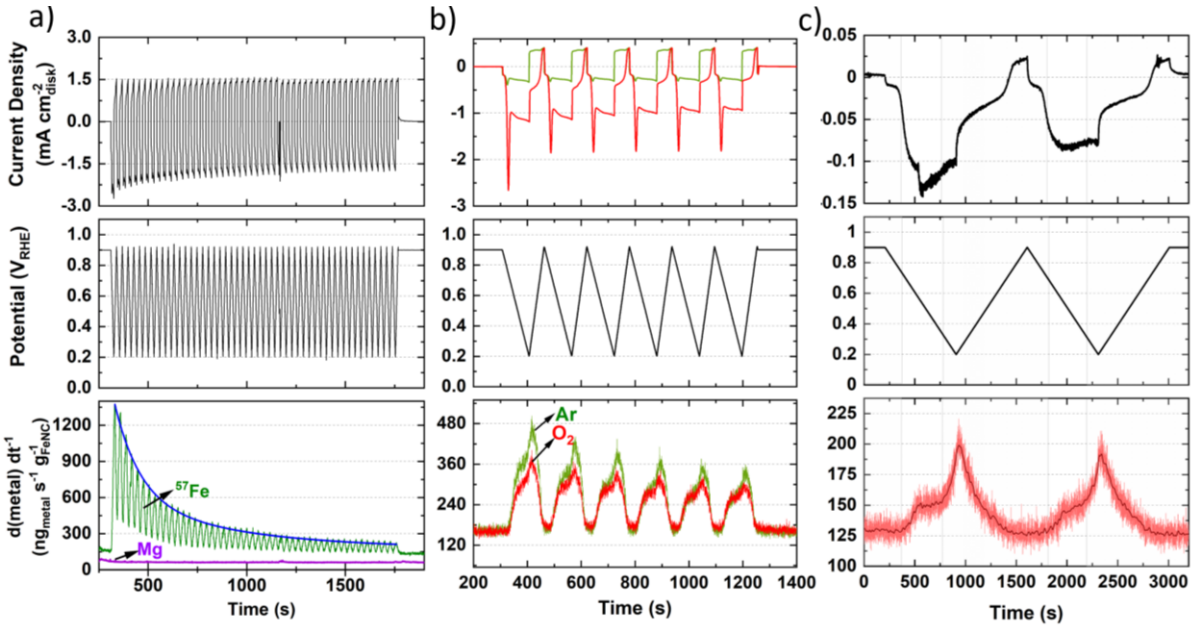


Figure 5.5. Online flow cell ICP-MS metal dissolution during a.) Initial 50 CVs at 50 mV s^{-1} under Ar-saturated 0.1 M $HClO_4$ with 0.2 mg_{FeNC} cm^{-2}. Blue line represents fitted exponential decay. b.) Six CV at 10 mV s^{-1} under Ar- (green) and O_2 (red)-saturated conditions. c.) Two slow CV scans at 1 mV s^{-1} under O_2-saturated 0.1 M $HClO_4$ with 0.2 mg_{FeNC} cm^{-2}. Dark red line represents fast Fourier transform smoothed data.

To evaluate differences in Fe detection and profiles over a longer period, 1 h AST or chronoamperometry (CA) were recorded in 0.1 M $HClO_4$ (**Figure 5.6a-b**) or 0.05 M H_2SO_4 (**Figure 5.6c**). Greater ^{57}Fe loading-normalized concentration is observed over the course of the AST under O_2 than Ar. ^{57}Fe concentration follows a slow decline under O_2 and rapid plateau above baseline under Ar (**Figure 5.6a**). 2.7±0.1% of total ^{57}Fe is detected during O_2 AST (**Figure 5.6d**), with a charge normalized Fe dissolution of 503±3 ng_{Fe} mg_{FeNC}^{-1} C^{-1} (**Figure 5.6e**). Meanwhile, half ^{57}Fe concentration is observed under Ar AST (**Figure 5.6d**, **Figure B4**); however, normalizing to the total charge passed shows approximately double, with 1022 ng_{Fe} mg_{FeNC}^{-1} C^{-1} (**Figure 5.6e**). *Pre-* and *post-mortem* bright-field TEM of these samples shows no formation of detectable nanoparticles under Ar or O_2 (**Figure B5**), indicating all Fe demetallation leads to dissolution at 25 °C, in agreement with former findings of Kumar et al.[15]

CA under O_2 at 0.2 V_{RHE} shows a large initial ^{57}Fe dissolution, which then decays over time, while CA at 0.6 V_{RHE} shows a small spike and lower overall dissolution (**Figure 5.6b**). After 30 mins, the current density and Fe dissolution are equivalent at 0.2 and 0.6 V_{RHE} CA. CA at 0.2 V_{RHE} ends with 4.6±0.4% of total ^{57}Fe and 686±166 ng_{Fe} mg_{FeNC}^{-1} C^{-1}. This is approximately

double the values at 0.6 V_{RHE}, with 2.2±0.1% ^{57}Fe and 358±61 ng_{Fe} mg_{FeNC}^{-1} C^{-1} (**Figure 5.6e**). This correlates with the observations from **Figure 5.5c**, where greatest Fe dissolution occurs around 0.20 V_{RHE}.

At the same pH in 0.05 M H_2SO_4 instead of 0.1 M $HClO_4$, O_2 AST shows a similar dissolution profile, with lower Fe detection but higher O_2 current densities (**Figure 5.6c**). This current is unexpected as O_2 solubility is higher in $HClO_4$ than H_2SO_4. Meanwhile the total ^{57}Fe loss is 2.3±0.1% in 0.05 M H_4SO_4 and slightly higher in 0.1 M $HClO_4$ with 2.7±0.1% (**Figure 5.6**Figure *5.6***d**). However, the charge normalized Fe dissolution is less than half in 0.05 M H_2SO_4, at 231±63 ng_{Fe} mg_{FeNC}^{-1} C^{-1} (**Figure 5.6**e).

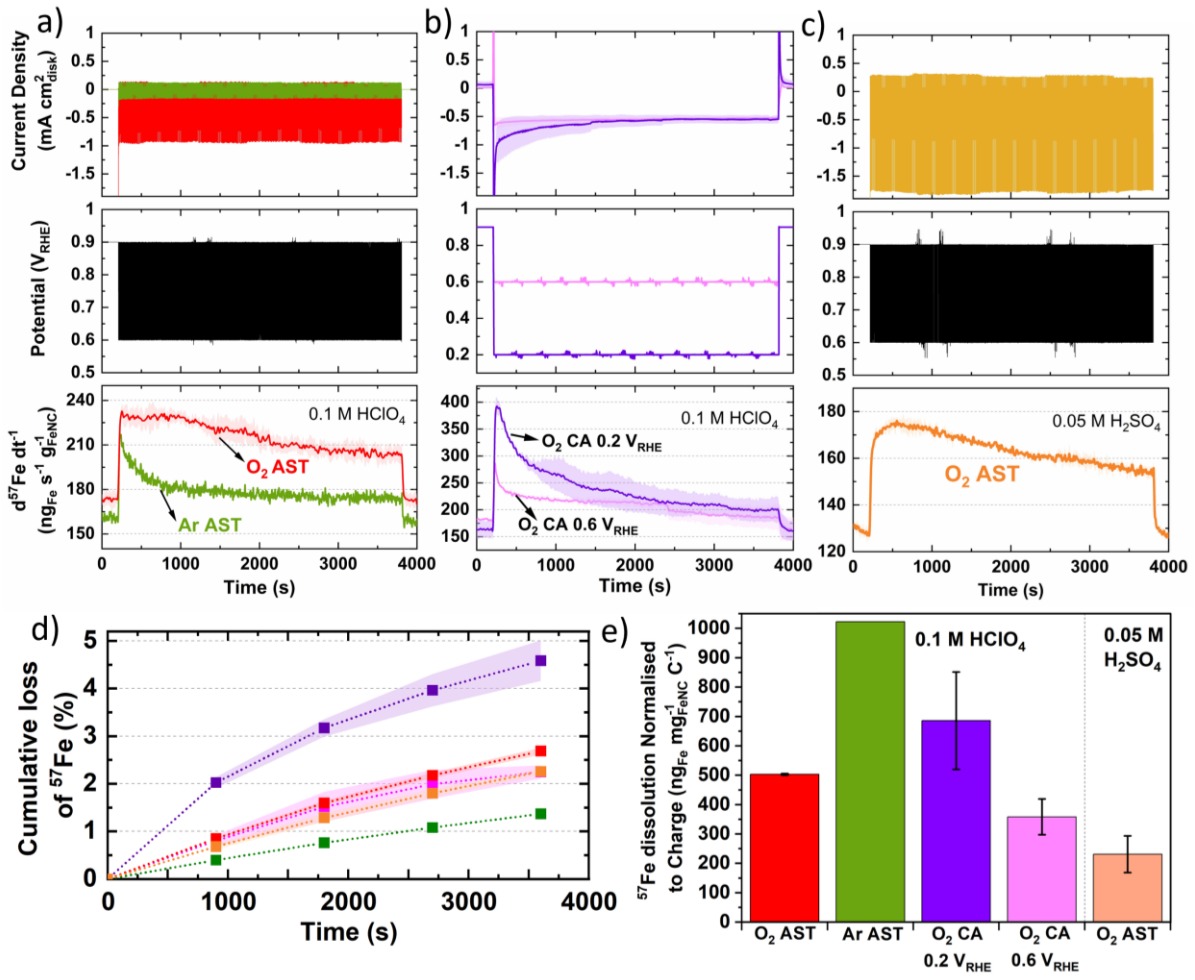


Figure 5.6. Online flow cell ICP-MS of TAP 900@^{57}Fe a.) AST under Ar and O_2-saturated 0.1 M $HClO_4$. b.) 0.2 and 0.6 V_{RHE} CA in O_2-saturated 0.1 M $HClO_4$ c.) AST under O_2-saturated 0.05 M H_2SO_4. Lighter and darker orange represent current density from two measurements. d.) Cumulative Fe loss. e.) Fe dissolution over varying stability test conditions. All tests over 1 h with 0.2 mg_{FeNC} cm^{-2}. Error in figures represent two repeat measurements.

5.3.3 80°C RDE AST

To mimic operational temperatures in a PEMFC, AST cycling (square potential steps between 0.9-0.6 $V_{RHE,\ iR\text{-}free}$ with 3 s holds) were conducted at 80 °C in an RDE cell (without rotation) in 0.1 M $HClO_4$. **Figure 5.7a** shows the initial O_2 reduction RDE performance and after 80 °C AST in O_2 and Ar-saturated conditions for TAP 900^{57}Fe. After 1,000 AST cycles the normalized kinetic activity at 0.75 $V_{RHE,\ iR\text{-}free}$ is comparable at 0.50±0.04 and 0.53±0.05 in Ar and O_2 conditions, respectively (**Figure 5.7b**). The similar degradation in activity can be explained by the limited charge passed over this time and improved hydrophobicity of the catalyst layer initially. After 8,000 cycles in 80 °C Ar-saturated electrolyte, the normalized kinetic current density falls to 0.26±0.06.

Ar-saturated CV following 80 °C Ar-saturated 8,000 AST cycles remains unchanged compared to fresh TAP 900@^{57}Fe (**Figure 5.7c**) and no large Fe particles are observed from post-mortem TEM (**Figure B6a-b**). Following 80 °C O_2-saturated 8,000 AST cycles, there is only 0.04±0.02 normalized activity remaining at 0.75 $V_{RHE,\ iR\text{-}free}$ (**Figure 5.7b**), while the limiting current density value appears only slightly impacted (**Figure 5.7a**). After 1000 O_2 AST cycles at 80 °C an increase in capacitive current is observed, which increases further after 8,000 cycles.

Figure 5.7c also shows the formation of two new reversible redox peaks after 8,000 O_2 AST cycles, suggesting a modified degradation process and a change in Fe speciation. One redox is centered at ca. 0.55 V_{RHE} and the second reversible and well-defined symmetric redox is centered at *ca.* 0.29 V_{RHE} (**Figure 5.7c**). See the Discussion section for further dialogue.

Post-mortem TEM after 80°C O_2 AST shows Fe nanoparticles (**Figure 5.7d**, **Figure B6c**) with shells or trails, remarkably similar to structures of Fe-catalyzed graphitization of carbon.[47] Encased Fe oxides particles were observed by Bae *et al*. following O_2 reduction at 80°C GDE with 2 h hold at 0.6 V_{RHE}.[14] Comparing normalized Fe Kβ XANES spectra (**Figure 5.7**e and **Figure S11**b), post-mortem 80°C O_2 AST TAP 900@Fe spectra confirms the presence of Fe_2O_3 particles, demonstrating the fate of remaining Fe in TAP 900@Fe after 80°C O_2 AST in RDE. Meanwhile, Fe Kβ XANES of TAP 900@Fe RDE ink shows a positive shift of the main edge, compared to TAP 900@Fe powder, which indicates an increase in the Fe oxidation state and/or coordination change. This signifies the inherent difference between the electrocatalyst and its electrode, as recently highlighted.[22]

Following 8,000 AST cycles at 80°C in Ar- and O_2-saturated conditions, electrolyte samples were withdrawn immediately and after 2 h holds under the gas saturated conditions for *ex situ* ICP-MS analysis. Following Ar and O_2-saturated cycling, 18% and 46% of total ^{57}Fe was detected in the liquid electrolyte, respectively (**Table B1, Supporting Note B1, Figure B8**). This corroborates with the online flow cell ICP-MS AST results (**Figure B4**), where greater Fe dissolution under O_2-saturated conditions is observed. Furthermore, online flow cell ICP-MS on TAP 900@^{57}Fe after 8,000 AST cycles in 80°C O_2-saturated electrolyte shows negligible ^{57}Fe dissolution (**Figure B9**). Fe dissolution was also not observed after 5,000 AST cycles (100 mV s^{-1}, 0.6-1.0 V_{RHE}, N_2-saturation) by Santori *et al.* for their NH_3 pyrolysed Fe-N-C.

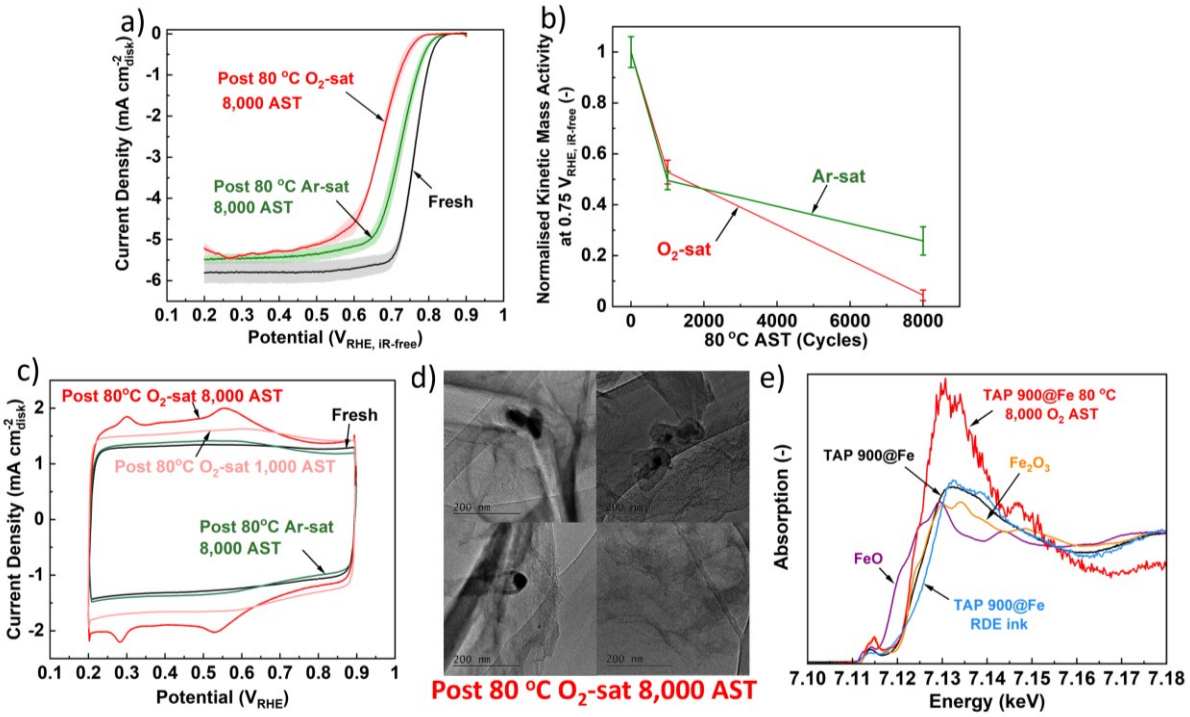


Figure 5.7. a.) Fresh and post AST TAP 900@^{57}Fe O_2 reduction with rotating disc electrode at 1600 rpm and 10 mV s^{-1} in 0.1 M $HClO_4$ thermostated at 25°C. O_2-Ar applied along with iR correction. 3rd cathodic scan shown. b.) Kinetic mass activity for the ORR measured at 25°C and normalised to initial value over varying 80°C AST cycles (3 s holds at 0.9 and 0.6 V_{RHE}). Error bars represent two repeat measurements. c.) 20th CV under Ar-saturated conditions (50 mV s^{-1}). All measurements in 0.1 M $HClO_4$ with 0.2 mg_{FeNC} cm^{-2}. d.) TEM of TAP900@^{57}Fe post 80°C O_2-saturated 8,000 cycle AST. e.) XANES of TAP 900@Fe and its ink, and post 8,000 AST cycles at 80°C in O_2, plus reference spectra of FeO and Fe_2O_3.

5.3.4 GDE O_2 Reduction and Degradation

While flow cell and high temperature RDE measurements proved insightful, the degradation rate in real PEMFCs may be different due to higher ORR rates and therefore ORR charge passed. To reach higher current densities and conditions comparable to PEMFCs, TAP 900@Fe

was tested in a GDE coupled to online ICP-MS in 0.1 M $HClO_4$ at 21±1 °C (referred to as 20 °C) and 74±1 °C (referred to as 75 °C).

Based on flow cell results, 50 CVs under Ar-saturation (50 mV s^{-1}, 0.9-0.2 V_{RHE}) were initially carried out to remove loosely bound Fe (**Figure B10a**). Interestingly, the CVs in GDE clearly show redox peaks centered at ca. 0.76 V_{RHE} which decrease with cycling. These peaks correspond to previously identified Fe^{III}/Fe^{II} redox from certain FeN_x sites.[17,48] These redox peaks were not visible under RDE (**Figure B10b**) and are further discussed in **Supplementary Note 3**.

O_2 reduction was measured in GDE before and after AST tests (**Figure 5.8**a-b,). Catalyst loadings varied between 0.7 to 1.0 mg_{FeNC} cm^{-2}, consequently corresponding mass activity plots are shown in **Figure B11a-b**. Compared to initial 20 °C O_2 reduction, after 20 °C Ar AST there is an apparent improvement in O_2 reduction performance at current densities up to 50 mA cm^{-2} (**Figure 5.8a**). This is assigned to improved wetting of TAP 900@Fe during the 20 °C Ar AST. Meanwhile, 20 °C O_2 AST shows noticeable performance degradation after only 200 cycles, with potential shift at 50 mA cm^{-2} of -50±30 mV (from 0.61±0.03 to 0.56±0.00 $V_{RHE, iR\text{-}free}$) compared to pristine 20 °C TAP 900@Fe (**Figure 5.8a**). At 50 mA cm^{-2}, 75 °C GDE pristine TAP 900@Fe shows an improved O_2 reduction potential of 0.68±0.01 $V_{RHE, iR\text{-}free}$. Although, after 75 °C O_2 200 AST cycles results in severe degradation to 0.58±0.03 $V_{RHE, iR\text{-}free}$ (**Figure 5.8b**).

5.3.5 Pre- and Post- GDE Protocol Characterisation

XPS peak fitting of fresh GDE C1s and O1s spectra is provided in **Figure B12a-b** with comparison of O1s between pre and post GDE protocol in **Figure 5.8**Figure *5.8***c**. Comparison of O1s XPS spectra for fresh GDE and after 20 °C Ar and O_2 protocols show comparable total O1s of 8.9-8.1 at.% (**Figure B12c**, **Table B3**), with slight reductions in C=O and C-O peaks for AST samples (**Figure 5.8c**). Meanwhile O1s after 75 °C O_2 protocol show a clear overall O1s increase, which results in 12.2 at.% O1s (**Figure B12c**). There is less discernible change in the C1s spectra, aside from reduction in C-N and C-C and increase in CF2 in all AST samples compared to the pristine TAP 900@Fe GDE (**Figure B13**). Raman spectra (**Figure B14**) for pristine and post Ar and O_2 20 °C GDE protocols show no discernable difference (I_d/I_g = 1.02-1.03), while there is a slight increase after 75 °C O_2 protocol (I_d/I_g = 1.05), indicating a minor increase in defects in the carbon structure.

Within the prepared TAP 900@Fe GDE no visible nanoparticles are detected using HAADF-STEM and STEM-EDX spectrum imaging (**Figure 5.8d**, **Figure B15a**). After 20 ^{o}C Ar protocol, one large Fe_xO_y nanoparticle is detected in the spectrum image, while at higher resolution HAADF-STEM small clusters are observed (**Figure 5.8e**, **Figure B15b**). Numerous Fe nanoparticles are observed following 20 ^{o}C O_2 protocol in GDE, which are assigned to Fe_xO_y based on overlaying the Fe and O EDX mapping (**Figure 5.8f**, **Figure B15c**).

Post 75 ^{o}C O_2 200 protocol no large Fe_xO_y particles are seen from EDX and limited Fe clusters from HAADF-STEM (**Figure 5.8g**, **Figure B15d**). No significant change from the pristine TAP 900@Fe structure is observed after 20 ^{o}C O_2 and Ar protocols, (**Figure B16a-c**); however, after 75 ^{o}C O_2 protocol a denser particle structure is observed (**Figure B16d**).

XRD on post-mortem GDE AST samples was conducted to try and deduce the type of Fe_xO_y, however either the lack of crystallinity, small particle size and/or low concentration meant no sharp peaks relating to Fe particles could be identified (**Figure B17**). The peak at 18.0^{o} is assigned to polytetrafluoroethylene, which arises from the Nafion backbone. It is worth mentioning that pristine TAP 900@Fe does not show a graphite peak at ~25.6^{o} (002), suggesting its amorphous or graphene-like structure, as confirmed from previous Raman analysis.[49]

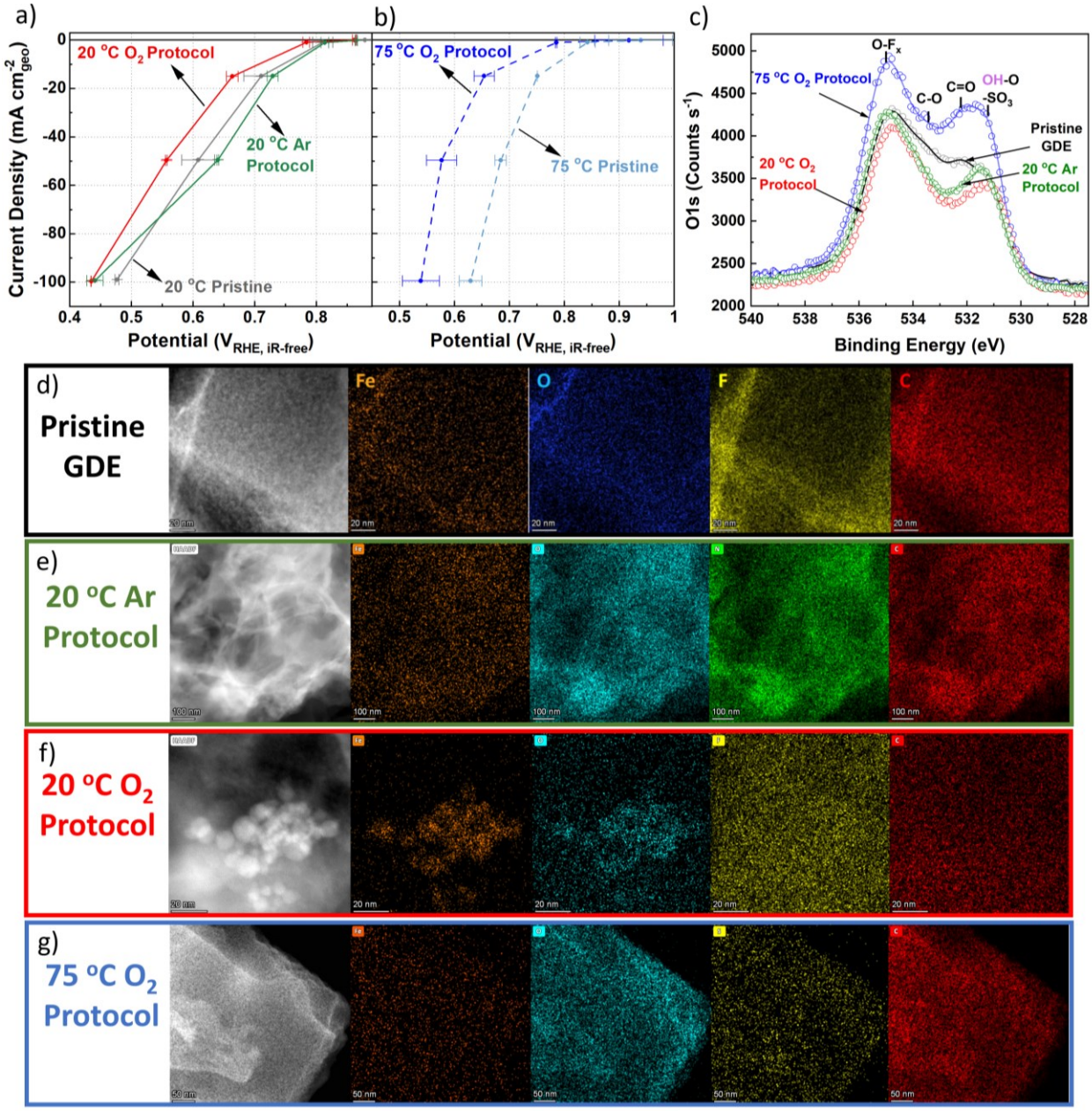


Figure 5.8. GDE current density in 0.1 M $HClO_4$ with 0.7-1.0 mg_{FeNC} cm^{-2} for a.) 25 °C O_2 reduction in GDE for pristine TAP 900@Fe, and after O_2 and Ar AST. b.) 75 °C O_2 reduction in GDE for pristine TAP 900@Fe and after 75 °C O_2 AST. Error represents two repeat measurements. 100% post iR correction was applied for O_2 measurements, while 50% was applied in situ and 50% post Ar measurements. Comparison of pristine and post protocol GDEs c.) O1s XPS d-g.) HAADF-STEM and STEM-EDX.

5.3.6 Online GDE ICP-MS

To elucidate the Fe dissolution mechanisms, online GDE ICP-MS was measured before, during and after the AST (**Figure 5.9**) for each of the conditions. For initial 20°C Ar (**Figure 5.9a**), Fe concentration above baseline occurs at 0.83 $V_{RHE, iR\text{-}free}$ and reaches a maximum concentration between 0.64-0.48 $V_{RHE, iR\text{-}free}$. Returning to 0.83 $V_{RHE, iR\text{-}free}$, Fe concentration returns to baseline levels. Initial 20 °C O_2 current step holds (**Figure 5.9a**) show a lower baseline Fe

concentration than 20°C Ar. A fall in Fe concentration below baseline levels is observed when increasing current density from -0.6 to -15 mA cm^{-2}, corresponding to 0.85±0.02 to 0.80±0.01 $V_{RHE, iR\text{-}free}$, respectively. When returning anodically to hold at -0.6 mA cm^{-2}, Fe concentration increases and only begins falling back to baseline once returning to hold at -0.05 mA cm^{-2}. Initial 75 °C O_2 current hold measurements show a higher baseline Fe concentration, with increased Fe concentration during holds at -0.6 to -15 mA cm^{-2}. Fe concentration then returns to approximate baseline values during holds at -50 and -100 mA cm^{-2}, corresponding to 0.66±0.04 and 0.62±0.04 $V_{RHE, iR\text{-}free}$, respectively. Returning anodically to holds at -15 and -0.6 mA cm^{-2} results in increased Fe concentration.

Moving to online AST monitoring (**Figure 5.9b**), 20 °C Ar shows increased Fe concentration at the beginning of the AST. Fe concentration then gradually decreases over time and falls back to baseline levels after the AST. To note, AST O_2 have the same number of cycles (200) in protocol as Ar (3 s holds at each potential), but O_2 ASTs took a longer duration because of the additional time to switch the applied current ranges between 3 s holds, which is not required in Ar AST protocol. During the AST, 20 °C O_2 shows a similar Fe concentration profile to current hold prior to AST (**Figure 5.9a**), with an initial Fe concentration spike, followed by reduced Fe concentration below baseline levels. Fe concentration then returns to baseline levels post AST, without displaying a dissolution spike. 75 °C O_2 also shows an initial spike in Fe concentration at the beginning of the AST, but then maintains baseline Fe concentration values during and post AST with no discernable change.

Post AST (**Figure 5.9c**), 20 °C Ar show Fe concentration significantly decreases across the whole potential range compared to prior to AST (**Figure 5.9a**). This suggests unstable Fe species have been depleted over the AST. Current step holds after 20 °C O_2 AST show a similar Fe concentration profile to measurements prior to AST, although a higher Fe concentration spike is observed post AST when stepping from -0.6 to -15 mA cm^{-2} (**Figure 5.9c**). Post AST 75 °C O_2 shows a symmetric Fe concentration profile when increasing and decreasing current. 75 °C O_2 GDE ICP-MS results correlate with HAADF-STEM and STEM-EDX observations (**Figure B15d**), where more Fe has dissolved rather than redeposited as particles, as is the case from 20 °C O_2.

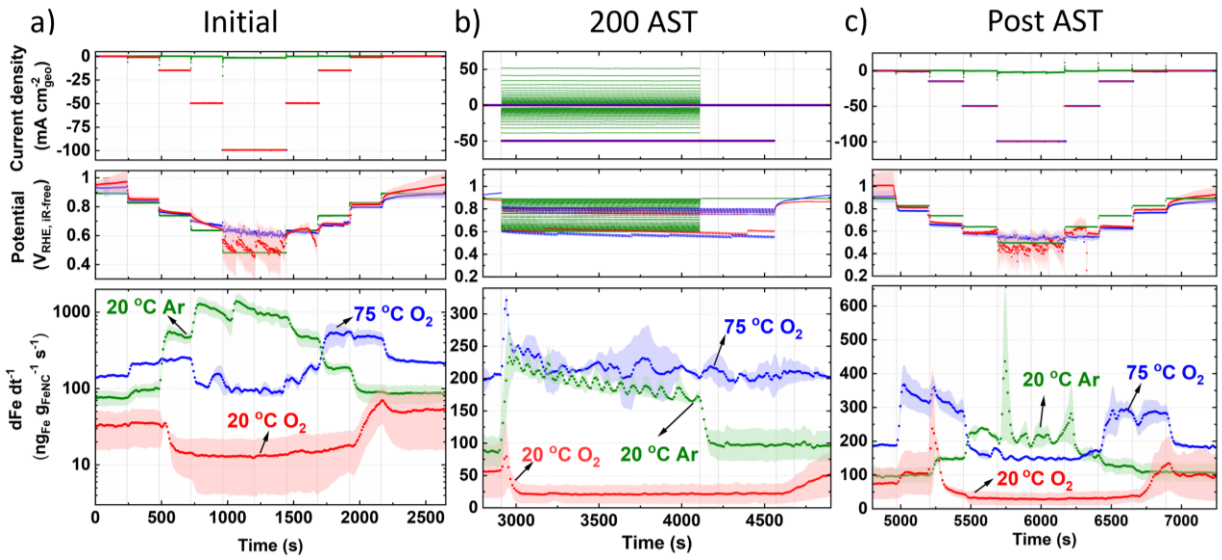


Figure 5.9. Fe dissolution under Ar and O_2 at 20 °C and O_2 at 75 °C in online GDE ICP-MS with 0.1 M $HClO_4$ and 0.7-1.0 mg_{FeNC} cm^{-2} a.) prior to AST (note y-axis is log-scale only in a). b.) 200 AST cycles. Under O_2, the current was held for 3 s intervals 200 times at -0.05 and -50 mA cm^{-2}, corresponding to ca. 0.85 and 0.6 $V_{RHE,\ iR\text{-}free}$, respectively. Under Ar, the potential was held for 3 s intervals 200 times between 0.9 and 0.6 $V_{RHE,\ iR\text{-}free}$. c.) Post AST. Error represents two repeat measurements.

5.4 Discussion

5.4.1 Flow Cell ICP-MS and RDE

Experiments in flow cell ICP-MS and RDE first confirm that the dissolution of Fe atoms is indeed the predominant degradation mechanism in this type of catalyst. In CV, two well-defined Fe dissolution peaks can be observed, with onset of 0.73 and 0.33 V_{RHE} on the cathodic scan (**Figure 5.5**c). The two ^{57}Fe concentration peaks could represent two different Fe species dissolving at different potentials, or different dissolution process with different formal potentials. Only one Fe concentration peak was resolved by Santori *et al*., with an onset of Fe concentration at *ca*. 0.75 V_{RHE} for their Ar-pyrolysed Fe-N-C in O_2-saturated 0.1 M H_2SO_4 at 2 mV s^{-1}.[10] Meanwhile Choi *et al.* observed the onset of increased Fe concentration at 0.77 V_{RHE}, with two distinguishable Fe dissolution peaks,[9] as observed here. The potential at which peak Fe concentration occurs is not discussed as this depends on mass transport, which changes with the electrochemical cell design and operating conditions.

It is noted that the onset of increased ^{57}Fe concentration at *ca.* 0.73 V_{RHE} on the cathodic scan (**Figure 5.5c**) coincides with the onset of the quinone-hydroquinone redox on the cathodic scan post 8,000 O_2 AST at 80°C (Figure *5.7***c**), and the second peak onset of increased ^{57}Fe concentration at 0.33 V_{RHE} on the cathodic scan coincides with the onset of the second reversible redox on the cathodic scan. While some publications have suggested that the dissolution of Fe atoms is caused by a change in their oxidation state, these experimental results would suggest that the stability of the FeN_x moieties is linked to the delocalization of electrons within the N-C matrix. This hypothesis relates to the seminal work of Ramaswamy *et al*., which showed that the electron-donating/attracting properties of the N-C matrix modulate the redox potential and the ORR activity of atomically dispersed Fe sites.[50] Choi *et al*. later demonstrated that hydroxyl and epoxy groups attract electrons from the N-C matrix and also lower the d-orbitals of Fe atoms, both effects contributing to lower the turnover frequency of Fe atoms.[16]

An initial exponential decay in Fe concentration in TAP 900@^{57}Fe was noted (**Figure 5.5a**), which was also observed by Choi *et al.* for their Fe-N-C catalyst.[8,9] In the case of TAP 900@$Fe^{57}Fe$, maximum Fe concentration is observed instantaneously upon potential cycling in Ar, whereas in the report of Choi *et al.* maximum Fe concentration is reached after 2-3 CVs.[8,9] This could be due to the vastly different catalyst structures between highly micro- and

mesoporous TAP 900@^{57}Fe with high active site utilization, and the bulky particle and predominantly microporous ZIF-8 derived Fe-N-C of Choi *et al*.[8,9] Alternatively, it could arise from mass transport effects from slow residence time in their flow cell. The structure of unmodified microporous ZIF-8 derived materials will have impeded mass transport, low active site utilization and therefore delayed detection of Fe dissolution. Differences in experimental setup and residence time calibration in this work and that of Choi *et al.* could also contribute to the observed time difference in Fe concentration detection.

Choi *et al*.[8] detected ~3% of total Fe detected over their initial 20 CVs in Ar-saturation (100 mV s^{-1}, 0.8 $mg_{Fe\text{-}N\text{-}C}$ cm^{-2}) for their purely microporous ZIF-derived Fe-N-C. While after 50 CVs (50 mV s^{-1}, 0.4 $mg_{Fe\text{-}N\text{-}C}$ cm^{-2}), TAP 900@^{57}Fe shows 15.2 ± 3.3% Fe detected. This again points to the different porosity and structure in TAP- and ZIF-derived materials, leading to different accessibility of Fe sites. Although, it should be noted, according to previous *ex situ* TAP900@^{57}Fe Mössbauer assignments (**Figure 4.5d**), *ca*. 11% of the Fe existed as inactive $FeCl_2{\cdot}4H_2O$. This species may represent some or all of the initially dissolved Fe species.

Results from **Figure 5.5b** (and **Figure B3e-f**) suggest that Fe concentration is independent of O_2 reduction under cyclic voltammetry (0.9-0.2 V_{RHE} at 10 mV s^{-1}) in flow cell. This is contrary to what is observed in **Figure 5.6a**, where Fe concentration is greater under O_2 than Ar under AST (step from 0.9 to 0.6 V_{RHE} with 3 s potential holds) flow cell conditions. This may be due to either the different potentials scanned (0.925-0.2 and 0.9-0.6 V_{RHE}), 6 CVs not providing enough cycles to distinguish changes in Fe concentration, or the AST protocol induces a change in Fe dissolution mechanism.

Considering **Figure 5.6e** and **Figure B4**, Zelenay and coworkers also observed from *ex situ* ICP-MS that $HClO_4$ dissolved more Fe from their polyaniline-derived Fe-N-C than H_2SO_4, which they attributed to differences in solubility of Fe perchlorates and sulfates.[6] This observation could also be attributed to the stronger SO_4^{2-} binding on the Fe site,[51] which reduces Fe dissolution. ClO_4^- is has been proposed to mimic non-specifically adsorbing properties of perfluoro sulfonic acid ionomers used in PEMFCs.[52] If true, this would imply AST measurements in H_2SO_4 in RDE and GDE would lead to slower FeNC degradation than in $HClO_4$ (at the same pH), when Fe dissolution is the main degradation mechanism.

The 74% activity loss after 8,000 cycles (0.9-0.6 V_{RHE}, 3 s holds) in Ar RDE at 80 °C for TAP 900@^{57}Fe (**Figure 5.7b**) is markedly greater than the ZIF-8 derived Fe-N-C of Kumar *et al.,* which showed only 25% of initial mass activity lost after 10,000 cycling (0.6-1.0 V_{RHE}) at 80 °C in Ar-saturated 0.1 M H_2SO_4.[53] This difference could be attributed to the difference in carbon structure and accessibility of active sites between the highly micro- and meso-porous TAP 900@Fe and purely microporous ZIF-derived Fe-N-C.

Fe dissolution in Ar-purged acidic electrolyte has previously been assigned to leaching of inactive Fe sites.[8,9] Here, the decrease in O_2 reduction performance following 80 °C Ar AST is attributed to active site dissolution, without redeposition into particles. This is because no particles are observed from TEM in **Figure B5b** and no change in CV in **Figure 5.7c**. The greater loss in activity after 80 °C O_2 AST (**Figure 3b**) is attributed to the combination of increased (>2x) active site demetallation (**Figure B8**) and oxidation of the carbon support (**Figure 5.7c**), which reduces turnover frequency of remaining active sites.[9,54]

Previous *ex-situ* Mössbauer of TAP 900@^{57}Fe found 41% of Fe as high spin $Fe^{III}N_x$ (**Figure 4.5d**), which has been identified as the more active but less durable FeN_x sites.[17] The amount of Fe detected from *ex situ* ICP-MS after 80 °C O_2 8,000 AST (46%) matches the percentage of high spin $Fe^{III}N_x$ sites (41±10%). These results indicate the Fe species contributing to O_2 reduction activity at high potentials (≥0.75 V_{RHE}) represent unstable Fe sites, which dissolved during the AST. Dissolved Fe will then precipitate into Fe_2O_3 under O_2 saturation, with some redeposited into the catalyst layer.

5.4.2 GDE ICP-MS

Under initial Ar in GDE ICP-MS (**Figure 5.9a**), the most significant increase in Fe concentration occurs when the potential drops from 0.83 to 0.74 V_{RHE}. This can be explained by the Fe^{III}/Fe^{II} redox transition at 0.76 V_{RHE} (**Figure B10**). It is worth noting that with a Fe-N-C, Fe atoms possess different formal redox and dissolution potentials depending on their coordinating ligands and extended local environment (number and size of graphene sheets,[55] oxygen functional groups[16,56]). This broad Fe^{III}/Fe^{II} redox range is also initially observed in **Figure B10**. Moreover, after the increases of Fe concentration during cathodic potential shifts, gradual declines in the Fe concentration are frequently observed. This is related to the fact that the location of the Fe within the Fe-N-C structure (outer catalyst layer surface or deeper within)

affects the transfer function and hence residence time. It should also be mentioned that the Fe concentration is remarkably high even after the preliminary 50 CVs in Ar (50 mV s^{-1}).

As mentioned in the RDE discussion section, O-containing groups on the carbon surface reduce the turnover frequency of Fe-N-Cs by modifying electron delocalization and weakening O_2-binding on FeN_x sites.[16] The limited change in XPS O1s spectra between pristine and 20 °C O_2 GDE protocol (**Figure 5.8c**) suggests performance degradation from 20 °C O_2 protocol (**Figure 5.8a**) is mainly attributed to active site demetallation. Meanwhile, the increase in O1s after 75 °C O_2 protocol (**Figure 5.8c**) causes reductions in TOF and FeN_x site density and the increased observation degradation. Reduction in TOF occurs due to reactive oxygen species catalyzing mild carbon corrosion.[15,16]

The high rate of degradation and Fe dissolution/redeposition can be attributed to the high percentage of unstable high spin $Fe^{III}N_x$ present (assuming the same type of sites are present between TAP 900@^{57}Fe and TAP 900@Fe). Additionally, according to density functional theory of Fe-N-C, the number and size of graphene sheets affects the dissolution potential.[55] Previous Raman analysis of TAP 900 determined an atomically thin carbon structure,[49] which therefore leads itself to possess less stable FeN_x sites.

This GDE ICP-MS concentration profile under 20 °C O_2 (**Figure 5.9a** and **c**) suggests Fe dissolution and subsequent detection by ICP-MS at low current density (-0.6 mA cm^{-2}). Meanwhile at higher current density (-15, -50 and -100 mA cm^{-2}) a process of Fe dissolution and redeposition locally into Fe_xO_y in the catalyst layer is proposed. This is supported by the increased observation of Fe_xO_y after O_2 GDE protocol from HAADF-STEM and EDX (**Figure 5.8f** and **Figure B15c**). Some Fe_xO_y is then dissolved at reduced current density at higher potentials. The observation of Fe_xO_y corroborates previous findings from *post-mortem* O_2 AST protocols.[15,17]

For equivalent O_2 current density, the potential is higher under 75 °C than 20 °C O_2 (**Figure 5.9a** and **c**), owing to higher intrinsic rates towards O_2 reduction (Arrhenius-like behaviour),[28] increased O_2 solubility and increased H^+ transport. Also, at 75 °C, increased H^+ causes the Fe_xO_y/Fe equilibrium to shift according to Le Chatelier's principle. The increased Fe concentration detected when stepping down in potential (cathodic direction) after post AST (**Figure 5.9c**) for O_2 GDE at 20 °C and 75 °C supports the hypothesis that Fe_xO_y builds up in the

catalyst layer at current densities of -50 mA cm^{-2} during the AST and is only released at lower current density holds (-1 mA cm^{-2} at 20 °C and 75 °C).

5.4.3 Kinetic Modelling

A microkinetic model of the system (**Figure 5.10a**, see **Appendix B** for equations) was developed to replicate the observations from GDE ICP-MS prior to AST at 20 °C in 0.1 M $HClO_4$ and evidence the hypothesis of the pivotal role of interfacial pH. Focus is made on the Fe concentration observed in GDE ICP-MS at 0.75 $V_{RHE,\ iR\text{-}free}$, corresponding to a current density of -15 and 0 mA cm^{-2}_{geo} under O_2 and Ar supply, respectively. Under these conditions, only the acidic O_2 reduction mechanism occurs, due to the shift in potential versus RHE with pH. For example, at 0.75 V_{RHE} in pH = 1, an increase to pH = 8 results in a potential of 1.16 V_{RHE}, where no O_2 reduction would occur. Therefore, there is no change of mechanism from acidic to alkaline O_2 reduction. The values of the Fe dissolution rate constant (k_{dis}) and the tortuosity factor (τ) in the catalyst layer were adjusted to semi-quantitatively simulate the time evolution of the Fe concentration signal monitored by GDE ICP-MS in Ar-saturated electrolyte. It was assumed the proton concentration in the catalyst layer is homogeneously distributed. The value of the proton consumption rate constant (k_r) and void volume (ε) were then varied to replicate the Fe concentration signal measured (**Figure 5.10b-d**). Good agreement between experiment and simulation are reached for the range of values considered ($0.2 \leq \varepsilon \leq 0.4$ and $100 \leq k_r \leq 400\ s^{-1}$). Values for τ ($1.8 \leq \tau \leq 2.2$) were within previously reported ranges.[57,58]

Figure 5.10e displays the corresponding simulated pH profile in the catalyst layer. The simulations predict a significantly lower concentration of detected Fe cations during O_2 reduction. This phenomenon is attributed to the precipitation of Fe^{3+} cations under the local conditions in the catalyst layer, with the Fe concentration resulting from the balance between Fe precipitation and redissolution. Indeed, simulations indicate that at -15 mA cm^{-2}_{geo}, the local pH at the interface between the Fe-N-C layer and the electrolyte solution is approximately 1.5 (**Figure 5.10e**). There is then a substantial and rapid increase in pH moving into the bulk catalyst layer (far from the liquid electrolyte), reaching pH values *ca*. 8-9. Consequently, only the region of the catalyst layer near the solution contributes to O_2 reduction. These conditions on the Fe Pourbaix diagram are depicted in **Figure 5.10f**. For the parameter values considered, >90% of the Fe-N-C layer experiences pH > 2.4, which would result in formation of Fe_2O_3. Pourbaix diagrams are dependent on temperature and

concentration of species. While it appears [Fe] is in order of 10^{-6} M, the Pourbaix diagram for [Fe] = 10^{-8} M at 25 °C can be found for comparison in **Figure B18**. Additionally, Pourbaix diagrams were developed from metal surfaces rather than single atoms, where DFT-based models have instead been developed,[55] although here it is appears the Fe-N-C system is sufficiently represented by the Pourbaix diagram for Fe surface.

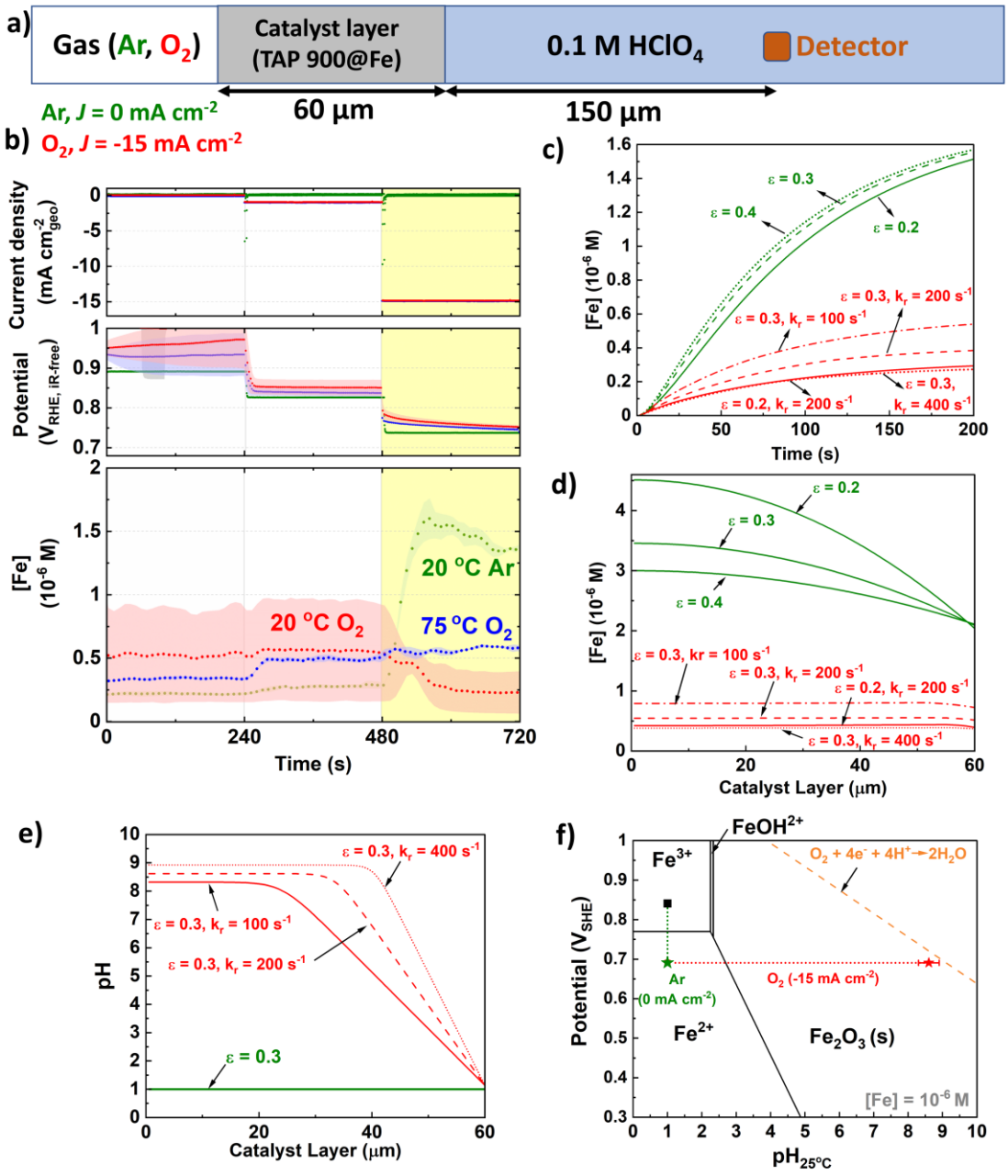


Figure 5.10. a.) Schematic depicting kinetically modelled system. b.) Initial GDE-ICP-MS data in terms of [Fe]. Simulated Fe concentration over c.) Time and d.) Catalyst Layer. e.) pH distribution across catalyst layer. k_r is the proton consumption rate constant and ε is the void volume. f.) Pourbaix diagram of Fe surface at 25 °C and [Fe] = 10^{-6} M with labelled points under O_2 (-15 mA cm^{-2}_{geo}) and Ar (0 mA cm^{-2}_{geo}) conditions. The error bar for O_2 represents variation of pH from different ε and k_r in Figure 5c. Fe Pourbaix diagram replotted from reference.[59]

5.5 Conclusion

The impact on the Fe concentration profile obtained with online flow cell and GDE ICP-MS setup was investigated in this study under inert (Ar) or active (O_2) conditions in 0.1 M $HClO_4$. The influence of temperature was also investigated in RDE (80 ^oC) and online GDE ICP-MS (75 ^oC). A microkinetic model was developed, which sufficiently represented the experimental conditions in the GDE ICP-MS system at 20 ^oC in Ar and O_2 (at -15 mA cm^{-2}), demonstrating a significant pH increase within the Fe-N-C layer under O_2 at -15 mA cm^{-2}. This pH increase results in formation of Fe_2O_3 species, which were experimentally confirmed from *post-mortem* characterization. Faster mass transport at 75 ^oC under O_2 supply resulted in higher Fe concentration detected by GDE ICP-MS and no observation of Fe_xO_y *post-mortem*. Future work will explore further kinetic modelling of the 75 ^oC system. Measured Fe dissolution under both Ar and O_2-saturated conditions in flow cell ICP-MS is proposed to arise from a lack of pH change from the limited current density (~1 mA cm^{-2}) and therefore low H^+ consumption. Observation of Fe_2O_3 after O_2-saturated 80 ^oC RDE AST are attributed to precipitation of dissolved Fe species from local O_2 concentration. These findings have important implications for PEMFC and GDE testing of thick catalyst layers.

References

1 US DOE - Hydrogen and Fuel Cell Technologies Office, *Hydrogen and Fuel Cell Technologies Office Multi-Year Research, Development, and Demonstration Plan. Section 3.4: Fuel Cells*, 2017.

2 S. Liu, C. Li, M. J. Zachman, Y. Zeng, H. Yu, B. Li, M. Wang, J. Braaten, J. Liu, H. M. Meyer, M. Lucero, A. J. Kropf, E. E. Alp, Q. Gong, Q. Shi, Z. Feng, H. Xu, G. Wang, D. J. Myers, J. Xie, D. A. Cullen, S. Litster and G. Wu, *Nat. Energy*, 2022, **7**, 652–663.

3 Y. Shao, J. Dodelet, G. Wu and P. Zelenay, *Adv. Mater.*, 2019, **31**, 1807615.

4 H. Zhang, L. Osmieri, J. H. Park, H. T. Chung, D. A. Cullen, K. C. Neyerlin, D. J. Myers and P. Zelenay, *Nat. Catal.*, 2022, 571–592.

5 K. Kumar, T. Asset, X. Li, Y. Liu, X. Yan, Y. Chen, M. Mermoux, X. Pan, P. Atanassov, F. Maillard and L. Dubau, *ACS Catal.*, 2021, **11**, 484–494.

6 M. Ferrandon, X. Wang, A. J. Kropf, D. J. Myers, G. Wu, C. M. Johnston and P. Zelenay, *Electrochimica Acta*, 2013, **110**, 282–291.

7 S. Liu, Q. Meyer, C. Jia, S. Wang, C. Rong, Y. Nie and C. Zhao, *Energy Environ. Sci.*, 2023, **16**, 3792–3802.

8 C. H. Choi, C. Baldizzone, G. Polymeros, E. Pizzutilo, O. Kasian, A. K. Schuppert, N. Ranjbar Sahraie, M.-T. Sougrati, K. J. J. Mayrhofer and F. Jaouen, *ACS Catal.*, 2016, **6**, 3136–3146.

9 C. H. Choi, C. Baldizzone, J.-P. Grote, A. K. Schuppert, F. Jaouen and K. J. J. Mayrhofer, *Angew. Chem. Int. Ed.*, 2015, **54**, 12753–12757.

10 P. G. Santori, F. D. Speck, J. Li, A. Zitolo, Q. Jia, S. Mukerjee, S. Cherevko and F. Jaouen, *J. Electrochem. Soc.*, 2019, **166**, F3311–F3320.

11 P. P. Lopes, *ACS Mater. Au*, 2023, **3**, 8–17.

12 K. Ehelebe, J. Knöppel, M. Bierling, B. Mayerhöfer, T. Böhm, N. Kulyk, S. Thiele, K. J. J. Mayrhofer and S. Cherevko, *Angew. Chem. - Int. Ed.*, 2021, **60**, 8882–8888.

13 F. R. Nikkuni, B. Vion-Dury, L. Dubau, F. Maillard, E. A. Ticianelli and M. Chatenet, *Appl. Catal. B Environ.*, 2014, **156–157**, 301–306.

14 G. Bae, M. M. Kim, M. H. Han, J. Cho, D. H. Kim, M.-T. Sougrati, J. Kim, K.-S. Lee, S. H. Joo, W. A. Goddard, H.-S. Oh, H. Kim, F. Jaouen and C. H. Choi, *Nat. Catal.*, 2023, 1–11.

15 K. Kumar, L. Dubau, M. Mermoux, J. Li, A. Zitolo, J. Nelayah, F. Jaouen and F. Maillard, *Angew. Chem. Int. Ed.*, 2020, **59**, 3235–3243.

16 C. H. Choi, H. K. Lim, M. W. Chung, G. Chon, N. Ranjbar Sahraie, A. Altin, M. T. Sougrati, L. Stievano, H. S. Oh, E. S. Park, F. Luo, P. Strasser, G. Dražić, K. J. J. Mayrhofer, H. Kim and F. Jaouen, *Energy Environ. Sci.*, 2018, **11**, 3176–3182.

17 J. Li, M. T. Sougrati, A. Zitolo, J. M. Ablett, I. C. Oğuz, T. Mineva, I. Matanovic, P. Atanassov, Y. Huang, I. Zenyuk, A. Di Cicco, K. Kumar, L. Dubau, F. Maillard, G. Dražić and F. Jaouen, *Nat. Catal.*, 2021, **4**, 10–19.

18 V. Goellner, C. Baldizzone, A. Schuppert, M. T. Sougrati, K. Mayrhofer and F. Jaouen, *Phys. Chem. Chem. Phys.*, 2014, **16**, 18454–18462.

19 R. Chenitz, U. I. Kramm, M. Lefèvre, V. Glibin, G. Zhang, S. Sun and J.-P. Dodelet, *Energy Environ. Sci.*, 2018, **11**, 365–382.

20 L. Osmieri, D. A. Cullen, H. T. Chung, R. K. Ahluwalia and K. C. Neyerlin, *Nano Energy*, 2020, **78**, 105209.

21 K. T. Santos, K. Kumar, L. Dubau, H. Ge, S. Berthon-Fabry, C. S. A. Vasconcellos, F. H. B. Lima, T. Asset, P. Atanassov, V. A. Saveleva, P. Glatzel, X. Li, F. Jaouen and F. Maillard, *J. Power Sources*, 2023, **564**, 232829.

22 V. A. Saveleva, K. Kumar, P. Theis, N. S. Salas, U. I. Kramm, F. Jaouen, F. Maillard and P. Glatzel, *ACS Appl. Energy Mater.*, 2023, **6**, 611–616.
23 J. Barrio, A. Pedersen, S. Ch. Sarma, A. Bagger, M. Gong, S. Favero, C. Zhao, R. Garcia-Serres, A. Y. Li, Q. Zhang, F. Jaouen, F. Maillard, A. Kucernak, I. E. L. Stephens and M. Titirici, *Adv. Mater.*, 2023, **35**, 2211022.
24 M. Primbs, Y. Sun, A. Roy, D. Malko, A. Mehmood, M.-T. Sougrati, P.-Y. Blanchard, G. Granozzi, T. Kosmala, G. Daniel, P. Atanassov, J. Sharman, C. Durante, A. Kucernak, D. Jones, F. Jaouen and P. Strasser, *Energy Environ. Sci.*, 2020, **13**, 2480–2500.
25 X. Wan, X. Liu, Y. Li, R. Yu, L. Zheng, W. Yan, H. Wang, M. Xu and J. Shui, *Nat. Catal.*, 2019, **2**, 259–268.
26 J.-Q. Zhong, K.-J. Yan, J. Yang, W.-H. Yang and X.-D. Yang, *ACS Catal.*, 2022, **12**, 9003–9010.
27 F. Jaouen, V. Goellner, M. Lefèvre, J. Herranz, E. Proietti and J. P. Dodelet, *Electrochimica Acta*, 2013, **87**, 619–628.
28 V. Gridin, J. Du, S. Haller, P. Theis, K. Hofmann, G. K. H. Wiberg, U. I. Kramm and M. Arenz, *Electrochimica Acta*, 2023, **444**, 142012.
29 D. Malko, A. Kucernak and T. Lopes, *Nat. Commun.*, 2016, **7**, 13285.
30 S. Rojas-Carbonell, K. Artyushkova, A. Serov, C. Santoro, I. Matanovic and P. Atanassov, *ACS Catal.*, 2018, **8**, 3041–3053.
31 M. Gong, A. Mehmood, B. Ali, K.-W. Nam and A. Kucernak, *ACS Catal.*, 2023, **13**, 6661–6674.
32 A. Bonnefont, *Curr. Opin. Electrochem.*, 2023, **39**, 1–8.
33 A. S. Varela, M. Kroschel, T. Reier and P. Strasser, *Catal. Today*, 2016, **260**, 8–13.
34 A. S. Varela, *Curr. Opin. Green Sustain. Chem.*, 2020, **26**, 100371.
35 A. Muthukrishnan and A. James, *Catal. Sci. Technol.*, 2022, **12**, 6246–6255.
36 G. Bae, M. W. Chung, S. G. Ji, F. Jaouen and C. H. Choi, *ACS Catal.*, 2020, **10**, 8485–8495.
37 M. Rouhet, S. Bozdech, A. Bonnefont and E. R. Savinova, *Electrochem. Commun.*, 2013, **33**, 111–114.
38 I. V. Zenyuk and S. Litster, *ECS Trans.*, 2013, **58**, 27–35.
39 F. Jaouen, M. Lefèvre, J.-P. Dodelet and M. Cai, *J. Phys. Chem. B*, 2006, **110**, 5553–5558.
40 J.-Y. Choi, L. Yang, T. Kishimoto, X. Fu, S. Ye, Z. Chen and D. Banham, *Energy Environ. Sci.*, 2017, **10**, 296–305.
41 X. Yin and P. Zelenay, *ECS Trans.*, 2018, **85**, 1239.
42 G. Zhang, X. Yang, M. Dubois, M. Herraiz, R. Chenitz, M. Lefèvre, M. Cherif, F. Vidal, V. P. Glibin, S. Sun and J.-P. Dodelet, *Energy Environ. Sci.*, 2019, **12**, 3015–3037.
43 J.-P. Dodelet, V. Glibin, G. Zhang, U. I. Kramm, R. Chenitz, F. Vidal, S. Sun and M. Dubois, *Energy Environ. Sci.*, 2021, **14**, 1034–1041.
44 X. Yin, E. F. Holby and P. Zelenay, *Energy Environ. Sci.*, 2021, **14**, 1029–1033.
45 Y.-P. Ku, K. Ehelebe, A. Hutzler, M. Bierling, T. Böhm, A. Zitolo, M. Vorokhta, N. Bibent, F. D. Speck, D. Seeberger, I. Khalakhan, K. J. J. Mayrhofer, S. Thiele, F. Jaouen and S. Cherevko, *J. Am. Chem. Soc.*, 2022, **144**, 9753–9763.
46 K. Ebner, L. Ni, V. A. Saveleva, B. P. L. Monnier, A. H. Clark, F. Krumeich, M. Nachtegaal, J. S. Luterbacher, U. I. Kramm, T. J. Schmidt and J. Herranz, *Phys. Chem. Chem. Phys.*, 2021, **23**, 9147–9157.
47 R. D. Hunter, J. Ramírez-Rico and Z. Schnepp, *J. Mater. Chem. A*, 2022, **10**, 4489–4516.
48 J. Li, S. Ghoshal, W. Liang, M.-T. Sougrati, F. Jaouen, B. Halevi, S. McKinney, G. McCool, C. Ma, X. Yuan, Z.-F. Ma, S. Mukerjee and Q. Jia, *Energy Environ. Sci.*, 2016, **9**, 2418–2432.

49 S. C. Sarma, J. Barrio, A. Bagger, A. Pedersen, M. Gong, H. Luo, M. Wang, S. Favero, C. Zhao, Q. Zhang, A. Kucernak, M. Titirici and I. E. L. Stephens, *Adv. Funct. Mater.*, 2023, 2302468.
50 N. Ramaswamy, U. Tylus, Q. Jia and S. Mukerjee, *J. Am. Chem. Soc.*, 2013, **135**, 15443–15449.
51 X. Wang, M. Ferrandon, J. H. Park, J.-J. Shen, A. J. Kropf, H. Zhang, P. Zelenay and D. J. Myers, *Electrochimica Acta*, 2023, **443**, 141934.
52 U. A. Paulus, T. J. Schmidt, H. A. Gasteiger and R. J. Behm, *J. Electroanal. Chem.*, 2001, **495**, 134–145.
53 K. Kumar, P. Gairola, M. Lions, N. Ranjbar-Sahraie, M. Mermoux, L. Dubau, A. Zitolo, F. Jaouen and F. Maillard, *ACS Catal.*, 2018, **8**, 11264–11276.
54 X. Xie, C. He, B. Li, Y. He, D. A. Cullen, E. C. Wegener, A. J. Kropf, U. Martinez, Y. Cheng, M. H. Engelhard, M. E. Bowden, M. Song, T. Lemmon, X. S. Li, Z. Nie, J. Liu, D. J. Myers, P. Zelenay, G. Wang, G. Wu, V. Ramani and Y. Shao, *Nat. Catal.*, 2020, **3**, 1044–1054.
55 E. F. Holby, G. Wang and P. Zelenay, *ACS Catal.*, 2020, **10**, 14527–14539.
56 P. Boldrin, D. Malko, A. Mehmood, U. I. Kramm, S. Wagner, S. Paul, N. Weidler and A. Kucernak, *Appl. Catal. B Environ.*, 2021, **292**, 120169.
57 S. Komini Babu, H. T. Chung, P. Zelenay and S. Litster, *ACS Appl. Mater. Interfaces*, 2016, **8**, 32764–32777.
58 S. J. Ridge, R. E. White, Y. Tsou, R. N. Beaver and G. A. Eisman, *J. Electrochem. Soc.*, 1989, **136**, 1902.
59 B. Beverskog and I. Puigdomenech, *Corros. Sci.*, 1996, **38**, 2121–2135.

Chapter 6: Fe-N-C PEMFC Optimisation: The Effect of Ionomer Loading

6.1 Introduction

There has been significant progress in Fe-N-C PEMFC performance, approaching that of Pt-based systems.[1,2] Still, there is ample room for Fe-N-C PEMFC improvement due to challenging catalyst layer optimisation.[3] This challenge arises from the lower volumetric activity of Fe-N-C compared to Pt-based cathodes, which necessitates the manufacture of ~10× thicker Fe-N-C layers (typically 60-150 $\mu m_{Fe\text{-}N\text{-}C}$ vs. 10-20 $\mu m_{Pt/C}$[3]). Therefore, cathodes require engineering and optimisation of inks, electrode preparation and properties of 3D catalyst layers for effective catalyst utilisation and maximised PEMFC performance.[4–6] These parameters require adaptation for each Fe-N-C catalyst owing to the vastly different catalyst properties, which arise from the diverse range of preparation routes.[7]

Of particular importance in PEMFCs is the amount of proton conducting ionomer, commonly Nafion, which consists of a side chain terminated with sulfonic acid groups and a main chain perfluorinated polymer backbone.[8] The ionomer loading should provide sufficient percolation into and between catalyst particles for suitable proton conduction, at the same time maintaining void space for efficient gas transport and stable catalyst layers.[4] The amount of Nafion infiltration in carbon agglomerates is dependent on the pore size distribution, ionomer loading and the amount of aggregation in solution.[9] Nafion micelle size depends on ionomer concentration, temperature, catalyst layer treatment, humidity, material properties of the carbon and potentially the electric field.[10] Micelles of Nafion have been observed from diameters of 2-20 nm, depending on the conditions and measurement technique.[11–15]

The optimal ionomer content is dependent on its distribution, which is affected by the deposition method, how the material is treated and the catalyst properties and surface chemistry.[4,16] Optimal I/C in Pt/C based cathodes can simply be determined by measuring the electrochemical surface area of Pt from the H adsorption/desorption area in cyclic voltammetry (CV) under inert conditions;[17] however, this optimisation method is not directly applicable to Fe-N-C. This is because the electrochemical surface area of Fe-N-C is not equivalent to the FeN_x active site density (sites g_{FeNC}^{-1} or sites cm_{FeNC}^{-3}), which is the relevant descriptor for Fe-N-C performance.[18] The FeN_x active site density can be quantified *in-situ*

from the Fe^{III}/Fe^{II} redox (0.76 V_{RHE}), which has previously been confirmed as arising from FeN_x active sites,[19–21] in particular high spin $Fe^{III}N_x$ sites.[20] However, quantification can be skewed by contributions from overlapping quinone/hydroquinone redox.[22] To this end, Fourier transform alternating current voltammetry (FTacV) has recently been developed as a new tool to precisely quantify the number of FeN_x sites and reaction kinetics from the Fe^{III}/Fe^{II} redox.[23,24] Using FTacV, it should follow that PEMFC performance correlates to active site density, assuming resistances do not significantly contribute. Nonetheless, some Fe-N-C do not exhibit Fe^{III}/Fe^{II} redox. For this, an *in-situ* electrochemical impedance spectroscopy (EIS)-based method was developed by Kucernak and co-workers to quickly identify ideal I/C for M-N-C-based PEMFC.[25] While EIS is a powerful tool to deconvolute contributions of different processes in a fuel cell (H^+ transport, kinetics, and O_2 and H_2O diffusion), understanding and correctly fitting EIS data is non-trivial. Recently, *in-situ* distribution of relaxation times (DRT) has evolved as a complimentary tool to deconvolute different processes and resistances within PEMFCs, using a model-free approach.[26] Even so, DRT analysis is complex, time-consuming and open to interpretation. DRT has been used recently in Fe-N-C-based PEMFCs to calculate and monitor the evolution in O_2 diffusion, H^+ transport and O_2 reduction kinetics over time and at different current densities.[27,28]

In this chapter, the previously developed TAP 900@Fe is incorporated into a PEMFC, with focus on optimising the I/C ratio. The catalyst and its electrode are characterised with a variety of *ex situ* measurements (N_2 sorption, scanning transmission electron microscopy and energy dispersive x-rays, X-ray diffraction, ICP-MS, electronic conductivity). PEMFC performance is evaluated based on a series of I/C ratios. The contributions of proton and electron resistance and active site density on PEMFC performance is based on advanced electrochemical methods (EIS, DRT and FTacV).

6.2 Experimental

6.2.1 Catalyst Preparation

The Fe-N-C catalyst (TAP 900@Fe) was prepared according to Section 3.2.1-3.2.2. In this Chapter, an additional pyrolysis was performed on TAP 900@Fe. 50-60 mg of TAP 900@Fe was placed in a quartz crucible, without a lid, inside a glass-tube oven (Thermo Scientific-Lindberg Blue M) under a flow of 300 mL min^{-1} 5% H_2/Ar (MAXIMA). The temperature was increased gradually from 25°C to 900°C at a rate of 20°C min^{-1} and maintained at 900°C for 1 hour before allowing it to cool naturally. The resulting product, TAP 900@Fe-900, exhibited a yield of approximately 60%.

6.2.2 RDE

Electrochemical oxygen reduction tests were carried out employing a Biologic VSP in Ar or O_2 (99.999% MAXIMA) saturated 0.1 M $HClO_4$ (Suprapur) electrolyte in a glass cell with a three-electrode configuration. A Pt wire saturated in H_2 purged electrolyte within a glass capillary served as the reference electrode and a glassy carbon rod as counter electrode. *iR* correction was applied post electrochemistry by determining the solution ohmic drop R (14 Ω) using the current interrupt technique with 50 kHz filter. A 5 mm glassy carbon rotating disk electrode (Pine) was polished with a micropolish cloth and 0.05 µm alumina suspension. 12.7 µL catalyst ink was drop-casted on to a freshly polished RDE; comprising 4 mg of the catalyst, 480 µL of 18.2 MW cm^{-1} deionised water, 480 µL of isopropanol and 40 µL of 5 wt.% Nafion prepared from diluting D-2021 (Ion Power). The ink was freshly sonicated for 30 mins in an ice-cooled bath sonicator (45 kHz, 50 W ultrasonic cleaner, MRC). The drop-cast ink was dried under rotation for 30 min under ambient air, leading to a catalyst loading of 0.26 $mg_{Fe\text{-}N\text{-}C}$ cm^{-2}. Cyclic voltammograms were obtained after purging the electrolyte for at least 15 min and recorded at 50 mV s^{-1} at 0 rpm for N_2 saturated (measurements at 10^{th} cycle displayed), and 10 mV s^{-1} at 1,600 rpm when the electrolyte was saturated with O_2 or N_2 (measurements at 3^{rd} cycle displayed). The capacitance was corrected in O_2 reduction performance by subtracting Ar saturated measurements from the O_2 saturated results. Measurements were repeated twice.

6.2.3 PEMFC

6.2.3.1 Electrode Manufacture

To prevent contamination, no tools or equipment containing Pt were utilized during the construction of the cathode. Inks for fuel cell testing were prepared at a concentration of 2

mg ml^{-1}, using a solution comprising a 1:1 mixture of isopropanol and water, with the addition of Nafion® solution (D2021, Ion Power) to achieve an I/C ratio ranging from 0.7 to 4.9 (wt. ratio). The mixture was subjected to ultrasonic treatment in an ice-cooled bath sonicator (45 kHz, 50 W ultrasonic cleaner, MRC) for 1 h, followed by stirring for 12-16 h. Subsequently, the cathode ink was applied automatically via spraying (Sono-Tek ExactaCoat, Sono-Tek Corporation) at a rate of 0.15 mL min^{-1}, employing an offset serpentine spray pattern on a 5 cm^2 gas diffusion layer (BC29, SGL Group) while maintaining a temperature of 95°C on a vacuum plate with an air shaping flow of 0.3 L min^{-1}. The gas diffusion layer was weighed both before and after the application of the cathode catalyst to determine the cathode catalyst loading (1.31±0.05 $mg_{Fe\text{-}N\text{-}C}$ cm^{-2}). The thickness of the catalyst layer was gauged using a micrometer (Insize). Additionally, 0.2 mg cm^{-2} of Nafion solution (1 mg Nafion ml^{-1} IPA) was sprayed onto the cathode subsequent to the application of the catalyst layer. Finally, the 5 cm^2 electrode was sectioned into 1 cm^2 pieces.

The anode was comprised of commercial 0.2 mg_{Pt} cm^{-2} on 22BB (Fuel Cells Etc), while the membrane used was Nafion® 212 (Ion Power). To assemble the components, the anode, N212, and cathode were hot-pressed (Auto Series, Carver) at 125°C for 5 mins under a pressure of 4,000 lbs (given the glass transition temperature of Nafion 212 at 123°C). The thickness of the MEA gaskets was selected to achieve 20-30% compression on the Gas Diffusion Layer (GDL), with the anode gasket measuring 170 µm and the cathode gasket measuring 220 µm. The PEMFC structure encompassed, on both the cathode and anode sides (from the outside to the centre), one gasket, one current collector, one graphite plate featuring a single serpentine flow field and a single channel, along with one 170 µm PTFE gasket for the anode and one 220 µm PTFE gasket for the cathode. Furthermore, 8 bolts in the PEMFC hardware were tightened with a torque of 4.5 Nm. The cell was heated to 80°C, and humidified gases were passed at 60°C and subsequently at 80°C for 20 minutes to hydrate the membrane.

6.2.3.2 Operation

Fuel cell testing was carried out utilizing a Scribner 850e system (Scribner Associates Inc.). Polarization curves were recorded under H_2-O_2 (where H_2, N_2, and air were 99.999% pure, from MAXIMA) at a back pressure of 1 bar_g, 100% relative humidity, and an operating temperature of 80°C, with gas flow rates set at 0.7 and 1.7 standard cm^3 min^{-1} (sccm) for both

the anode and cathode. The polarization curves were measured at a rate of 50 mV s^{-1}, ranging from the open circuit potential to 0.2 V vs the anode and back to the open circuit potential. The results represent an average of two scans from repeated measurements. Cyclic voltammetry was performed under N_2-H_2 (cathode-anode) with a flow rate of 0.3 sccm at 50 mV s^{-1} between 1.0-0.1 V, with 10 scans conducted to ensure a stable response.

Electrochemical impedance spectroscopy was conducted using a Biologic SP-300, covering a frequency range of 200,000–0.1 kHz with 20 points per decade and a perturbation amplitude of 10 mV. Before each EIS measurement, the cell was held at 0.3 V vs the anode for 30 seconds. The flow rates and conditions for this test were identical to those used in the polarization and cyclic voltammetry tests. Additionally, measurements were taken at 0.3 V vs the anode under N_2-H_2 (cathode-anode) and at 50 and 100 mA cm^{-2} under O_2-H_2 (cathode-anode) using the same cell conditions as described above.

6.2.3.3 FTacV

The measurements followed a previously reported method.[23] Fourier-Transformed alternating current voltammetry were conducted using a Biologic SP-300 potentiostat. Cells conditions were same as above under H_2-N_2. Initial voltage, E_i, was 0.55 V; final voltage, E_f, was 0.95 V; sine wave frequency, f, of 0.119 Hz; d.c. scan rate, v, of 0.476 mV s^{-1}; amplitude of sine wave, ΔE, of 130 mV; and time step for data acquisition, dt, of 0.8 ms.

Modelling was conducted on Matlab. Only one site was considered in FTacV simulations.

The scan rate is determined by:

$$\boldsymbol{v = \frac{f_s \Delta E}{2^N}} \qquad \textbf{Equation 6.1}$$

Where f_s is the sampling rate (Hz), ΔE the potential window of the measurement and N is an integer (between 16-19).

The frequency is based on:

$$\boldsymbol{f = \frac{f_s J}{2^N}} \qquad \textbf{Equation 6.2}$$

Where J is the number of complete sine wave cycles (0-2π) employed.

6.2.3.4 Equations

The geometric site density (SD_{geo}, site g^{-1}) from Fe^{III}/Fe^{II} redox was calculated on the following:

$$SD_{geo} = \frac{Q_{Fe}}{F} \quad \textbf{Equation 6.3}$$

Where Q_{Fe} is the Fe^{III}/Fe^{II} redox charge (C cm^{-2}), F is Faraday's constant (96485 C mol^{-1}).

TOF values in PEMFC at 0.80 V were based:

$$TOF = \frac{i_{geo}}{e^{-} \times SD_{geo}} \quad \textbf{Equation 6.4}$$

Where i_{geo} is the current density at 0.8 V (mA cm^{-2}) and e^{-} is the charge of one electron (1.6×10^{-19} C).

High frequency resistance (HFR) corrected cell potential ($E_{HFR\text{-}free}$) is applied via:

$$E_{HFR-free} = E_{cell} + (i_{geo} \times HFR) \quad \textbf{Equation 6.5}$$

6.2.3.5 DRT

All EIS measurements were confirmed for linearity, causality and stability by the Kramers-Kronig relations using the LIN-KK software developed by Ivers-Tiffée *et al.*[29], the residuals did not exceed 1%, and thus were concluded to be valid. The DRT analysis was performed using the DRT Tools software developed by Ciucci and Chen.[30] The regularization parameter was selected to be in the order of 10^{-3}, which is a typical value for fuel cells.[31] The resistance of the processes was calculated by integrating the area under the corresponding peaks.

The impedance can be described by **Equation 6.6**:

$$Z(f) = R_{\infty} + \int_{-\infty}^{\infty} \frac{\gamma(\ln \tau)}{1 + i2\pi f\tau} d\ln\tau \quad \textbf{Equation 6.6}$$

where Z is the impedance, f is the frequency, R_{∞} is the high frequency resistance, τ is the relaxation time, and $\gamma(\ln \tau)$ is the DRT function.

6.2.4 Characterisation

6.2.4.1 SEM

For the creation of SEM cross-sections of the MEA, the MEA underwent initial placement in liquid nitrogen for a duration of 30 seconds, following which it was cut using a scalpel. The thicknesses of the MEA components were assessed utilizing ImageJ software. The SEM analysis was conducted employing Quanta FEG 250 at 15 kV and 5,500 magnification.

6.2.4.2 HAADF-STEM and EDX

The structure and chemical makeup of TAP 900@Fe900 were analysed via scanning transmission electron microscopy (HR-STEM) and energy-dispersive X-ray spectroscopy (EDX) utilizing a Thermo Fisher Titan STEM (G2 80–200) equipped with a Cs probe corrector (CEOS) and a high-angle annual dark-field (HAADF) detector, operating at 200 kV. To prepare the TEM samples, the catalyst powders were dispersed into a methanol solution, which was subsequently drop-cast onto a copper grid coated with an amorphous holey carbon film.

6.2.4.3 Ex-Situ Electronic Conductivity

The comparative electronic conductivity of the powders was assessed through a two-point method, as detailed in a previously documented procedure.[32,33] The powders were positioned within a Teflon die (0.25" diameter) and compacted using a micrometer (INSIZE 3109 micrometer) which served a dual purpose: firstly, to gauge the thickness of the compacted powder, and secondly, to apply an identical compacting force to the various samples utilizing the instrument's friction thimble. Electrical clips were then inserted into two apertures located at either end of the Teflon die, enabling resistivity measurements to be taken with a multimeter.

The resistivity of the spray-coated catalyst layers (ρ_{res}) was determined employing the four-point probe technique, as specified in **Equation 6.7**, subsequently allowing the computation of electronic conductivity (σ_e) according to **Equation 6.8**:

$$\rho_{res} = \frac{\pi}{ln2} \left(\frac{V}{I}\right) t \qquad \textbf{Equation 6.7}$$

$$\sigma_e = \frac{1}{\rho_{res}} \qquad \textbf{Equation 6.8}$$

Where *t* represents the thickness of the spray-coated catalyst layer, *V* denotes the recorded potential drop, and *I* refers to the designated current during the measurement. This equation is used when the sample thickness is less than half of the probe spacing (1 mm).[34] It is assumed that the catalyst layers behave as semi-infinite two-dimensional sheets, enabling the applied currents to distribute across the surface of the catalyst layer. The multimeter (Agilent 34401A) was employed to capture both the voltage and current data, with the reported error encompassing four repeated measurements.

6.3 Results and Discussion

6.3.1 Catalyst Powder Characterisation

Prior to PEMFC implementation, critical catalyst properties are determined. The initial catalyst was synthesized as previously reported, via Mg ionothermal templating and pyrolysis with 2,4,6–Triaminopyrimidine (TAP), followed by Fe-Mg cation exchange and acid washing steps, creating TAP 900@Fe.[35] The relative electronic conductivity (**Supporting Note C1**) of TAP 900@Fe powder from two probe pellet measurements was found to be insufficient when compared to PMF-011904 and commercial carbons (**Figure C1**). To increase the electronic conductivity of TAP 900@Fe, a second pyrolysis at 900°C (20°C min heating rate with 1 h hold) under 5% H_2/95% Ar (300 mL min^{-1}) was conducted. The over two orders of magnitude increase in electronic conductivity from TAP 900@Fe to TAP 900@Fe900 (**Figure S2**) can be explained by the reduction in N content from 11.6 to 2.6 at.% (**Figure S2, Supporting Note C2**). The high amount of surface oxygen groups in TAP 900@Fe900 (O = 11.5 wt.%) is expected to help enable an even ionomer distribution and favourable ionomer/Fe-N-C interaction in PEMFC.[16] The surface Fe content (XPS) in TAP 900@Fe900 is 1.0 wt.%, while the bulk (ICP-MS) is 1.2±0.1 wt.% (**Table C1**). The near equivalent Fe content from ICP-MS and XPS demonstrate the bulk properties of TAP 900@Fe900 are equivalent to the surface properties, indicating a highly porous and accessible structure.

High angle annular dark field scanning transmission electron microscopy (HAADF-STEM) of TAP 900@Fe900 particles (**Figure 6.1a** and **C4**) confirms the accessible and anisotropic carbon structure created by the Mg templating method. Higher magnification images (**Figure 6.1a** and **S4**) show a combination of homogeneously dispersed atomic metal atoms and small metallic clusters (<5 nm). Meanwhile in some locations larger metallic particles (20-40 nm) are observed in TAP 900@Fe900. However, there was no observation of sharp and well-defined peaks relating to metal particles from XRD measurements of TAP 900@Fe900 (**Figure C5**). This suggests these particles are either non-crystalline or their size is below the detection limit of the XRD equipment. Energy dispersive x-ray spectroscopy on one of the 40 nm diameter metallic particles (**Figure C6a**) shows a core-shell structure with an Fe core (30 nm diameter) and Fe_xO_y shell (5 nm radius). Similar Fe/Fe-O core/shell nanoparticles have been reported under reductive pyrolysis of Fe.[36] The nanometric metallic clusters (<5 nm) appear to be Fe_xO_y (**Figure C6b**), which can spontaneously form in contact with air.[37] Cryo ^{57}Fe

Mössbauer would be required for conclusive Fe_xO_y confirmation.[1,38] EDX spectra (**Figure C7**) also show Si and Ca contamination, while Cl and S detected could arise from the acid washing steps (2 M HCl and 0.5 M H_2SO_4).

From N_2 sorption (**Figure 6.1b**), TAP 900@Fe900 shows a BET specific surface area of 3,506±48 $m^2\ g^{-1}$, which is even greater than previously reported value for TAP 900 (3,293 $m^2\ g^{-1}$, Chapter 3). This is also significantly higher than other Fe-N-C materials to date (typically 450-1,600 $m^2\ g^{-1}$),[18,39,40] and greater than previous reports based on Mg-templating (1,514-2,780 $m^2\ g^{-1}$).[41–44] No hysteresis is observed across the sorption curve, indicating an open pore structure. Considering the pore size distribution, regions of N_2 adsorption have previously been differentiated into micropores (P/P_0<0.2, <2 nm) in primary carbon particles, mesopores from the void space inside agglomerates (2−20 nm), and meso- and macro-porous void space inside aggregates of agglomerates (>50 nm).[45] TAP 900@Fe900 pore size distribution from the NLDFT 2D heterogeneous surface model (**Figure 6.1c**) is primarily bimodal, centred at pore diameters of 0.6 and 1.9 nm, with significant pore volume across the entire mesopore range. This pore size distribution is similar to previously reported TAP 900 (**Figure 4.2b**),[35] with slightly reduced micropore volume in TAP 900@Fe900 (0.55 versus 0.75 $cm^3\ g^{-1}$, **Figure C8**). Meanwhile a significant increase in the mesopore volume is observed in TAP 900@Fe900 (2.78 versus 1.95 $cm^3\ g^{-1}$, **Figure C8**). These changes are attributed to the collapse of micropores into mesopores during the second pyrolysis. The high total pore volume of TAP 900@Fe900 (3.33 $cm^3\ g^{-1}$) is similar to the Mg-templated approach with adenine initially reported by Fellinger and coworkers (up to 3.86 $cm^3\ g^{-1}$),[41] although adenine led to a tubular carbon structure, while TAP leads to an open carbon structure.

The high mesopore volume is expected to provide a large volume for Nafion accessibility and filling.[46] Considering this point further, Gasteiger and coworkers [47] suggested the amount of Nafion required to fill up that volume can be simply calculated, based on the ionomer density (ρ_{Nafion} = 1.75 g cm^{-3} at 100% relative humidity with Nafion EW 1100,[48] **Equation 6.9**).

$$I/C = \frac{V_{cum} \times \rho_{ionomer}}{x_{carbon}} \qquad \textbf{Equation 6.9}$$

Where V_{cum} is the cumulative pore volume ($cm^3\ g_{Fe\text{-}N\text{-}C}^{-1}$) and $\rho_{ionomer}$ is the density of ionomer (Nafion = 1.75 g cm^{-3} at water content of 15 H_2O/SO_3 [48]). x_{carbon} is assumed ~ 1.

Based on this, a second lefthand y-axis is shown in **Figure 6.1c** which calculates the I/C ratio required to fill pore volumes. On the basis that, micelles of Nafion have shown diameters between 2-20 nm,[11–15] I assume that pore sizes below 2 nm would be inaccessible, as demarcated in **Figure 6.1c**. Nonetheless, an Fe-N-C consisting of shallow micropores in a graphene-like carbon structure could allow Nafion penetration into micropores. To entirely fill the mesopore volume would require an of I/C = 5.3. Of course, complete pore filling would be detrimental to O_2 accessibility and therefore PEMFC performance. Additionally, this calculation does not account for filling the macropores (>50 nm); it does however provide an early indication that a high I/C may be required for TAP 900@Fe900 to sufficiently cover the surface and fill the pores.

Screening the electrochemical activity in O_2-saturated 0.1 M $HClO_4$ in RDE (0.26 $mg_{Fe\text{-}N\text{-}C}$ cm^{-2}, 10 mV s^{-1}), the second pyrolysis in TAP 900@Fe900 leads to an improved O_2 reduction activity (**Figure 6.1d**). The kinetic mass activity is 12.2±1.1 A $g_{Fe\text{-}N\text{-}C}^{-1}$ at 0.8 $V_{RHE,\ iR\text{-}free}$, which is nearly twice that of TAP 900@Fe (6.6±1.7 A $g_{Fe\text{-}N\text{-}C}^{-1}$). The improved performance of TAP 900@Fe900 may be attributed to an increase in FeN_x active site density compared to TAP 900@Fe (discussed later).

Rather than investigating the effect of I/C at RDE level, where performance does not translate directly to PEMFC,[39,49,50] focus is instead made directly on TAP 900@Fe900 in PEMFC

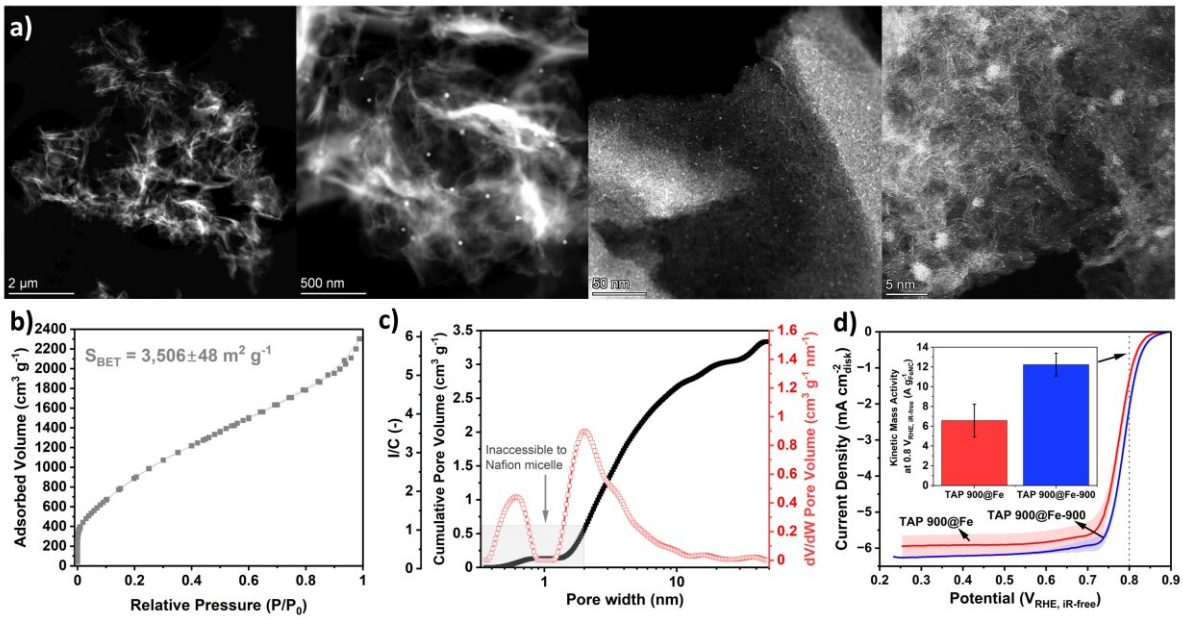


Figure 6.1. TAP 900@Fe900 a.) HAADF-STEM at different length scales showing particle structure, metallic particles, and single metal atoms. b.) N_2 sorption c.) corresponding pore size distribution and

cumulative pore volume from 2D-NLDFT heterogenous surface model. d.) O_2 reduction activity from 3rd cathodic scan in RDE at 1,600 rpm in O_2-saturated 0.1 M $HClO_4$ with 10 mV s^{-1} scan rate and 0.26 $mg_{Fe\text{-}N\text{-}C}$ cm^{-2}. Capacitance correction applied by subtraction of Ar-saturated conditions. Inset of kinetic mass activity, with error in TAP 900@Fe900 representing two repeat measurements.

6.3.2 I/C Ratio

Fe-N-C inks (1:1 wt. ratio of isopropanol:H_2O) with a range of I/C ratios (0.7, 1.4, 2.1, 2.8, 3.5, 4.2 and 4.9) were prepared, where I/C of 0.7 is in the range commonly used for Fe-N-C.[20,38,49,51] I/C was increased until PEMFC performance decreased. It is known that the Nafion morphology can significantly change depending on the catalyst to solvent mass ratio.[9] As I/C increases, the mass ratio of catalyst to total solvent decreases. Unfortunately, this effect cannot be avoided based on the experimental methodology.

6.3.3 SEM and Catalyst Layer Thickness

To prepare the electrodes, inks were ultrasonically spray-coated in an automated fashion. Visual observations of the increasing Nafion loading on freshly spray coated Fe-N-C layers are shown in **Figure 6.2.** It should be noted these layers also include 0.2 mg cm^{-2} Nafion sprayed over the surface of the catalyst layer at the end of spray coating the catalyst. This was to help adhesion of the GDE to the membrane during hot pressing and to minimise electrode-membrane contact resistance.[52,53] It is expected that after hot pressing, the Nafion would distribute throughout the catalyst layer and the Nafion membrane would bound with Fe-N-C layer. At the lowest I/C of 0.7, cracks are present in the catalyst layer, while at I/C = 3.5 Nafion appears to have saturated the catalyst layer, with over saturation becoming even more visibly severe at I/C = 4.9.

While the Fe-N-C loading was maintained at 1.30±0.06 $mg_{Fe\text{-}N\text{-}C}$ cm^{-2} for different I/C ratios, the catalyst coated layer prior to hot pressing shows noticeable changes in thickness (**Figure C9a**). Thickness reduced from 105±3 µm at I/C= 0.7 down to 75±3 µm at I/C=2.8. This is better visualised in **Figure C9b** as an increase in the density of the catalyst layer. This suggests Nafion helps TAP900@Fe900 to better align or stack, up to a I/C ratio of 3.5, where maximum catalyst layer density of 177±5 $mg_{Fe\text{-}N\text{-}C}$ cm^{-3} is found prior to hot pressing. SEM cross-sections at I/C of 3.5 after MEA hot pressing (**Figure C10**) show a reduced thickness (60±5 µm) and consequently increased density of 227±19 $mg_{Fe\text{-}N\text{-}C}$ cm^{-3} (**Figure C9a-b**). This reduction is expected to arise from hot pressing reducing the pore size and volume of TAP 900@Fe900.[54] At I/C≥4.2, Nafion saturation causes a reduction in catalyst layer density (**Figure C9b**).

At I/C=0.7, TAP 900@Fe900 layers show around three times lower density than other Fe-N-C for similar I/C ratios of 0.6-0.7 (**Figure 6.3**a).[38,49,51,55] Commercial Fe-N-C (PMF-011904) shows a catalyst layer density of 385±22 $mg_{Fe\text{-}N\text{-}C}$ cm^{-3} at I/C=0.7, which is approximately equivalent to the recent report by Li *et al*.[55] for the same PMF-011904 and I/C, although deposited by wedge-bar coating. Other Fe-N-C with the similar I/C = 0.6-0.7 show catalyst layer density in a similar range (547-333 $mg_{Fe\text{-}N\text{-}C}$ cm^{-3}), which is comparable to the commonly referenced carbon black density (400 mg_{carbon} cm^{-3}).[56] The low mass density of TAP900@Fe900 (**Figure 3a**) partly arises from its high meso-porosity, with the remaining owing to its disordered structure preventing efficient particle stacking (**Figure 1a**).

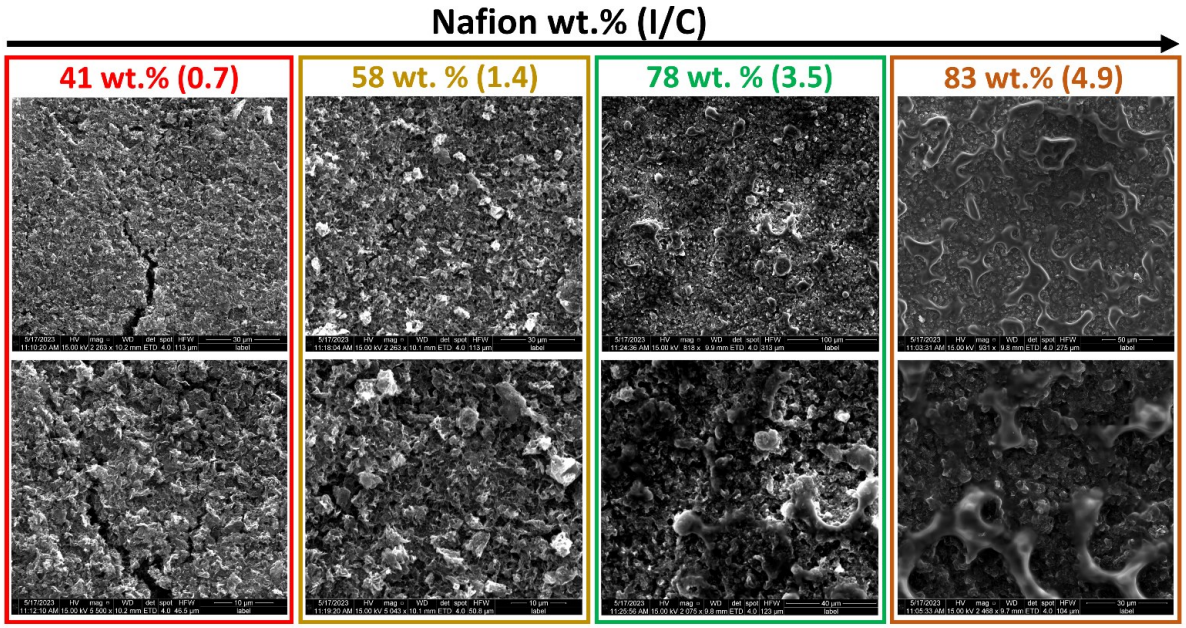


Figure 6.2. SEM images of TAP 900@Fe900 layer (prior to hot pressing) with increasing ratio of I/C.

6.3.4 Void Volume and Carbon Structure

Methods are available to calculate the volume fraction and packing density of spherical particles from weight fractions,[57] or using nano-CT.[9] As discussed by Li *et al.,*[55] catalyst layers consisting of spherical carbon particles with typical Fe-N-C I/C ratios of 0.65-0.80 should possess void volumes in excess of 50%,[8] which can therefore facilitate swelling of ionomer at high relative humidity. They proposed that if I/C increases further, there is increasing possibility of carbon particles becoming electrically isolated, thus lowering the electrode electronic conductivity.[57] However, these void volume calculations and I/C ratios are not applicable to TAP 900@Fe900. This is due to TAP 900@Fe900 exhibiting a highly porous structure with anisotropic arrangement of carbon planes (**Figure 6.1a**) without graphite

diffraction peaks (**Figure C5**), suggesting an atomically thin and/or amorphous carbon framework. The carbon structure in TAP-derived materials has also been determined as atomically thin (~1 layer) from previous Raman analysis.[58] Graphene-based supports as cathodes for PEMFC have previously been investigated,[59] although, to date, they have not shown promise for high performance in electrodes due to graphene stacking, which prevents reactant and product accessbility.[59] Unlike graphene, the structure of TAP 900@Fe900 particles (**Figure 6.1a**) does not appear to support tight stacking of carbon. This indicates that TAP 900@Fe900 can therefore support a large void volume for Nafion infiltration and high I/C in PEMFC, but limited Fe-N-C loading due to low catalyst mass density. The structure and Nafion filling comparison between TAP 900@Fe900, an activated carbon black spherical particle-based and graphene and is schematically shown in **Figure 6.3**b.

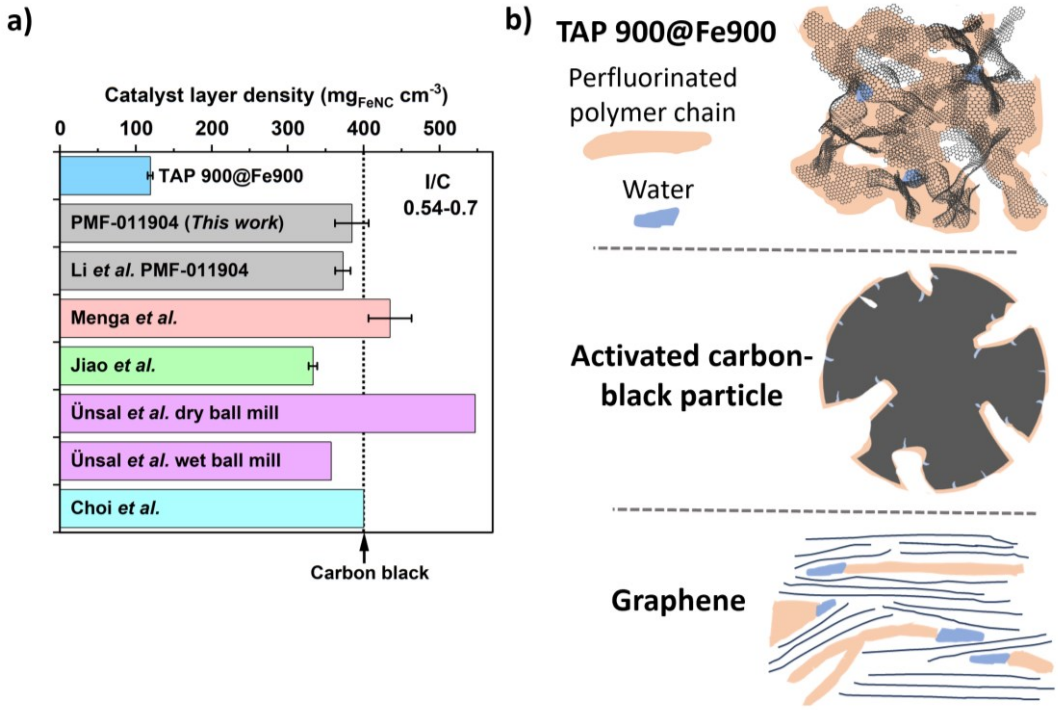


Figure 6.3. Comparison to reported Fe-N-C catalyst layer density values prior to hot pressing for TAP 900@Fe900, Li *et al*.[55] for commercial Fe-N-C PMF-011904 and previously reported Fe-N-C from Menga *et al*.,[60] Ünsal *et al*.[49] dry and wet-ball milled. ZIF-derived Fe-N-C from Jiao *et al*.[61] and polyaniline-derived Fe-N-C of Choi *et al*.[51] Carbon black for reference as horizontal dotted line (400 mg_{carbon} cm^{-3}).[56] b.) Schemes depicting ionomer coverage and structure of activated TAP 900@Fe900, activated carbon black and graphene.

6.3.5 Electronic Conductivity

Ex-situ in-plane four probe measurements (**Figure 6.4**a) of spray-coated TAP900@Fe900 at 0.7≤I/C≤1.4 show the catalyst layer has sufficient electronic conductivity for high current

density in PEMFC (>100 S m^{-1} [62]). Still, at these low I/C values, the electronic conductivity is not particularly high, likely due to a combination of low density and packing fraction (**Figure 6.3**a)[63,64] and high O content (**Table C1**).[65] Meanwhile, at higher I/C, ex-situ in-plane electronic conductivity falls below 100 S m^{-1} and plateaus at 2.7 S m^{-1} for 4.2≤I/C≤4.9. It should be noted an additional layer of Nafion (0.2 mg_{Nafion} cm^{-2}) was sprayed over the surface of the catalyst, which could reduce the measured in-plane electronic conductivity. Under compression in PEMFC the electrical conductivity of carbon will improve, although the through-plane electronic conductivity has been reported to be 8-1,000 times lower than the in-plane.[55,66] It is also noted that the *in-situ* electronic conductivity under 100% relative humidity conditions, as typically employed for Fe-N-C in PEMFC, would be significantly reduced.[57] For instance, *in-situ* Fe-N-C electron conductivity determined by EIS from Reshetenko *et al*. found variation between 10-105 S m^{-1} (**Figure 4a**).[67]

6.3.6 Site Density, Specific Capacitance and Active Site Utilisation

Next, single cell membrane electrode assemblies containing TAP900@Fe900 cathodes (1.31±0.05 $mg_{Fe\text{-}N\text{-}C}$ cm^{-2}) were manufactured by hot pressing. Fully assembled PEMFCs were initially run at 80°C under inert condition (N_2/H_2, 0.3 sccm), with 100% relative humidity. See Methods section for further details. First, analysing cyclic voltammetry (**Figure C10**), the specific capacitance (between 0.2-0.4 V_{anode}) plateaus between 2.1≤I/C≤3.5 (199 to 208 F g^{-1}). Meanwhile, the integrated area of the Fe^{III}/Fe^{II} redox at 0.76 V_{RHE}, which represents the number of high spin FeN_x sites,[20] continues to increase, reaching a maximum of 3.75±0.08×10^{19} sites $g_{Fe\text{-}N\text{-}C}^{-1}$ at I/C of 4.2. At I/C of 4.9, the site density begins to fall. This integrated site density of TAP 900@Fe900 is greater than the previously reported value of TAP 900@Fe from *in situ* nitrite stripping (2.52×10^{19} sites $g_{Fe\text{-}N\text{-}C}^{-1}$, based on five electron nitrite stripping process, Chapter 3), which can contribute to the improved RDE performance (**Figure 6.1**d). Additionally, the total site density in PEMFC may be higher as non-high spin FeN_x sites have been proposed to be redox inactive (and less active).[20]

The FeN_x site density from Fe^{III}/Fe^{II} redox can also be determined from FTacV. In this method, alternating current voltammetry can be used to deconvolute the faradaic and non-faradaic processes[68] and the Fourier transform converts the response in the time domain to the frequency domain, where higher-order harmonics are easily filtered in the power spectrum. The fifth harmonic provided sufficient removal of capacitive contributions, with symmetrical

peaks. The site density can then be obtained from simulations. A recently developed simplified model can be used where capacitance and resistance remain low,[24] however this was not suitable in this work, hence a Matlab modelled was developed.[24]

Site density from FTacV follows a very similar trend and values obtained from direct Fe^{III}/Fe^{II} redox integration from 0.7≤I/C≤4.2 (**Figure 6.4b** and **Figure C11**). However, the FTacV derived active site density shows a significant decrease to 1.23×10^{19} sites $g_{Fe\text{-}N\text{-}C}^{-1}$ at I/C = 4.9. This result appears to an artifact when compared to the integrated Fe^{III}/Fe^{II} redox value at the same I/C ($3.43\pm0.55\times10^{19}$ sites $g_{Fe\text{-}N\text{-}C}^{-1}$). This artefact may either arise from a collapse in the model, which assumes electron conductivity to exceed proton conductivity, and sites are modelled to be in the same plane. At this high I/C, this assumption may no longer be true, as shown by ex-situ electronic conductivity measurements (**Figure 6.4**a). The *in-situ* and through-plane electronic conductivity is likely to be even lower due to ionomer swelling. Also, the poor quality of the experimental FTacV data at I/C = 4.9 may be

The peak active site density corresponds to an active site utilisation (relative to bulk Fe content from ICP-MS, **Equation 4.2**) of 29.2±3.7% (**Figure C12**). This is lower than previously found for TAP 900@Fe (52%). The reduced active site utilisation in TAP900Fe900 likely results from formation of metallic nanoparticles (**Figure 6.1a**), which were not present in TAP900Fe. Also, only high spin $Fe^{III}N_x$ may be counted from Fe^{III}/Fe^{II} redox.[20] Additionally, in the liquid electrolyte RDE environment with thin catalyst layers (from lower loadings, e.g. 0.2 $mg_{Fe\text{-}N\text{-}C}$ cm^{-2}) the active sites are more electrochemically accessible, whereas in PEMFCs, with higher catalyst loading, bulky Nafion micelles may not directly access all FeN_x active sites, since FeN_x have been proposed to be located in water-filled micropores.[69,70] This suggestion comes from the observation that the site density only begins falling at I/C of 4.9 due to a reduction in specific capacitance (**Figure 6.4b**). This specific capacitance reduction suggests loss of electrical contact for some parts of the catalyst layer.

An interesting observation is the well-defined and large Fe^{III}/Fe^{II} redox in PEMFC conditions at 80°C and 25°C, but the complete absence in RDE at 25°C (**Figure C13**). This suggests the microenvironment in RDE inhibits the Fe^{III}/Fe^{II} redox, potentially caused by the electrolyte anion (ClO_4^-) in RDE balancing the charge of high spin $Fe^{III}N_x$ sites. Although, it has been previously calculated ClO_4^- is weakly adsorbing with FeN_x active sites,[71,72] mimicking properties of non-adsorbing perfluoro-sulfonic acid ionomer.[73,74]

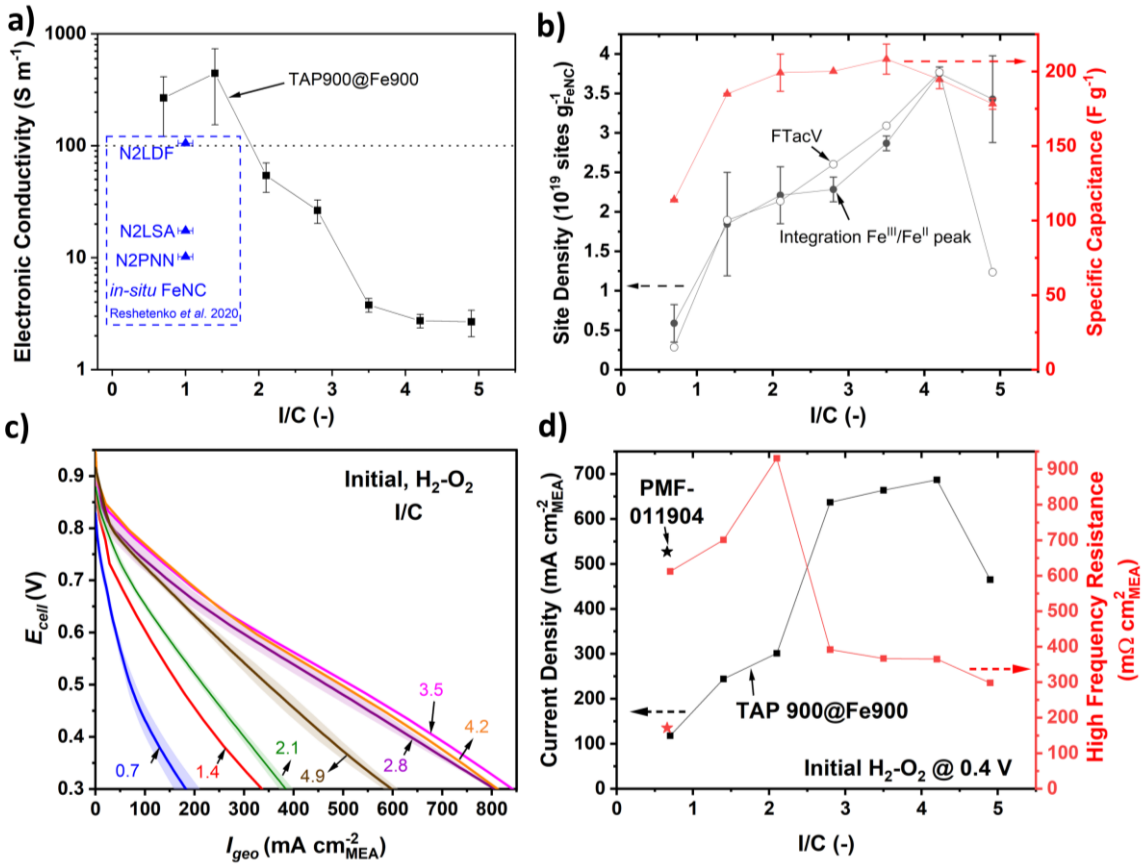


Figure 6.4. Effect of changing I/C ratio with TAP 900@Fe900 on a.) Ex situ four probe electronic conductivity. Error bars represent four repeat measurements. Blue triangles represent Fe-N-C data from Reshetenko *et al.*[67] b.) Change in site density and specific capacitance. Site density calculated based on either FTacV (empty circles) or integration of Fe^{III}/Fe^{II} redox (filled circles) in CVs under N_2/H_2 (0.3 sccm). Specific capacitance based on potential range between 0.2-0.4 $V_{vs\ anode}$. Error bars represent two repeat measurements. c.) Initial H_2-O_2 (0.7/1.7 sccm flow rate) cathodic scan at 1 bar_g back pressure and 80°C. Cathode: 1.31±0.05 $mg_{Fe\text{-}N\text{-}C}$ cm^{-2} on Sigracet BC29. Anode: 0.2 mg_{Pt} cm^{-2} on Sigracet 22BB, with Nafion® 212 membrane. d.) Current density and high frequency resistance after 20 min hold at 0.4 V in H_2/O_2.

6.3.7 PEMFC Performance

After CVs, the varying I/C ratios were tested in PEMFC under H_2/O_2 conditions (**Figure 6.4c**). A clear trend is evident where I/C≤2.1 and I/C≥4.9 display significantly lower performance. Meanwhile the performance at 2.8≤I/C≤4.2 is similar. For I/C = 4.2, at 0.8 $V_{vs\ anode}$ the initial current density of 65 mA cm^{-2} equates to a turnover frequency (TOF) of 9.73±0.07 e^- $site^{-1}$ s^{-1} (**Equation 6.4**). This TOF is nearly five times greater than the reported value of Snitkoff-Sol *et al.* for PMF-011904 in PEMFC (2.10 e^- $site^{-1}$ s^{-1}, also under H_2/O_2, 1 bar_g).[23]

A comparison of initial current density and high frequency resistance (HFR) at 0.4 $V_{vs\ anode}$ is visualised in **Figure 6.4d**. HFR is arises from the proton resistance of the membrane and through-plane electronic resistances, arising from flow fields, GDLs and electrodes, and

contacts between those layers, plus external components (e.g., current leads).[25,55,75] As I/C increased, the current density also increased, up to a maximum of 687 mA cm^{-2} at I/C = 4.2 and then falls significantly at I/C = 4.9 to 465 mA cm^{-2}. This trend in current density follows the trend of active site density (**Figure 6.4b**). Unexpectedly, the HFR increases, up to an excessively high maximum of 931 mΩ cm^{-2} at I/C = 2.1, before falling in the range of 392-298 mΩ cm^2 at higher I/C. These lower HFR values are still far higher than for PMF-011904 (I/C = 0.66) which showed HFR of 171 mΩ cm^2. Since the PEMFC is 1 cm^2, this HFR is still far higher than previously reported HFR values for PMF-011904 (~14-16 mΩ cm^2 – normalised to 1 cm^2 at 2 $mg_{Fe\text{-}N\text{-}C}$ cm^{-2}),[50] suggesting MEA fabrication is contributing to the high HFR here.

Considering instead HFR-free performance (**Figure C14**, **Equation 6.5**), I/C = 2.8 reaches high current densities of 115 mA cm^{-2} and 875 mA cm^{-2} at 0.8 and 0.6 $V_{vs\ anode,\ HFR\text{-}free}$, respectively, for a relatively low Fe-N-C loading of 1.28 $mg_{Fe\text{-}N\text{-}C}$ cm^{-2}. The initial intrinsic TOF of TAP 900@Fe900, based on 0.8 $V_{HFR\text{-}free}$ at I/C = 3.5 equates to 16.6 e^- $site^{-1}$ s^{-1}. These results signify the potential of TAP 900@Fe900 with further PEMFC optimisation.

Although, it should be noted that while the gravimetric site density of TAP 900@Fe900 is reasonably high, the volumetric site density (0.73×10^{19} sites cm^{-3}) would restrict performance in terms of its volumetric activity (19.3 A cm^{-3}). As previously highlighted by Gasteiger *et al.*,[56] volumetric activity is a key PEMFC performance metric for Fe-N-C due to the limited catalyst thickness (~100 μm) before mass transport would become debilitating. Gasteiger *et al.* calculated that a *costless* catalyst would need to reach 130 A cm^{-3} (at 0.8 $V_{ir\text{-}free}$, 1 bar O_2-H_2) to compete with Pt/C. TAP 900@Fe900 is over an order of magnitude below volumetric activity requirements (**Figure 6.5**), similar to other state-of-the-art Fe-N-C (21-45 A cm^{-3}).[2,76,77]

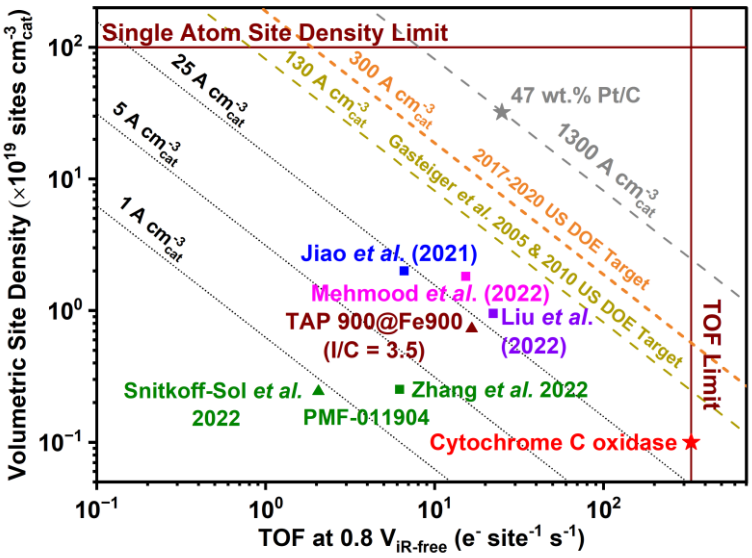


Figure 6.5. Volumetric site density and TOF of TAP 900@Fe900 (I/C = 3.5), state-of-the-art Fe-N-C and targets. See Figure 1.5b for appropriate references of literature and targets.

6.3.8 EIS

To better understand the PEMFC performance trend and areas for optimisation, EIS Nyquist and Bode phase angle plots are shown with HFR compensation in **Figure 6.6**. EIS data without HFR compensation is shown in **Figure C15**. The combination of blocking conditions, in absence of a faradaic reaction (N_2-H_2, **Figure 6.6a**) and the finite thickness of the ionomer film manifests as a shift in the phase angle from 45° to nearly 90° with decreasing frequency for an ideal homogenous catalyst layer.[78] Deviation from the purely capacitive line (90°) at low frequency has been considered to originate from adsorption/diffusion processes at the surface of the catalyst.[79] This can arise from inhomogeneous proton diffusion, low and/or inhomogeneous ionomer coverage and increasing proton resistance down the pore, as observed for I/C 0.7 and 1.4. The impedance response at these I/C matches well with a pore of decreasing Nafion cross-sectional area down the pore.[25,80] This is equivalent to a simple model of an electrolyte-filled pore which shrinks down the pore and therefore increases resistance.[25,80] For I/C between 2.1 and 4.2, a homogeneous ionomer coverage is suggested due to the minor deviation from 90° at low frequency. This pore can be represented as a cylinder due to the uniform ionomer thickness and therefore resistance down the pore.[25,80] Excessively thick ionomer coverage within pores has been likened to a pore with a narrow entry and wide body, leading to impeded gas transport. While these proposed pore models are an oversimplification of the complex structure present in the catalyst layer, they provide a basis to understanding the impedance data. In **Figure 6.6b** and **Figure C16** no clear mass

transport phenomena are observed since EIS were conducted within a low current regime (50-100 mA cm^{-2}).

From Bode plots under blocking conditions (N_2/H_2, **Figure 6.6c**), Kucernak and coworkers previously determined the best performing Fe-N-C displayed phase angle close to 90° in the low frequency region, and then maintained close to 45° phase angle at high frequency.[25] A phase angle below 30° at high frequency was indicative of too high I/C ratio, while deviation below 90° at low frequency indicated too low ionomer content and poor coverage.[25] For TAP 900@Fe900 (**Figure 6.6c**), I/C of 0.7 and 1.4 display angles of 63° and 72° at low frequency, respectively, (0.1 Hz) and 89° and 77° at high frequency (10,000 Hz). This implies too little Nafion at these I/C ratios. Meanwhile, 2.8≤ I/C ≤4.2 show ideal phase angles of 45° at high frequency and 84° at low frequency, suggesting suitable I/C. At higher I/C of 4.9 the phase angle at low frequency falls to 78° while the high frequency is maintained close to 45° (47°). The high frequency response suggests the ionomer coverage is saturated. The reduced phase angle at low frequency could arise from the reduced electrode capacitance (**Figure 6.4b**), which dominates the response there. The transmission line model used by Kucernak and coworkers did not account for electronic conductivity,[25] which has recently been confirmed as significant in thick Fe-N-C layers,[55] and certainly affects performance in TAP 900@Fe900 (**Figure 6.4a**).

It should be considered that EIS was performed under galvanostatic conditions, where the overpotential to reach 50 and 100 mA cm^{-2} significantly varies for the I/C range (**Figure 6.4c**).

From these results it appears the cumulative mesopore pore size volume from N_2 sorption (**Figure 1c**) can serve as a suitable method to provide an initial starting point for I/C loading.

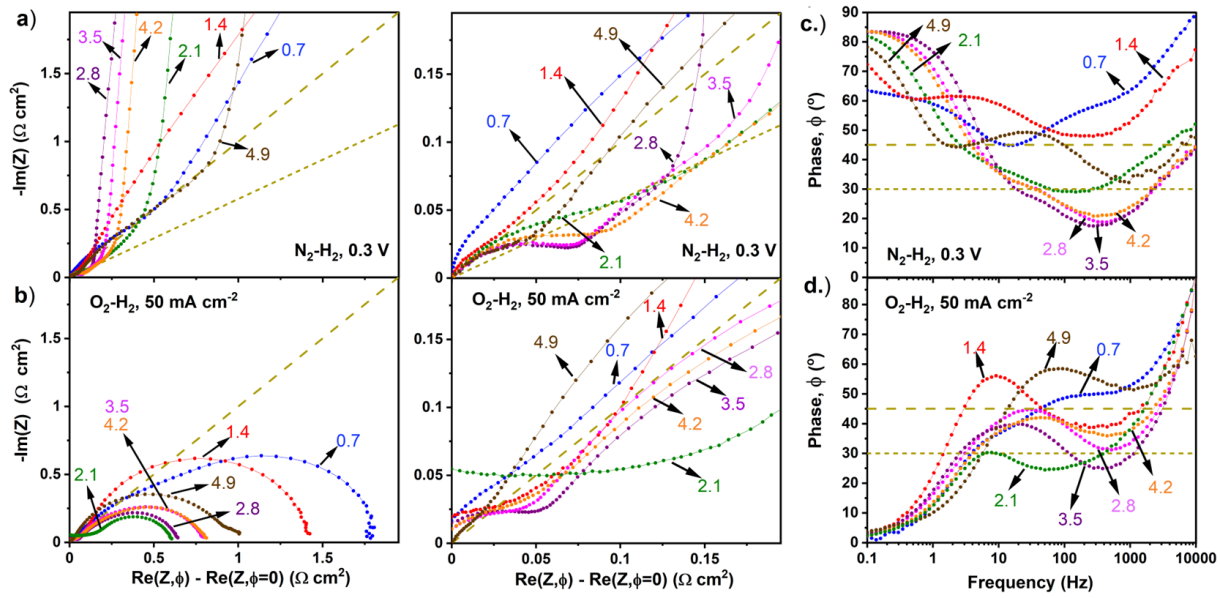


Figure 6.6. Nyquist plots at different I/C ratios under a.) N_2-H_2 at 0.3 $V_{vs\ anode}$ with middle panel: magnified axis. c.) O_2-H_2 at 50 mA cm^{-2} with middle panel: magnified axis. High frequency resistance was compensated for (removal of Re(Z,ϕ=0)). Bode phase angle plots under c.) N_2-H_2 at 0.3 $V_{vs\ anode}$ (0.3 sccm) and d.) O_2-H_2 (0.7 and 1.7 sccm) at 50 mA cm^{-2}. Long and short dashed lines represent 45° and 30° phase angle lines, respectively. EIS from 200,000–0.1 kHz with 20 points per decade and perturbation amplitude of 10 mV.

6.3.9 DRT

To further understand EIS results, DRT analysis was performed. In short, the impedance can be described by **Equation 6.6**, which represents the total cell impedance as an infinite sum of in series connected parallel resistance-capacitance circuits with a characteristic relaxation time corresponding to the electrochemical process occurring. DRT enables a much clearer representation of the electrochemical process occurring than the Nyquist plot and does not require complex modeling of the system to accurately quantify the resistance of such processes.[27] Each process was assigned to a specific peak in **Figure C17** and the resistance calculated by integrating the area under each peak. 4 distinct peaks were identified as follows: P1 in the low frequency region corresponding to O_2 diffusion, P2 at the medium frequency corresponding to ORR, and P3 & P4 at the high frequency region corresponding to H^+ transport through the catalytic layer and through the membrane, respectively.[26,81] This led to **Figure 6.7a-b**, which shows resistance to O_2 reduction and diffusion, plus H^+ resistance in the membrane and catalyst layer at 50 and 100 mA cm^{-2} (H_2/O_2).

As expected, proton resistance from the membrane is relatively consistent across the I/C ratios, except for I/C = 2.1 where there is a noticeable increase. This falls in line with observations from EIS of higher ohmic resistance (**Figure C15**) and increased HFR (**Figure**

6.4d). Again, this is ascribed to a MEA manufacturing fault which appears to be reproducible in performance.

At 50 mA cm^{-2}, proton resistance in the catalyst layer appears significantly higher at I/C = 0.7 (0.4 Ω) than at higher I/C values, which range from 0.09 - 0.03 Ω. From the modelling of Jaouen *et al.* (see Electronic Conductivity), they also found H^+ conductivity of 5 S m^{-1} would be required for high current density.[62] From the DRT derived proton resistance, the H^+ conductivity can be calculated (**Figure C18**). It appears H^+ conductivity in the catalyst layer should not limit the PEMFC performance at high current density as values are >5 S m^{-1} for I/C≥ 1.4.

The amount of pore infiltration by ionomer will increase the gas transport resistance, especially at high relative humidity (100% used here) where ionomer swells.[9] Here, EIS was not measured under H_2/Air or at high current density, where O_2 mass transport limitations would be more prevalent. Still, from DRT it can be resolved that O_2 diffusion resistance increases at I/C = 4.9 even at low current densities considered (50-100 mA cm^{-2}, **Figure 6.7**). This in turn contributes to the increased resistance to O_2 reduction kinetics, due to limited O_2 supply.

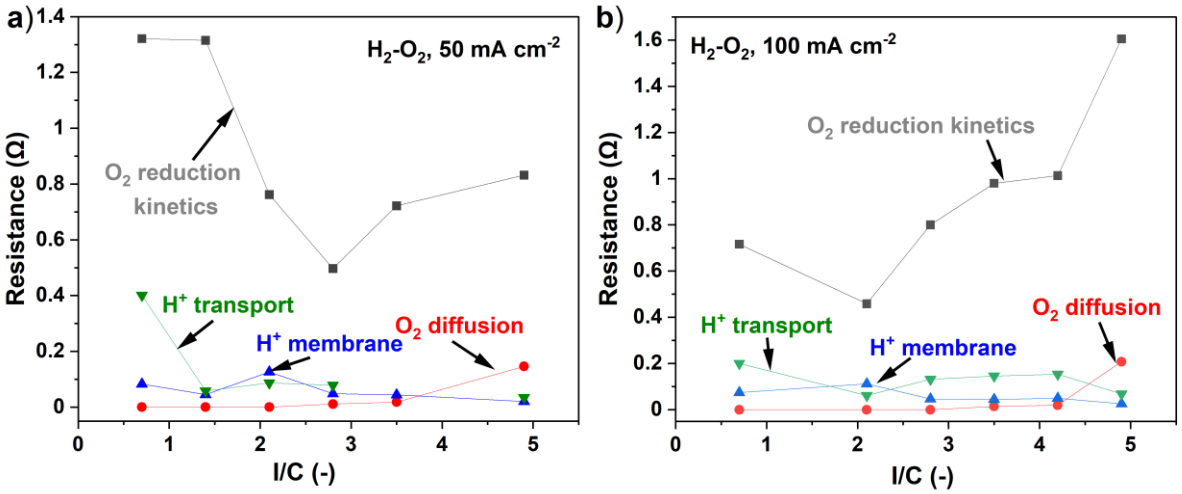


Figure 6.7. DRT analysis under H_2/O_2 at a.) 50 mA cm^{-2} b.) 100 mA cm^{-2}.

6.4 Conclusion

The PEMFC performance of a novel Fe-N-C with high porosity and surface area was evaluated. I show how the I/C needs to be tailored to the porosity of the Fe-N-C, where the mesopore volume from N_2 sorption can provide a reasonable initial I/C value. By resolving the contributions of different electrochemical factors using *in-situ* EIS, DRT, and FTacV, I show for the first time, there is a trade-off between the increasing accessible active site density and increasing the O_2 diffusion resistance and electronic resistivity. At too low ionomer loading (I/C≤2.1) the ionomer does not homogenously cover the catalyst surface, therefore active sites within pores are not ionically accessible and thus not utilised. Under optimal I/C loading in HFR-free conditions at 0.8 V, TAP 900@Fe900 presents similar initial volumetric activity to recent state-of-the-art Fe-N-C (19 vs. 21-45 A cm^{-3}). Meanwhile, at too high ionomer loading (I/C≥4.9) the ionomer saturates pores, which restrict O_2 access and causes electrical isolation of particles, thus leading to detrimental performance. These findings provide a new pathway to accelerated optimisation of highly porous Fe-N-C cathodes in PEMFCs using emerging electrochemical techniques.

References

1 A. Mehmood, M. Gong, F. Jaouen, A. Roy, A. Zitolo, A. Khan, M. Sougrati, M. Primbs, A. M. Bonastre, D. Fongalland, G. Drazic, P. Strasser and A. Kucernak, *Nat. Catal.*, 2022, **5**, 311–323.

2 S. Liu, C. Li, M. J. Zachman, Y. Zeng, H. Yu, B. Li, M. Wang, J. Braaten, J. Liu, H. M. Meyer, M. Lucero, A. J. Kropf, E. E. Alp, Q. Gong, Q. Shi, Z. Feng, H. Xu, G. Wang, D. J. Myers, J. Xie, D. A. Cullen, S. Litster and G. Wu, *Nat. Energy*, 2022, **7**, 652–663.

3 L. Osmieri and Q. Meyer, *Curr. Opin. Electrochem.*, 2022, **31**, 1–9.

4 T. A. M. Suter, K. Smith, J. Hack, L. Rasha, Z. Rana, G. M. A. Angel, P. R. Shearing, T. S. Miller and D. J. L. Brett, *Adv. Energy Mater.*, 2021, **11**, 2101025.

5 A. B. Jorge, R. Jervis, A. P. Periasamy, M. Qiao, J. Feng, L. N. Tran and M.-M. Titirici, *Adv. Energy Mater.*, 2020, **10**, 1902494.

6 Y. Wang, M. J. Larsen, S. Rojas, M.-T. Sougrati, F. Jaouen, P. Ferrer, D. Gianolio and S. Berthon-Fabry, *J. Power Sources*, 2021, **514**, 230561.

7 T. Asset, F. Maillard and F. Jaouen, in *Supported Metal Single Atom Catalysis*, eds. P. Serp and D. P. Minh, Wiley, 2022, pp. 531–582.

8 W. Gu, D. R. Baker, Y. Liu and H. A. Gasteiger, in *Handbook of fuel cells*, John Wiley & Sons, Ltd. Chichester, 2010.

9 S. Komini Babu, H. T. Chung, P. Zelenay and S. Litster, *ACS Appl. Mater. Interfaces*, 2016, **8**, 32764–32777.

10 A. Ignaszak, S. Ye and E. Gyenge, *J. Phys. Chem. C*, 2009, **113**, 298–307.

11 R. Hiesgen, D. Eberhardt, E. Aleksandrova and K. A. Friedrich, *Fuel Cells*, 2006, **6**, 425–431.

12 D. B. Spry, A. Goun, K. Glusac, D. E. Moilanen and M. D. Fayer, *J. Am. Chem. Soc.*, 2007, **129**, 8122–8130.

13 T. D. Gierke, G. E. Munn and F. C. Wilson, *J. Polym. Sci. Polym. Phys. Ed.*, 1981, **19**, 1687–1704.

14 H. Uchida, J. M. Song, S. Suzuki, E. Nakazawa, N. Baba and M. Watanabe, *J. Phys. Chem. B*, 2006, **110**, 13319–13321.

15 K. A. Mauritz and R. B. Moore, *Chem. Rev.*, 2004, **104**, 4535–4586.

16 K. Artyushkova, M. J. Workman, I. Matanovic, M. J. Dzara, C. Ngo, S. Pylypenko, A. Serov and P. Atanassov, *ACS Appl. Energy Mater.*, 2018, **1**, 68–77.

17 E. Passalacqua, F. Lufrano, G. Squadrito, A. Patti and L. Giorgi, *Electrochimica Acta*, 2001, **46**, 799–805.

18 M. Primbs, Y. Sun, A. Roy, D. Malko, A. Mehmood, M.-T. Sougrati, P.-Y. Blanchard, G. Granozzi, T. Kosmala, G. Daniel, P. Atanassov, J. Sharman, C. Durante, A. Kucernak, D. Jones, F. Jaouen and P. Strasser, *Energy Environ. Sci.*, 2020, **13**, 2480–2500.

19 Q. Jia, N. Ramaswamy, H. Hafiz, U. Tylus, K. Strickland, G. Wu, B. Barbiellini, A. Bansil, E. F. Holby, P. Zelenay and S. Mukerjee, *ACS Nano*, 2015, **9**, 12496–12505.

20 J. Li, M. T. Sougrati, A. Zitolo, J. M. Ablett, I. C. Oğuz, T. Mineva, I. Matanovic, P. Atanassov, Y. Huang, I. Zenyuk, A. Di Cicco, K. Kumar, L. Dubau, F. Maillard, G. Dražić and F. Jaouen, *Nat. Catal.*, 2021, **4**, 10–19.

21 L. Osmieri, R. K. Ahluwalia, X. Wang, H. T. Chung, X. Yin, A. J. Kropf, J. Park, D. A. Cullen, K. L. More, P. Zelenay, D. J. Myers and K. C. Neyerlin, *Appl. Catal. B Environ.*, 2019, **257**, 117929.

22 K. Kinoshita and J. A. S. Bett, *Carbon*, 1973, **11**, 403–411.

23 R. Z. Snitkoff-Sol, A. Friedman, H. C. Honig, Y. Yurko, A. Kozhushner, M. J. Zachman, P. Zelenay, A. M. Bond and L. Elbaz, *Nat. Catal.*, 2022, **5**, 163–170.

24 A. Friedman, R. Z. Snitkoff-Sol, H. C. Honig and L. Elbaz, *Electrochimica Acta*, 2023, **463**, 142865.
25 D. Malko, T. Lopes, E. A. Ticianelli and A. Kucernak, *J. Power Sources*, 2016, **323**, 189–200.
26 M. Heinzmann, A. Weber and E. Ivers-Tiffée, *J. Power Sources*, 2018, **402**, 24–33.
27 S. Liu, Q. Meyer, C. Jia, S. Wang, C. Rong, Y. Nie and C. Zhao, *Energy Environ. Sci.*, 2023, **16**, 3792–3802.
28 Q. Meyer, S. Liu, Y. Li and C. Zhao, *J. Power Sources*, 2022, **533**, 231058.
29 M. Schönleber, D. Klotz and E. Ivers-Tiffée, *Electrochimica Acta*, 2014, **131**, 20–27.
30 F. Ciucci and C. Chen, *Electrochimica Acta*, 2015, **167**, 439–454.
31 Y. Yurko and L. Elbaz, *Electrochimica Acta*, 2023, **463**, 142877.
32 O. Marciano, S. Gonen, N. Levy, E. Teblum, R. Yemini, G. D. Nessim, S. Ruthstein and L. Elbaz, *Langmuir*, 2016, **32**, 11672–11680.
33 L. Elbaz, C. R. Kreller, N. J. Henson and E. L. Brosha, *J. Electroanal. Chem.*, 2014, **720–721**, 34–40.
34 F. M. Smits, *Bell Syst. Tech. J.*, 1958, **37**, 711–718.
35 J. Barrio, A. Pedersen, S. Ch. Sarma, A. Bagger, M. Gong, S. Favero, C. Zhao, R. Garcia-Serres, A. Y. Li, Q. Zhang, F. Jaouen, F. Maillard, A. Kucernak, I. E. L. Stephens and M. Titirici, *Adv. Mater.*, 2023, **35**, 2211022.
36 V. G. Chandrashekhar, T. Senthamarai, R. G. Kadam, O. Malina, J. Kašlík, R. Zbořil, M. B. Gawande, R. V. Jagadeesh and M. Beller, *Nat. Catal.*, 2022, **5**, 20–29.
37 K. T. Santos, K. Kumar, L. Dubau, H. Ge, S. Berthon-Fabry, C. S. A. Vasconcellos, F. H. B. Lima, T. Asset, P. Atanassov, V. A. Saveleva, P. Glatzel, X. Li, F. Jaouen and F. Maillard, *J. Power Sources*, 2023, **564**, 232829.
38 D. Menga, J. L. Low, Y.-S. Li, I. Arčon, B. Koyutürk, F. Wagner, F. Ruiz-Zepeda, M. Gaberšček, B. Paulus and T.-P. Fellinger, *J. Am. Chem. Soc.*, 2021, **143**, 18010–18019.
39 F. Jaouen, V. Goellner, M. Lefèvre, J. Herranz, E. Proietti and J. P. Dodelet, *Electrochimica Acta*, 2013, **87**, 619–628.
40 H. Ge, N. Bibent, K. Teixeira Santos, K. Kumar, J. Jaxel, M.-T. Sougrati, A. Zitolo, M. Dupont, F. Lecoeur, M. Mermoux, V. Martin, L. Dubau, F. Jaouen, F. Maillard and S. Berthon-Fabry, *ACS Catal.*, 2023, **13**, 1149–1163.
41 J. Pampel, A. Mehmood, M. Antonietti and T.-P. Fellinger, *Mater. Horiz.*, 2017, **4**, 493–501.
42 J.-C. Li, Y. Meng, R. Ma, H. Hu, S. Zhao, Y. Zhu, P.-X. Hou and C. Liu, *ACS Appl. Mater. Interfaces*, 2021, **13**, 58576–58584.
43 J. Barrio, A. Pedersen, J. Feng, S. Ch. Sarma, M. Wang, A. Y. Li, H. Yadegari, H. Luo, M. P. Ryan, M.-M. Titirici and Ifan. E. L. Stephens, *J. Mater. Chem. A*, 2022, **10**, 6023–6030.
44 A. Mehmood, G. Ali, B. Koyutürk, J. Pampel, K. Y. Chung and T.-P. Fellinger, *Energy Storage Mater.*, 2020, **28**, 101–111.
45 T. Soboleva, X. Zhao, K. Malek, Z. Xie, T. Navessin and S. Holdcroft, *ACS Appl. Mater. Interfaces*, 2010, **2**, 375–384.
46 E. Antolini, *Appl. Catal. B Environ.*, 2009, **88**, 1–24.
47 Y. Liu, C. Ji, W. Gu, J. Jorne and H. A. Gasteiger, *J. Electrochem. Soc.*, 2011, **158**, B614.
48 A. Kusoglu and A. Z. Weber, *Chem. Rev.*, 2017, **117**, 987–1104.
49 S. Ünsal, M. Bozzetti, Y.-C. Chen, R. Girod, A. Berger, J. S. Diercks, S. Gialamoidou, J. Lyu, M. Medarde, H. A. Gasteiger, V. Tileli, T. J. Schmidt and J. Herranz, *J. Electrochem. Soc.*, 2023, **170**, 074502.
50 A. M. Damjanović, B. Koyutürk, Y.-S. Li, D. Menga, C. Eickes, H. A. El-Sayed, H. A. Gasteiger, T.-P. Fellinger and M. Piana, *J. Electrochem. Soc.*, 2021, **168**, 114518.

51 J.-Y. Choi, L. Yang, T. Kishimoto, X. Fu, S. Ye, Z. Chen and D. Banham, *Energy Environ. Sci.*, 2017, **10**, 296–305.
52 S. A. Mauger, J. R. Pfeilsticker, M. Wang, S. Medina, A. C. Yang-Neyerlin, K. C. Neyerlin, C. Stetson, S. Pylypenko and M. Ulsh, *J. Power Sources*, 2020, **450**, 227581.
53 S. Shahgaldi, I. Alaefour and X. Li, *Appl. Energy*, 2018, **225**, 1022–1032.
54 T. Suzuki, H. Tanaka, M. Hayase, S. Tsushima and S. Hirai, *Int. J. Hydrog. Energy*, 2016, **41**, 20326–20335.
55 Y.-S. Li, D. Menga, H. A. Gasteiger and B. Suthar, *J. Electrochem. Soc.*, 2023, **170**, 094503.
56 H. A. Gasteiger, S. S. Kocha, B. Sompalli and F. T. Wagner, *Appl. Catal. B Environ.*, 2005, **56**, 9–35.
57 D. R. P. Morris, S. P. Liu, D. Villegas Gonzalez and J. T. Gostick, *ACS Appl. Mater. Interfaces*, 2014, **6**, 18609–18618.
58 S. C. Sarma, J. Barrio, A. Bagger, A. Pedersen, M. Gong, H. Luo, M. Wang, S. Favero, C. Zhao, Q. Zhang, A. Kucernak, M. Titirici and I. E. L. Stephens, *Adv. Funct. Mater.*, 2023, 2302468.
59 T. A. M. Suter, A. J. Clancy, N. Rubio Carrero, M. Heitzmann, L. Guetaz, P. R. Shearing, C. Mattevi, G. Gebel, C. A. Howard, M. S. P. Shaffer, P. F. McMillan and D. J. L. Brett, *Nanomaterials*, 2021, **11**, 2530.
60 D. Menga, F. Ruiz-Zepeda, L. Moriau, M. Šala, F. Wagner, B. Koyutürk, M. Bele, U. Petek, N. Hodnik, M. Gaberšček and T. Fellinger, *Adv. Energy Mater.*, 2019, **9**, 1902412.
61 L. Jiao, J. Li, L. L. Richard, Q. Sun, T. Stracensky, E. Liu, M. T. Sougrati, Z. Zhao, F. Yang, S. Zhong, H. Xu, S. Mukerjee, Y. Huang, D. A. Cullen, J. H. Park, M. Ferrandon, D. J. Myers, F. Jaouen and Q. Jia, *Nat. Mater.*, 2021, **20**, 1385–1391.
62 F. Jaouen, E. Proietti, M. Lefèvre, R. Chenitz, J.-P. Dodelet, G. Wu, H. Taek Chung, C. Marie Johnston and P. Zelenay, *Energy Environ. Sci.*, 2011, **4**, 114–130.
63 D. Pantea, H. Darmstadt, S. Kaliaguine and C. Roy, *Appl. Surf. Sci.*, 2003, **217**, 181–193.
64 B. Marinho, M. Ghislandi, E. Tkalya, C. E. Koning and G. de With, *Powder Technol.*, 2012, **221**, 351–358.
65 D. Pantea, H. Darmstadt, S. Kaliaguine, L. Sümmchen and C. Roy, *Carbon*, 2001, **39**, 1147–1158.
66 M. Ahadi, M. Tam, J. Stumper and M. Bahrami, *Int. J. Hydrog. Energy*, 2019, **44**, 3603–3614.
67 T. Reshetenko, A. Serov, M. Odgaard, G. Randolf, L. Osmieri and A. Kulikovsky, *Electrochem. Commun.*, 2020, **118**, 106795.
68 A. Bard and L. Faulkner, *Electrochemical Methods: Fundamentals and Applications*, John Wiley & Sons, New York, 2001.
69 F. Jaouen, M. Lefèvre, J.-P. Dodelet and M. Cai, *J. Phys. Chem. B*, 2006, **110**, 5553–5558.
70 R. Chenitz, U. I. Kramm, M. Lefèvre, V. Glibin, G. Zhang, S. Sun and J.-P. Dodelet, *Energy Environ. Sci.*, 2018, **11**, 365–382.
71 K. Holst-Olesen, M. Reda, H. A. Hansen, T. Vegge and M. Arenz, *ACS Catal.*, 2018, **8**, 7104–7112.
72 X. Wang, M. Ferrandon, J. H. Park, J.-J. Shen, A. J. Kropf, H. Zhang, P. Zelenay and D. J. Myers, *Electrochimica Acta*, 2023, **443**, 141934.
73 U. A. Paulus, T. J. Schmidt, H. A. Gasteiger and R. J. Behm, *J. Electroanal. Chem.*, 2001, **495**, 134–145.
74 M. Ferrandon, X. Wang, A. J. Kropf, D. J. Myers, G. Wu, C. M. Johnston and P. Zelenay, *Electrochimica Acta*, 2013, **110**, 282–291.
75 Y. Liu, M. Murphy, D. Baker, W. Gu, C. Ji, J. Jorne and H. A. Gasteiger, *ECS Trans.*, 2007, **11**, 473.

76 A. Mehmood, M. Gong, F. Jaouen, A. Roy, A. Zitolo, A. Khan, M. Sougrati, M. Primbs, A. M. Bonastre, D. Fongalland, G. Drazic, P. Strasser and A. Kucernak, *Nat. Catal.*, 2022, **5**, 311–323.
77 L. Jiao, J. Li, L. L. Richard, Q. Sun, T. Stracensky, E. Liu, M. T. Sougrati, Z. Zhao, F. Yang, S. Zhong, H. Xu, S. Mukerjee, Y. Huang, D. A. Cullen, J. H. Park, M. Ferrandon, D. J. Myers, F. Jaouen and Q. Jia, *Nat. Mater.*, 2021, **20**, 1385–1391.
78 A. Ch. Lazanas and M. I. Prodromidis, *ACS Meas. Sci. Au*, 2023, **3**, 162–193.
79 E. M. Davis, C. M. Stafford and K. A. Page, *ACS Macro Lett.*, 2014, **3**, 1029–1035.
80 H. Keiser, K. D. Beccu and M. A. Gutjahr, *Electrochimica Acta*, 1976, **21**, 539–543.
81 G. Avioz Cohen, D. Gelman and Y. Tsur, *J. Phys. Chem. C*, 2021, **125**, 11867–11874.

Chapter 7: Comparative techno-economic and life-cycle analysis of Pt/C versus Fe-N-C

7.1 Introduction

Forecasts suggest that Pt-based cathode catalysts are anticipated to constitute the most significant individual cost component of an 80 kW PEMFC stack, especially at a production rate of 500,000 stacks per year.[1] The fluctuating prices of Pt and the subsequent sensitivity of catalyst costs are also poised to significantly impact fuel cell expenses, thereby posing challenges for wider-scale commercialization.[2] South Africa and Russia collectively contributed a substantial portion of the world's Pt supply between 2017 and 2021, with South Africa accounting for 65–74% and Russia for 10–14%.[3] Additionally, the current industrial recycling of Pt remains limited, with the total recycling rate being less than 30%, and in the automotive sector, it is below 55%.[3,4] This heavy reliance on fresh Pt supplies is unfavourable due to its dependence on global supply chains and trade agreements. Therefore, in the UK and EU, Pt is classified as a critical raw material owing to its substantial global supply risk and economic susceptibility.[4,5]

Efforts in research have been focused on finding alternatives to Pt for the PEMFC cathode, primarily aiming to reduce the costs of PEMFC systems to meet the 30 USD kW^{-1} target outlined by the US Department of Energy (DOE).[1,6] Recent advancements have significantly enhanced the activity and stability of Fe-N-C catalysts in PEMFCs.[7] However, the current state-of-the-art synthesis of Fe-N-C typically involves multiple steps, often requiring two energy-intensive pyrolysis stages. Although simpler and scalable approaches to single-atom Fe-N-C synthesis exist, these methods generally compromise the ORR activity.[8,9] Several companies, including Pajarito Powder, LLC (USA),[10,11] Nisshinbo Holdings Inc. (Japan),[12,13] and more recently, Celcibus AB (Sweden),[14] have made substantial investments in the commercial development of Fe-N-C catalysts. Pajarito Powder recently showcased initial performance results in H_2-air PEMFCs using their Fe-N-C cathode catalyst, demonstrating comparable performance to commercial Pt/C and nearly reaching US DOE durability targets (60–119 mV vs. 30 mV loss target at 0.8 A cm^{-2} after 30,000 cycles between open circuit potential and 0.6 V).[10]

As the technology readiness level and performance of Fe-N-C catalysts continue to advance, it becomes crucial to evaluate their environmental impact and commercial feasibility in comparison to Pt-based catalysts. This evaluation can be effectively conducted through life-cycle assessments (LCA) and techno-economic analyses (TEA). While both LCA and TEA have been implemented in assessing PEMFCs, including some examinations of critical materials,[15] there has been a restricted emphasis on the assessment of Pt-based electrocatalysts.[16]

Stropnik et al. have approximated that a mere 0.75 g of Pt contributes approximately 60% of the overall environmental impact during the production of a 1 kW PEMFC system.[17] This finding aligns with the understanding that Pt production leads to the emission of around 10,000 kg CO_2-eq kg^{-1}, in stark contrast to the emission of only about 1 kg CO_2-eq kg^{-1} during Fe production.[18] Subsequently, Stropnik and colleagues discovered, in an optimistic scenario for a 48 kW PEMFC stack, that the impact on climate change could potentially decrease by 54% if 95% of the Pt were to be recycled.[19] The feasibility of using recycled Pt in PEMFCs has already been demonstrated,[20] and reports from the EU suggest that about 76% of Pt in end-of-life PEMFCs can already be recovered using laboratory-scale processes.[21,22]

A recent EU report, which compared a carbon nanotube-based Fe-N-C and Pt/C cathode catalyst, indicated that the global warming potential (GWP), human toxicity, abiotic depletion, and eutrophication impacts of Fe-N-C might surpass those of Pt/C.[23] Additionally, the report highlighted that the fluorine-containing Nafion™ membrane and ionomer could be the dominant components responsible for environmental impacts in systems with comparable performance.[23] However, developments in alternative membranes, such as Pemion™, have emerged, aiming to address environmental concerns related to per- and polyfluoroalkyl substances, which could potentially face a ban in the EU in the near future.

Gasteiger et al. determined in 2005 that for a cost-free Pt-free cathode catalyst to be economically feasible in a PEMFC, it would need to exhibit at least 10% of the activity of Pt under equivalent conditions.[24] Although Fe-N-C catalysts have achieved this milestone, one must also consider the material and manufacturing costs associated with these catalysts. A techno-economic analysis conducted in 2015, comparing a polyaniline-based Fe-N-C catalyst with a low material cost ranging from 74 to 129 USD kg^{-1} to a specialized Pt-based alloy catalyst priced at approximately 41,000 USD kg^{-1}, concluded that the Fe-N-C catalyst would require an enhancement in power density from 330 mW cm^{-2} to 475 mW cm^{-2} at 0.5 V to

compete with the Pt-based catalyst, although this assessment was solely based on material costs.[25] Furthermore, to the best of my knowledge, the environmental life cycle impacts of Fe-N-C catalyst production have not been quantified yet, and there has been a lack of comparative analysis regarding the environmental impacts of Pt/C and Fe-N-C electrocatalysts in a PEMFC cathode.

In this chapter, I present a comprehensive analysis that compares the techno-economic and environmental aspects of substituting Pt/C electrocatalysts with Fe-N-C electrocatalysts for O_2 reduction in an 80 kW PEMFC stack. The analysis primarily focuses on the initial ORR activity while disregarding degradation. A cradle-to-gate life cycle assessment (LCA), encompassing the consideration of critical process uncertainties and their impacts in a sensitivity analysis was conducted. Additionally, a spectrum of potential future scenarios are evaluated. Furthermore, a detailed cost analysis of both catalysts, considering a large-scale deployment scenario entailing the production of 500,000 PEMFC stacks annually was explored. This cost analysis is carried out using a dynamic learning curve method, which allows understanding of the potential cost implications with increased production.

7.2 Experimental

7.2.1 Life Cycle Analysis

The focus on the cathode electrocatalyst, as illustrated in **Figure 7.1a**, is driven by its significant impact on PEMFC efficiency, cost, lifetime, and environmental footprint. Given the ongoing efforts to replace Pt-based cathode catalysts, a thorough comparison between the two electrocatalysts is imperative. It's worth noting that the comparison is made on a dry basis, thereby excluding both the ionomer and inks used for depositing catalysts in the LCA.

For the assessment, OpenLCA 1.11 is employed, along with the ecoinvent 3.6 database.[26] The LCA process adheres to the four phases outlined in the ISO standards (14040:2006 and 14044:2006/AMD 2:2020), encompassing the following stages: (1) Goal and scope definition, (2) Inventory analysis, (3) Impact assessment, (4) Interpretation.[27]

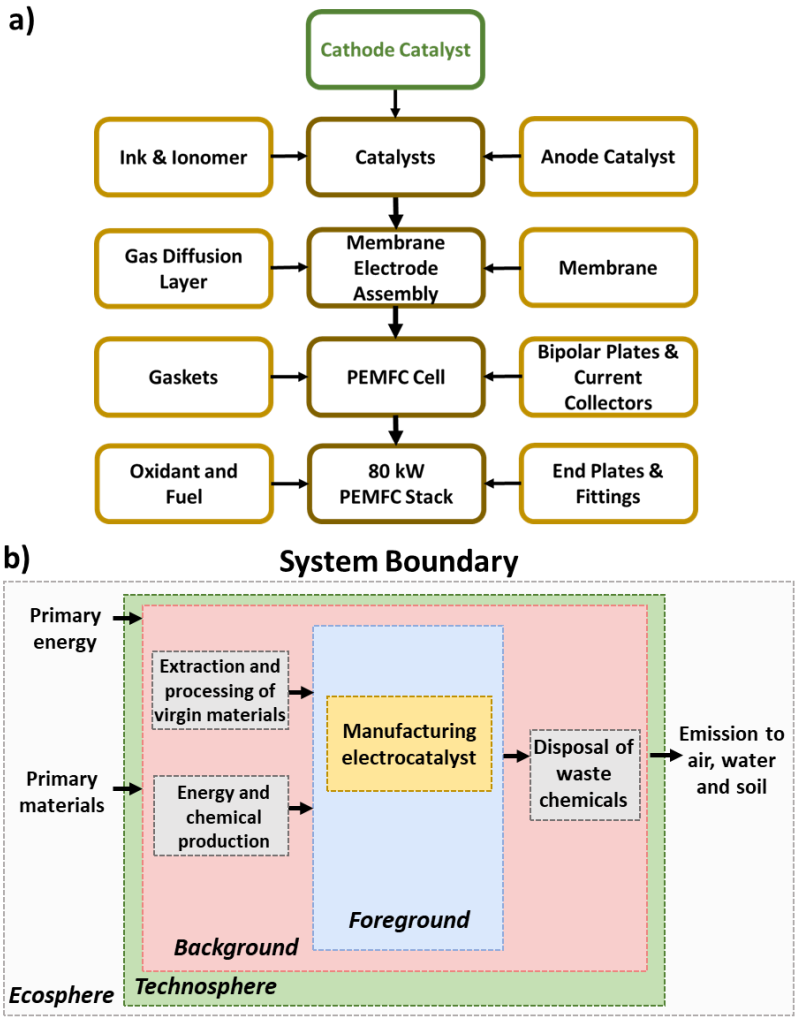


Figure 7.1. a.) PEMFC stack component hierarchy, with highlighted focus on the cathode catalyst. b) System boundary of the PEMFC cathode electrocatalyst LCA. Reproduced from ref [28] under Creative Commons CC BY 3.0.

7.2.2 Goal and Scope

The primary objective of the LCA is to conduct a comprehensive comparison of the environmental impacts associated with the manufacturing phase of Pt/C and Fe-N-C cathode electrocatalysts in the context of an 80 kW PEMFC stack intended for light-duty vehicle applications. This evaluation is designed to aid stakeholders and policymakers in making informed decisions regarding future investments in PEMFC cathode catalyst development, while also providing essential insights to the research community and the general public.

In the baseline scenario, the geographical location is set at the global level, allowing for a comprehensive analysis of the environmental impacts of both Pt/C and Fe-N-C electrocatalysts. Adopting a cradle-to-gate scope for the LCA (as shown in **Figure 7.1b**), all processes from raw material extraction to electrocatalyst production are considered, without requiring any allocation since Pt/C and Fe-N-C are the sole products under consideration.

To establish a common ground for comparison, the use phase of the electrocatalysts is factored in by setting the functional unit as the mass of cathode catalyst (in grams) necessary for a PEMFC stack to deliver an 80-kW power output at 0.657 V. The impact of the electrocatalyst amount is accounted for in a post hoc scenario analysis. Although Fe-N-C currently exhibits less stability than Pt/C, it is assumed in this study that Fe-N-C will eventually attain operation lifetimes equivalent to those of Pt/C. Furthermore, while the baseline scenario assumes no recycling for the spent electrocatalysts, the effects of Pt recycling are investigated in the post hoc scenario analysis. It is important to note that the LCA in this context does not incorporate detailed aspects such as the treatment of spent electrocatalysts, catalyst degradation, or the PEMFC lifetime, as these aspects are beyond the scope of this paper and are intended for future research.

The key performance characteristics of the 80 kW PEMFCs considered in the analysis are presented in **Table 7.1**. The Pt/C cathode electrocatalyst is designed based on the 2020 US DOE target, with a performance of 0.125 mg_{Pt} cm^{-2} specifically tailored for light-duty fuel cell vehicles utilizing PEMFC technology.[2,29] This configuration corresponds to approximately 20 g of Pt/C catalyst per functional unit (80 kW). For more detailed information see **Appendix D**.

In contrast, the Fe-N-C electrocatalyst performance is assumed to be equivalent to that of a Pajarito Powder Fe-N-C catalyst, with an anticipated power density of 290 mW cm^{-2}.[10]

Consequently, the estimated amount of Fe-N-C catalyst required per functional unit is approximately 690 g (**Appendix D**). The baseline scenario, therefore, facilitates a comparison between 20 g of Pt/C and 690 g of Fe-N-C, providing a comprehensive understanding of the relative efficiencies and environmental impacts of the two electrocatalysts.

Table 7.1. Performance, operating conditions, and components of the PEMFC stack in the baseline scenario for Pt/C and Fe-N-C. Operating temperatures and pressure are assumed to be identical in both systems (80 °C, 1 bar_g, H_2-air). Reproduced from ref [28] under Creative Commons CC BY 3.0.

Parameter	Pt/C	Fe-N-C
Power density at 0.657 V (mW cm^{-2})	1,160	290
Cathode catalyst loading (mg_{Pt} cm^{-2} or $mg_{Fe\text{-}N\text{-}C}$ cm^{-2})	0.125	2.5
Active cells (–)	380	11,035
Cell active area (cm^2)	185	25
Total cathode catalyst required (g)	20	690

7.2.3 Life Cycle Inventory

7.2.3.1 Pt/C Synthesis

The Pt/C synthesis process, as illustrated in **Figure 7.2a**, is primarily based on polyol syntheses reported in literature sources.[30,31] This process utilizes chloroplatinic acid, the most prevalent Pt salt precursor in the industry, as a key starting material.[32] The scale-up methodology begins with the combination of 40 mM chloroplatinic acid with a solution comprising 0.4 M NaOH in ethylene glycol.[30] Subsequently, 1 M HCl is introduced into the Pt colloidal solution to induce the precipitation of the nanoparticle suspension, followed by centrifugation of the mixture on three occasions, with the supernatant discarded after each round. The retrieved Pt nanoparticles are then blended with carbon black in acetone before being subjected to a mixing and drying process. The resulting Pt/C powder is subsequently dried in an air oven before undergoing a heat activation procedure in a furnace,[33,34] ultimately leading to the production of the final Pt/C catalyst.

The initial laboratory-scale values of various chemicals involved in the Pt/C production process, such as sodium hydroxide, ethylene glycol, chloroplatinic acid, hydrochloric acid, deionized water, and carbon black, were determined for a 50 wt.% Pt/C, and adjusted to a 46 wt.% Pt/C. The quantity of acetone was derived by scaling an 8 g Pt/C laboratory process.[31] Energy inputs were sourced from a previously simulated 1 kg Pt/C manufacturing process,[33,34] then downscaled to 20 g, assuming 90% efficiency of electric heat ovens, and excluding the carbon support precursor processing.

In the scaling process, the reactants were adjusted according to stoichiometric ratios, with a 20% relative reduction in solvents, as recommended in literature.[35] Material losses during the Pt/C production, typically estimated at approximately 3% in manufacturing quotations, were not considered negligible in this analysis. All unreacted inputs were considered waste chemicals in the outlet stream. The foreground inventories for the baseline 20 g Pt/C electrocatalyst are summarized in **Table 7.2** and illustrated on the process diagram in **Figure 7.2a** (with additional details available in Table D2). Given the absence of data for chloroplatinic acid in the Ecoinvent 3.6 database, a separate process was created based on literature data (see **Equation D1** & **Table D1**).[2]

7.2.3.2 Fe-N-C Synthesis

The preparation method and reactants for the Fe-N-C electrocatalyst, as depicted in **Figure 7.2b**, are primarily based on patents filed by the University of New Mexico.[36–38] The procedure involves the initial mixing of the N-C precursor (nicarbazin) with the Fe precursor (iron nitrate nonahydrate) and the hard template silica (Cab-O-Sil amorphous fumed) in a planetary ball mill for a period of 1 h. Subsequently, the mixture is subjected to pyrolysis in a N_2 environment at a flow rate of 100 cc min^{-1}. The temperature is gradually raised at a rate of 10°C min^{-1} until it reaches 900°C, where it is held for 1.5 hours before being allowed to cool naturally.

The resulting material undergoes a thorough washing process with 25% hydrofluoric acid (HF) for a duration of 12 h to eliminate the silica template. Subsequent washing with copious amounts of deionized water continues until the material reaches a neutral pH, achieved using a filtration pump for a period of 4 h. The wet material is then dried in an air oven at 85 °C for 8 h, after which the same pyrolysis process is repeated to yield the final Fe-N-C catalyst.

In the synthesis of the Fe-N-C electrocatalyst, all energy inputs are scaled linearly from the 25 g Fe-N-C production, derived from laboratory data (as outlined in **Table D5**). It is assumed that the entire production process, including the use of large-scale furnaces, could be electrified at scale. The reactants are scaled in accordance with stoichiometric ratios, with the water used as a solvent adjusted with a relative reduction of 20% as recommended in the literature.[35] Material losses during production are overlooked, except during the pyrolysis stage. Based on expert opinion and prior laboratory data from the University of New Mexico, it is assumed that 80% of the nicarbazin precursor is wasted during the Fe-N-C process due to the initial pyrolysis.

The amount of required HF is calculated based on the quantity of silica, with an additional 20% added to ensure the complete consumption of silica. Given the unavailability of data for SiF_4 in the ecoinvent 3.6 database, its environmental impact is assimilated to that of HF, with the assumption that the input and output flows of HF are equal. In the baseline scenario, all output streams, except for the catalyst, are treated as waste (refer to the Scenario subsection below). The foreground inventories for the baseline 690 g Fe-N-C are summarized in **Table 7.2** and depicted in **Figure 7.2b**, with additional detailed information provided in **Table D6**.

Considering that data for iron nitrate nonahydrate and nicarbazin are also unavailable in ecoinvent 3.6, a separate process is created for the former, with inputs determined using weight distribution data (as shown in **Table D3**). For the latter, an equimolar mix of 2-Nitroaniline and 2-Pyridinol is assumed to be equivalent to the nicarbazin precursor (as described in **Table D4**). Any energy inputs associated with the production of these two precursors are omitted in this analysis.

Table 7.2. Manufacturing inputs and outputs for Pt/C and Fe-N-C catalyst baseline scenarios. Reproduced from ref [28] under Creative Commons CC BY 3.0.

Pt/C (20 g)		**Fe-N-C (690 g)**	
Input	Amount	Input	Amount
Acetone (g)	768	Activated silica (kg)	1.38
Carbon black (g)	10.0	Hydrogen fluoride (kg)	2.21
Chloroplatinic acid (g)	17.7	Iron nitrate nonahydrate (kg)	0.345
Ethylene glycol (kg)	2.05	Nicarbazin (kg)	3.46
Sodium hydroxide (g)	23.3	Water, deionised (kg)	111
Water, deionised (kg)	39.7	Electricity (MJ)	5,393
Hydrochloric acid (g)	255		
Electricity (MJ)	4.43		
Output	Amount	Output	Amount
Acetone, waste (g)	768	Silica, waste (kg)	1.11
Hydrochloric acid, waste (g)	255	Fe-N-C Catalyst (g)	690
Pt/C (g)	20	Hydrogen Fluoride, waste (kg)	2.21
Sodium Hydroxide, waste (g)	23.3	Nicarbazin, waste (kg)	2.76
Wastewater (kg)	39.7	Wastewater (kg)	111
Ethylene Glycol, waste (kg)	2.05		

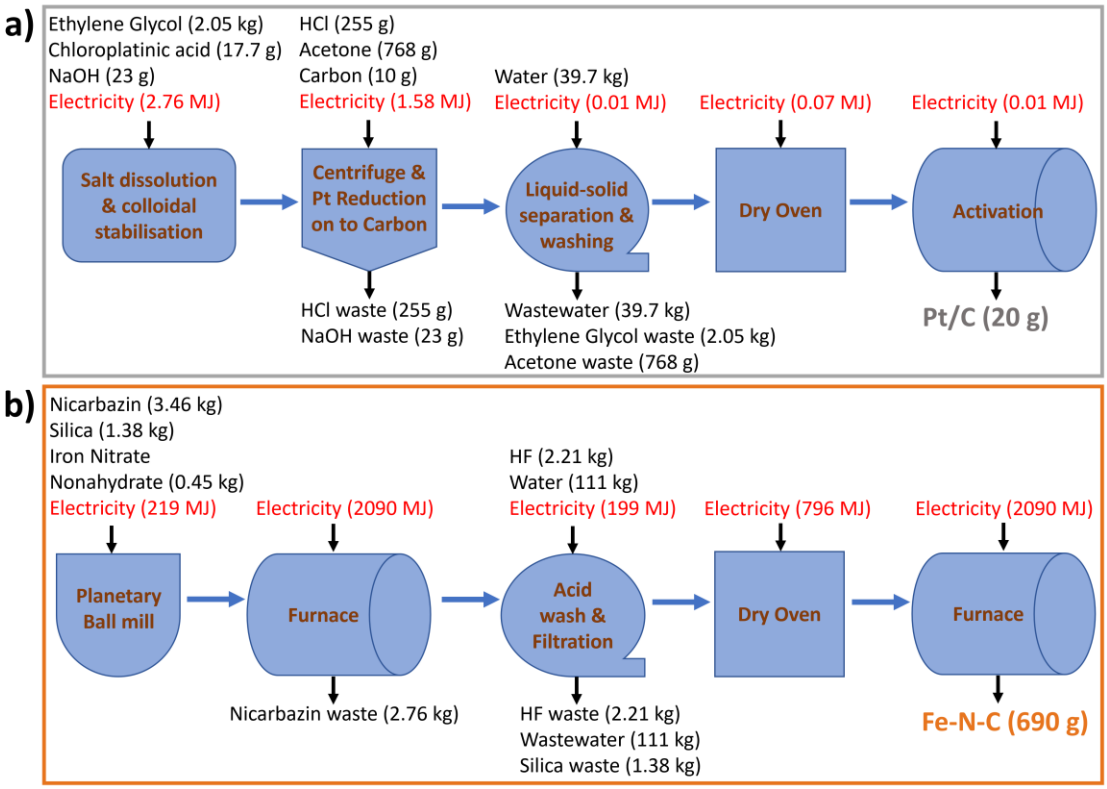


Figure 7.2. Process diagrams with material and energy inventories to produce baseline a) 20 g Pt/C, b) 690 g Fe-N-C. Reproduced from ref [28] under Creative Commons CC BY 3.0.

7.2.4 Impact Assessment

In the assessment, both the foreground and background inventories undergo translation into environmental impacts during the life-cycle impact assessment (LCIA) phase using the ReCiPe 2016 methodology, selected based on the hierarchist perspective, which is grounded in the cultural theory of scientific agreement and common policy principles.[39,40,41] This approach aligns with a medium-term perspective of 100 years for evaluating the environmental impacts, as per the Kyoto Protocol and Paris agreement.

Among the 17 midpoint indicators in ReCiPe 2016, focus is made on the following aspects: global warming potential, fossil fuel scarcity, mineral resource scarcity, marine eutrophication, freshwater eutrophication, acidification potential, and human toxicity potential. These indicators collectively capture various dimensions of environmental impact, ranging from climate change implications to the depletion of essential resources and the impacts of hazardous substances on human health and the environment.

To address the limitations of ReCiPe 2016 in accounting for HF in certain indicators, such as acidification potential and human toxicity potential,[42] the CML 2001 methodology is adopted

in those cases. The midpoint indicators are further aggregated into endpoint categories for three areas of protection: human health, ecosystem quality, and resource scarcity. The human health indicator is expressed in disability-adjusted life-years (DALY), representing the number of years a person lives with a disability following a disease or accident. The ecosystem quality indicator is employed to gauge the extent of local species loss integrated over time, denoted as species × year. Additionally, the resource scarcity metric assigns a monetary value to the potential burdens associated with future mineral and fossil resource extraction, quantified in US$ 2013. Both of these endpoint indicators are determined using the ReCiPe 2016 methodology, ensuring a comprehensive and standardized assessment of the environmental impacts across various dimensions. To incorporate the impact of HF into the analysis, the human health indicator is recalculated by converting point units in ReCiPe 2008 to disability-adjusted life-years (DALY) in ReCiPe 2016, taking into account a world normalization factor of 73.3 and an average weighting factor of 400, as outlined in existing literature. The selected characterization methods for both the midpoint and endpoint impacts are compiled and presented in **Table 7.3**.

Table 7.3. Midpoint and endpoint impact categories used. Reproduced from ref [28] under Creative Commons CC BY 3.0.

Impact	Category	Characteristic model	Units
Mid-point	Global warming potential	ReCiPe 2016	kg CO_2-eq
	Acidification potential	CML 2001	kg SO_2-eq
	Fossil Resource Scarcity	ReCiPe 2016	kg oil-eq
	Marine Eutrophication	ReCiPe 2016	kg N-eq
	Freshwater Eutrophication	ReCiPe 2016	kg P-eq
	Human toxicity potential	CML 2001	kg 1,4-DCB-eq
	Mineral Resource Scarcity	ReCiPe 2016	kg Cu-eq
End-point	Human Health	ReCiPe 2008	DALY
	Ecosystem Quality	ReCiPe 2016	Species × Year
	Resource	ReCiPe 2016	USD 2013

To capture the monetary valuation of these environmental impacts, a process of monetization is employed, allowing the endpoint environmental burdens to be quantified in monetary units. This approach facilitates a direct comparison of the environmental impacts both within and across manufacturing processes. The selected monetization factors are based on the approach initially developed by Weidema and colleagues,[43,44] which assign a monetary value to human health damage categories based on the income generated annually through extending an individual's life by one year. This approach has been extended to encompass ecosystem damage, as per the factors outlined in **Table D7**, provided by Dong *et al*.[45], reflecting the hierarchist perspective.

7.2.5 Interpretation

The concluding stage of the LCA involves interpreting the outcomes and ensuring that the deductions are firmly supported, encompassing the assessment of uncertainties and the analysis of potential scenarios. Among the various factors that could introduce uncertainties in the calculations, uncertainties associated with the foreground inventory data are explored, given that the inventories for the Fe-N-C process were extrapolated from scaled-up laboratory procedures.[46] Furthermore, a series of catalyst scenarios to accommodate forthcoming technological advancements are established, aiming to decrease catalyst loading and minimize raw material utilization while enhancing the efficiency of production processes.

7.2.5.1 Uncertainty Quantification

An uncertainty analysis was conducted by simultaneously propagating the uncertainty in the foreground process inputs to all the midpoint and endpoint impact indicators. This was accomplished using Monte Carlo analysis, generating 1,000 Sobol samples. The uncertainty intervals, set at ±20% around the nominal process input values for both catalyst syntheses, were determined based on expert opinions. Owing to the limited data available, these uncertain parameters were assumed to follow triangular probability distributions.[47]

In a subsequent step, the same sampled scenarios in a global sensitivity analysis (GSA) to quantify the contribution of each uncertain input to the overall impact variance was employed. The software SobolGSA was utilized for this purpose, utilizing random sampling-high dimensional model representations surrogates to calculate Sobol sensitivity indices.[48,49] It should be noted that each contribution from the uncertain inputs adds up separately to the impact variances by design, resulting in identical first- and total-order Sobol indices that collectively sum up to 1. Further comprehensive information can be found **Appendix D**.

7.2.5.2 Scenario Analysis

Apart from the fundamental assumption of 100% virgin Pt supply in the baseline, two additional scenarios considering Pt recycling rates of 55% and 75% are established. These scenarios were designed to reflect current practices in industrial automotive Pt recycling,[3,4] findings from reported lab-scale experiments,[21,50,51] and guidelines outlined by the EU.[22] The two Pt recycling scenarios, for the sake of simplicity, do not encompass the infrastructure and energy requirements associated with the Pt recycling process. Consequently, the recycled Pt

could be perceived as a reduction in Pt usage, aligning with the EU's targeted goal of achieving a 71% reduction in Pt usage by 2030, relative to the values recorded in 2017.[52]

A scenario also considers a reduction in Pt/C from 20 g to 15 g, acknowledging the ongoing trend of minimizing Pt quantities in PEMFCs.[53] Conversely, no recycling scenario was analysed for Fe-N-C, given that it primarily comprises economical or abundant materials. To reflect recent developments in the synthesis of silica-templated Fe-N-C catalysts demonstrating comparable performance without the use of HF,[54] a distinct scenario with no HF input or output was added.

Considering the significant electricity demand in the current synthesis of Fe-N-C catalysts, multiple electricity mixes are explored, including the EU average, Poland, and Sweden, in addition to the global average electricity mix. Given that large-scale production of Fe-N-C catalysts would likely utilize a different furnace instead of a tube furnace, an additional scenario assuming that the power consumption for producing 690 g Fe-N-C with a muffle furnace would be equivalent to that required for producing 25 g Fe-N-C with a tube furnace, consistent with data provided by furnace manufacturers.

Lastly, two scenarios are formulated focused on improved catalyst performance, aiming to reduce the necessary catalyst quantities to 380 g Fe-N-C and 15 g Pt/C, respectively. These comprehensive scenarios were designed to capture and evaluate various potential developments and advancements in the production and application of both Pt/C and Fe-N-C electrocatalysts within the context of the PEMFC stack manufacturing process.

7.2.6 Techno-economic Analysis

A dynamic cost estimation using learning curves was used to assess the impact of catalyst production costs relative to other components of the proton exchange membrane fuel cell (PEMFC) on the overall cost of the PEMFC stack. This analysis was conducted across various production scales, aligning with previous studies on PEMFC production.[55,56] The investigation encompassed a production rate spanning from 1,000 to 500,000 stacks per year. The lower production rate represents the practical limit for mass production in the automotive industry, while the upper rate corresponds to the output associated with a highly popular individual automobile model.[32] It is important to note that the analysis primarily focused on the stack cost, with the cost of the PEMFC balance of plant being excluded from the scope of this study.

7.2.6.1 Dynamic Cost Estimation using Learning Curves

A learning curve represents the process through which human activity accumulates knowledge or experience as a result of continuous production. In **Equation 7.1**, the product cost at production level *i*, Y_i depends on the cumulative number of products, X_i, the progress ratio, *r*, and a given constant *A*. The progress ratio *r* is related to the parameter *F*, which describes how much the production cost is reduced upon doubling the cumulative production through **Equation 7.2**.[55,57] For instance, an F value of 80% means for the cost to be reduced by 20% each time the cumulative production volume is doubled.

$$Y_i = AX_i^{-r} \qquad \textbf{Equation 7.1}$$

$$F = 2^{-r} \qquad \textbf{Equation 7.2}$$

Values for the learning curve parameter, *F*, are reported to fall within the range of 74–95%.[55,56] For this analysis a representative *F* value of 86.4% for the catalysts was selected. This choice is derived from the baseline Fe-N-C (690 g) production, which achieves an equivalent production cost relative to the 380 g Fe-N-C + muffle furnace scenario at a production rate of 500,000 stacks per year. The data provided by Mock and Schmid [56] are utilized for the remaining PEMFC components.

To estimate the production costs for Pt/C and Fe-N-C, quotes were obtained from Alibaba and other pertinent manufacturers. Calculations for processing costs are based on the calculated utility consumption, incorporating plant cost factors derived from industry insights and knowledge (**Tables D8** and **D9**). To model the Pt/C cathode catalyst, a straightforward process was employed that achieves the 2020 US DOE target performance, considering the market price of bulk precursors and electricity consumption. Considering that contemporary de-alloyed Pt-based cathode PEMFC catalysts meeting the US DOE performance criteria exhibit elevated material and processing costs, the calculated Pt/C cathode and anode catalyst process costs as the value at 500,000 stacks per year in the learning curve were applied (**Table D10**). The cost estimation for the Pt/C anode catalyst was computed under the assumption of an equivalent Pt/C production process but with a reduced loading of 0.025 $mg_{Pt}\ cm^{-2}$, resulting in the cost being divided by five. In determining the costs of the other PEMFC components in the Pt/C system at a production rate of 1,000 stacks per year, previous values provided by James et al. for their 2020 scenario.[2] For comparative purposes, a separate learning curve

calculation based on the cost of a PtCo/C cathode catalyst was sourced from James et al.[2] (**Table D11**).

In the case of the Fe-N-C cathode catalyst, market prices were used for bulk precursors and electricity into the cost estimation. Setting the production rate at 1,000 stacks per year, the cost calculation was based on the material and process costs derived from the modeled Fe-N-C catalyst synthesis. This production rate of 1,000 stacks per year was chosen under the assumption that the performance of Fe-N-C could potentially be enhanced, leading to a reduction in production costs at higher production rates. Given that the total required coating area for the Fe-N-C catalyst is 3.9 times greater than that for Pt/C, owing to the lower power output of the catalyst, the cost of Fe-N-C PEMFC components was adjusted at the production rate of 1,000 stacks per year in accordance with the increased surface area in the Fe-N-C system relative to the Pt/C system (**Table D12**).

7.2.6.2 Sensitivity Analysis

Historical data suggests that the price of Pt has demonstrated fluctuations, doubling and halving over the course of the past two decades in comparison to the average price.[58] In light of this, a sensitivity analysis was performed by adjusting the price of both Pt/C and Fe-N-C catalysts, ranging from a decrease of 50% to an increase of 100%. Given the volatile nature of electricity prices in the market, the sensitivity analysis was extended to include variations in electricity prices, spanning from a reduction of 75% and an increase of 200%. Furthermore, a sensitivity analysis was conducted on the F value utilized in the learning curves (**Equation 7.2**), examining the impact of values ranging from 74% to 95%.

7.2.7 Pt demand Forecasting

Using projections outlined in forecasts of PEMFC-based fuel cell electric vehicle production,[59,60] an estimation of future Pt consumption originating from PEMFC usage was conducted. In this analysis, I adhered to the consideration that 10% of the total annual Pt production [3] would serve as the consumption threshold for the deployment of a new technology,[61] such as PEMFC for transportation purposes. This analysis was based on 80 kW PEMFC light-duty vehicles and their corresponding Pt usages and recycling targets.[22,29,52]

7.3 Results

7.3.1 Life Cycle Assessment

The LCA findings for the baseline Pt/C (20 g) and Fe-N-C (690 g) cathode catalysts in PEMFC are condensed in the bar charts and spider chart in **Figure 7.3**. Replacing Pt/C with Fe-N-C results in decreased impacts in mineral resource scarcity, acidification potential, and freshwater eutrophication, while impacts are expected to rise in the remaining four categories of human toxicity potential, global warming potential, fossil resource scarcity, and marine eutrophication simultaneously (**Figure 7.3h**). The global warming potential (**Figure 7.3a**) and fossil resource scarcity (**Figure 7.3b**) associated with Fe-N-C (1130 kg CO2-eq, 286 kg oil-eq) are 70% and 35% higher, respectively, compared to those of Pt/C (659 kg CO2-eq, 213 kg oil-eq). This disparity is primarily ascribed to the substantial electricity demand from the prolonged two-step high-temperature pyrolysis process during the synthesis of Fe-N-C (**Tables D5** & **D6**), which is characteristic of Fe-N-C materials and significantly surpasses the energy requirements of Pt/C production. Additionally, regarding human toxicity potential (**Figure 7.3e**), the impact of Fe-N-C (7,140 kg 1.4-DCB-eq) is three times greater than that of Pt/C (2,300 kg 1,4-DCB-eq), primarily attributed to the generation and disposal of significant quantities of HF (**Table D6**).

The utilization of Fe-N-C leads to a threefold increase in marine eutrophication (**Figure 7.3c**) impacts (0.09 kg N-eq) compared to Pt/C (0.03 kg N-eq) owing to the release of nitrogen from the nicarbazin precursor (constituting 60% of the contribution) employed in the synthesis of Fe-N-C. However, the scenario is reversed for freshwater eutrophication (**Figure 7.3d**), acidification potential (**Figure 7.3f**), and mineral resource scarcity (**Figure 7.3g**, where the impacts of Fe-N-C (0.55 kg P-eq, 8.4 kg SO2-eq, 1.0 kg Cu-eq) are reduced by 34%, 75%, and 99% respectively, compared to those of Pt/C (0.83 kg P-eq, 8.4 kg SO2-eq, 1.0 kg Cu-eq). Most Pt/C impacts in all these categories stem from Pt mining and refining activities, which impose a significantly heavier burden compared to the acquisition of raw materials for Fe-N-C. It is worth noting that the inter-quartile ranges in the projected midpoint indicators, obtained by propagating the uncertainty of the foreground inventory, do not overlap for any of the comparisons in **Figure 7.3a-g**, thus reinforcing the findings. The outcomes of the global sensitivity analysis suggest that the primary factors influencing this variability are the quantities of electricity, HF, and nicarbazin utilized in the production of Fe-N-C (**Table D13**),

and the quantities of chloroplatinic acid and electricity employed in the production of Pt/C (**Table D14**).

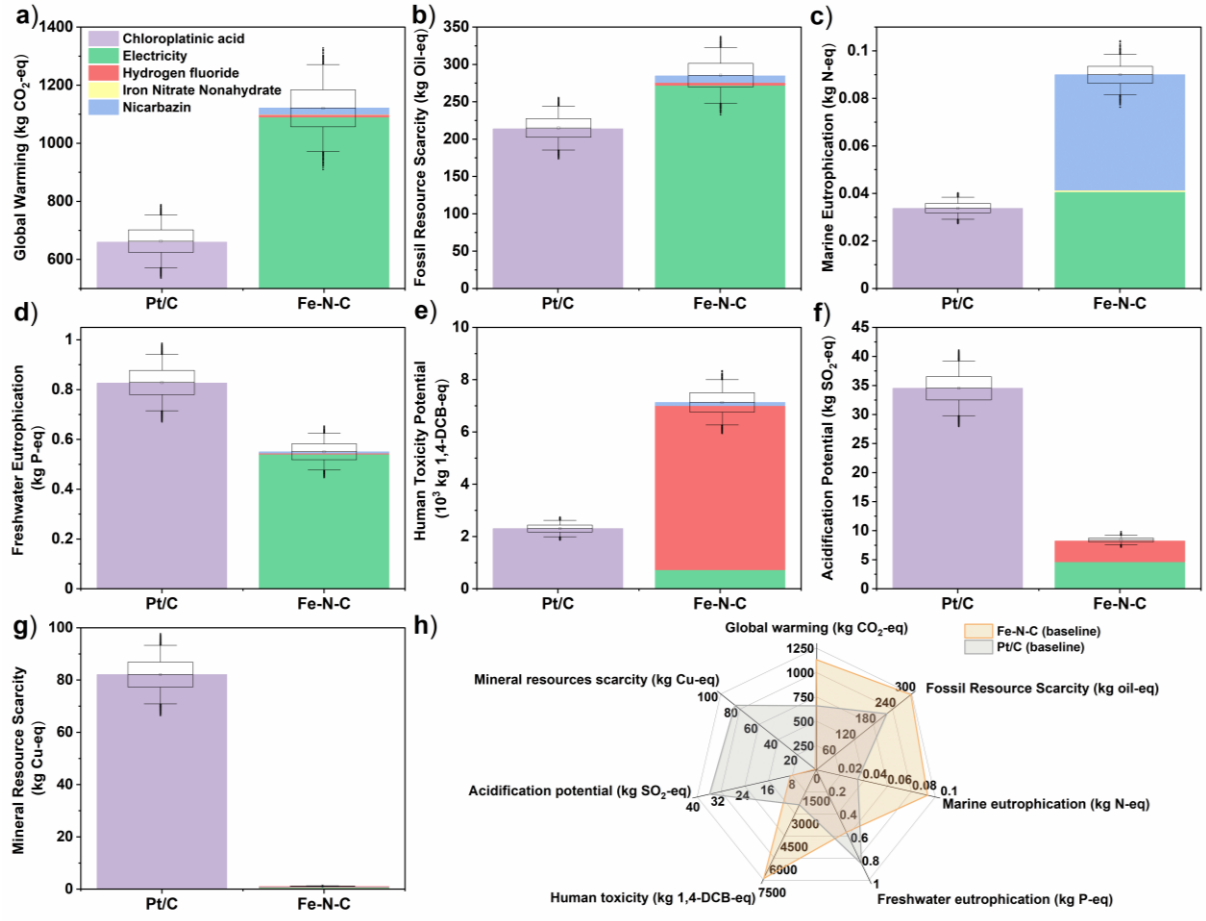


Figure 7.3. Comparison of midpoint impact indicators of baseline Pt/C (20 g) and Fe-N-C (690 g). a) Global warming potential (kg CO_2-eq). b) Fossil resource scarcity. c) Marine Eutrophication (kg N-eq). d) Freshwater eutrophication (kg P-eq). e) Human toxicity potential (kg 1,4-DCB-eq). f) Acidification potential (kg SO_2-eq). g) Mineral resource scarcity (kg Cu-eq). The main activities contributing to each mid-point indicator are reported on each bar. The boxes on each bar represent the inter-quartile range of uncertainty scenarios, with central line showing the median and central dot the mean, and the lower and upper whiskers extending the box to the 5th and 95th percentiles, outliers represented by dots. h) Spider chart summary of baseline Fe-N-C and Pt/C midpoint indicators. Reproduced from ref [28] under Creative Commons CC BY 3.0.

The LCA findings for all three endpoint damage categories, including human health, ecosystems quality, and resource scarcity, are presented in the bar charts shown in **Figure 7.4a-c** for the baseline Pt/C (20 g) and Fe-N-C (690 g) scenario (**Table D20**). These charts reveal a distinct scenario compared to the midpoint indicators, demonstrating that the Fe-N-C catalyst significantly surpasses Pt/C in terms of ecosystems quality (-89%) and human health (-36%), with a slight edge in resource scarcity (-9%). The contributions of midpoints to endpoints outlined in **Table D17** aid in comprehending this transition. In terms of ecosystems

quality, the impacts related to land use (4.6×10-5 Species·Year) and acidification potential (0.7×10-5 Species·Year) attributed to Pt/C production far overshadow the predominant impact associated with Fe-N-C production resulting from global warming (0.3×10^{-5} Species·Year). Concerning human health, the heightened impact of particulate matter formation for Pt/C (1.4×10^{-3} DALY) supersedes the amplified climate change impact for Fe-N-C (1.0×10^{-3} DALY). Moreover, the human toxicity is comparatively lower for Fe-N-C when considering cancerous human toxicity (conversion factor 3.3×10^{-6} DALY/kg 1,4-DCB eq) and non-cancerous human toxicity (conversion factor 2.3×10^{-7} DALY/kg 1,4-DCB eq) induced by HF alone. Lastly, concerning resource scarcity, the environmental load stemming from Pt mining on mineral resources is counterbalanced by the greater load of Fe-N-C production on fossil resources due to its significantly higher energy requirement.

These findings are substantiated by the inter-quartile ranges in projected endpoint indicators, which exhibit no overlapping values between Fe-N-C and Pt/C within the human health (**Figure 7.4a**) and ecosystems quality (**Figure 7.4b**) categories, and limited overlap in the resource scarcity (**Figure 7.4c**) category. The global sensitivity analysis identifies the dominant sources of uncertainty as the quantities of chloroplatinic acid and electricity involved in Pt/C production (**Table D19**), along with the quantities of electricity and, to a lesser extent, HF implicated in Fe-N-C production (**Table D20**). However, it is important to note that endpoint indicators are subject to more substantial uncertainties compared to midpoint indicators, especially concerning uncertainties in the life-cycle (background) emissions and the LCIA characterization factors, which were not specifically quantified in this study. Therefore, it is crucial for future research efforts to delve deeper into the phenomenon of burden-shifting observed between the greater global warming impact (for Fe-N-C) and the end-point impacts on human health and ecosystems quality (for Pt/C).

The comparison between the alternative Fe-N-C and Pt/C scenarios and their respective baseline scenarios for endpoint categories is illustrated in **Figure 7.4d-f** (**Table D20**). Notably, in the case of Fe-N-C production, the utilization of a muffle furnace demonstrates the most significant potential for improvement across all three damage areas, namely human health (-48%), ecosystems quality (-70%), and resources (-68%). This outcome was expected considering the predominant impact of electricity consumption on Fe-N-C effects, highlighting the intriguing possibility that employing a muffle furnace could yield even greater benefits

compared to reducing the quantity of Fe-N-C catalyst to 380 g from the baseline scenario. Similarly, transitioning from a global to a European electricity supply could result in substantial environmental benefits in terms of human health (-26%), ecosystems quality (-25%), and resources (-35%) due to the reduced carbon intensity. However, it is important to note that such a transition might lead to an increase in both freshwater (+16%) and marine (+11%) eutrophication potentials at the midpoint level owing to the higher proportion of brown coal (lignite) in current European supplies compared to the global average.[41] The considerable influence of the electricity mix on the environmental aspects of Fe-N-C production is additionally illustrated in **Figures D2** & **D3** (**Tables D16** & **D21**). Specifically, a mix characterized by a high proportion of renewables and low carbon intensity, as observed in Sweden, has the potential to substantially decrease all three damage areas, namely human health (-76%), ecosystems quality (-72%), and resources (-81%). Conversely, a mix heavily dependent on coal, as seen in Poland, would significantly exacerbate the impacts on human health (+35%) and ecosystems quality (+69%). In contrast, the scenario without the use of HF would yield more moderate benefits, resulting in -16% reduction in impacts on human health compared to the baseline scenario, with minimal effects on other endpoints. At the midpoint level, the most significant advantage of eliminating HF lies in the reduction of impacts on human toxicity (-88%) and acidification potential (-55%). However, these two categories hold relatively less significance when aggregated into the human health endpoint indicator (**Table S17**). Regarding Pt/C production, reducing the quantity of catalyst or increasing Pt recycling demonstrates a considerable benefit across all environmental impact categories, aligning with the predominant impact of chloroplatinic acid on Pt/C effects. Notably, in the case of the best-case scenario involving 75% Pt recycling, the reductions from the baseline Pt/C scenario are approximately 75% in all endpoint and midpoint impact categories. Moreover, the scenario of 75% Pt recycling outperforms all Fe-N-C improvement scenarios in terms of impacts on human health and resources. However, Fe-N-C still exhibits significantly lower burdens in terms of endpoint ecosystems quality and midpoint acidification potential and mineral resource scarcity compared to any of the Pt/C scenarios. It is also important to note that the anticipated impacts on human health and resources in the muffle furnace scenario of Fe-N-C production remain within 20–30% of those in the optimistic 75% Pt recycling scenario, underscoring the substantial potential for improvement offered by the Fe-N-C catalyst.

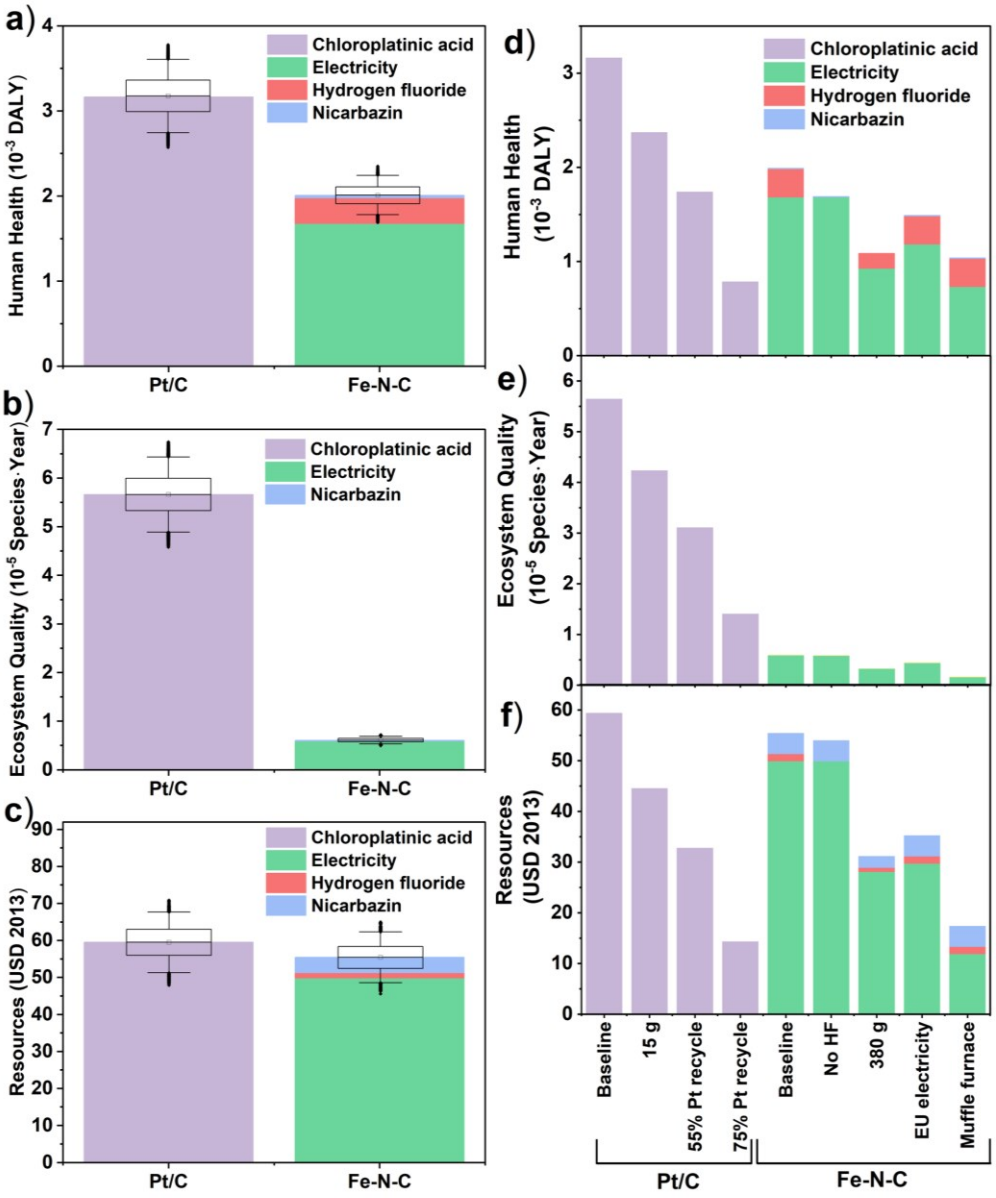


Figure 7.4. Left: Comparison of endpoint impact indicators of baseline Pt/C (20 g) and Fe-N-C (690 g). a) Human health (10^{-3} DALY). b) Ecosystem quality (10^{-5} Species·Year). c) Resource scarcity (USD 2013). The boxes on each bar represent the inter-quartile range of uncertainty scenarios, with central line showing the median and central dot the mean, and the lower and upper whiskers extending the box to the 5th and 95th percentiles. **Right**: Scenarios of Fe-N-C (baseline, no HF, 380 g, EU electricity) and Pt/C (baseline, 15 g, 55% and 75% Pt recycling for endpoint categories: d) Human health (10^{-3} DALY). e) Ecosystem quality (10^{-5} Species·Year). f) Resource (USD 2013). Reproduced from ref [28] under Creative Commons CC BY 3.0.

7.3.2 Techno-economic Analysis

The costs associated with the materials, utilities, and manufacturing of cathode catalysts are consolidated in **Tables D8** & **D9**. The material costs for Fe-N-C amount to 50.6 USD $kg^{-1}_{Fe\text{-}N\text{-}C}$, with more than 70% originating from the N-C precursor (nicarbazin). In contrast, the material costs for Pt/C are significantly higher, reaching 13,600 USD per kilogram of Pt/C, with 98% of

the cost attributed to the Pt precursor (chloroplatinic acid). When considering the material costs normalized kW^{-1} of PEMFC, the cost for Fe-N-C is calculated to be 0.44 USD kW^{-1}, while for Pt/C, it is 3.39 USD kW^{-1} (**Figure D4a**). In the event of implementing Pt recycling, the cost of Pt/C could become comparable to that of Fe-N-C. Furthermore, if 75% Pt recycling were achieved, the material feedstock cost could be comparable to the baseline Fe-N-C at 0.85 USD kW^{-1}. Corresponding with these findings, the production costs of Pt/C exhibit an approximate 1:1 ratio with variations in feedstock prices, while Fe-N-C is relatively less sensitive (refer to **Figure D4b**). In the scenario where the price of Pt doubles, as observed in 2008, while Fe-N-C feedstock prices remained constant, the material cost of the PEMFC cathode using Pt/C would become 15 times higher than that of Fe-N-C. Conversely, the production costs of Fe-N-C are highly susceptible to fluctuations in electricity prices, while those of Pt/C show relatively low sensitivity (**Figure D4c**).

The learning curve analysis of Pt/C and Fe-N-C is visualized in **Figure 7.5a-b** (**Tables S10** & **D12** for detailed information), accompanied by the breakdown of Fe-N-C and Pt/C PEMFC components shown in **Figure D5**. At a rate of 500,000 stacks $year^{-1}$, the Pt/C cathode constitutes 25% of the PEMFC stack cost and amounts to 3.4 USD kW^{-1}, whereas the Fe-N-C contributes merely 2% of the stack cost and is 0.79 USD kW^{-1}. This outcome is related to the total PEMFC stack cost being significantly lower for Pt/C compared to Fe-N-C cathode stacks, standing at 13.8 USD kW^{-1} in contrast to 41.6 USD kW^{-1}, respectively. The observed disparity is attributed to the 3.9-fold increase in the required surface area of the Fe-N-C cathode system, assuming that this increase similarly affects the costs of other components. This amplified area completely offsets the advantage of the reduced cost of the cathode catalyst in the Fe-N-C system. For instance, in a PEMFC with a Fe-N-C cathode, the Pt-based anode might end up consuming more Pt than in an all Pt-based PEMFC if the Pt consumption at the anode scales with the surface area.

Consequently, the cost of the PEMFC stack is influenced by the performance of the Fe-N-C power density, as well as the applied *F* value, which denotes the extent to which the production cost decreases with the doubling of cumulative production (refer to **Figure D6**). For the simulated system with an F value of 86.4% for the catalysts, the baseline Fe-N-C would need to achieve a power density of 874 mW cm^{-2} at 0.657 V, representing a 200% improvement (resulting in a reduction to 230 $g_{Fe\text{-}N\text{-}C}$) to become competitive in cost with the

Pt/C-based cathode at a production rate of 500,000 stacks per annum (refer to **Figure 7.5c**). When considering an *F* value of 74% for all Fe-N-C-based PEMFC components, only a 34% improvement to 0.392 mW cm^{-2} is necessary to attain cost parity with the Pt/C-based system. However, with the Fe-N-C stack featuring an *F* value of 95%, it is unable to match the Pt/C stack cost (with *F* value of 86.4%) within the considered power density range. While this study modelled a simple and inexpensive Pt/C cathode process, it is important to note that meeting the performance targets set by the US DOE often necessitates the utilization of de-alloyed Pt-based catalysts. Consequently, the cost of an equivalent-performing yet more expensive Pt-based de-alloyed cathode catalyst (PtCo/C) was also assessed (detailed information available in **Table D11** & **Figure D7**). The de-alloyed PtCo/C proves to be costlier due to additional processing steps.7 Specifically, at a rate of 500,000 stacks $year^{-1}$, the higher cost of the PtCo/C precursor (amounting to 3.93 USD kW^{-1}), which constitutes 27.4% of the component costs, leads to a PEMFC stack cost of 14.3 USD kW^{-1}. This value is lower than the 15.5 USD kW^{-1} estimated by James *et al*. for a 2020 PEMFC automotive system employing PtCo/C,[2] which can be attributed to the applied learning curve rate in this analysis. To achieve a cost parity equivalent to that of the considered PtCo/C cathode PEMFC at a rate of 500,000 stacks $year^{-1}$, the baseline Fe-N-C would need to attain a power density of 0.842 W cm-2 at 0.657 V, or 0.781 W cm^{-2} for the PtCo/C system reported by James *et al*. (**Figure 7.5c**).[2]

Incorporating the monetization of environmental impacts into the costs associated with catalyst materials and processing significantly affects the cathode catalyst cost (refer to **Figure 7.5d**). It is essential to note, however, that the monetization factors employed (**Table D7**) are subject to considerable uncertainty, thereby rendering the monetized impacts as rough estimates in terms of magnitude.[43] Across all catalyst scenarios, the environmental externalities exceed the material and processing costs. For the baseline Fe-N-C, these environmental externalities contribute up to 5.50 USD kW^{-1}, while the material and processing costs amount to 2.92 USD kW^{-1}. The situation is more pronounced for the baseline Pt/C, where the environmental externality costs reach 18.23 USD kW^{-1}, as opposed to the material and process costs of 3.41 USD kW^{-1}. Notably, Pt/C exhibits a much greater impact on ecosystem quality compared to Fe-N-C, leading to the highest monetized externality of 12.03 USD kW^{-1} (as illustrated in **Figure 7.3**). Opting for the improved Fe-N-C scenario (380 $g_{Fe\text{-}N\text{-}C}$ + muffle furnace) results in a reduced total process and environmental externality cost of 2.10

USD kW^{-1}. Similarly, in the case of the 75% Pt recycling scenario, the total cost diminishes to 5.41 USD kW^{-1}. Costs associated with labour, fixed costs, overheads, and depreciations are insignificant for Pt/C due to the production of only 20 $g_{Pt/C}$ required for an 80 kW PEMFC, while the production of 690 $g_{Fe\text{-}N\text{-}C}$ incurs 0.49 USD kW^{-1} for these costs. Additionally, electricity costs for the baseline Fe-N-C are substantial at 1.98 USD kW^{-1} but insignificant for Pt/C. However, the electricity requirements for Fe-N-C can be reduced to 0.28 USD kW^{-1} for the 380 $g_{Fe\text{-}N\text{-}C}$ scenario utilizing the muffle furnace.

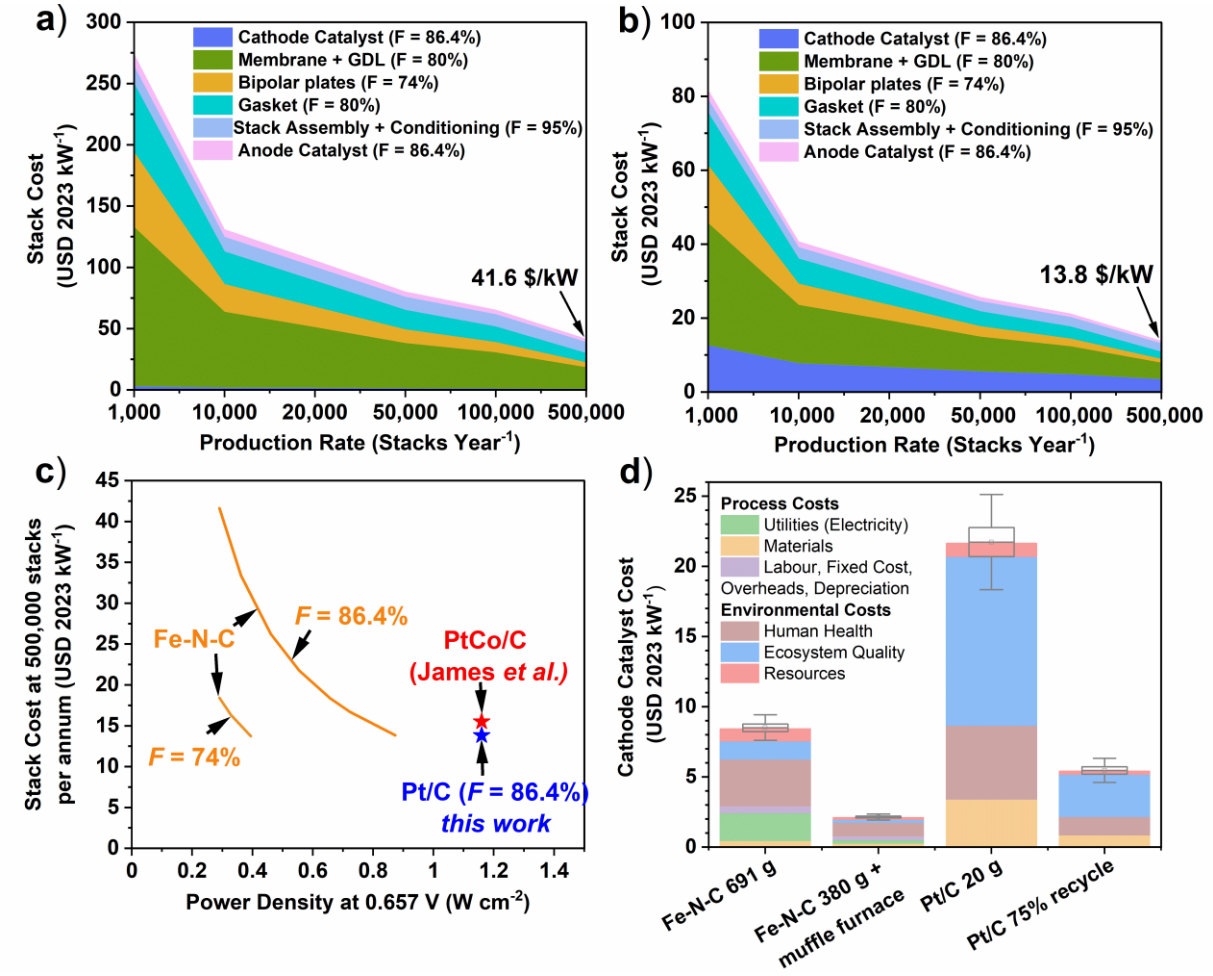


Figure 7.5. Learning curve analysis of 80 kW PEMFC stack cost with production rate for baseline cathode catalysts with F = 86.4% a) Fe-N-C (690 g_{FeNC}). b) Pt/C (20 $g_{Pt/C}$). c). Variation of PEMFC stack cost at 500,000 stacks with power density for different F values for Fe-N-C compared to target Pt-based 80 kW PEMFC systems, including PtCo/C of James et al. (2018) d) Breakdown of the total process and environmental production costs for baseline Fe-N-C (690 $g_{Fe\text{-}N\text{-}C}$),Pt/C (20 $g_{Pt/C}$),Fe-N-C 380 $g_{Fe\text{-}N\text{-}C}$ + muffle furnace and 75% Pt recycling scenarios. Box and whisker plots are drawn using the endpoint uncertainty scenarios, with monetization applied. Reproduced from ref [28] under Creative Commons CC BY 3.0.

Turning attention to examining whether the supply of Pt can meet the anticipated future demands from the deployment of PEMFCs to produce FCEVs. This matter has been thoroughly

discussed in recent studies.[62,63] Here, I aim to provide a fresh perspective on this issue in **Figure 7.6** (and **Figure D8**). The criterion is grounded in ensuring that Pt demand does not surpass 10% of the supply for a novel technology.[3] Even if the combined global Government targets for FCEV deployment by 2030 (totalling 2.5 million FCEVs) were manufactured within a single year, the consumption of Pt would still not exceed 10% of the Pt supply, considering the US DOE 2020 Pt specific power density target values, even in the absence of any Pt recycling. Should the EU's 2030 Pt specific power density and Pt recycling targets be achieved, Pt supply constraints would not pose a hindrance to PEMFC production, even if the highest 2040 target of FCEVs on the road (anticipated to reach 15 million FCEVs[59]) were produced within one year. However, it is essential to note that this brief analysis does not account for the fact that most of the Pt production originates from a single country, South Africa, and as a result, the supply of Pt could potentially be vulnerable to disruptions.

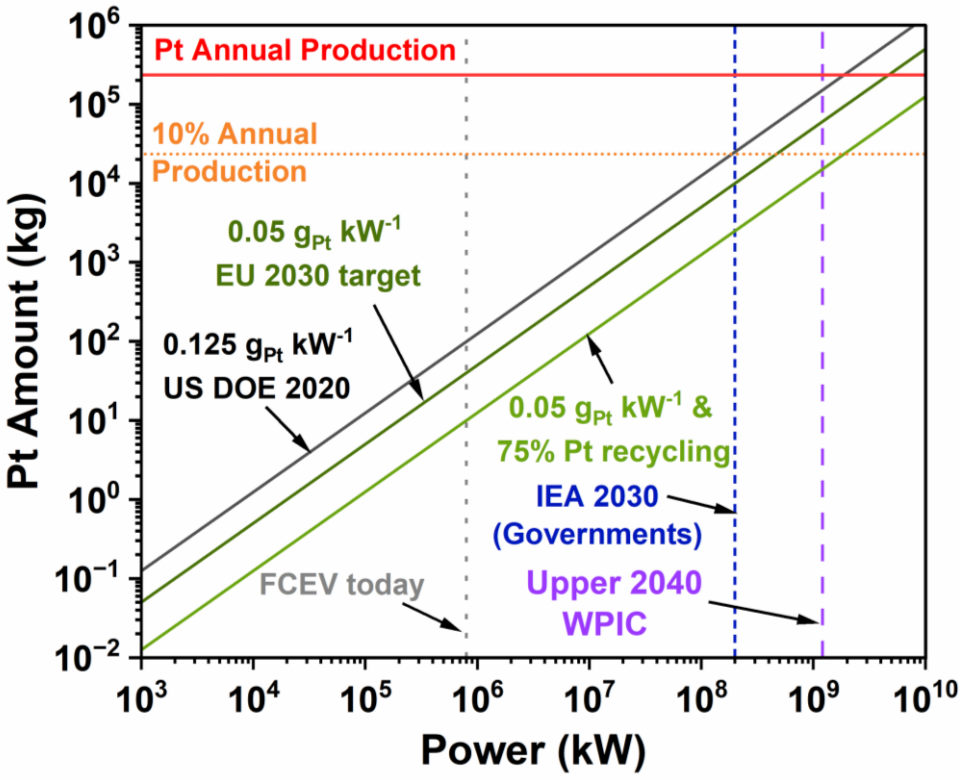


Figure 7.6. Amount of Pt required for PEMFC power at different Pt specific power density (US DOE 2020,[29] EU 2030 [52] and 75% Pt recycling targets[22]) as a function of scale. Assumed 80 kW fuel cell electricity vehicle production. IEA 2030 Government targets (vertical dash blue)[60] and upper limit scenario given by upper 2040 WPIC (vertical dash purple).[59] Figure design is inspired from Hubert et al.[64] Reproduced from ref [28] under Creative Commons CC BY 3.0.

7.4 Discussion

In this section, I engage a discussion of the results in relation to prior research and their methodologies. The evaluation of Pt/C revealed an emission of 8.4 kg CO_2-eq kW^{-1}, based on 0.125 mg_{Pt} cm^{-2}, when normalized to power for the global warming impact. Various previous reports (as summarized in Figure S8) calculated a range between 6.5 and 14.6 CO_2-eq kW^{-1}, with catalyst loadings spanning from 0.15 to 0.60 mg_{Pt} cm^{-2}.[15,16,34,65] Notably, these assessments did not account for the impact of preparing the catalyst inks for deposition. Discrepancies in environmental impacts arise from variations in impact factors across background database processes, diverse assumed performance of Pt-based catalysts, and differences in Pt compositions. Earlier findings have highlighted that the Pt-based catalyst constitutes a significant proportion, ranging from 6% to 24%, of the total global warming contribution for a fuel cell stack.[15,34,65] Additionally, according to the discoveries of Usai *et al*.,[65] the Pt-based catalyst plays a substantial role across other impact categories, contributing between 33-76%, although other components also contribute to the environmental impact during the manufacture of PEMFC vehicles. Notably, as Evangelisti *et al*. highlighted,[34] even with zero Pt loading, fuel cell vehicles during the manufacturing phase could still exhibit a higher environmental impact compared to internal combustion engine vehicles.

The optimization of the heating temperature, rate, duration, and the number of pyrolysis steps in the production of Fe-N-C catalysts merits careful consideration due to the substantial environmental impact resulting from the energy-intensive nature of these processes. A study by James et al.[25] highlighted that in a poly-aniline derived Fe-N-C production, operating at 500,000 systems $year^{-1}$, manufacturing costs were primarily attributed to the acid washing process (49%), while the carbon support constituted the most substantial material cost (34%). In this context, they estimated the Fe-N-C cost to range between 74 -129 USD kg^{-1},[25] which aligns closely with findings here (90.8 USD kg^{-1} with F = 86.4%). Notably, in their investigation, the one-hour pyrolysis in a rotary kiln only contributed to 3% of the manufacturing costs, whereas in this work, I scaled the electricity input for the Fe-N-C manufacturing process based on a tube furnace approach. Specifically, it is observed that significant reductions in electricity requirements, costs, and subsequently, environmental impacts of Fe-N-C production, could be achieved by utilizing a muffle furnace (**Figure 7.4d-f**). Further reductions in energy

consumption could be realized when manufacturing Fe-N-C at scale through the implementation of heat integration techniques such as pinch analysis. These reductions would enable the low technology readiness of the Fe-N-C catalyst to attain electricity consumption levels that are more comparable to those of the high technology readiness optimized Pt/C process.

Considering the carbon intensity of electricity, it is important to highlight that the EU is targeting carbon-neutrality in its electricity production by 2040. In such a scenario, the cumulative impact of Fe-N-C on climate change, human health, ecosystems quality, and resources would all become negligible compared to those associated with Pt/C. Notably, in countries where the electricity mix includes a substantial share of renewables, as exemplified by Sweden (the location of the commercial Fe-N-C manufacturer Celcibus AB), the environmental impacts of Fe-N-C production would be significantly alleviated (as demonstrated in **Figures D2** & **D3**). Additionally, the impact on human toxicity could be further mitigated through the adoption of alternative production methods, such as those that eliminate the use of HF (**Figure D1e**).

In the context of degradation, it is important to note the recent advancements in LCA models that incorporate degradation effects, as demonstrated by Stropnik *et al*.[66] and the integration of durability-adjusted operating conditions for TEA models, as highlighted by James *et al*.[67] In this study, the degradation of the PEMFC was not considered due to the practical requirements for light-duty automotive applications, which necessitate meeting the stringent US DOE target of 8,000 hours,[29] or the corresponding EU 2030 targets of 7,000 hours.[52] Current research indicates that while high-activity Fe-N-C catalysts have only been tested for several hundred hours in PEMFCs,[7] they could potentially be partially regenerated in-situ for short periods using simple electrochemical protocols.[68]. This stands in contrast to Pt catalysts, which require an ex-situ recovery process for regeneration. It is worth mentioning that Fe-N-C based catalysts may also find applications in small-scale, short-term backup power scenarios, as evidenced by the emergency power/Wi-Fi backpack recently showcased by Ballard System Ltd. and Nisshinbo.[69]

In the realm of Pt-based PEMFCs, significant advancements have been made over the past three decades, resulting in an order of magnitude reduction (as depicted in Figure S9). Notably, Toyota has achieved a 72% reduction, from 0.93±0.25 to 0.26±0.07 g_{Pt} kW^{-1}, in their

2008 PEMFC model, followed by an additional 58% reduction to 0.11±0.03 g_{Pt} kW^{-1} in their 2020 2nd generation Mirai.[53] The EU has set targets to reduce the Pt content in PEMFCs to 0.05 g_{Pt} kW^{-1} by 2030;[52] however, there are concerns that increased Pt instability at these reduced future target loadings might impede their realization.[70] Nevertheless, the convergence of ideal scenarios involving Pt reduction and the fulfilment of recycling targets could lead to minimal environmental impacts.

Regarding the analysis of the learning curve, the typical range for F values spans from 74%-95%[55,57] with 86.4% chosen as the nominal value in this study. As emphasized in the Results section, the F value significantly influences the stack costs. Predicting the actual realized F value remains challenging; however, based on the previously observed minimum F value of 74%, an 80 kW Fe-N-C-based PEMFC would need to exhibit an improvement of at least 34% from 290 mW cm-2 to be on par with the Pt/C-based system delivering 1,160 mW cm-2. Similarly, current non-precious metal hydrogen evolution catalysts for proton exchange membrane electrolysers demonstrate a similar requirement for enhanced performance across most operating regimes to replace precious metal catalysts.[64]

Future work could consider the effect on Fe-N-C LCA for other common synthetic strategies, such as recent state-of-the-art Fe-N-C derived from zeolitic imidazolate framework 8.[7] Broader environmental contextualization in terms of planetary boundaries or comparison to other technologies, such as batteries, would also provide further critical insights. Future comparison of the use and disposal phase of the catalysts could be developed based on degradation[66] and recycling.[20] Design for manufacture and assembly methodology could be used to track annual cost impact of catalyst developments.[67]

7.5 Conclusion

In this chapter I presented a comparative analysis of various scenarios in terms of LCA and TEA to produce a silica-templated Fe-N-C and a Pt/C cathode catalyst, in constructing an 80 kW PEMFC stack. The findings indicate that electricity consumption and Pt mining constitute the primary drivers of environmental impacts and costs in the manufacturing of Fe-N-C and Pt/C catalysts, respectively. The application of monetization factors reveals that the cost of environmental impact exceeds the material and processing costs for both catalysts. At an annual production rate of 500,000 stacks, the transition from Pt/C to Fe-N-C could reduce the material and processing cost of the cathode catalyst from 2.92 to 0.79 USD kW^{-1}. However, the increased cost of all other components stemming from the roughly fourfold greater surface area of the Fe-N-C cathode system results in a PEMFC stack cost of 41.6 USD kW^{-1}, in contrast to 13.8 USD kW^{-1} for Pt/C. At the nominal F value of 86.4%, an Fe-N-C-based PEMFC would need to achieve 874 mW cm^{-2} at 0.657 V, equivalent to a 200% improvement in performance, to attain the same PEMFC stack cost as the 0.125 mg_{Pt} cm^{-2} Pt/C cathode catalyst delivering 1,160 mW cm^{-2}. This underscores the necessity for further enhancements in the activity of Fe-N-C cathode catalysts, while the substantial discrepancy in durability between Fe-N-Cs and Pt/C has yet to be considered. Lastly, I considered whether the current Pt supply can meet the anticipated Pt demand from PEMFC deployment for FCEV production.

References

1 S. T. Thompson and D. Papageorgopoulos, *Nat. Catal.*, 2019, **2**, 558–561.
2 B. D. James, J. M. Huya-Kouadio, C. Houchins and D. A. DeSantis, *Mass Production Cost Estimation of Direct H2 PEM Fuel Cell Systems for Transportation Applications: 2018 Update*, 2018.
3 Johnson Matthey, *PGM market report, May*, 2022.
4 European Commission, *Critical Raw Materials Resilience: Charting a Path towards greater Security and Sustainability*, 2020.
5 British Geological Survey, *UK criticality assessment of technology critical minerals and metals*, 2022.
6 S. T. Thompson, A. R. Wilson, P. Zelenay, D. J. Myers, K. L. More, K. C. Neyerlin and D. Papageorgopoulos, *Solid State Ion.*, 2018, **319**, 68–76.
7 S. Liu, C. Li, M. J. Zachman, Y. Zeng, H. Yu, B. Li, M. Wang, J. Braaten, J. Liu, H. M. Meyer, M. Lucero, A. J. Kropf, E. E. Alp, Q. Gong, Q. Shi, Z. Feng, H. Xu, G. Wang, D. J. Myers, J. Xie, D. A. Cullen, S. Litster and G. Wu, *Nat. Energy*, 2022, **7**, 652–663.
8 B. Koyutürk, E. M. Farber, F. E. Wagner, T.-P. Fellinger and D. Eisenberg, *J. Mater. Chem. A*, 2022, **10**, 19859–19867.
9 J. Feng, R. Cai, E. Magliocca, H. Luo, L. Higgins, G. L. F. Romario, X. Liang, A. Pedersen, Z. Xu, Z. Guo, A. Periasamy, D. Brett, T. S. Miller, S. J. Haigh, B. Mishra and M.-M. Titirici, *Adv. Funct. Mater.*, 2021, **31**, 2102974.
10 Pajarito Powder LLC, *Active and Durable PGM-free Cathodic Electrocatalysts for Fuel Cell Application*, 2021.
11 Pajarito Powder, https://pajaritopowder.com/, (accessed September 10, 2021).
12 D. Banham, T. Kishimoto, Y. Zhou, T. Sato, K. Bai, J. I. Ozaki, Y. Imashiro and S. Ye, *Sci. Adv.*, 2018, **4**, eaar7180.
13 *Fuel Cells Bull.*, 2017, **2017**, 1.
14 Celcibus AB, https://celcibus.com/, (accessed September 30, 2023).
15 M. Miotti, J. Hofer and C. Bauer, *Int. J. Life Cycle Assess.*, 2017, **22**, 94–110.
16 C. Bauer, J. Hofer, H. J. Althaus, A. Del Duce and A. Simons, *Appl. Energy*, 2015, **157**, 871–883.
17 R. Stropnik, A. Lotrič, A. Bernad Montenegro, M. Sekavčnik and M. Mori, *Energy Sci. Eng.*, 2019, **7**, 2519–2539.
18 S. Kosai and E. Yamasue, *Sci. Total Environ.*, 2019, **651**, 1764–1775.
19 M. Mori, D. Iribarren, J. Cren, E. Cor, A. Lotrič, J. Gramc, B. Drobnič, L. Rey, F. Campos-Carriedo, G. Puig-Samper, E. Bargiacchi, J. Dufour and R. Stropnik, *Int. J. Hydrog. Energy*, 2023, 1–17.
20 L. Duclos, R. Chattot, L. Dubau, P. X. Thivel, G. Mandil, V. Laforest, M. Bolloli, R. Vincent and L. Svecova, *Green Chem.*, 2020, **22**, 1919–1933.
21 L. Duclos, L. Svecova, V. Laforest, G. Mandil and P.-X. Thivel, *Hydrometallurgy*, 2016, **160**, 79–89.
22 M. Mori, A. Lotric and R. Stropnik, *D4.3 Case studies with new strategiesin dismantling and recycling stage (HyTechCycling)*, Ljubljana, 2019.
23 J. Cren, J. A. Jacques, C. Paulus, R. Couturier and B. Andre, *PEGASUS: D4.1-Life Cycle Assessment*, 2021.
24 H. A. Gasteiger, S. S. Kocha, B. Sompalli and F. T. Wagner, *Appl. Catal. B Environ.*, 2005, **56**, 9–35.

25 B. D. James, *DOE Hydrogen and Fuel Cells Program Review Fuel Cell Vehicle and Bus Cost Analysis*, 2015.
26 G. Wernet, C. Bauer, B. Steubing, J. Reinhard, E. Moreno-Ruiz and B. Weidema, *Int. J. Life Cycle Assess.*, 2016, **21**, 1218–1230.
27 ISO 14040, *Environmental management—life cycle assessment—principles and framework*, 2006.
28 A. Pedersen, J. Pandya, G. Leonzio, A. Serov, A. Bernardi, I. Stephens, M.-M. Titirici, C. Petit and B. Chachuat, *Green Chem.*, 2023, **25**, 10458–10471.
29 US DOE - Hydrogen and Fuel Cell Technologies Office, *Hydrogen and Fuel Cell Technologies Office Multi-Year Research, Development, and Demonstration Plan. Section 3.4: Fuel Cells*, 2017.
30 M. Inaba, J. Quinson, J. R. Bucher and M. Arenz, *J. Vis. Exp.*, 2018, **2018**, 1–10.
31 M. Chourashiya, R. Sharma, S. Gyergyek and S. M. Andersen, *Mater. Chem. Phys.*, 2022, **276**, 125439.
32 B. D. James, J. M. Huya-Kouadio, C. Houchins and D. A. DeSantis, *Final Report: Mass Production Cost Estimation of Direct H2 PEM Fuel Cell Systems for Transportation Applications (2012-2016)*, Strategic Analysis Inc., Golden, CO (United States), 2016.
33 S. Evangelisti, C. Tagliaferri, D. Brett and P. Lettieri, in *Modern Developments in Catalysis*, World Scientific, 2017, pp. 289–312.
34 S. Evangelisti, C. Tagliaferri, D. J. L. Brett and P. Lettieri, *J. Clean. Prod.*, 2017, **142**, 4339–4355.
35 F. Piccinno, R. Hischier, S. Seeger and C. Som, *J. Clean. Prod.*, 2016, **135**, 1085–1097.
36 A. Serov, B. Halevi, K. Artyushkova, P. Atanassov and U. Martinez, *NON-PGM CATHODE CATALYSTS FOR FUEL CELL APPLICATION DERIVED FROM HEAT RREATED HETEROATOMIC AMINES PRECURSORS (9,634, 331)*, 2017.
37 A. Serov, B. Halevi, K. Artyushkova and P. Atanassov, *CATHODE CATALYSTS FOR FUEL CELLS (9,515,323)*, 2016.
38 A. Serov and P. Atanassov, *NON-PGM CATALYSTS FOR ORR BASED ON CHARGE TRANSFER ORGANIC COMPLEXES (9,673,456)*, 2017.
39 Fuel Cell and Hydrogen - Joint Undertaking, *Guidance Document for performing LCAs on Fuel Cells and H_2 Technologies*, 2011.
40 R. Clift, A. Doig and G. Finnveden, *Process Saf. Environ. Prot.*, 2000, **78**, 279–287.
41 M. A. J. Huijbregts, Z. J. N. Steinmann, P. M. F. Elshout, G. Stam, F. Verones, M. Vieira, M. Zijp, A. Hollander and R. van Zelm, *Int. J. Life Cycle Assess.*, 2017, **22**, 138–147.
42 V. Aryan, M. Font-Brucart and D. Maga, *Prog. Photovolt. Res. Appl.*, 2018, **26**, 443–459.
43 B. P. Weidema, *J. Ind. Ecol.*, 2015, **19**, 20–26.
44 M. Pizzol, B. Weidema, M. Brandão and P. Osset, *J. Clean. Prod.*, 2015, **86**, 170–179.
45 Y. Dong, M. Hauschild, H. Sørup, R. Rousselet and P. Fantke, *J. Clean. Prod.*, 2019, **209**, 538–549.
46 H. A. Baaqel, A. Bernardi, J. P. Hallett, G. Guillén-Gosálbez and B. Chachuat, *ACS Sustain. Chem. Eng.*, 2023, **11**, 7157–7169.
47 S. Kotz and J. R. V. Dorp, *Beyond Beta: Other Continuous Families Of Distributions With Bounded Support And Applications*, World Scientific, 2004.
48 I. M. Sobol, *Global sensitivity indices for nonlinear mathematical models and their Monte Carlo estimates*, 2001, vol. 55.
49 R. S. C. Lambert, F. Lemke, S. S. Kucherenko, S. Song and N. Shah, *Math. Comput. Simul.*, 2016, **128**, 42–54.

50 L. Duclos, M. Lupsea, G. Mandil, L. Svecova, P.-X. Thivel and V. Laforest, *J. Clean. Prod.*, 2017, **142**, 2618–2628.
51 A. Valente, D. Iribarren and J. Dufour, *Int. J. Hydrog. Energy*, 2019, **44**, 20965–20977.
52 *Fuel Cells and Hydrogen 2 Joint Undertaking Key Performance Indicators*, 2021.
53 T. Yoshizumi, H. Kubo and M. Okumura, *SAE Tech. Pap.*, 2021, **2021-01–0740**, 1–6.
54 A. Cosenza, L. Delafontaine, A. Ly, H. Wang, E. Murphy, Y. Liu, S. Specchia and P. Atanassov, *J. Power Sources*, 2023, **556**, 1–10.
55 H. Tsuchiya and O. Kobayashi, *Int. J. Hydrog. Energy*, 2004, **29**, 985–990.
56 P. Mock and S. A. Schmid, *J. Power Sources*, 2009, **190**, 133–140.
57 Batelle, *Manufacturing Cost Analysis of 100 and 250 kW Fuel Cell Systems for Primary Power and Combined Heat and Power Applications*, 2010, vol. 98.
58 Johnson Matthey, PGM prices and trading, https://matthey.com/products-and-markets/pgms-and-circularity/pgm-management, (accessed December 20, 2022).
59 T. Raymond, E. Sterck and B. Clifford, *PLATINUM ESSENTIALS Fuel cell electric vehicles are forecast to drive material long-term demand growth for platinum*, 2022.
60 International Energy Agency, *The Future of Hydrogen*, 2019.
61 A. B. Laursen, J. Sehested, I. Chorkendorff and P. C. K. Vesborg, *Chin. J. Catal.*, 2018, **39**, 16–26.
62 G. Reverdiau, A. Le Duigou, T. Alleau, T. Aribart, C. Dugast and T. Priem, *Int. J. Hydrog. Energy*, 2021, **46**, 39195–39207.
63 K. D. Rasmussen, H. Wenzel, C. Bangs, E. Petavratzi and G. Liu, *Environ. Sci. Technol.*, 2019, **53**, 11541–11551.
64 M. A. Hubert, L. A. King and T. F. Jaramillo, *ACS Energy Lett.*, 2022, **7**, 17–23.
65 L. Usai, C. R. Hung, F. Vásquez, M. Windsheimer, O. S. Burheim and A. H. Strømman, *J. Clean. Prod.*, 2021, **280**, 125086.
66 R. Stropnik, N. Mlakar, A. Lotrič, M. Sekavčnik and M. Mori, *Int. J. Hydrog. Energy*, 2022, **47**, 24223–24241.
67 B. D. James, *Fuel Cell Cost and Performance Analysis 2022 DOE Hydrogen and Fuel Cells Program Annual Merit Review and Peer Evaluation Meeting Presentation*, 2022.
68 P. Boldrin, D. Malko, A. Mehmood, U. I. Kramm, S. Wagner, S. Paul, N. Weidler and A. Kucernak, *Appl. Catal. B Environ.*, 2021, **292**, 120169.
69 D. Banham, J. Y. Choi, T. Kishimoto and S. Ye, *Adv. Mater.*, 2019, **31**, 1–6.
70 G. P. Keeley, S. Cherevko and K. J. J. Mayrhofer, *ChemElectroChem*, 2016, **3**, 51–54.

Chapter 8: Concluding Remarks

8.1 Conclusion

The chapters in this thesis outline significant advancements in the development of:

Chapter 4) A synthesis pathway for record high active site utilisation Fe-N-C, which is thoroughly characterised. The synthesis method opens avenues to development of highly porous M-N-C materials suitable for various applications (electrochemical CO_2 reduction, supercapacitor, electrochemical CO_2 swing adsorption). The impact of axial ligands and N coordination environment on O_2 reduction activity is also highlighted.

Chapter 5) Understanding the *operando* Fe dissolution mechanism of Fe-N-C in 0.1 M $HClO_4$ under a range of conditions (O_2 vs Ar, 0-100 mA cm^{-2}, 20°C and 75°C). The insights gained from kinetic modelling exposes the significant local pH increase in the catalyst layer under O_2 GDE at 20°C, which leads to formation of Fe_2O_3. This indicates GDEs with thick catalyst layers should be avoided.

Chapter 6) Electrochemical tools and methods (EIS, FTacV and DRT) for optimising M-N-C PEMFC performance. Critically, I demonstrate site density and PEMFC performance continue to improve at unprecedented high I/C values (>2.8), owing to the high mesoporosity. There is, however, a trade-off between improved site density and other parameters, such as electronic conductivity and O_2 mass transport.

Chapter 7) LCA as a tool to compare environmental impacts of electrocatalysts. The LCA has informed more sustainable synthesis pathways based on “hot spot” steps such as pyrolysis. The monetized environmental externalities highlight the impact of the synthesis pathway. From this work, a new performance target for M-N-C to compete with Pt-based catalysts is calculated based on a techno-economic approach.

No research is without its shortcomings. These are discussed below:

Chapter 4) It has recently come to light that in situ nitrite stripping can also probe N-C sites.[1,2] To accurately determine the N-C site in TAP 900@Fe requires a range of Fe loadings due to the Mg templating approach, where MgN_x could also be probed by nitrite stripping. While TAP 900@Fe shows impressive active site density, the TOF is very low, meaning the O_2 activity is not state-of-the-art. Alternative metal loading approaches could be employed in future to improve the intrinsic TOF of the FeN_x sites.

Chapter 5) Based on optimum I/C results in Chapter 5 (2.1<I/C<4.9), it may be that the I/C ratio used in GDE (I/C = 1.4) restricted performance. The lower ionomer coverage could then influence the degradation mechanism. Also, based on the uniquely high porosity and surface area of the Fe-N-C studied, the results and mechanisms may not be representative of other Fe-N-Cs.

Chapter 6) EIS measurements were not conducted at high current (or low potential), which would better reveal the impact of mass transport. PEMFC performance was also only evaluated under H_2-O_2, rather than more practical H_2-air. The work did not investigate how the ionomer is distributed through catalyst layer, using methods such as nano-computed tomography.

Chapter 7) In the LCA, the impact of Nafion, which has a large environmental impact, is not considered. Also, the use phase and disposal of the catalysts is not evaluated, although this is based on the fact the current Fe-N-C stability is far below that of Pt/C and the study was not a prospective LCA.

Avenues for future research in the context of chapters in this thesis and the wider M-N-C community are discussed in the next section.

8.2 Future Work and Perspectives

8.2.1 Stability

8.2.1.1 Predicting Stability with Descriptors

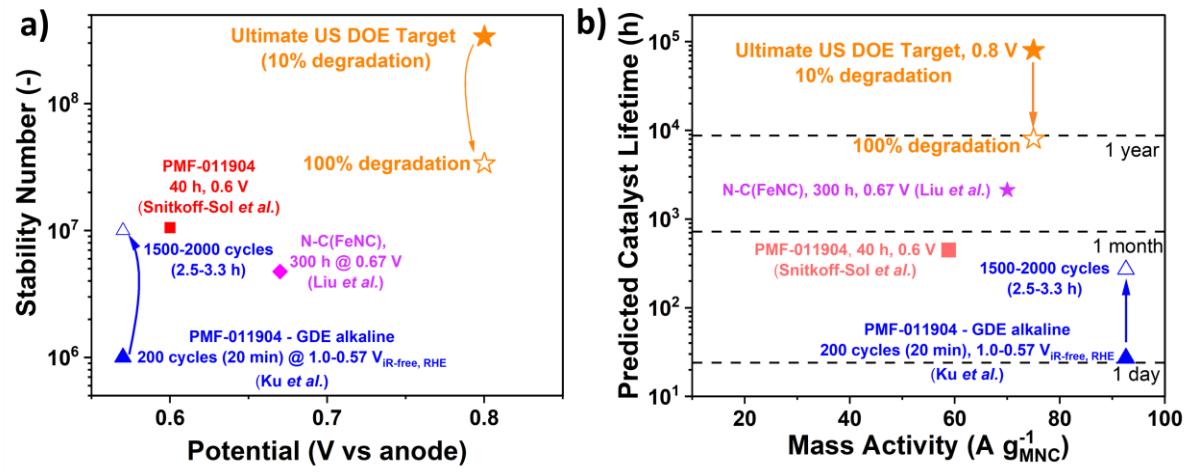


Figure 8.1. a.) Stability Number and b.) Predicted Catalyst Lifetime. Ultimate US DOE light duty vehicle target of 8,000 h (with 10% degradation) at 0.3 A cm^{-2} and 0.8 V_{RHE} (equivalent to 75 A $g_{M\text{-}N\text{-}C}^{-1}$ based on 4 $mg_{M\text{-}N\text{-}C}$ cm^{-2} and 1 x 10^{20} sites $g_{M\text{-}N\text{-}C}^{-1}$). Plus predicted catalyst lifetime and initial measured mass activity for reports of Fe-N-C: Snitkoff-Sol et al.[3] Pajarito Powder FeNC (PMF 011904) 40 h at 0.6 V (H_2/O_2 300 cm^3 min^{-1}, 1 bar_g). Liu et al.[4] N-C(FeNC) 300 h at 0.67 V (H_2/air 200 cm^3 min^{-1}). Ku et al.[5] PMF 011904 FeNC 1.0 to 0.57 $V_{iR\text{-}free\ RHE}$ (0 to -125 mA cm^{-2}) with 3 s holds (GDE, 0.1 M NaOH). Figure b.) reproduced from reference [6] under Creative Commons CC-BY 3.0.

It is crucial to devise techniques and descriptors capable of forecasting a catalyst's lifespan through a fundamental comprehension at the active site level. In this regard, Cherevko and collaborators introduced the stability number, *S*, often referred to as the electrochemical turnover number. This parameter is applicable to all electrocatalysts and facilitates the calculation of the anticipated catalyst lifespan (as shown in **Equation 8.1**).[7]

$$t = \frac{S \times z \times F \times m}{j \times M} \qquad \textbf{Equation 8.1}$$

t stands for the lifetime of the active metal (s). *z* signifies the number of electrons consumed per O_2 molecule (assume 4). *F* corresponds to the Faraday constant (96,485 C mol^{-1}). *m* denotes the mass of the accessible active element (g cm^{-2}). *j* represents the current density (A cm^{-2}). *M* is the molar mass of the active element (g mol^{-1}).

To meet the ultimate U.S. Department of Energy (DOE) PEMFC target of 8,000 hours with less than 10% degradation at 0.3 A cm^{-2} and 0.8 V, a stability number of 3.37×10^8 is required. In terms of mass activity, it equals 75 A $g_{M\text{-}N\text{-}C}^{-1}$ based on 4 $mg_{M\text{-}N\text{-}C}$ cm^{-2} and 1×10^{20} sites $g_{M\text{-}N\text{-}C}$. Although the stability number and lifetime of M-N-C in acidic electrolytes or PEMFC have not

been reported thus far, they can be estimated. Extrapolating from state-of-the-art nitrogen-carbon coated Fe-N-C (N-C(Fe-N-C)) by Liu *et al*.,[4] a feasible lifetime of 2,121 hours at 0.67 V with an initial current density of approximately 70 A g_{FeNC}^{-1} can be projected (**Figure 8.1**). Catalyst lifetime can also be estimated by tracking changes in site density, as demonstrated by Elbaz and colleagues.[3] For a commercial Fe-N-C (Pajarito Powder PMF-011904), the catalyst's predicted lifetime in PEMFC, evaluated after a 40-hour hold at 0.6 V, was 447 hours at 58.8 A g^{-1} (**Figure 8.1**).[3]

The catalyst lifetime calculated from the stability number may overestimate PEMFC operation longevity, as not all catalyst degradation pathways directly impact the number of active sites (e.g., attack from reactive oxygen species reducing TOF), and some degree of activity recovery is possible. It is, therefore, essential to gain a better understanding of these complexities, where separating the influences of distinct degradation mechanisms can help pinpoint crucial factors affecting the stability of M-N-C catalysts.[8] Although it poses challenges, the development of rates and descriptors for these various degradation pathways would provide valuable insights to the scientific community.

8.2.1.2 Improving Stability

One of the most significant challenges faced with M-N-C catalysts is stabilizing the inherently high surface energy of low-coordinated single atoms. Moreover, there is a dilemma where catalysts that are intrinsically active tend to be less stable. For instance, Liu *et al.* showed by providing atomic N-C coating to their Fe-N-C they could enhance stability, although with a noticeable reduction in activity.[4] Still, this method opens new avenues for research, including exploring other potentially more stable coatings and using controlled deposition techniques for model studies, such as atomic layer deposition.

Other strategies to enhance stability include modifying the catalyst support; for example, boron carbide has been used in Pt-based catalysts for this purpose.[9] Additionally, nanoparticle radical scavengers have proven effective in minimizing oxidative attack,[10–12] although they may block active sites and not be optimally situated near active sites. More desirable scavengers could be single atom scavengers doped within the catalyst support,[11] located near the active site due to the short lifetime of reactive oxygen species. Secondary metal atoms are often doped within M-N-C to improve activity and stability, with some initial investigations beginning to understand the improvement in performance.[13] Pt atoms have been successfully

incorporated into Fe-N-C with performance improvement understood,[14] although more cost-effective dopants are desirable for future applications.

Beyond enhancing the degradation resistance of the catalyst, tuning the operating conditions of PEMFCs can also minimize catalyst degradation. This can be accomplished through model development, identifying key degradation parameters, as demonstrated for Pt-based catalysts.[15]

8.2.2 Synthesis

The primary limitation in the synthesis of M-N-Cs hitherto has been the pyrolysis phase, which induces conductivity and activates the N-C scaffold. Following this step, the resulting material exhibits a somewhat stochastic arrangement and dispersion of atomic constituents, thereby constraining precise control over the active site. An intrinsically electrically conductive MOF containing Ni-N_4 sites has demonstrated notable efficacy in H_2O_2 production without the necessity for a pyrolysis step.[16] However, this achievement was only realized once the issue of mass transport limitation was accounted for.[16] Future efforts can thus focus on enhancing mass transport in such MOF materials and fine-tuning selectivity towards H_2O production for PEMFCs. Moreover, these well-defined crystalline catalysts would facilitate fundamental and model studies that have not been feasible thus far for M-N-Cs.

8.2.3 Characterisation

A significant challenge in working with M-N-Cs lies in their characterization, often necessitating access to national synchrotron facilities and specialized microscopy tools. Increasing the density of active sites within these materials could allow the utilization of techniques that were previously insensitive due to their detection limits. For example, advancements in laboratory-based X-ray absorption equipment, such as those offered by easyXAFS LLC, may be applicable to certain high-loading single atom M-N-C catalysts. Additionally, laboratory-based X-ray pair distribution function (XPDF) is an underutilized technique within the community, holding the potential to provide spatial resolution of the local and longer-range order of the M-N-C structure.

Nevertheless, it is essential for the scientific community to exercise caution when drawing conclusions from bulk characterization techniques. As discussed in **Chapter 4**, a significant portion (typically ranging from 70% to 90%) of active sites in M-N-C materials are often not

electrochemically engaged (based on 5 e^- nitrite stripping).[17,18] Consequently, operando characterization techniques that probe the entire bulk of M-N-C layers, such as Mössbauer spectroscopy, XAS, or XPDF, will measure both accessible and inaccessible active sites. This complicates the separation of the contributions of activity and stability among various MN_x sites. To address this challenge, a potential solution is to combine in situ electrochemical probing techniques, like FTacV, with bulk operando techniques, such as XAS or Mossbauer spectroscopy.

8.2.4 Optimising PEMFC Performance

To achieve high-performance M-N-C-based proton exchange membrane fuel cells (PEMFCs), it is crucial to consider both the catalyst's active site and the design and morphology of the catalyst layer simultaneously. Previous reports on PEMFC performance have largely focussed on meeting the US DOE activity targets of 0.044 A cm^{-2} at 0.9 $V_{RHE,\ iR\text{-}free}$.[19] However, for practical applications, achieving the U.S. DOE activity target of 0.3 A cm^{-2} at 0.8 V_{RHE} is even more critical. To meet high current demands, the catalyst layers in PEMFCs must be approximately ten times thicker when using M-N-C catalysts due to their lower mass activity compared to Pt/C. This necessitates further research in the design of thicker electrodes with optimized pore structures and properties that minimize losses in proton and electron conductivity while ensuring sufficient O_2 accessibility. Nature can serve as a source of inspiration for catalyst layer design.[20] New architectural concepts, such as grooving,[21] can also be explored for M-N-C catalysts. Techniques for engineering, manufacturing, and characterizing thick electrodes can be adapted from the battery literature.[22] Furthermore, gaining a better understanding of gas and water flow within thick M-N-C cathode layers is essential for comprehending and optimizing PEMFC performance. This could be achieved through multi-phase modelling, possibly employing deep learning methodologies, as demonstrated recently for a Pt-based PEMFC system.[23]

8.2.5 M-N-C: Beyond PEMFCs and electrocatalysis

The extensive research conducted on M-N-C catalysts for oxygen reduction has generated a substantial repository of well-characterized materials that can serve as a foundation for advancements in other fields. In essence, these endeavours enable subsequent research to "stand on the shoulders of giants." In electrocatalysis beyond O_2 reduction, M-N-C have been shown as efficient and selective for CO_2 reduction to CO,[24,25] nitrite reduction to ammonia,[26]

and recently carbonyl reduction.[27] Meanwhile, beyond electrocatalysts, M-N-C have been demonstrated for thermo-catalytic aerobic oxidation,[28] hydrogenation,[29] enzyme mimicking for synthetic drug exploration,[30] among others. This diverse range of applications suggests that commercial opportunities for M-N-Cs may extend beyond the realm PEMFCs.

References

1 M. Gong, A. Mehmood, B. Ali, K.-W. Nam and A. Kucernak, *ACS Catal.*, 2023, **13**, 6661–6674.
2 A. Mehmood, M. Gong, F. Jaouen, A. Roy, A. Zitolo, A. Khan, M. Sougrati, M. Primbs, A. M. Bonastre, D. Fongalland, G. Drazic, P. Strasser and A. Kucernak, *Nat. Catal.*, 2022, **5**, 311–323.
3 R. Z. Snitkoff-Sol, A. Friedman, H. C. Honig, Y. Yurko, A. Kozhushner, M. J. Zachman, P. Zelenay, A. M. Bond and L. Elbaz, *Nat. Catal.*, 2022, **5**, 163–170.
4 S. Liu, C. Li, M. J. Zachman, Y. Zeng, H. Yu, B. Li, M. Wang, J. Braaten, J. Liu, H. M. Meyer, M. Lucero, A. J. Kropf, E. E. Alp, Q. Gong, Q. Shi, Z. Feng, H. Xu, G. Wang, D. J. Myers, J. Xie, D. A. Cullen, S. Litster and G. Wu, *Nat. Energy*, 2022, **7**, 652–663.
5 Y.-P. Ku, K. Ehelebe, A. Hutzler, M. Bierling, T. Böhm, A. Zitolo, M. Vorokhta, N. Bibent, F. D. Speck, D. Seeberger, I. Khalakhan, K. J. J. Mayrhofer, S. Thiele, F. Jaouen and S. Cherevko, *J. Am. Chem. Soc.*, 2022, **144**, 9753–9763.
6 A. Pedersen, A. Bagger, J. Barrio, F. Maillard, I. Stephens and M.-M. Titirici, *J. Mater. Chem. A*, 2023, **11**, 23211–23222.
7 S. Geiger, O. Kasian, M. Ledendecker, E. Pizzutilo, A. M. Mingers, W. T. Fu, O. Diaz-Morales, Z. Li, T. Oellers, L. Fruchter, A. Ludwig, K. J. J. Mayrhofer, M. T. M. Koper and S. Cherevko, *Nat. Catal.*, 2018, **1**, 508–515.
8 S. Ünsal, R. Girod, C. Appel, D. Karpov, M. Mermoux, F. Maillard, V. A. Saveleva, V. Tileli, T. J. Schmidt and J. Herranz, *J. Am. Chem. Soc.*, 2023, **145**, 7845–7858.
9 C. Jackson, G. T. Smith, D. W. Inwood, A. S. Leach, P. S. Whalley, M. Callisti, T. Polcar, A. E. Russell, P. Levecque and D. Kramer, *Nat. Commun.*, 2017, **8**, 1–11.
10 H. Xie, X. Xie, G. Hu, V. Prabhakaran, S. Saha, L. Gonzalez-Lopez, A. H. Phakatkar, M. Hong, M. Wu, R. Shahbazian-Yassar, V. Ramani, M. I. Al-Sheikhly, D. Jiang, Y. Shao and L. Hu, *Nat. Energy*, 2022, **7**, 281–289.
11 Y. Chu, E. Luo, Y. Wei, S. Zhu, X. Wang, L. Yang, N. Gao, Y. Wang, Z. Jiang, C. Liu, J. Ge and W. Xing, *Chem Catal.*, 2023, **3**, 100532.
12 D. Shin, S. Bhandari, M. F. Tesch, S. A. Bonke, F. Jaouen, S. Chabbra, C. Pratsch, A. Schnegg and A. K. Mechler, *J. Energy Chem.*, 2022, **65**, 433–438.
13 F. Luo, A. Roy, M. T. Sougrati, A. Khan, D. A. Cullen, X. Wang, M. Primbs, A. Zitolo, F. Jaouen and P. Strasser, *J. Am. Chem. Soc.*, 2023, **145**, 14737–14747.
14 G. Bae, M. M. Kim, M. H. Han, J. Cho, D. H. Kim, M.-T. Sougrati, J. Kim, K.-S. Lee, S. H. Joo, W. A. Goddard, H.-S. Oh, H. Kim, F. Jaouen and C. H. Choi, *Nat. Catal.*, 2023, 1–11.
15 R. K. Ahluwalia, X. Wang, J.-K. Peng, V. Konduru, S. Arisetty, N. Ramaswamy and S. Kumaraguru, *J. Electrochem. Soc.*, 2021, **168**, 044518.
16 R. G. Mariano, O. J. Wahab, J. A. Rabinowitz, J. Oppenheim, T. Chen, P. R. Unwin and M. Dincă, *ACS Cent. Sci.*, 2022, **8**, 975–982.
17 M. Primbs, Y. Sun, A. Roy, D. Malko, A. Mehmood, M.-T. Sougrati, P.-Y. Blanchard, G. Granozzi, T. Kosmala, G. Daniel, P. Atanassov, J. Sharman, C. Durante, A. Kucernak, D. Jones, F. Jaouen and P. Strasser, *Energy Environ. Sci.*, 2020, **13**, 2480–2500.
18 J. Barrio, A. Pedersen, S. Ch. Sarma, A. Bagger, M. Gong, S. Favero, C.-X. Zhao, R. Garcia-Serres, A. Y. Li, Q. Zhang, F. Jaouen, F. Maillard, A. Kucernak, I. E. L. Stephens and M.-M. Titirici, *Adv. Mater.*, 2023, **35**, 2211022.
19 Office of Energy Efficiency and Renewable Energy, *Fuel Cell Technologies Office: Multi-Year Research, Development, and Demonstration Plan: 3.4 Fuel Cells*, Washington, 2016.
20 J. Barrio, A. Pedersen, S. Favero, H. Luo, M. Wang, S. Ch. Sarma, J. Feng, L. T. T. Ngoc, S. Kellner, A. Y. Li, A. B. Jorge Sobrido and M.-M. Titirici, *Chem. Rev.*, 2023, **123**, 2311–2348.
21 C. H. Lee, W. J. M. Kort-Kamp, H. Yu, D. A. Cullen, B. M. Patterson, T. A. Arman, S. Komini Babu, R. Mukundan, R. L. Borup and J. S. Spendelow, *Nat. Energy*, 2023, **8**, 685–694.

22 A. M. Boyce, D. J. Cumming, C. Huang, S. P. Zankowski, P. S. Grant, D. J. L. Brett and P. R. Shearing, *ACS Nano*, 2021, **15**, 18624–18632.
23 Y. D. Wang, Q. Meyer, K. Tang, J. E. McClure, R. T. White, S. T. Kelly, M. M. Crawford, F. Iacoviello, D. J. L. Brett, P. R. Shearing, P. Mostaghimi, C. Zhao and R. T. Armstrong, *Nat. Commun.*, 2023, **14**, 745.
24 W. Ju, A. Bagger, G.-P. Hao, A. S. Varela, I. Sinev, V. Bon, B. Roldan Cuenya, S. Kaskel, J. Rossmeisl and P. Strasser, *Nat. Commun.*, 2017, **8**, 1–9.
25 A. S. Varela, W. Ju, A. Bagger, P. Franco, J. Rossmeisl and P. Strasser, *ACS Catal.*, 2019, **9**, 7270–7284.
26 Z.-Y. Wu, M. Karamad, X. Yong, Q. Huang, D. A. Cullen, P. Zhu, C. Xia, Q. Xiao, M. Shakouri, F.-Y. Chen, J. Y. (Timothy) Kim, Y. Xia, K. Heck, Y. Hu, M. S. Wong, Q. Li, I. Gates, S. Siahrostami and H. Wang, *Nat. Commun.*, 2021, **12**, 2870.
27 W. Ju, A. Bagger, N. R. Saharie, S. Möhle, J. Wang, F. Jaouen, J. Rossmeisl and P. Strasser, *Commun. Chem.*, 2023, **6**, 1–6.
28 J. S. Bates, M. R. Johnson, F. Khamespanah, T. W. Root and S. S. Stahl, *Chem. Rev.*, 2023, **123**, 6233–6256.
29 A. Y. Li, A. Pedersen, J. Feng, H. Luo, J. Barrio, J. Roman, K. K. (Mimi) Hii and M.-M. Titirici, *Green Chem.*, 2022, **24**, 7574–7583.
30 X. Liu, J. Li, A. Zitolo, M. Gao, J. Jiang, X. Geng, Q. Xie, D. Wu, H. Zheng, X. Cai, J. Lu, F. Jaouen and R. Li, *J. Am. Chem. Soc.*, 2023, **145**, 3108–3120.

Appendix A (Chapter 4): Synthesis of a Porous and High Active Site Utilisation Fe-N-C with Penta Coordination via Mg templating

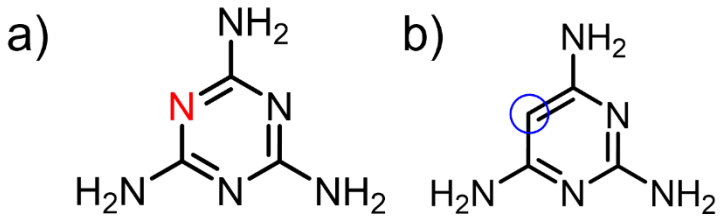
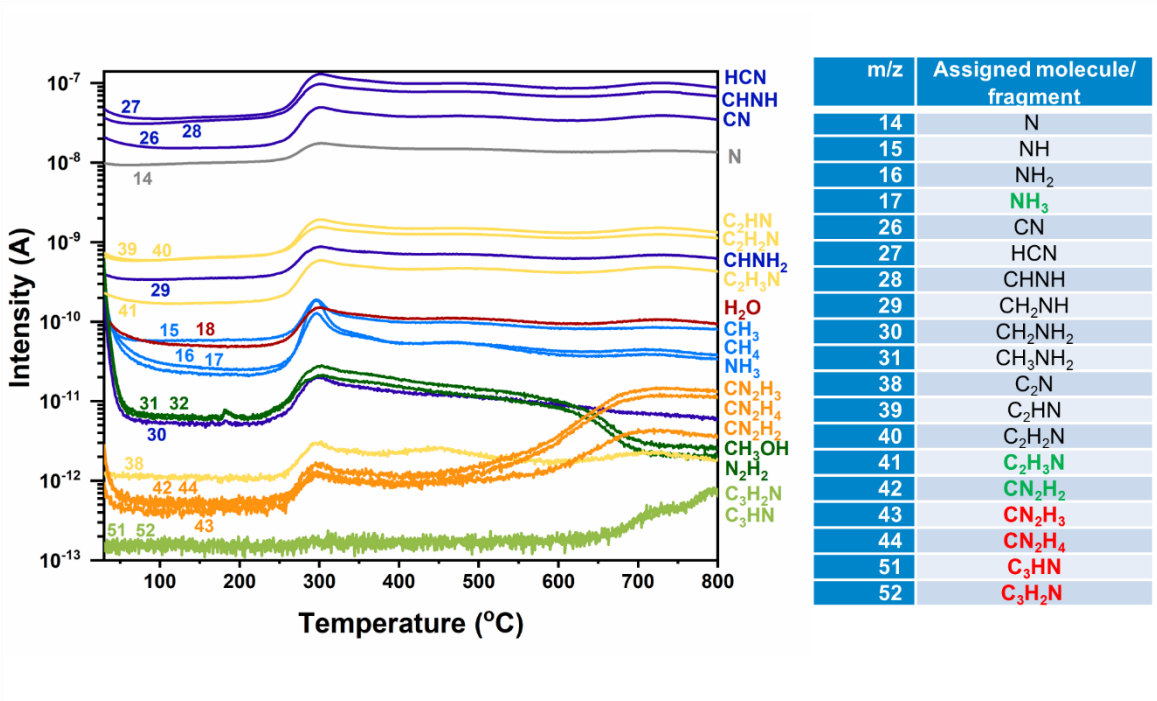
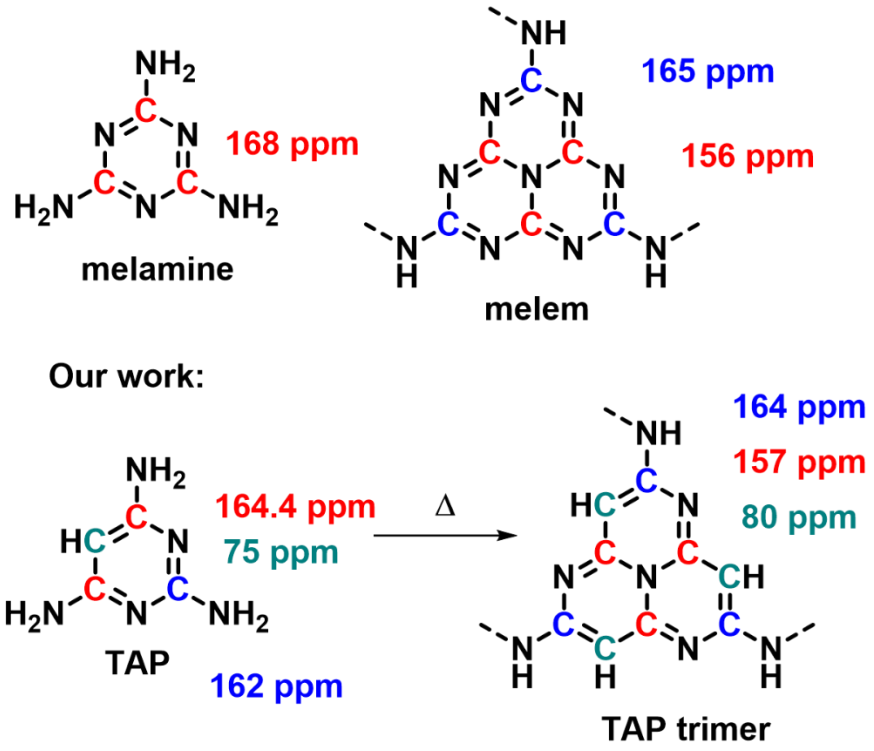


Figure A1. Chemical Structure of a.) melamine and b.) 2,4,6-Triaminopyrimidine (TAP). Reproduced from ref [36] under Creative Commons CC BY 3.0.

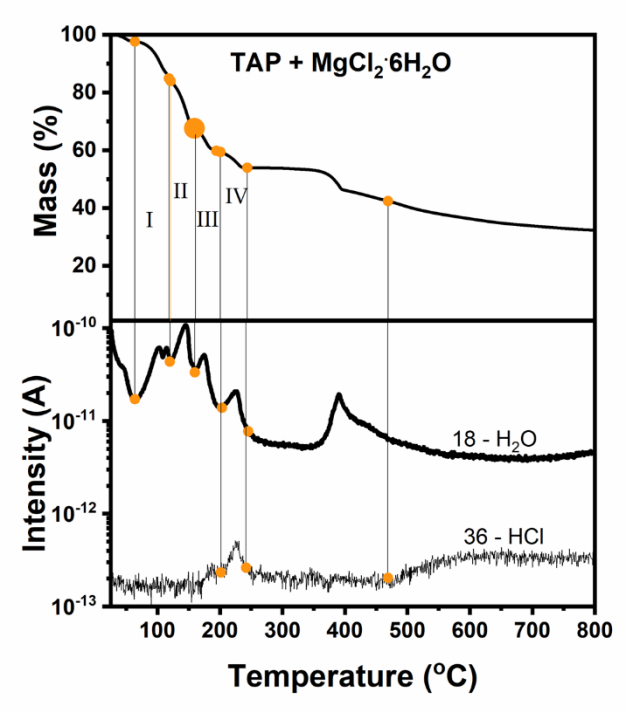


m/z	Assigned molecule/ fragment
14	N
15	NH
16	NH_2
17	NH_3
26	CN
27	HCN
28	CHNH
29	CH_2NH
30	CH_2NH_2
31	CH_3NH_2
38	C_2N
39	C_2HN
40	C_2H_2N
41	C_2H_3N
42	CN_2H_2
43	CN_2H_3
44	CN_2H_4
51	C_3HN
52	C_3H_2N

Figure A2. TGA-MS of TAP with corresponding table of assigned m/z fragments. Reproduced from ref [36] under Creative Commons CC BY 3.0.

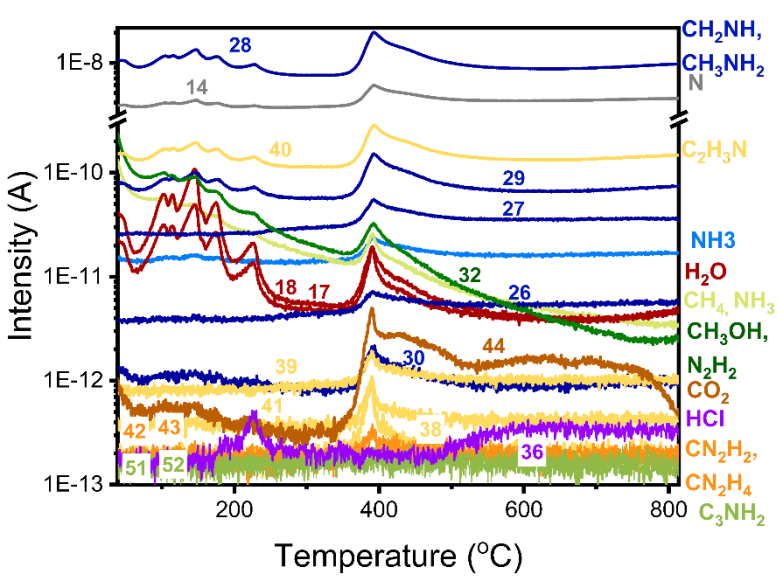


Scheme A1. Labelled NMR chemical shifts of melamine and melem from Schnick and co-workers (top),[1,2] and of TAP and the product of TAP pyrolysis at mild temperatures (bottom). Reproduced from ref [36] under Creative Commons CC BY 3.0.



Temperature (°C)	Mass loss (%)	Product
65-120	10	$MgCl_2 \cdot 4H_2O$
120-160	16	$MgCl_2 \cdot 2H_2O$
160-195	7	$MgCl_2 \cdot H_2O$
195-245	7	$MgCl_2$ - MgOHCl

Figure A3. Change in mass in TGA during pyrolysis of TAP with $MgCl_2 \cdot 6H_2O$. Reproduced from ref [36] under Creative Commons CC BY 3.0.



m/z	Assigned molecule/fragment
14	N
15	NH
16	NH_2
17	NH_3
26	CN, C_2H_2
27	HCN
28	CHNH, C_2H_4, N_2
29	CH_2NH
30	CH_2NH_2
31	CH_3NH_2
32	CH_3OH
36	HCl
38	C_2N
39	C2HN
40	C_2H_2N
41	C_2H_3N
42	CN_2H_2
43	CN_2H_3
44	CN_2H_4 - CO_2
51	C_3HN
52	C_3H_2N $(CN)_2$

Figure A4. TGA-MS of TAP with $MgCl_2 \cdot 6H_2O$ with corresponding assignment of fragments from m/z values. Reproduced from ref [36] under Creative Commons CC BY 3.0.

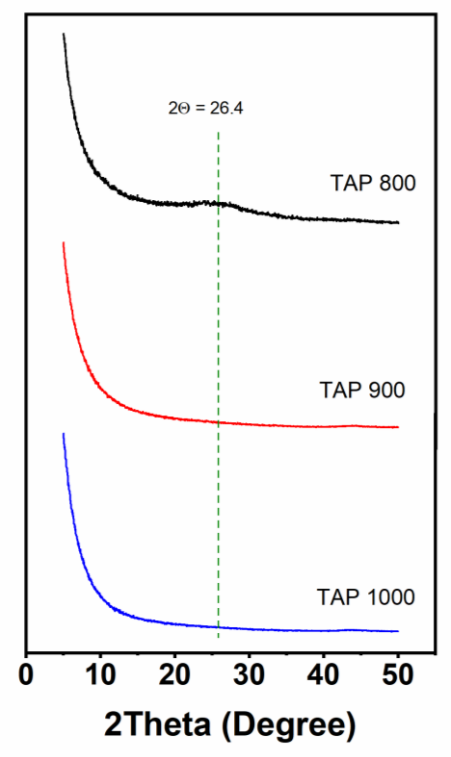


Figure A5. XRD of TAP 800, 900 and 1000. Reproduced from ref [36] under Creative Commons CC BY 3.0.

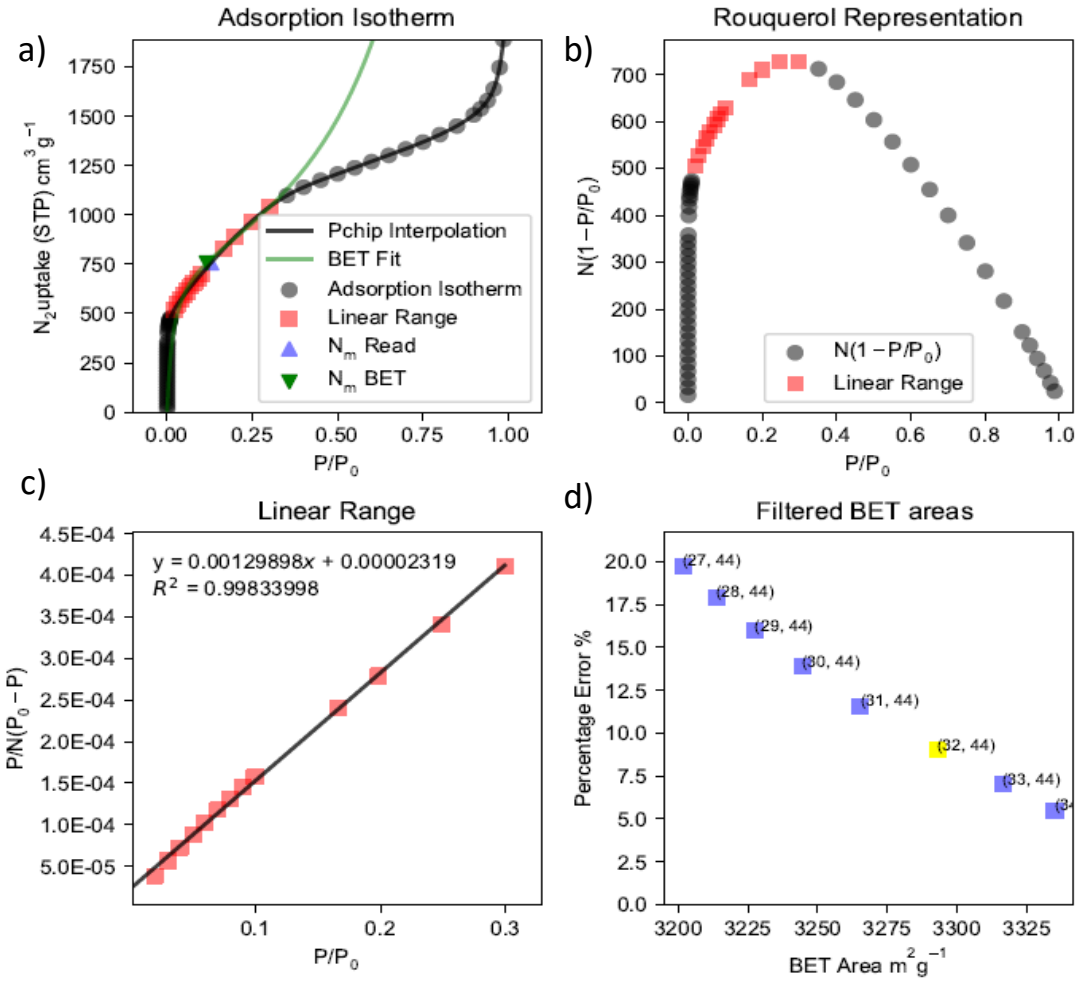


Figure A6. Outputs from BET Surface Identification software[3] for TAP 900 N_2 sorption a.) Adsorption isotherm. b.) Red points highlighted represent 10 accepted data points based Rouquerol method. c.) Corresponding regression criteria in the linear range ($R^2 \geq 0.995$). d) Output BET specific surface areas and corresponding error %. The yellow data is the selected value for TAP 900. Reproduced from ref [36] under Creative Commons CC BY 3.0.

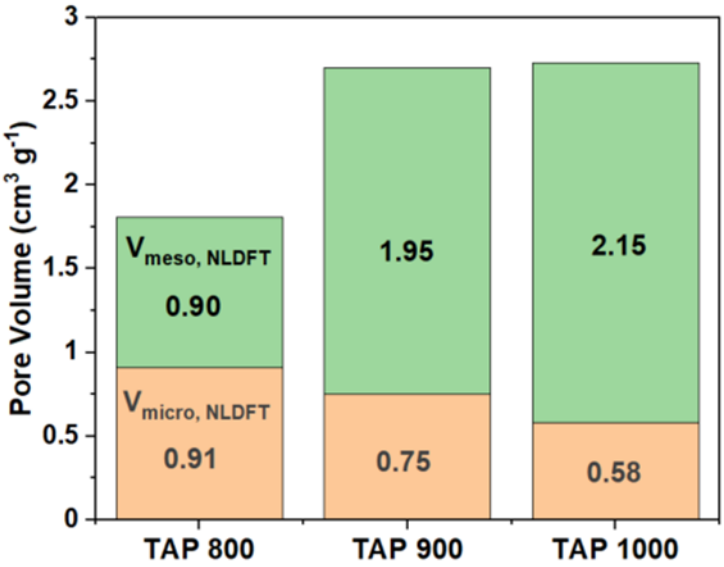


Figure A7. Total pore volumes of TAP 800, 900 and 1000 in the micro and meso-pore region based on N_2 adsorption with 2D-NLDFT heterogeneous surface carbon model in SAIEUS software. Reproduced from ref [36] under Creative Commons CC BY 3.0.

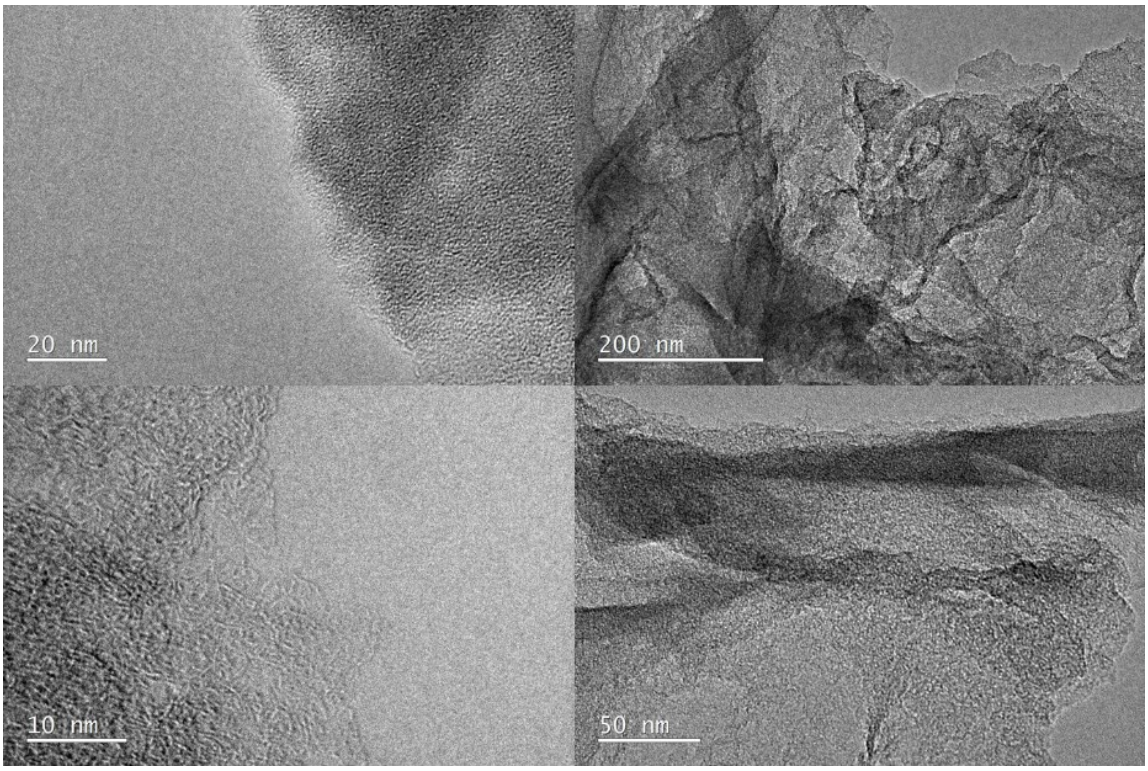


Figure A8. TEM images of TAP 900 showing atomically thin carbon structure. Reproduced from ref [36] under Creative Commons CC BY 3.0.

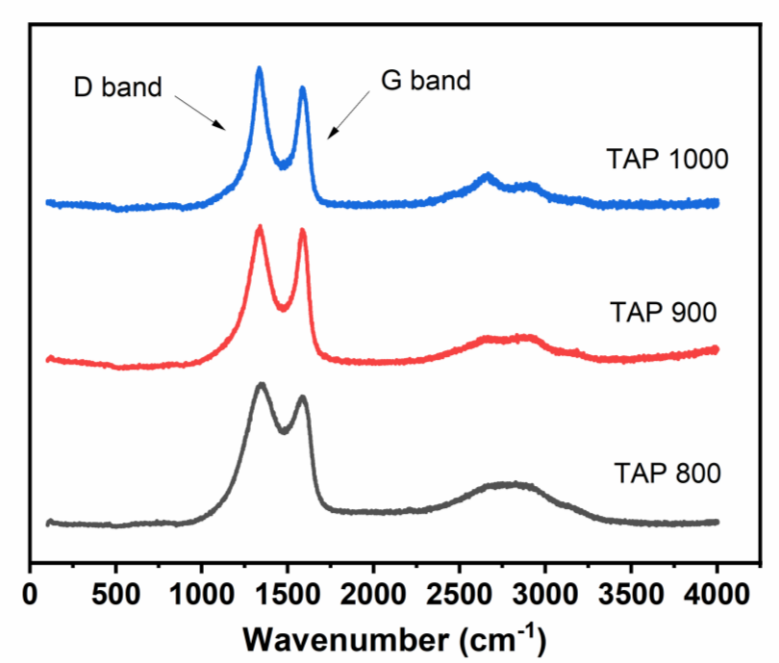


Figure A9. Raman spectra of TAP-derived materials with D and G bands indicated. Reproduced from ref [36] under Creative Commons CC BY 3.0.

Table A 1. Surface elemental composition of TAP 800, 900 and 1000 from XPS. Reproduced from ref [36] under Creative Commons CC BY 3.0.

Element	Atomic % 800	Atomic % 900	Atomic % 1000
C1s	73.2	92.9	95.1
N1s	23.5	4.5	1.8
O1s	3.3	2.6	3.2

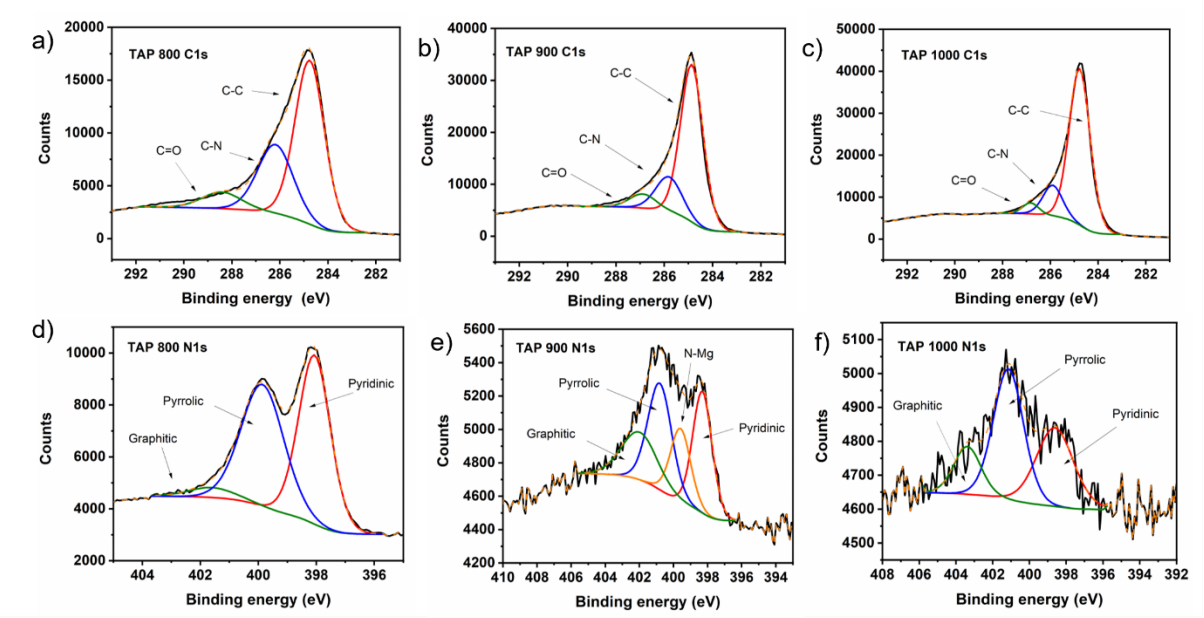


Figure A10. XPS of TAP 800, 900 and 1000 a-c.) C1s and d-f.) N1s with fitted peaks labelled. Reproduced from ref [36] under Creative Commons CC BY 3.0.

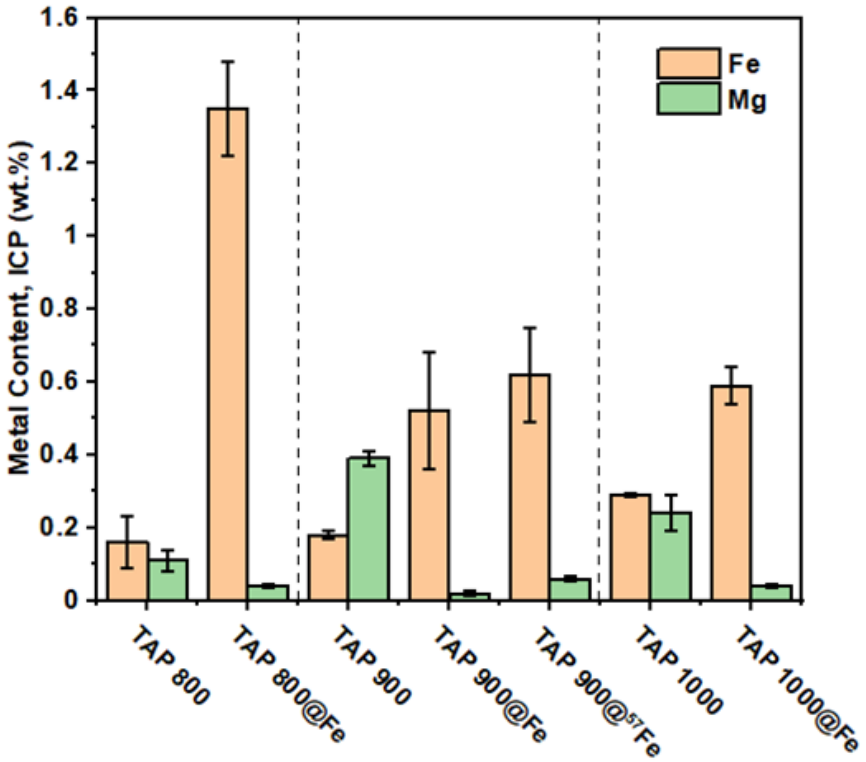


Figure A11. Average metal content Mg and Fe (wt.%) from ICP-MS for TAP 800-1000 and for same materials after Fe loading. Error bars represent standard deviation for two independent measurements of each material, except TAP 900@Fe and TAP 900@^{57}Fe, where four and three independent measurements were carried out, respectively. Reproduced from ref [36] under Creative Commons CC BY 3.0.

Table A2. Surface contribution of different N components in TAP 900 and TAP 900@Fe from XPS. Reproduced from ref [36] under Creative Commons CC BY 3.0.

Material	Pyridinic	N-M	Pyrrolic
TAP 900	29.2	18.0	31.5
TAP 900@Fe	16.9	34.5	37.6

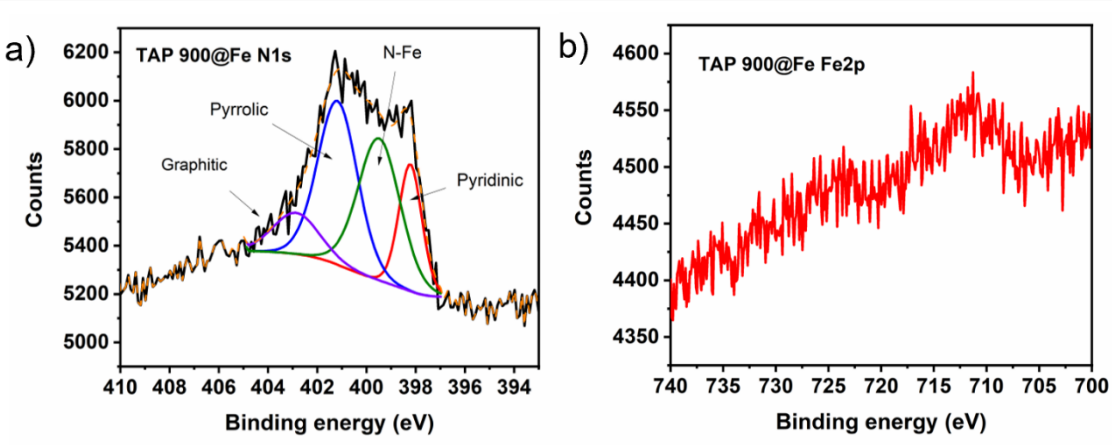


Figure A12. XPS of TAP 900@Fe a.) N1s and b.) Fe2p. Reproduced from ref [36] under Creative Commons CC BY 3.0.

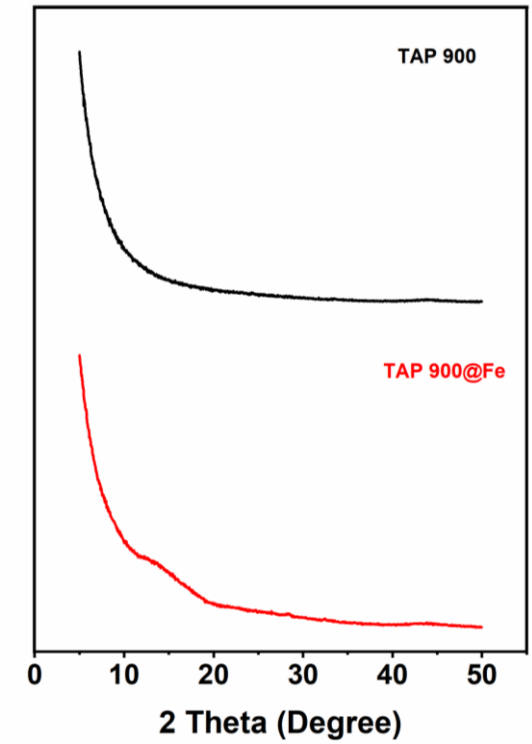


Figure A13. Comparison of XRD for TAP 900 and TAP 900@Fe. Reproduced from ref [36] under Creative Commons CC BY 3.0.

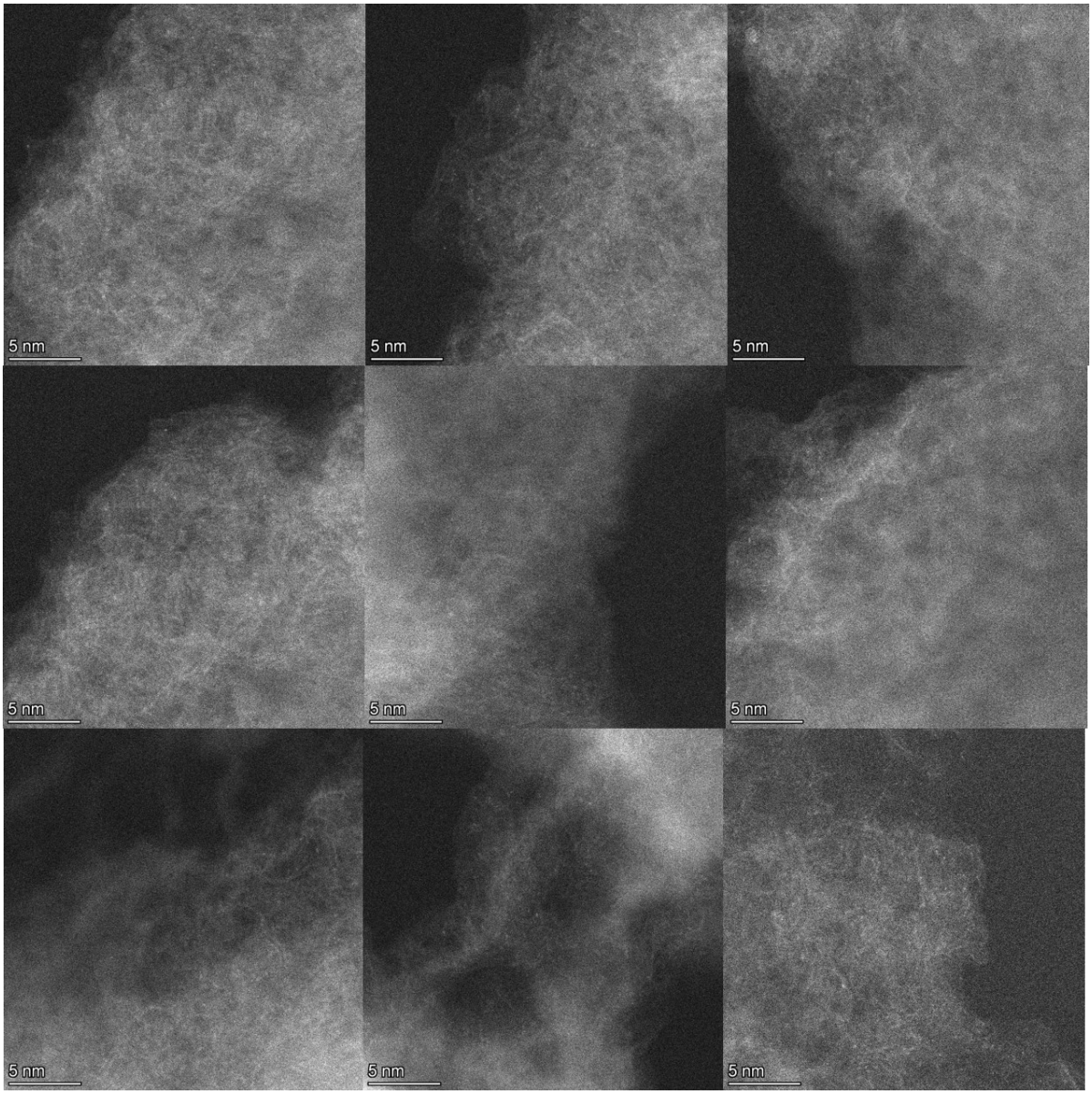


Figure A14. HAADF-STEM (with aberration correction) of TAP 900@Fe in different locations demonstrating the atomic metal dispersion without nanoparticle clustering. Reproduced from ref [36] under Creative Commons CC BY 3.0.

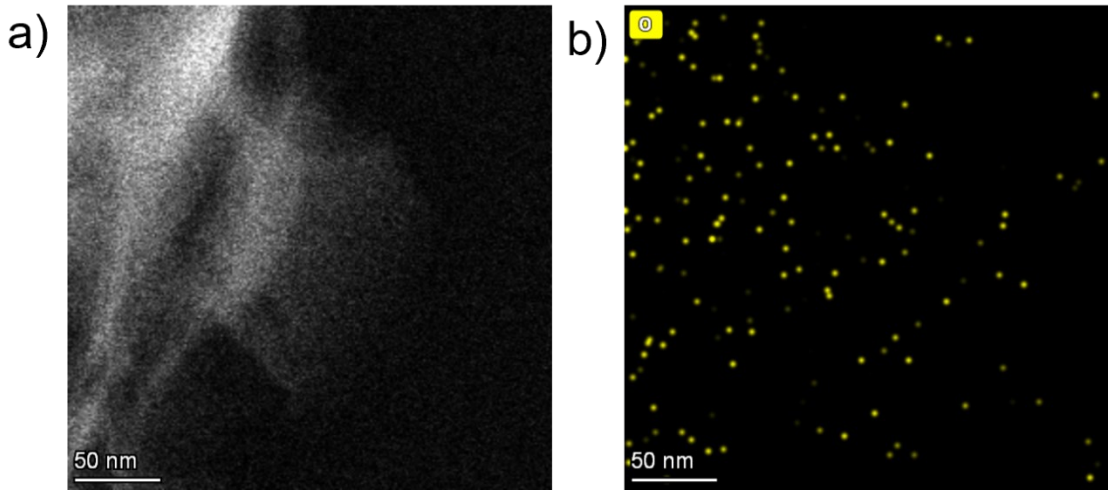


Figure A15. HAADF-STEM and corresponding O EDX mapping. Reproduced from ref [36] under Creative Commons CC BY 3.0.

Table A3. Fitting parameters applied in ^{57}Fe Mössbauer simulation. Reproduced from ref [36] under Creative Commons CC BY 3.0.

Assignment	**Fe^{III} HS**	**Fe^{II} IS**	**Fe^{II} HS**	**Fe^{II} LS**	**Fe^{III} HS**
Composition	**D1**	**D2**	**D3**	**D4**	**D5**
Contribution (%)	**41**	**17**	**13**	**18**	**11**
S	5/2	1	2	0	5/2
***D* (cm^{-1})**	8.0	18.2	2.0		0.4
E/D	0.00	0.14	0.09		0.30
***δ* ($mm\ s^{-1}$)**	**0.47**	**0.40**	**0.85**	**0.55**	**0.39**
***ΔE$_Q$* ($mm\ s^{-1}$)**	**1.05**	**2.29**	**-4.01**	**-0.64**	**-2.40**
η	0.00	0.50	0.66	0.83	0.59
Euler EFG/ZFS α, β, γ (°)	75, 80, 0	0, 0, 0	27, 42, 0	0, 0, 0	86, 74, 70
***Γ* ($mm\ s^{-1}$)**	**0.69**	**1.00**	**0.60**	**0.48**	**0.39**
-A/ g$_n$ β$_n$ (T)	22.5, 14.4, 13.5	19.8, 19.5, 22.7	22.8, 24.0, 23.1		24.0, 21.3, 21.3

Where *S* is the spin number, *D* is the axial zero-field splitting parameter, *E/D* is the rhombicity parameter, ***δ*** is the isomer shift, *ΔE$_Q$* is quadrupole splitting, *η* is the asymmetry parameter, *Γ* is the linewidth (full width half maximum), *-A* is the hyperfine coupling tensor (components

along the main axis, which are assumed to be the same as those of the ZFS tensor), g_n is the ^{57}Fe nuclear g-factor and β_n the nuclear Bohr magneton.

The spin-Hamiltonian used in the simulations was as follows:

$$\widehat{\boldsymbol{H}} = \boldsymbol{D}\left[\widehat{\boldsymbol{S}}_{\boldsymbol{z}}^{\boldsymbol{2}} - \frac{\boldsymbol{S(S+1)}}{\boldsymbol{3}} + \frac{\boldsymbol{E}}{\boldsymbol{D}}\left(\widehat{\boldsymbol{S}}_{\boldsymbol{x}}^{\boldsymbol{2}} - \widehat{\boldsymbol{S}}_{\boldsymbol{y}}^{\boldsymbol{2}}\right)\right] + \boldsymbol{\beta B}_{\boldsymbol{ext}} \cdot \widetilde{\boldsymbol{g}} \cdot \widehat{\boldsymbol{S}} + \frac{\Delta \boldsymbol{E}_{\boldsymbol{Q}}}{\boldsymbol{6}\sqrt{\boldsymbol{1} + \frac{\boldsymbol{\eta}^{\boldsymbol{2}}}{\boldsymbol{3}}}}\left[\boldsymbol{3}\widehat{\boldsymbol{I}}_{\boldsymbol{z}}^{\boldsymbol{2}} - \boldsymbol{I(I+1)} + \boldsymbol{\eta}\left(\widehat{\boldsymbol{I}}_{\boldsymbol{x}}^{\boldsymbol{2}} - \widehat{\boldsymbol{I}}_{\boldsymbol{y}}^{\boldsymbol{2}}\right)\right] - \boldsymbol{g}_{\boldsymbol{n}}\boldsymbol{\beta}_{\boldsymbol{n}}\left(\boldsymbol{B}_{\boldsymbol{ext}} - \frac{\langle \widehat{\boldsymbol{S}} \rangle \cdot \widetilde{\boldsymbol{A}}}{\boldsymbol{g}_{\boldsymbol{n}}\boldsymbol{\beta}_{\boldsymbol{n}}}\right) \cdot \widehat{\boldsymbol{I}}$$

Supplementary Note A1

The D5 signal can be attributed to the rhombic EPR signal, characterized by a rhombicity parameter (E/D) of 0.3 in the Mössbauer spin-Hamiltonian. This might appear contradictory since the rhombic signal dominates in EPR; however, it's important to note that the axial EPR signal is broad and spreads across the range of g = 2 to g = 6, while the rhombic component is distinct and sharp. The D5 component exhibits isomer shift (δ) and quadrupole splitting (ΔEQ) values that are comparable to those of D2 (17%), where D2 has been previously associated with Fe^{II} IS (Intermediate Spin) or low spin (LS) based on DFT calculations for different FeN4 sites, oxidation states, and spin states. Nevertheless, Mössbauer measurements conducted under a magnetic field clearly reveal distinct signals for D2 (associated with Fe^{II} IS) and D5 (associated with Fe^{III} HS, high spin). The presence of two separate Fe^{III} HS components in the material aligns with the EPR findings. The parameters of the D3 Fe^{II} HS component (13%) are consistent with those of $FeCl_2{\cdot}4H_2O$, with the same isomer shift value obtained here (δ = 0.85 mm s^{-1}), albeit with a different ΔE_Q value. The persistence of $FeCl_2{\cdot}4H_2O$ remnants is reasonable, given the wet synthesis process that involves a $FeCl_2$ precursor. However, it is somewhat surprising considering the acid washing and filtration steps used on the highly porous TAP 900@Fe material, which were expected to remove all such species from the catalyst. Finally, a Fe^{II} LS (Low Spin) component (D4 = 18%) is also identified, featuring a ΔE_Q value similar to LS $Fe^{II}(phen)_3$ complexes.[4–6] LS $Fe^{II}(phen)_3$ has a coordination number of six for Fe-N, obstructing the adsorption of key reaction intermediates by blocking the Fe active site. It is posited that such an active site may emerge following the coordination of Mg with TAP reaction intermediates (as depicted in Scheme 4.1).

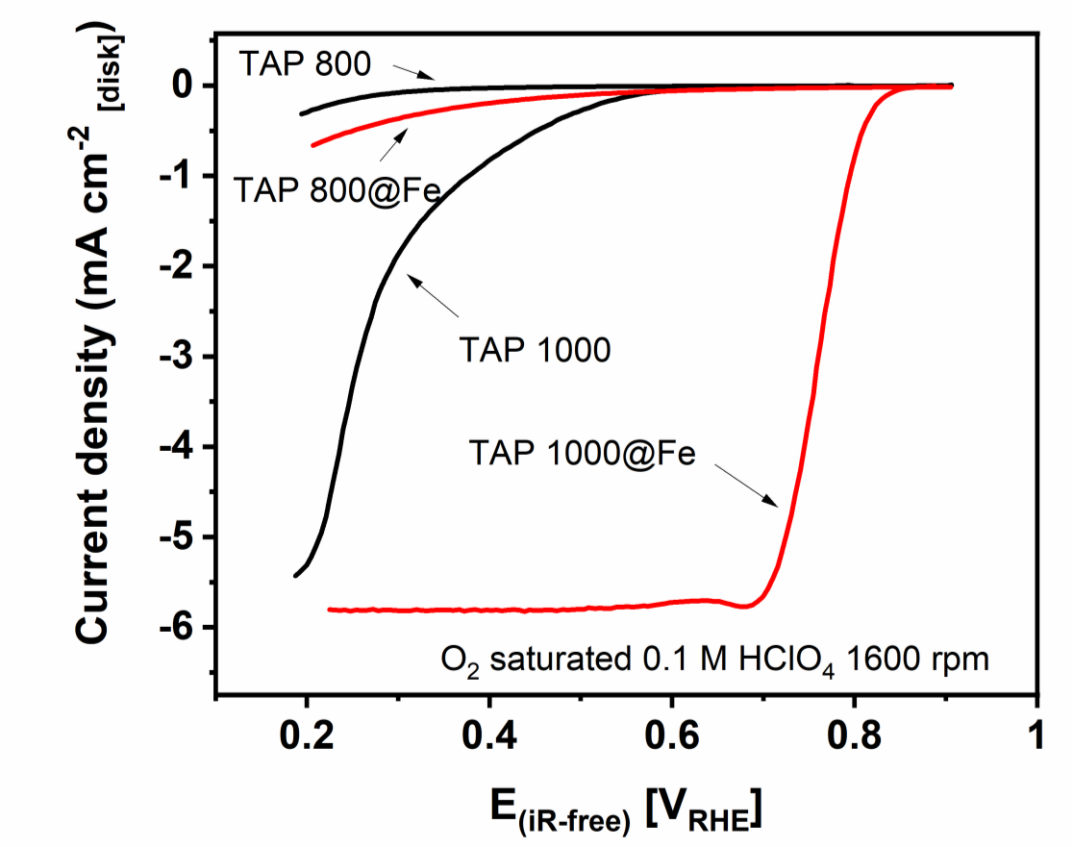


Figure A16. Cathodic scan of the cyclic voltammogram in O_2-saturated 0.1 M $HClO_4$ at 1600 rpm and 10 mV s^{-1}. Capacitance correction obtained by subtracting N_2 saturated cyclic voltammetry at 1600 rpm from the O_2 saturated result. All measurements shown with iR correction, 0.26 $mg_{Fe\text{-}N\text{-}C}$ cm^{-2} and room temperature electrolyte. Reproduced from ref [36] under Creative Commons CC BY 3.0.

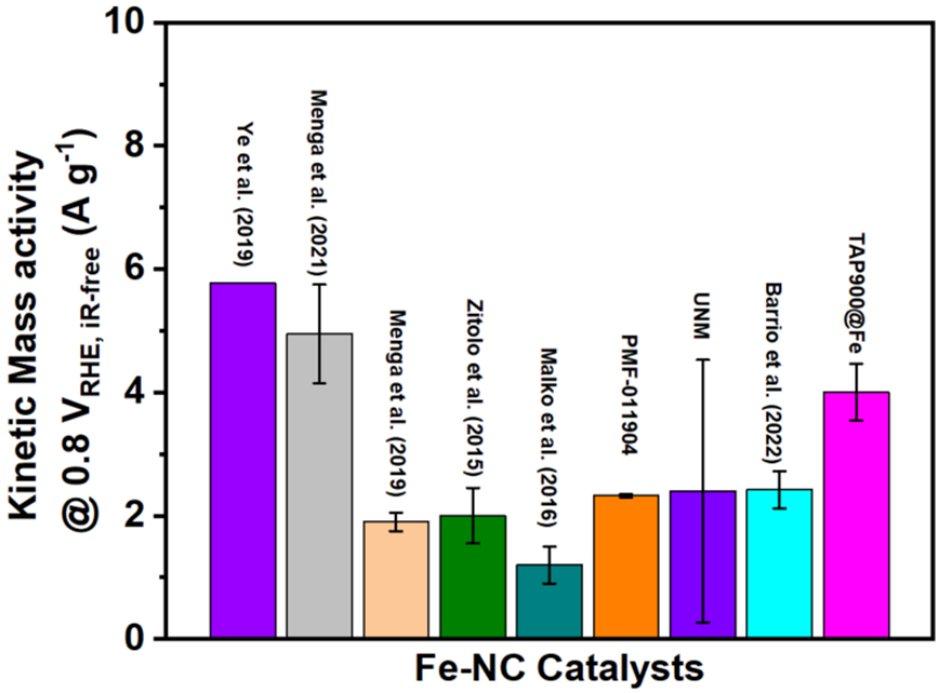


Figure A17. Comparison of initial O_2 reduction kinetic mass activity at 0.8 V_{RHE} of reported Fe-N-Cs. Reproduced from ref [36] under Creative Commons CC BY 3.0.

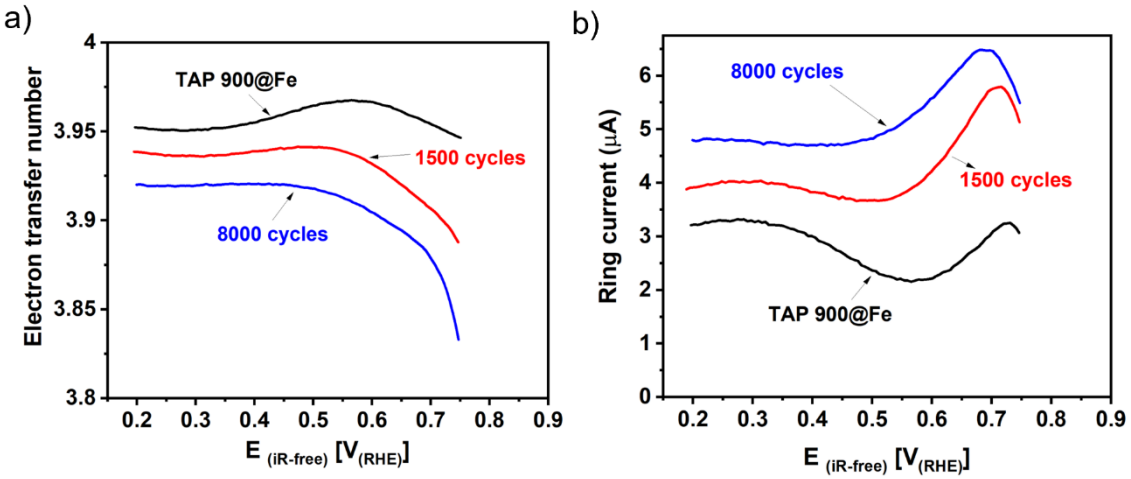


Figure A18. Fresh TAP 900@Fe and after 1,500 and 8,000 accelerated stress test cycles (100 mV s^{-1}, 0.8-0.4 V_{RHE}, O_2-saturated with Pt ring applied at 1.27 V_{RHE}) in RRDE with 0.26 $mg_{Fe\text{-}N\text{-}C}$ cm^{-2} a.) Electron transfer number. b.) Rotating ring current for the oxidation of H_2O_2. Reproduced from ref [36] under Creative Commons CC BY 3.0.

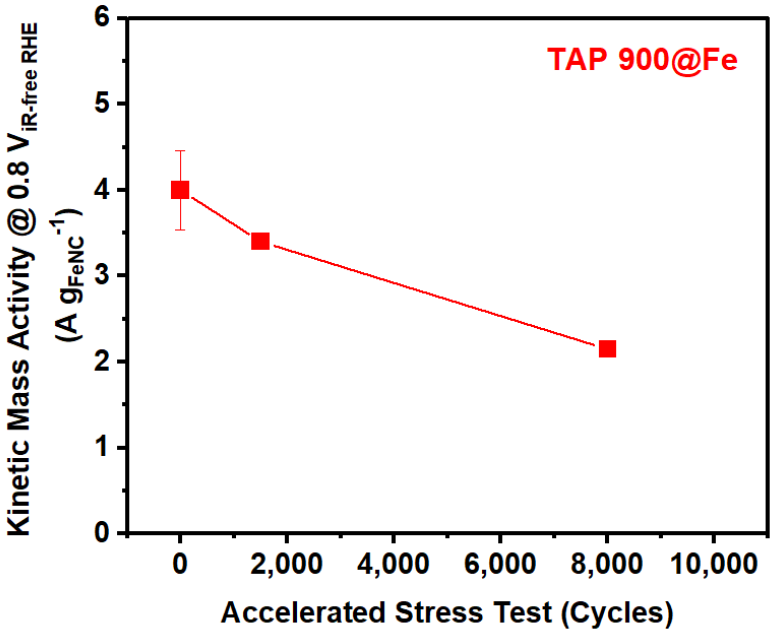


Figure A19. Decrease in kinetic mass activity of TAP 900@Fe over accelerated stress test in O_2-saturated 0.1 M $HClO_4$ between 0.8-0.40 V_{RHE} at 100 mV s^{-1} with Pt ring applied at 1.27 V_{RHE} throughout. Reproduced from ref [36] under Creative Commons CC BY 3.0.

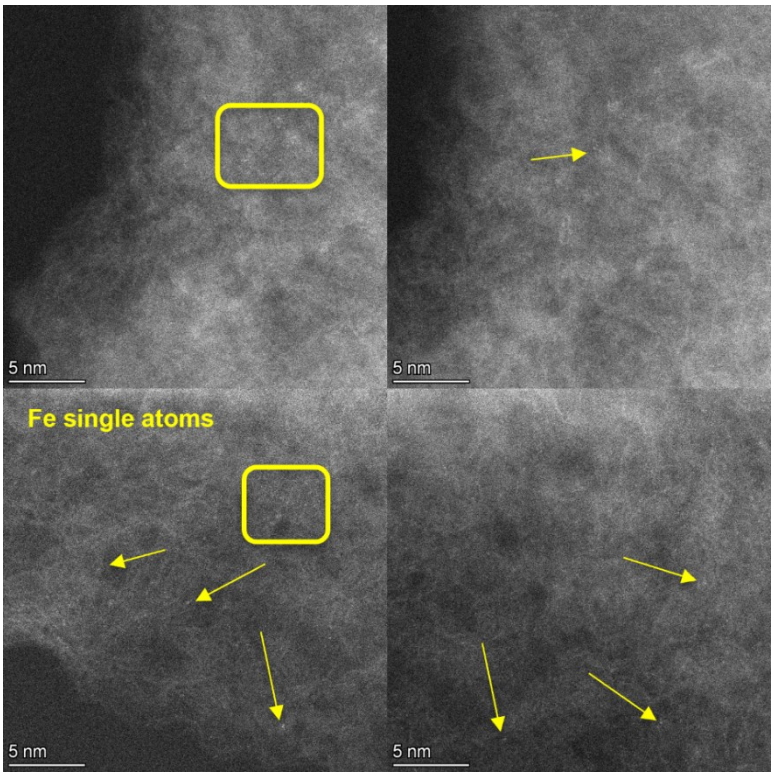


Figure A20. HAADF-STEM of TAP 900@Fe post 8,000 accelerated stress test cycles between 0.8-0.4 V_{RHE} (100 mV s^{-1}) under O_2-saturation showing metal atoms still atomically dispersed without clustering. 0.8 $mg_{Fe\text{-}N\text{-}C}$ cm^{-2} of TAP 900@Fe was used for the accelerated stress test to obtain suitable sample for the HAADF-STEM measurement. Reproduced from ref [36] under Creative Commons CC BY 3.0.

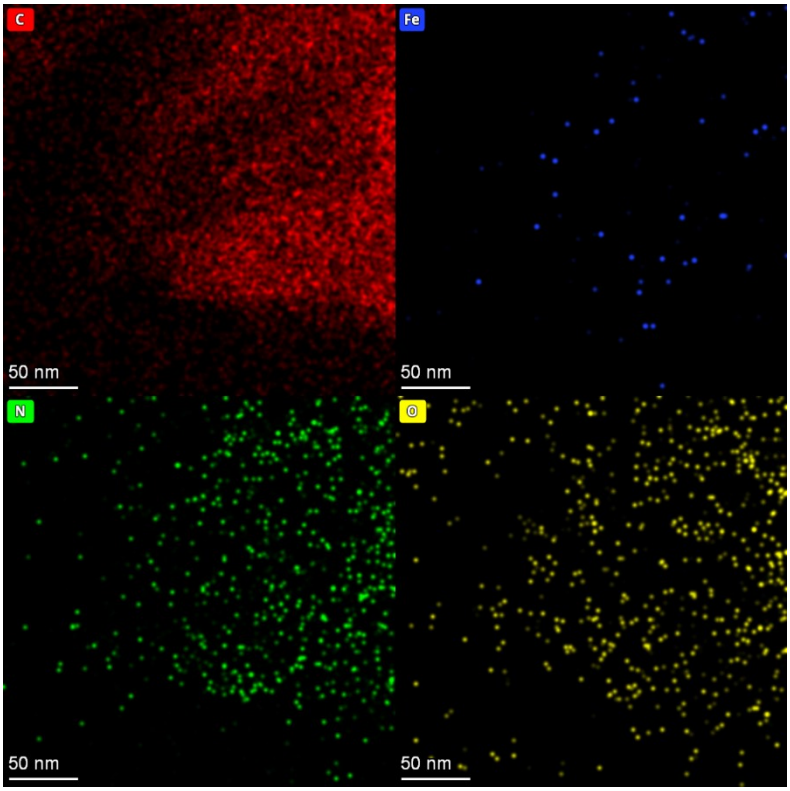


Figure A21. EDX elemental mapping of C, Fe, N, and O for TAP 900@Fe after 8000 accelerated stress test cycles between 0.8-0.4 V_{RHE} (100 mV s^{-1}) under O_2-saturation. 0.8 $mg_{Fe\text{-}N\text{-}C}$ cm^{-2} of TAP 900@Fe was used for the accelerated stress test to obtain suitable sample for measurement. Reproduced from ref [36] under Creative Commons CC BY 3.0.

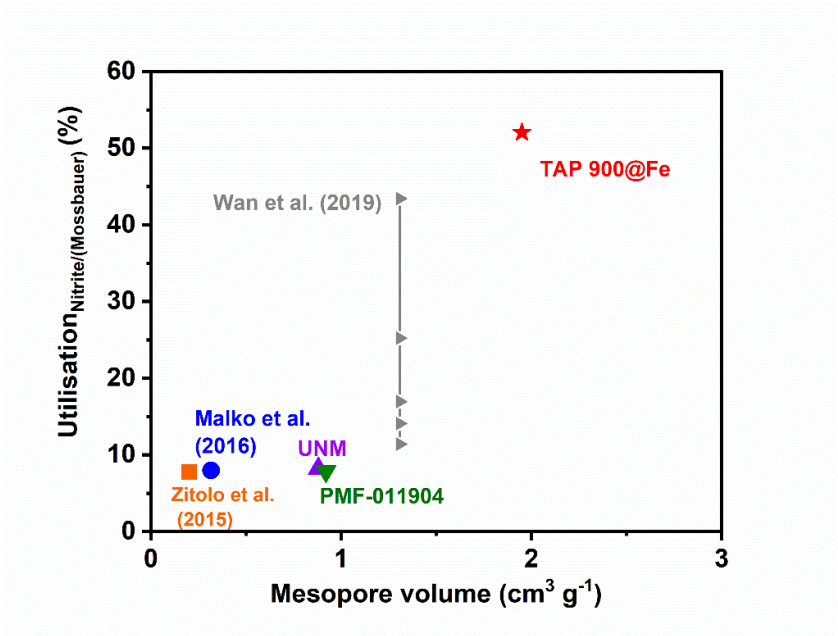


Figure A22. Comparison of $Utilisation_{Nitrite/(Mossbauer)}$ versus mesopore volume for various reported Fe-N-C. Mesopore volume data for Jiao et al. and Mehmood et al. was not reported. Reproduced from ref [36] under Creative Commons CC BY 3.0.

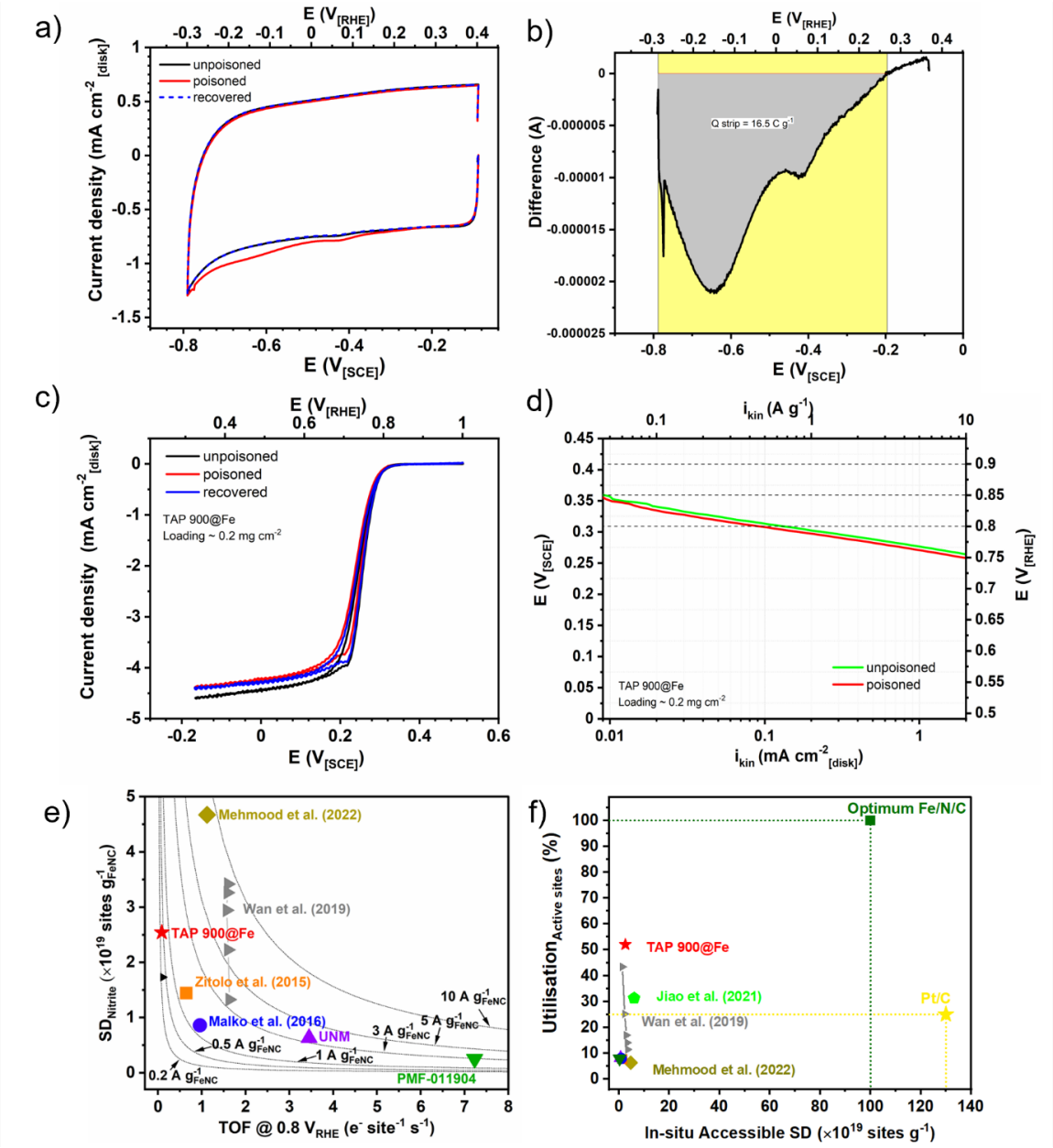


Figure A23. a.) Cyclic voltammetry (10 mV s^{-1}, 1,600 rpm, N_2-saturation) of TAP 900@Fe at fresh, poisoned, and recovered stages of nitrite stripping protocol. b.) Corresponding stripping charge associated with the reduction of nitrite molecules. c.) RDE O_2 reduction (5 mV s^{-1}, 1,600 rpm, O_2-saturation) of TAP 900@Fe at fresh, poisoned, and recovered stages of in-situ nitrite stripping protocol with 0.2 $mg_{Fe\text{-}N\text{-}C}$ cm^{-2}. d.) Corresponding shift of kinetic O_2 reduction activity upon nitrite poisoning. e.) Mass isoactivity at 0.80 V_{RHE} and comparison to Fe-NC catalysts of; Zitolo et al.,[7] Malko et al.,[8] University New Mexico and Pajarito Powder Inc. commercial catalyst PMF-011904,[9] Mehmood et al.,[10] Wan et al.,[11] and Jiao et al..[12] A portion of data obtained is replotted from ref.[13] All reported electrochemical measurements with 0.2 $mg_{Fe\text{-}N\text{-}C}$ cm^{-2} loading (except Wan et al. who reported with 0.27 $mg_{Fe\text{-}N\text{-}C}$ cm^{-2}) in 0.5 M sodium acetate buffer (pH 5.2) with RDE. f.) Comparison of accessible SD and active site utilisation reported for Fe-N-Cs and theoretical optimum Fe-N-C highlighted in green dash, and Pt/C in yellow dash. Pt/C SD calculated from 100 m^2 g_{Pt}^{-1} in PEMFC, as calculated by Mehmood et al.,[10] while Pt utilisation assumes 3 nm Pt particles with subsequent 25% electrochemical utilisation. Reproduced from ref [36] under Creative Commons CC BY 3.0.

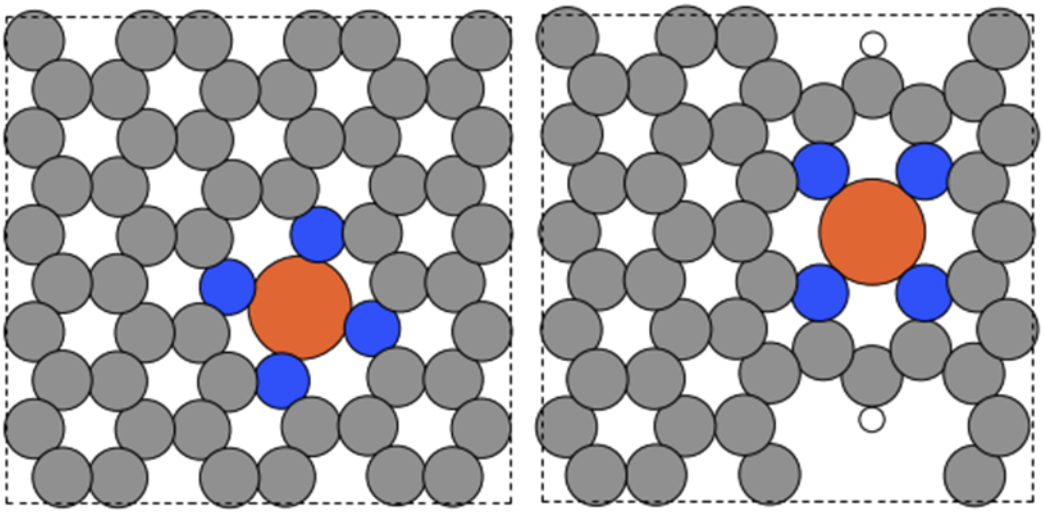


Figure A24. Chemical structures of (Left) FeN_4-pyridine and (Right) FeN_4-pyrrole. Orange = Fe, Blue = N, Grey = C and White = H. Reproduced from ref [36] under Creative Commons CC BY 3.0.

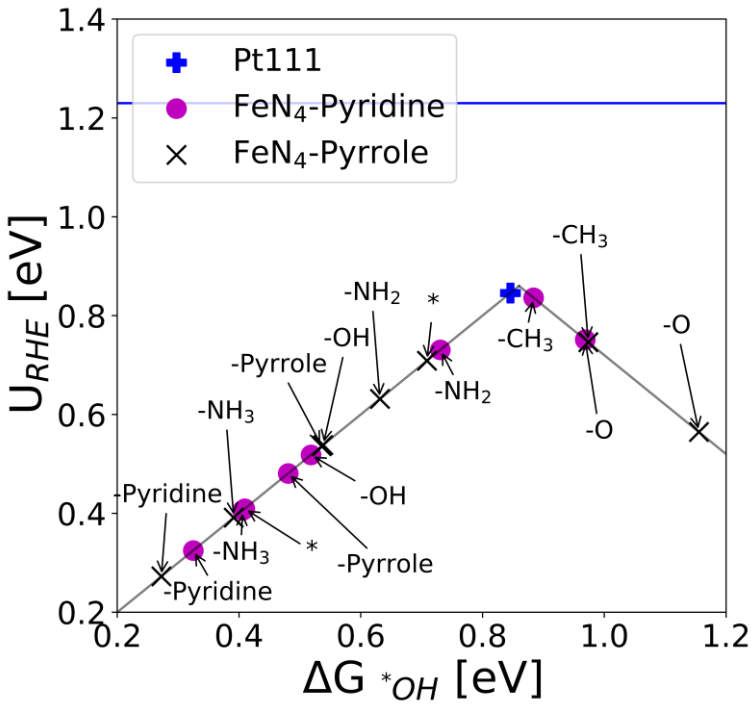


Figure A25. DFT calculated O_2 reduction activity volcano based on *OH binding energies for a series of FeN_4 pyridine and pyrrole sites with pyridine or pyrrole axial ligands. Pt(111) highlighted in blue cross. Here an using a *OH solvation energy of –0.3 eV was applied to all data points. Reproduced from ref [36] under Creative Commons CC BY 3.0.

References

1 B. V. Lotsch, M. Döblinger, J. Sehnert, L. Seyfarth, J. Senker, O. Oeckler and W. Schnick, *Chem. – Eur. J.*, 2007, **13**, 4969–4980.

2 B. Jürgens, E. Irran, J. Senker, P. Kroll, H. Müller and W. Schnick, *J. Am. Chem. Soc.*, 2003, **125**, 10288–10300.

3 J. W. M. Osterrieth, J. Rampersad, D. Madden, N. Rampal, L. Skoric, B. Connolly, M. D. Allendorf, V. Stavila, J. L. Snider, R. Ameloot, J. Marreiros, C. Ania, D. Azevedo, E. Vilarrasa-Garcia, B. F. Santos, X.-H. Bu, Z. Chang, H. Bunzen, N. R. Champness, S. L. Griffin, B. Chen, R.-B. Lin, B. Coasne, S. Cohen, J. C. Moreton, Y. J. Colón, L. Chen, R. Clowes, F.-X. Coudert, Y. Cui, B. Hou, D. M. D'Alessandro, P. W. Doheny, M. Dincă, C. Sun, C. Doonan, M. T. Huxley, J. D. Evans, P. Falcaro, R. Ricco, O. Farha, K. B. Idrees, T. Islamoglu, P. Feng, H. Yang, R. S. Forgan, D. Bara, S. Furukawa, E. Sanchez, J. Gascon, S. Telalović, S. K. Ghosh, S. Mukherjee, M. R. Hill, M. M. Sadiq, P. Horcajada, P. Salcedo-Abraira, K. Kaneko, R. Kukobat, J. Kenvin, S. Keskin, S. Kitagawa, K. Otake, R. P. Lively, S. J. A. DeWitt, P. Llewellyn, B. V. Lotsch, S. T. Emmerling, A. M. Pütz, C. Martí-Gastaldo, N. M. Padial, J. García-Martínez, N. Linares, D. Maspoch, J. A. Suárez del Pino, P. Moghadam, R. Oktavian, R. E. Morris, P. S. Wheatley, J. Navarro, C. Petit, D. Danaci, M. J. Rosseinsky, A. P. Katsoulidis, M. Schröder, X. Han, S. Yang, C. Serre, G. Mouchaham, D. S. Sholl, R. Thyagarajan, D. Siderius, R. Q. Snurr, R. B. Goncalves, S. Telfer, S. J. Lee, V. P. Ting, J. L. Rowlandson, T. Uemura, T. Iiyuka, M. A. Veen, D. Rega, V. Van Speybroeck, S. M. J. Rogge, A. Lamaire, K. S. Walton, L. W. Bingel, S. Wuttke, J. Andreo, O. Yaghi, B. Zhang, C. T. Yavuz, T. S. Nguyen, F. Zamora, C. Montoro, H.-C. Zhou, A. Kirchon and D. Fairen-Jimenez, *Adv. Mater.*, 2022, 2201502.

4 J. F. Duncan and K. F. Mok, *J. Chem. Soc. Inorg. Phys. Theor.*, 1966, 1493–1496.

5 C. Gallenkamp, U. I. Kramm, J. Proppe and V. Krewald, *Int. J. Quantum Chem.*, 2021, **121**, e26394.

6 R. L. Collins, R. Pettit and W. A. Baker, *J. Inorg. Nucl. Chem.*, 1966, **28**, 1001–1010.

7 A. Zitolo, V. Goellner, V. Armel, M. T. Sougrati, T. Mineva, L. Stievano, E. Fonda and F. Jaouen, *Nat. Mater.*, 2015, **14**, 937–942.

8 D. Malko, T. Lopes, E. Symianakis and A. R. Kucernak, *J. Mater. Chem. A*, 2015, **4**, 142–152.

9 M. Primbs, Y. Sun, A. Roy, D. Malko, A. Mehmood, M.-T. Sougrati, P.-Y. Blanchard, G. Granozzi, T. Kosmala, G. Daniel, P. Atanassov, J. Sharman, C. Durante, A. Kucernak, D. Jones, F. Jaouen and P. Strasser, *Energy Environ. Sci.*, 2020, **13**, 2480–2500.

10 A. Mehmood, M. Gong, F. Jaouen, A. Roy, A. Zitolo, A. Khan, M. Sougrati, M. Primbs, A. M. Bonastre, D. Fongalland, G. Drazic, P. Strasser and A. Kucernak, *Nat. Catal.*, 2022, **5**, 311–323.

11 X. Wan, X. Liu, Y. Li, R. Yu, L. Zheng, W. Yan, H. Wang, M. Xu and J. Shui, *Nat. Catal.*, 2019, **2**, 259–268.

12 L. Jiao, J. Li, L. L. Richard, Q. Sun, T. Stracensky, E. Liu, M. T. Sougrati, Z. Zhao, F. Yang, S. Zhong, H. Xu, S. Mukerjee, Y. Huang, D. A. Cullen, J. H. Park, M. Ferrandon, D. J. Myers, F. Jaouen and Q. Jia, *Nat. Mater.*, 2021, **20**, 1385–1391.

13 A. Mehmood, M. Gong, F. Jaouen, A. Roy, A. Zitolo, A. Khan, M. Sougrati, M. Primbs, A. M. Bonastre, D. Fongalland, G. Drazic, P. Strasser and A. Kucernak, *Nat. Catal.*, 2022, **5**, 311–323.

Appendix B (Chapter 5): Fe Dissolution in Fe-N-C Electrocatalysts during Acidic Oxygen Reduction: Impact of Local pH

The concentrations of proton (C_H), Fe (C_{Fe}) and hydroxides ions (C_{OH}) as a function to time (t) and space (x) are modelled by solving a system of partial differential equations describing the effect of mass transport and of reactions in the catalyst layer and in the electrolyte.

In the catalyst layer:

$$\frac{\partial C_{Fe}}{\partial t} = D_{Fe,eff}\frac{\partial^2 C_{Fe}}{\partial x^2} + k_{dis}\left(1 - H\left(\frac{C_{Fe}\,K_e{}^3}{C_H{}^3 K_S} - 1\right)\right)$$

$$\frac{\partial C_H}{\partial t} = D_{H,eff}\frac{\partial^2 C_H}{\partial x^2} + 3k_{dis}\;\; H\left(\frac{C_{Fe}\,K_e{}^3}{C_H{}^3 K_S} - 1\right) - k_r C_H + k_{fw} - k_{bw} C_H C_{OH}$$

$$\frac{\partial C_{OH}}{\partial t} = D_{OH,eff}\frac{\partial^2 C_{OH}}{\partial x^2} + k_{fw} - k_{bw} C_H C_{OH}$$

In solution:

$$\frac{\partial C_{Fe}}{\partial t} = D_{Fe}\frac{\partial^2 C_{Fe}}{\partial x^2}$$

$$\frac{\partial C_H}{\partial t} = D_H\frac{\partial^2 C_H}{\partial x^2} + k_{fw} - k_{bw} C_H C_{OH}$$

$$\frac{\partial C_{OH}}{\partial t} = D_{OH}\frac{\partial^2 C_{OH}}{\partial x^2} + k_{fw} - k_{bw} C_H C_{OH}$$

The reactions considered in the model are:

- the self-ionization of water, $H_2O = H^+ + OH^-$ (k_{fw}=1.4 × 10^{-3} M s^{-1}, k_{bw}= 7 · 10^{10} M^{-1} s^{-1})[1]
- the Fe dissolution, k_{dis} = 8 · 10^{-11} s^{-1} in O_2 and 4 × 10^{-11} s^{-1} in Ar (applied from reproducing experimental data)
- the Fe precipitation: $Fe^{3+} + 3H_2O = Fe(OH)_3 + 3\,H^+$ (solubility constant of $Fe(OH)_3$, K_s=2.8 ·10^{-39})[2]

D_{Fe} = 6 × 10^{-6} cm^2 s^{-1},[3] while D_H is estimated by using the expression for the diffusion coefficient of binary electrolyte:

$$D_H = \frac{2D_{H^+} \cdot D_{ClO_4}}{D_{H^+} + D_{ClO_4}} = 2.72 \cdot 10^{-5}\ \text{cm}^2\ \text{s}^{-1}$$

In the catalyst layer, the effective diffusion coefficient was calculated using the Bruggeman equation:[4]

$$D_{i,eff} = D_i \cdot \varepsilon^{3/2}$$

Where ε is the volume fraction of the aqueous phase in the catalyst layer.

From the Bruggeman model:

$$\tau = \frac{1}{\sqrt{\varepsilon}}$$

Where τ is the tortuosity factor.

The system of partial differential equations is solved for the initial conditions, at $t = 0$, $C_{Fe} = 0$ and $C_H = 10^{-4}$ M, $C_{OH} = 10^{-10}$ M. The following boundary conditions are used:

At the gas phase/catalyst layer interface at $x = 0$:

$$D_{Fe,eff}\ \frac{\partial C_{Fe}}{\partial x} = 0$$

$$D_{H,eff}\ \frac{\partial C_H}{\partial x} = 0$$

$$D_{OH}\ \frac{\partial C_{OH}}{\partial x} = 0$$

At the catalyst layer/liquid electrolyte interface at $x = 60$ µm:

$$D_{Fe,eff}\ \frac{\partial C_{Fe}}{\partial x} = D_{Fe}\frac{\partial C_{Fe}}{\partial x}$$

$$D_H\ \frac{\partial C_H}{\partial x} = -\frac{j}{F}$$

Where j=-15 mA cm^{-2} is the faradaic current density under O_2 reduction conditions.

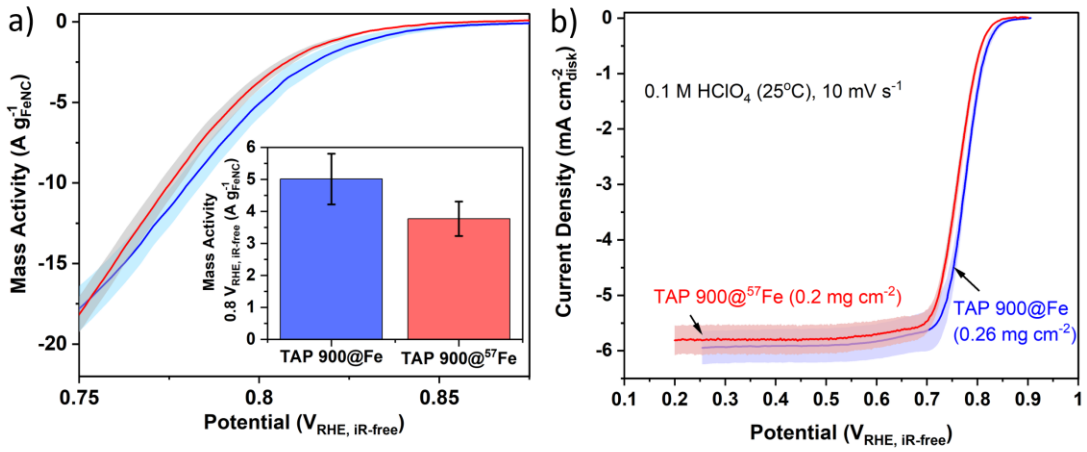


Figure B1. Comparison between TAP 900@Fe and TAP 900@^{57}Fe for a.) Mass activity, with inset showing mass activity at 0.8 $V_{RHE, iR-free}$ b.) Current density. O_2 reduction in 0.1 M $HClO_4$ at 10 mV s^{-1} and 1600 rpm. O_2-Ar correction applied. TAP 900@Fe data re-plotted from previous work.[5] Error represents standard deviation from at least four repeat measurements, and is highlighted with red and blue colors.

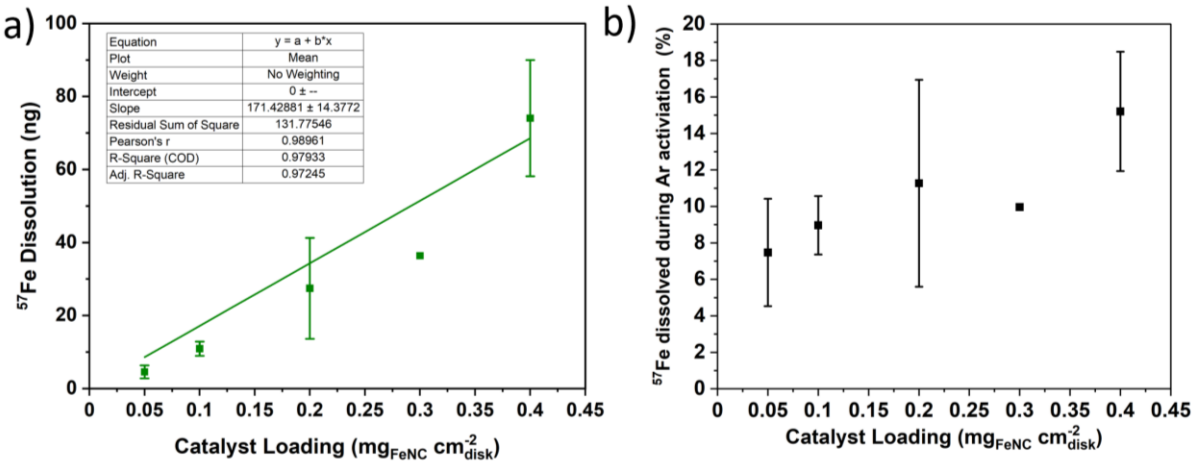


Figure B2. a.) Amount of ^{57}Fe dissolution with varying catalyst loading over cyclic voltammetry at 50 mV s^{-1}. b.) Corresponding percentage of total catalyst ^{57}Fe dissolved. Error bars represent standard deviation of at least four separate measurements.

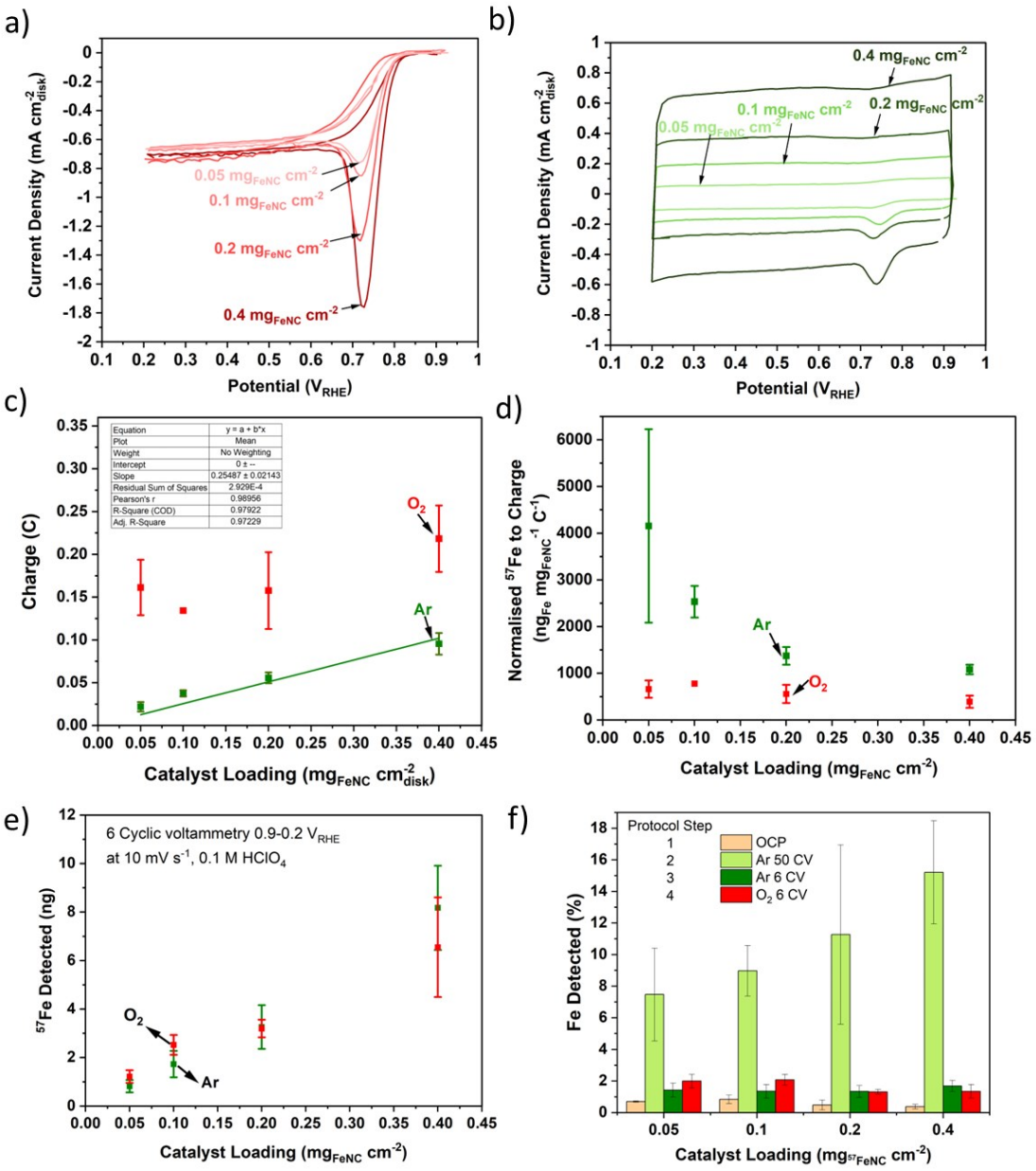


Figure B3. Flow cell under a.) O_2-saturated conditions, with O_2 - Ar correction applied. b.) Ar-saturated conditions. c.) Charge passed over six CV. d.) ^{57}Fe concentration normalised to charge passed and e.) ^{57}Fe at varying catalyst loading over six CV. f.) Percentage of ^{57}Fe detected at different stages of protocol. Error bars represent minimum of four repeat measurements.

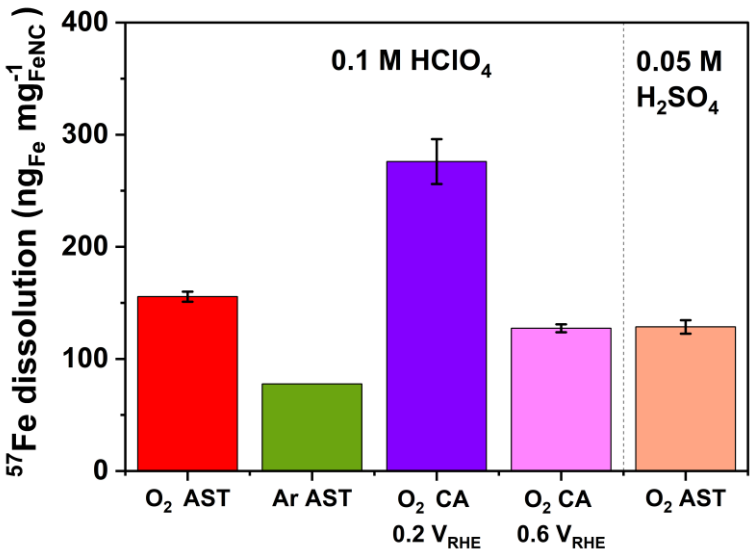


Figure B4. ^{57}Fe dissolution over different stability tests. All tests over 1 h with 0.2 mg_{FeNC} cm^{-2}.

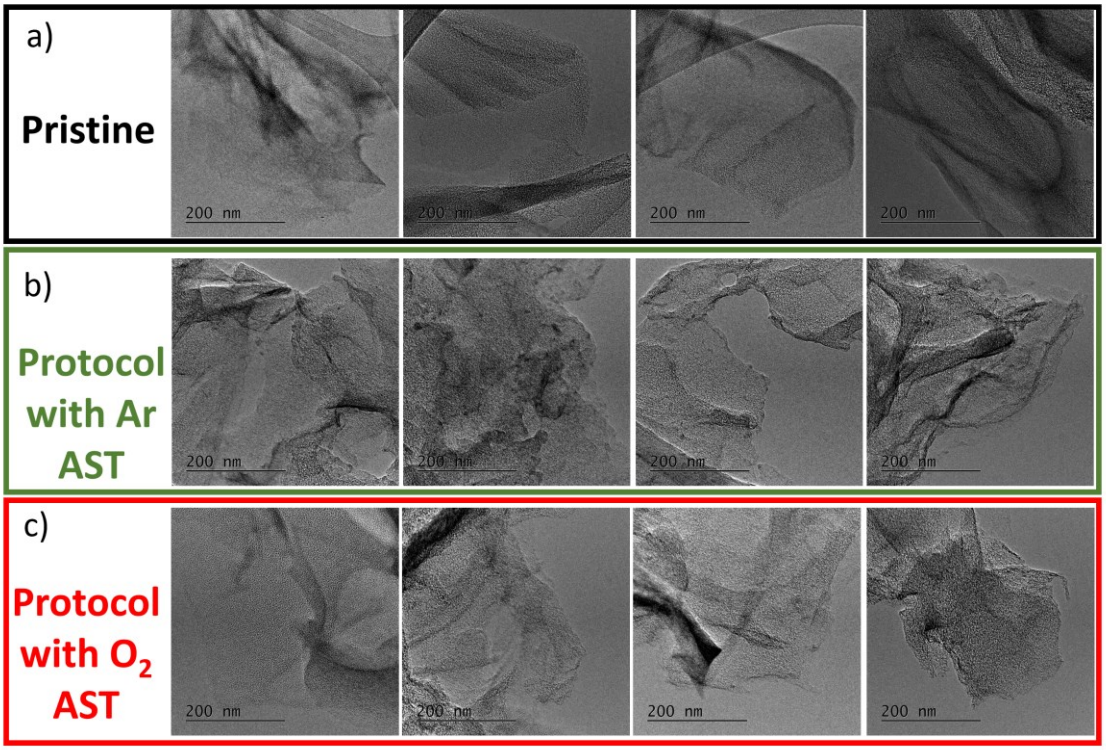


Figure B5. Bright-field TEM of TAP 900@^{57}Fe a.) Pristine. After protocol with AST in flow cell with b.) Ar-saturation. c.) O_2-saturation.

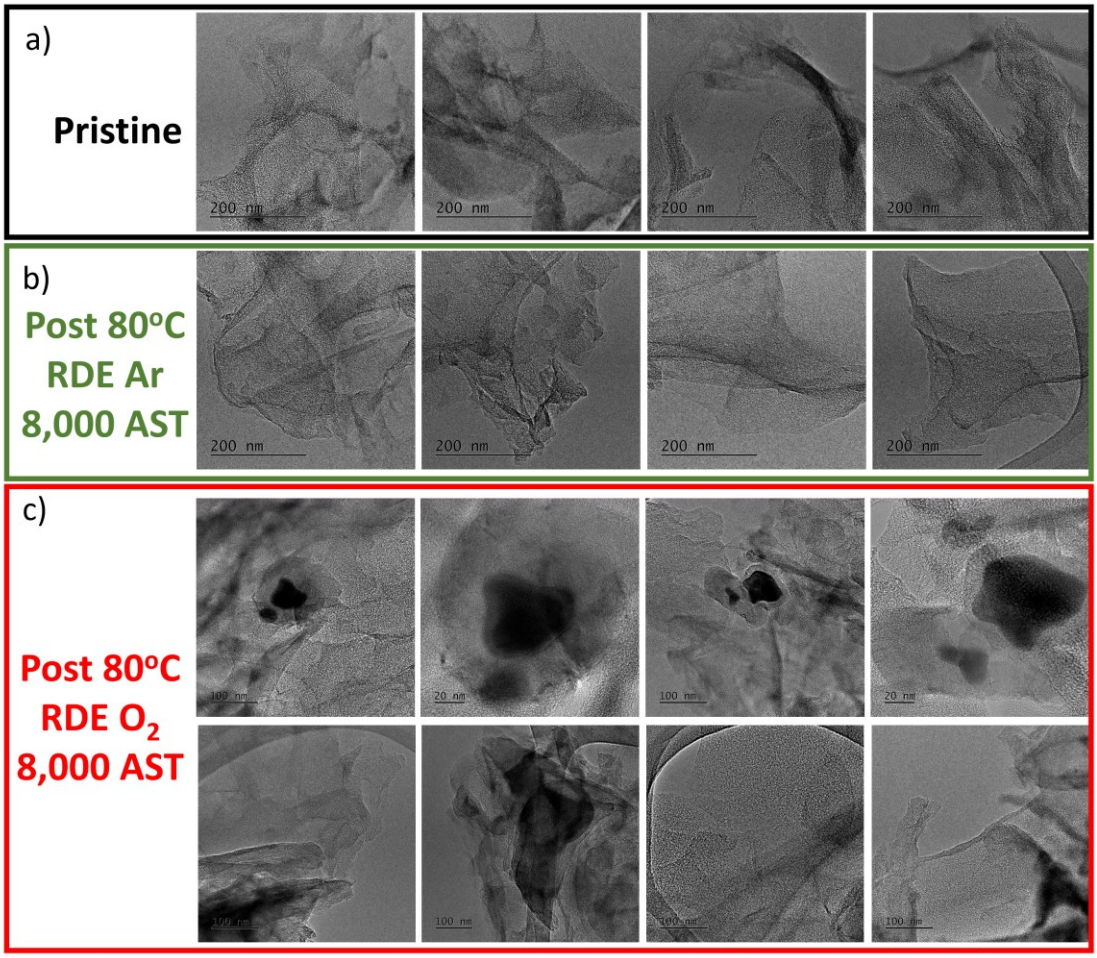


Figure B6. Bright-field TEM of TAP 900@^{57}Fe a.) Pristine. After 8,000 AST cyclic voltammetry in RDE (no rotation) between 0.9-0.6 V_{RHE} (3 s hold) in 80°C 0.1 M $HClO_4$ with b.) Ar-saturation. c.) O_2-saturation.

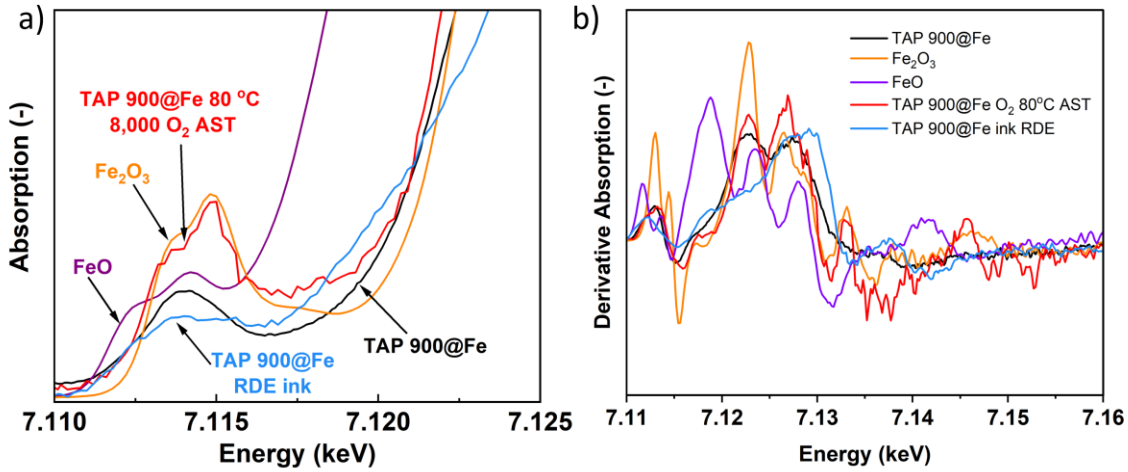


Figure B7. TAP 900@Fe and post-mortem 8,000 O_2 AST at 80°C in RDE, compared with FeO and Fe_2O_3 references *ex-situ* a.) Pre-edge XANES and b.) First-derivative spectra with 10-point Savitsky-Golay smoothing.

Table B1. *Ex situ* ICP-MS analysis measured ^{56}Fe and ^{57}Fe dissolution after 8,000 AST cycles at 80°C.

Sample	Protocol	Sample taken	^{56}Fe measured (ppb)	^{57}Fe measured (ppb)	^{57}Fe corrected (ppb)
TAP900@^{57}Fe	8k cycles AST 80°C Ar	Immediately	8.4	0.48	0.290
		after 2h holds at OCP	8.6	0.50	0.305
	8k cycles AST 80°C O_2	Immediately	3.9	0.73	0.639
		after 2h holds at OCP	4.7	0.83	0.720
Pt/C	8k cycles AST 80°C O_2	Immediately	4.4	0.07	-0.028
		after 2h holds at OCP	5.0	0.10	-0.015
Blank			0.2	0.009	0.004
			0	0	0.000

Supporting Note B1:

Pt/C was used as a reference to determine ^{56}Fe contamination within the electrochemical cell. The corrected ^{57}Fe was found from the following equation:

$$^{57}Fe_{corrected} = {}^{57}Fe_{measured} - (0.0212 \times ({}^{56}Fe_{measured}/0.918)) \qquad \textbf{Equation B0.1}$$

Where 2.12% is the natural abundance of ^{57}Fe and 91.8% is the natural abundance of ^{56}Fe.

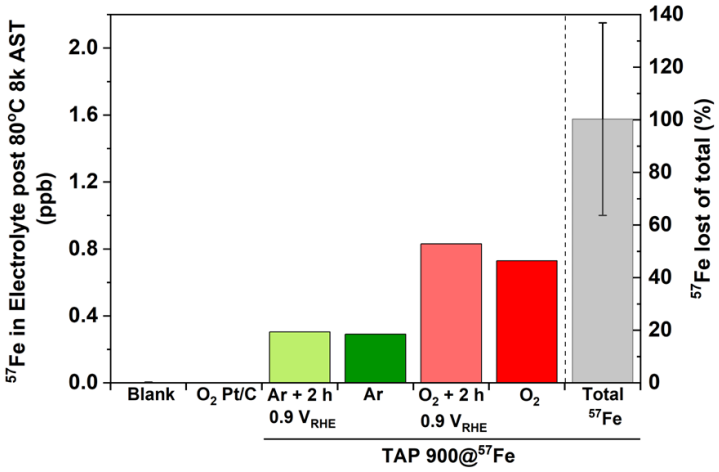


Figure B8. *Ex situ post-mortem* ICP-MS ^{57}Fe dissolution after 8,000 AST cycles at 80°C for Pt/C and TAP 900@^{57}Fe. TAP 900@^{57}Fe was held at 0.9 V_{RHE} for 2 h before a second ICP-MS measurement was performed.

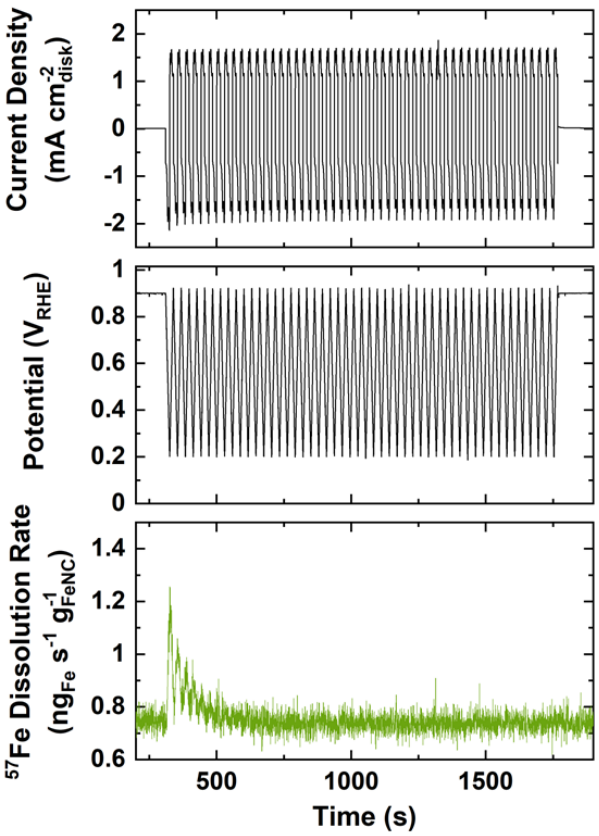


Figure B9. 50 Ar-saturated cycles at 50 mV s^{-1} in operando ICP-MS flow cell setup following 8,000 O_2-saturated AST cycles at 80°C in RDE. All measurements between 0.9-0.2 V_{RHE} with 0.2 mg_{FeNC} cm^{-2} in 0.1 M $HClO_4$.

Supplementary Note 2:

Regarding identification of the redox couple at 0.29 V_{RHE} in Figure 3c, the redox couple coincides with Fe^{III}-N/Fe^{II}-N complexes in ethylenediaminetetraacetic acid, EDTA (0.35 V_{RHE} pH 1),[6] or polyaniline, PANI (leucoemeraldine to emeraldine, ca. 0.43 V_{RHE} pH 1), [7] although their redox couples are not symmetric at low pH so appears unlikely. Alternatively, redox couples of ferrihydrite/Fe^{II} (0.25-0.45 V_{RHE}, pH 1) or lepidocrocite γ-FeOOH/Fe^{II} (0.27 V_{RHE}, pH 1),[8] are possible candidates. Meanwhile hematite α-Fe_2O_3/Fe^{2+} appears too low at 0.07 V_{RHE} (pH 1).[8] The redox couple could also be caused by a non-Fe species such as S^0/HS^- where S comes from Nafion (0.27 V_{RHE}).[8] Quinone-hydroquinone redox can occur at these low potentials, [9] although the defined redox peak is uncharacteristic of those redox species.

The high potential redox could be deconvoluted into two peaks with quinone/hydroquinone and adsorbed Fe^{III}/Fe^{II} on those sites.[10]

Table B2. Comparison to Literature for Redox identification.

Redox Couple	Potential (V_{RHE})	Reference	Comment
This work	0.29	This work	
Ferrihydrite/Fe2+	0.25-0.45	[8]	
γ-FeOOH/Fe^{II}	0.27	[8]	
Leucoemeraldine/emeraldine	0.43	[7]	Literature shows not symmetric redox
EDTA	0.35	[6]	
α-Fe_2O_3/Fe^{2+}	0.07	[8]	Too low potential

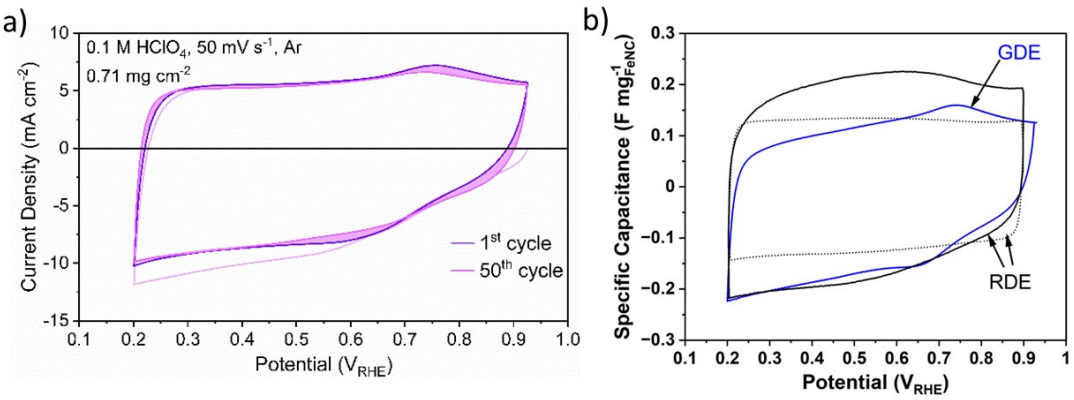


Figure B10. a.) Example of the 50 CVs measured at 50 mV s^{-1} in Ar condition before online GDE-ICP-MS measurement. The Fe redox peak decreases with each cycle. b.) Comparison of mass specific capacitance between RDE and GDE. The same Nafion loading (weight ratio of 1.4:1 Nafion:FeNC) was used in both GDE and RDE (0.2 $mg_{Fe\text{-}N\text{-}C}$ cm_{disk}^{-2}, solid line) measurement. RDE grey line represents CV with 0.5:1 Nafion:FeNC.

Supplementary Note 3:

To the best of my knowledge the appearance of Fe redox in GDE (but not RDE) has not been reported before and could be the result of the accessible structure of TAP 900@Fe and a change in the microenvironment of the FeN_x sites.[11] Perhaps in the flooded RDE the normally redox active $Fe^{3+}N_x$ sites have their charge neutralized by ClO^{4-} which are present on both sides of the $Fe^{3+}N_x$ sites within a graphene sheet. This is supported by the decreasing redox peak with cycling in Ar as the GDE becomes wetted with cycling. This will be studied further in future work.

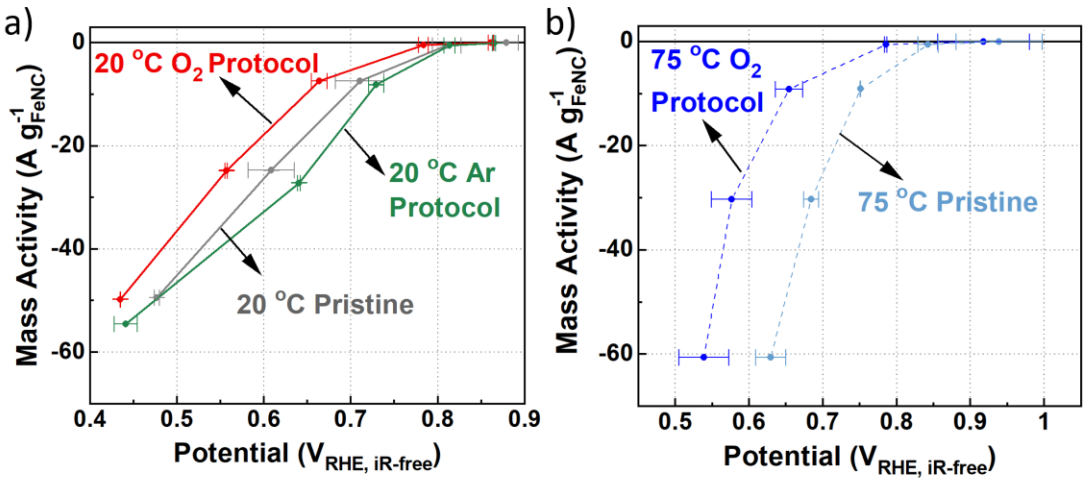


Figure B11. Mass activity of GDE at a.) 20 °C O_2 reduction in GDE for pristine TAP 900@Fe, and after O_2 and Ar 20 °C GDE protocols. b.) 75°C O_2 reduction in GDE for pristine TAP 900@Fe and after O_2 GDE 75 °C GDE.

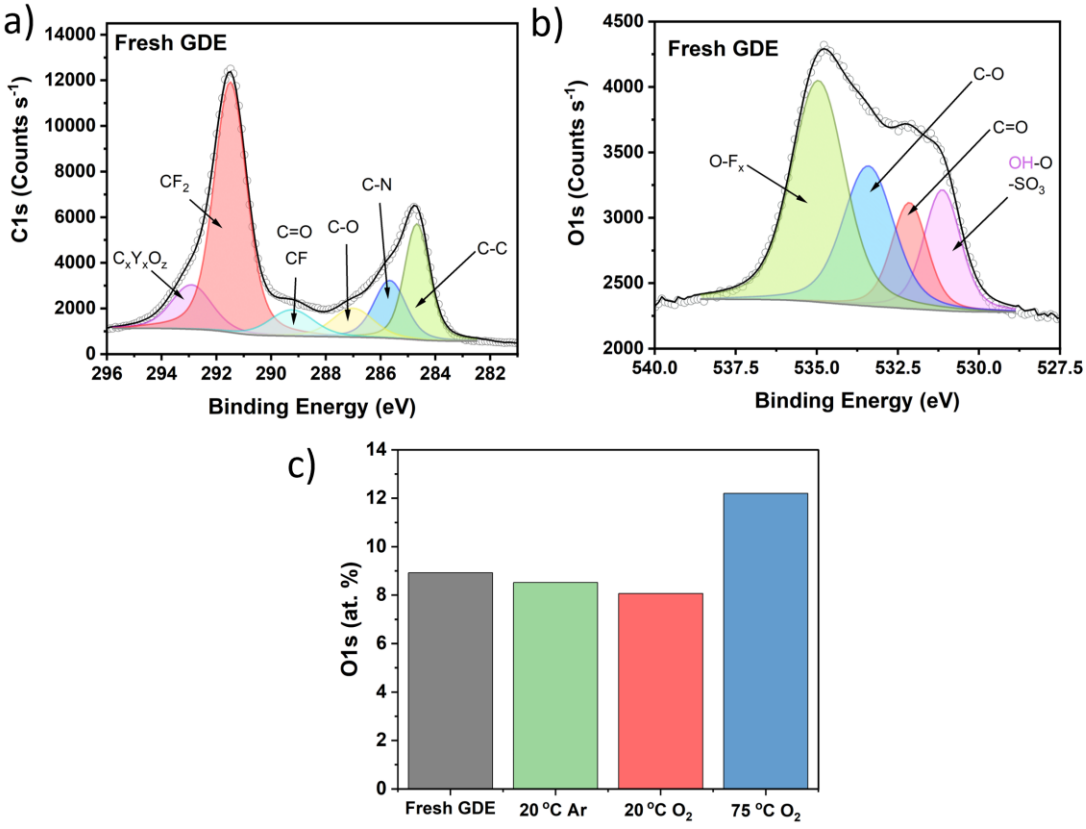


Figure B12. Peak fitting of fresh TAP 900@Fe GDE for a.) C1s and b.) O1s. c.) Total O1s content in at.% for GDE samples. The content is based on counts from only C and O.

Table B3. Relative content in at.% considering only C and O in GDE.

XPS Peak	Fresh	Post GDE 20 °C Ar	Post GDE 20 °C O_2	Post GDE 75 °C O_2
C1s	91.08	91.48	91.93	87.8
O1s	8.92	8.52	8.07	12.2

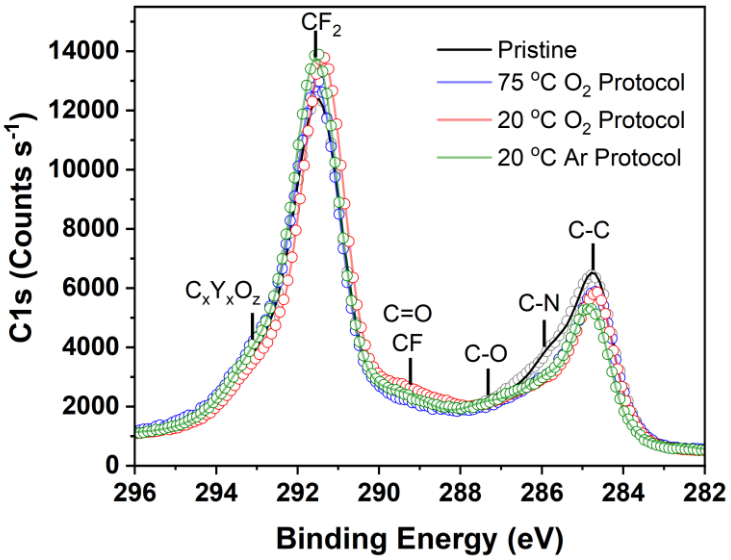


Figure B13. Comparison of C1s for fresh and *post-mortem* GDE samples.

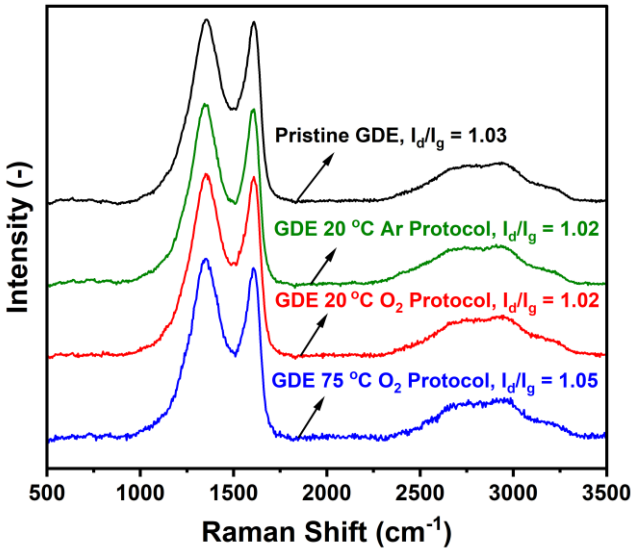


Figure S14. Raman spectroscopy of pristine TAP 900@Fe on GDE, and post GDE Protocol at 20 °C (Ar and O_2) and 75 °C (O_2).

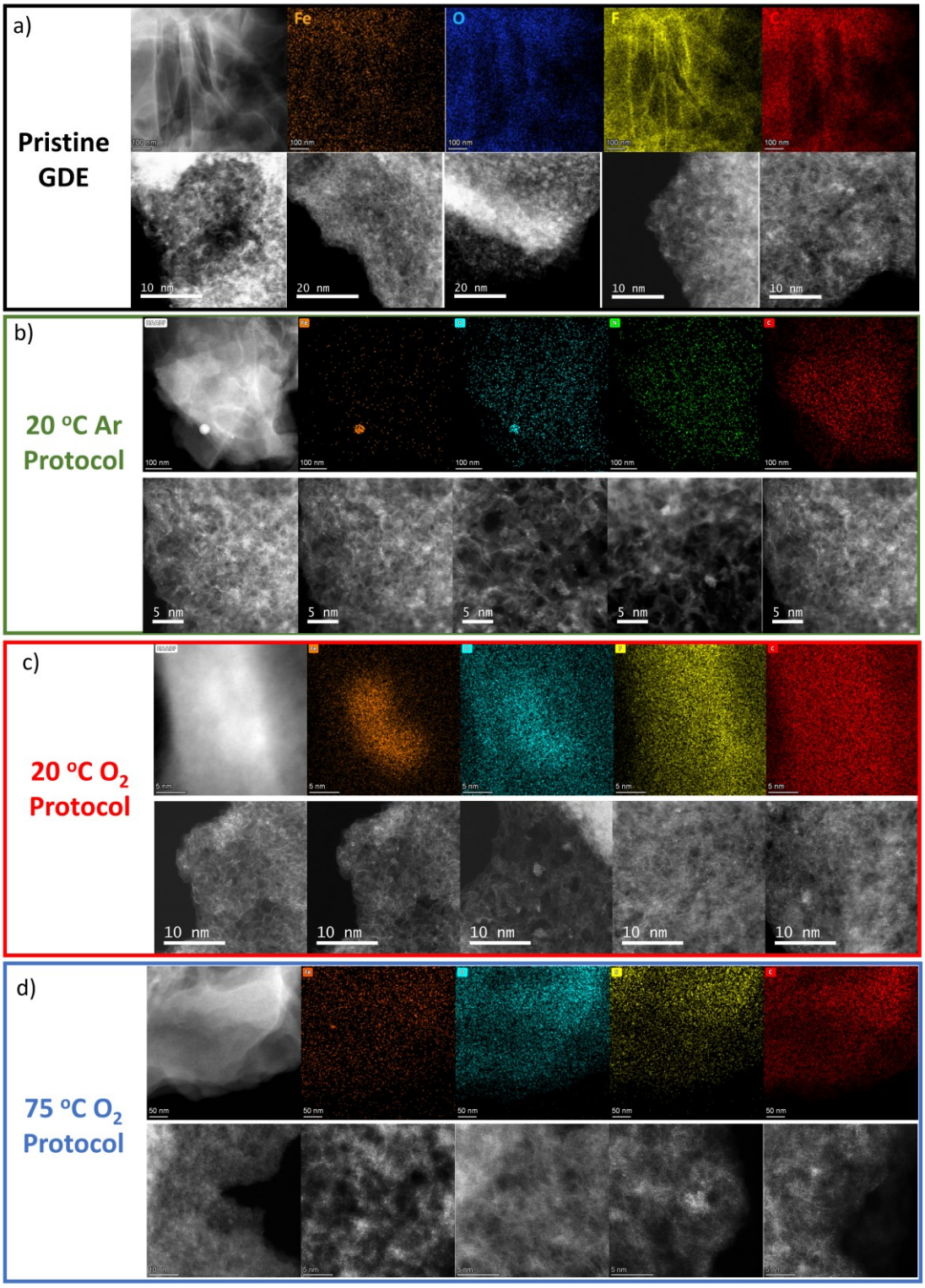


Figure B15. a.) STEM-EDX spectrum images (top) and HAADF-STEM (bottom and left) of a.) Pristine GDE b.) Post 20 °C Ar Protocol c.) Post 20 °C O_2 Protocol. d.) Post 75 °C O_2 Protocol.

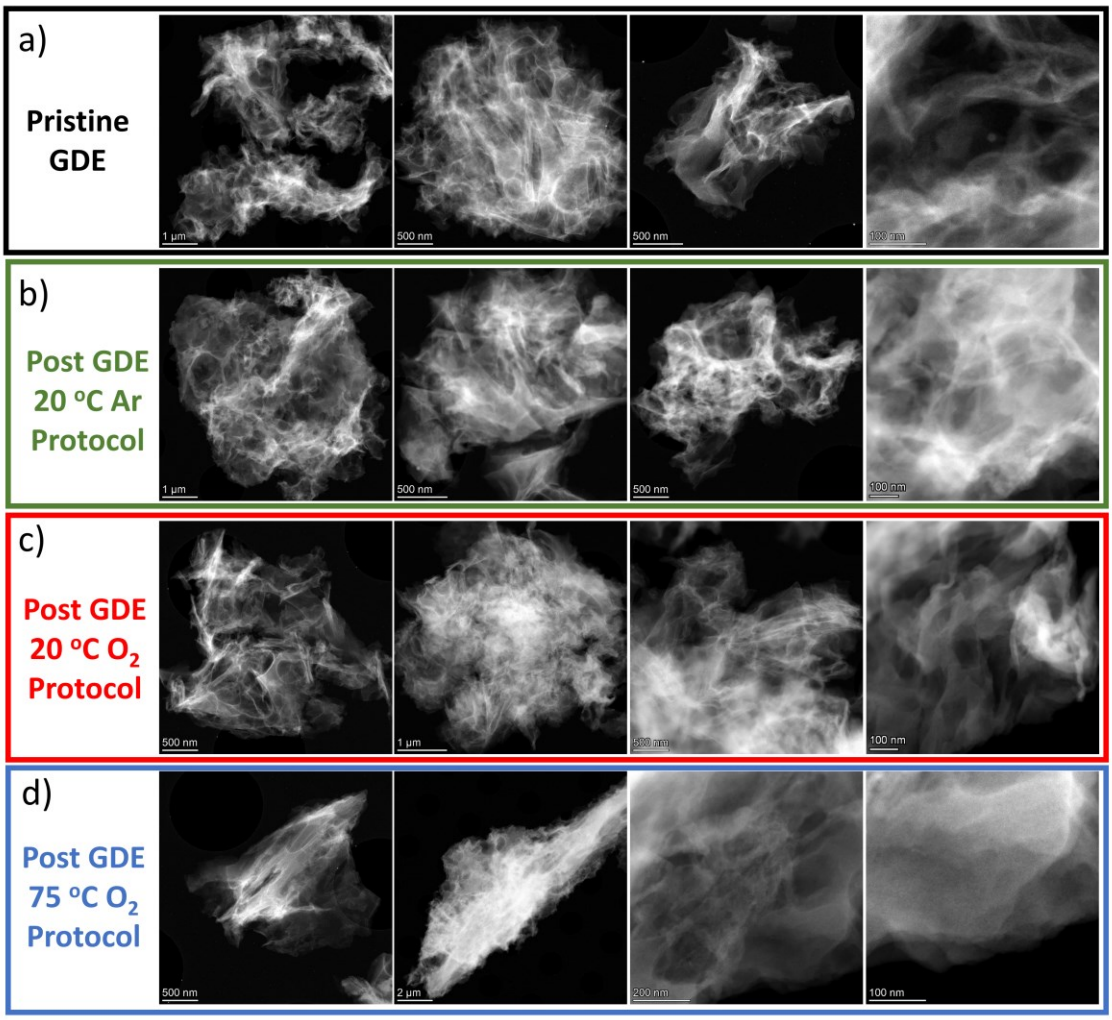


Figure B16. HAADF-STEM of TAP 900@Fe structure in a.) pristine GDE. Post GDE Protocols in b.) 20 °C Ar. c.) 20 °C O_2. d.) 75 °C Ar O_2.

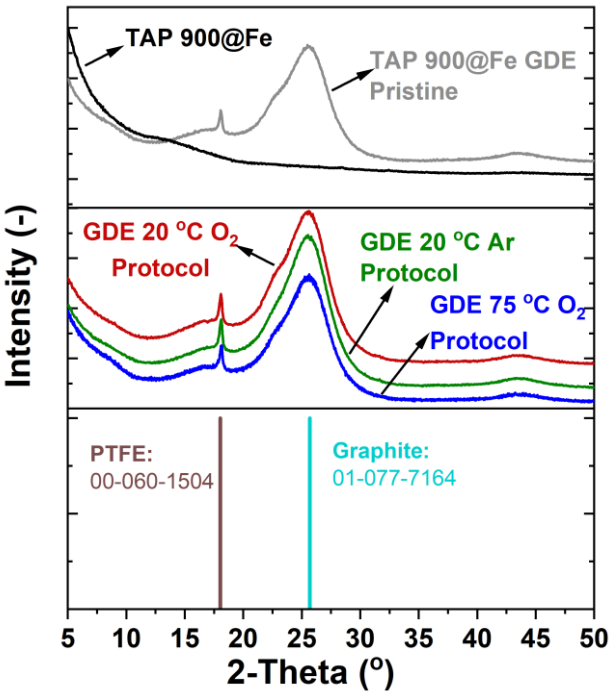


Figure B17. XRD of pristine TAP 900@Fe, prepared on GDE and post GDE protocols, with peaks of PTFE and graphite labelled.

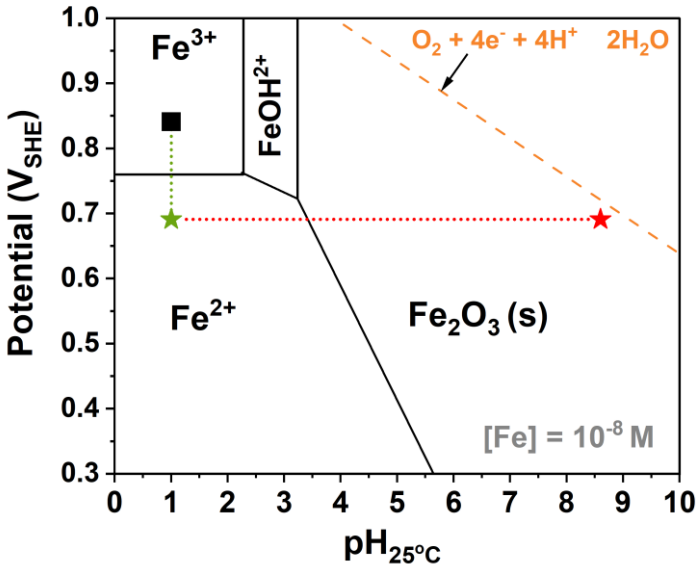


Figure B18. Pourbaix diagram of Fe at 25 °C and [Fe] = 10^{-8} M. Data replotted from ref.[12]

References

1 M. Rouhet, S. Bozdech, A. Bonnefont and E. R. Savinova, *Electrochem. Commun.*, 2013, **33**, 111–114.
2 P. Vanýsek, *CRC Handbook of Chemistry and Physics*, CRC Press, Boca Raton, USA, 92nd edn., 2011.
3 J. Newman and K. E. Thomas-Alyea, *Electrochemical Systems*, John Wiley & Sons, Third., 2004.
4 B. Tjaden, S. J. Cooper, D. J. Brett, D. Kramer and P. R. Shearing, *Curr. Opin. Chem. Eng.*, 2016, **12**, 44–51.
5 J. Barrio, A. Pedersen, S. Ch. Sarma, A. Bagger, M. Gong, S. Favero, C. Zhao, R. Garcia-Serres, A. Y. Li, Q. Zhang, F. Jaouen, F. Maillard, A. Kucernak, I. E. L. Stephens and M. Titirici, *Adv. Mater.*, 2023, **35**, 2211022.
6 K. Shimizu, R. Hutcheson, M. D. Engelmann and I. Francis Cheng, *J. Electroanal. Chem.*, 2007, **603**, 44–50.
7 F. Huerta, C. Quijada, F. Montilla and E. Morallón, *J. Electroanal. Chem.*, 2021, **897**, 115593.
8 B. Thamdrup, in *Advances in Microbial Ecology*, ed. B. Schink, Springer US, Boston, MA, 2000, pp. 41–84.
9 K. Kinoshita and J. A. S. Bett, *Carbon*, 1973, **11**, 403–411.
10 D. Li, C. Batchelor-McAuley, L. Chen and R. G. Compton, *J. Phys. Chem. Lett.*, 2020, **11**, 1497–1501.
11 J.-Q. Zhong, K.-J. Yan, J. Yang, W.-H. Yang and X.-D. Yang, *ACS Catal.*, 2022, **12**, 9003–9010.
12 B. Beverskog and I. Puigdomenech, *Corros. Sci.*, 1996, **38**, 2121–2135.

Appendix C (Chapter 6): Fe-N-C PEMFC Optimisation: The Effect of Ionomer Loading

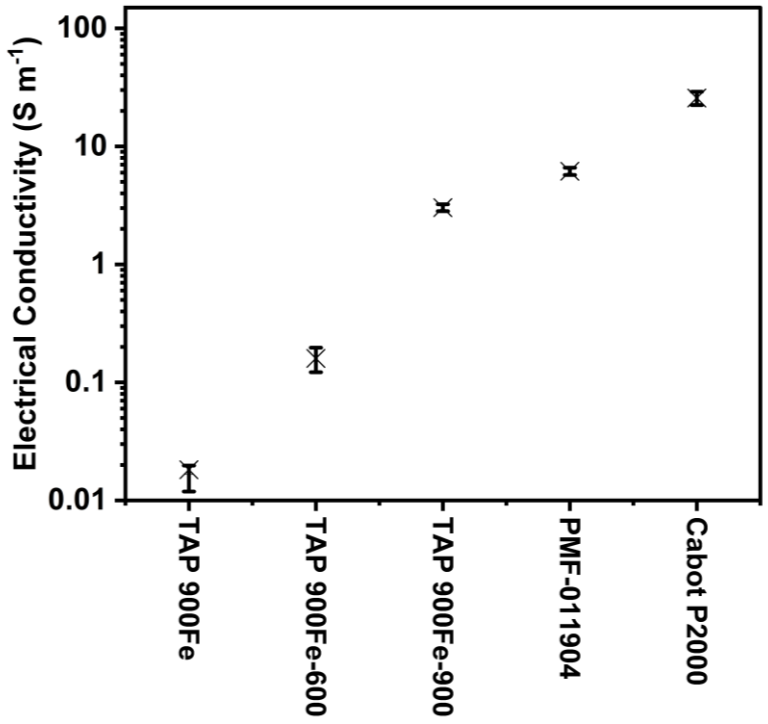


Figure C1. Electrical conductivity determined from two probe pellet method for TAP-derived materials, commercial FeNC (PMF-011904) and commercial carbon (Cabot P2000).

Supporting Note C1:

The electrical conductivity measured by the two-probe pellet method provides a relative comparison of electrical conductivity rather than absolute values.[1,2] The electrical conductivity values of PMF-011904 and Cabot P2000 are known to at least one order of magnitude greater than those reported with this method.

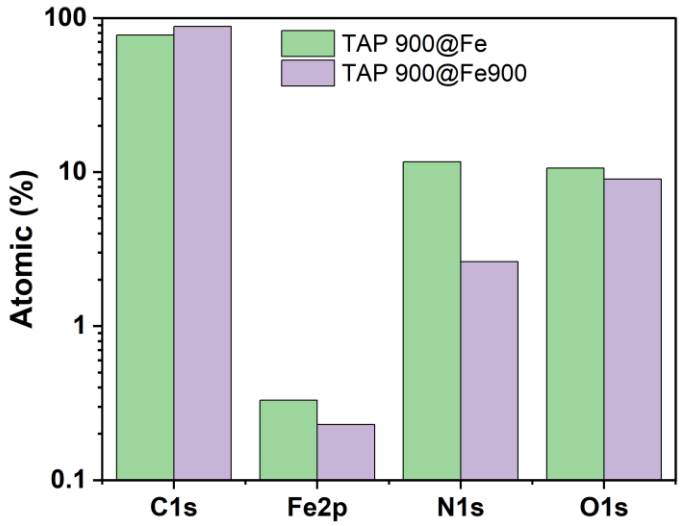


Figure C2. Comparison of surface composition between TAP 900@Fe and TAP 900@Fe900.

Supporting Note 2:

TAP 900@Fe in Chapter 4 showed Fe, N and O content of 0.14, 4.5 and 2.6 at.% from XPS, respectively. This is significantly lower than the values reported here (**Figure C2**). This difference is attributed to the lower hydration of the Mg precursor ($MgCl_2 \cdot 6H_2O$) in this work. Here, a fresh bottle of $MgCl_2 \cdot 6H_2O$ was used, whereas in the previous work the $MgCl_2 \cdot 6H_2O$ may have been in a more hydrated state (e.g. $MgCl_2 \cdot 9H_2O$ or $MgCl_2 \cdot 12H_2O$) due to its highly hydroscopic nature. The hydration state of the Mg precursor and its impact on the catalyst properties is the subject of future work.

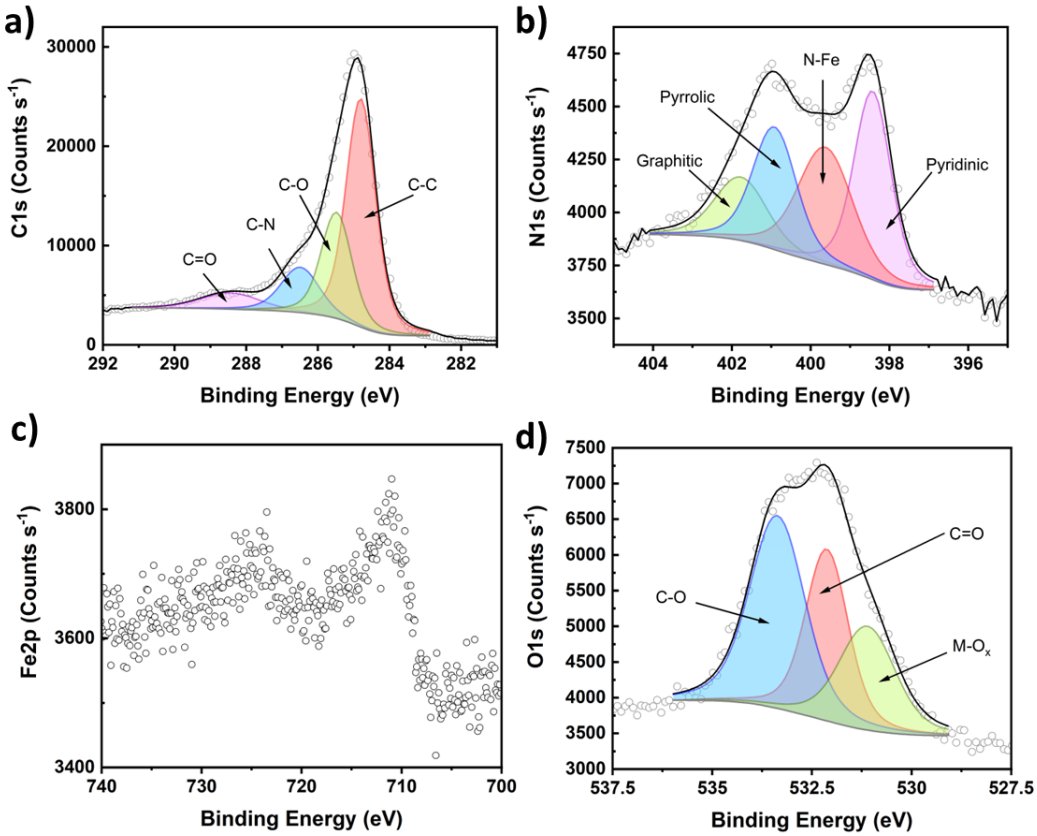


Figure C3. TAP 900@Fe900 XPS of a.) C1s b.) N1s, c.) Fe2p and d.) O1s.

Table C 1. Composition of TAP900@Fe900 from XPS and ICP-MS.

Element	XPS		ICP-MS
	Atomic (%)	Weight (%)	Weight (%)
C	88.1	84.5	
Fe	0.2	1.0	1.2±0.1
N	2.6	2.9	
O	9.0	11.5	

Table C 2. Percentage contribution of different N1s peaks in TAP 900@Fe900

Peak	%
Graphitic	15.0
Pyrrolic	24.2
N-Fe	29.0
Pyridinic	31.8

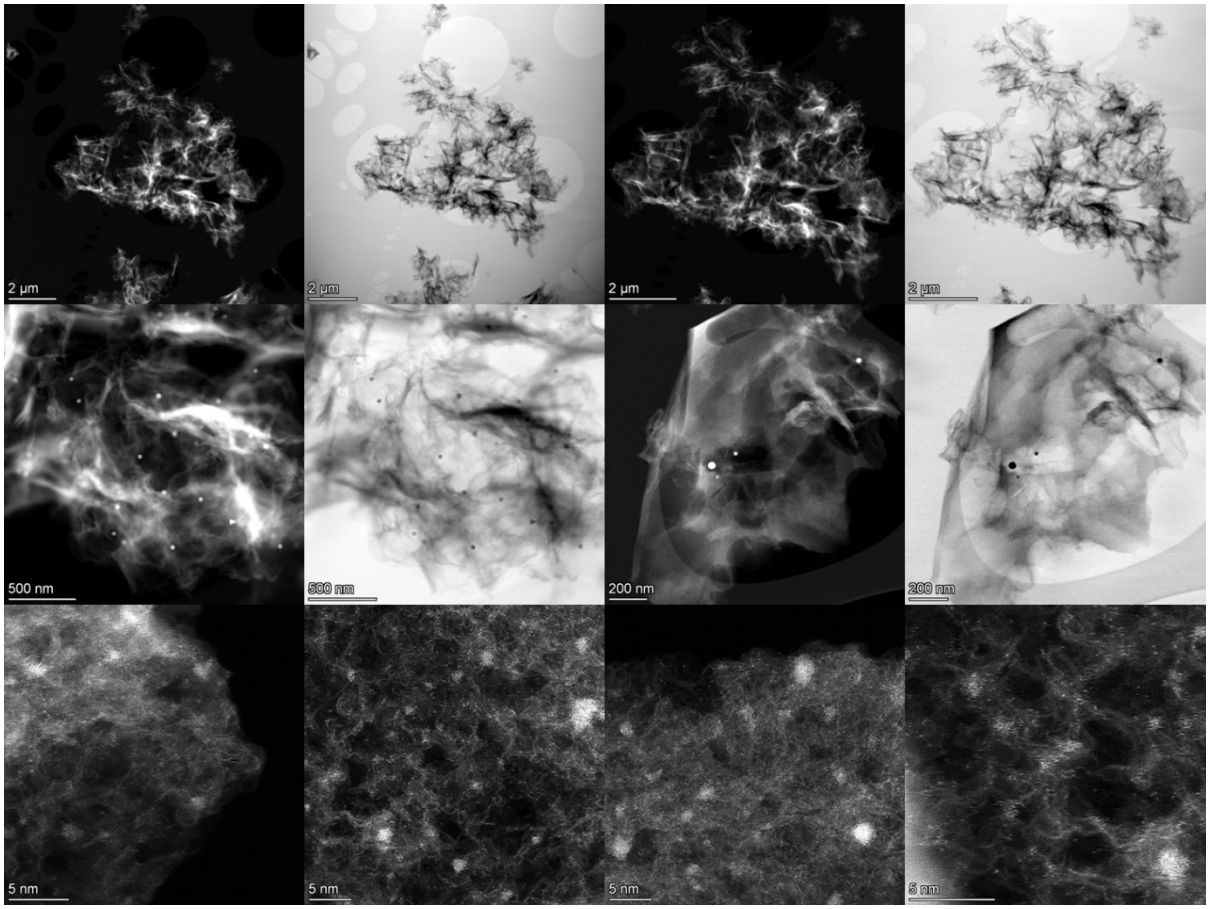


Figure C4. HAADF-STEM (with some bright field images) at different scales of TAP 900@Fe900.

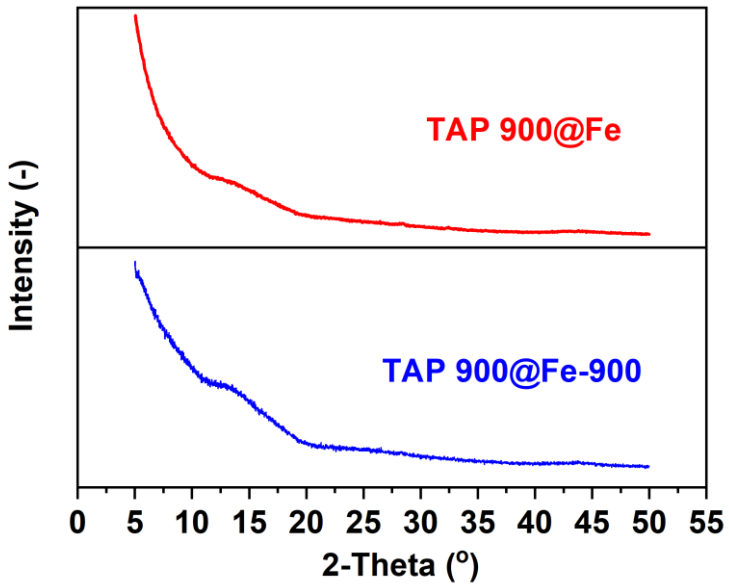


Figure C5. XRD of TAP 900@Fe and TAP 900@Fe-900.

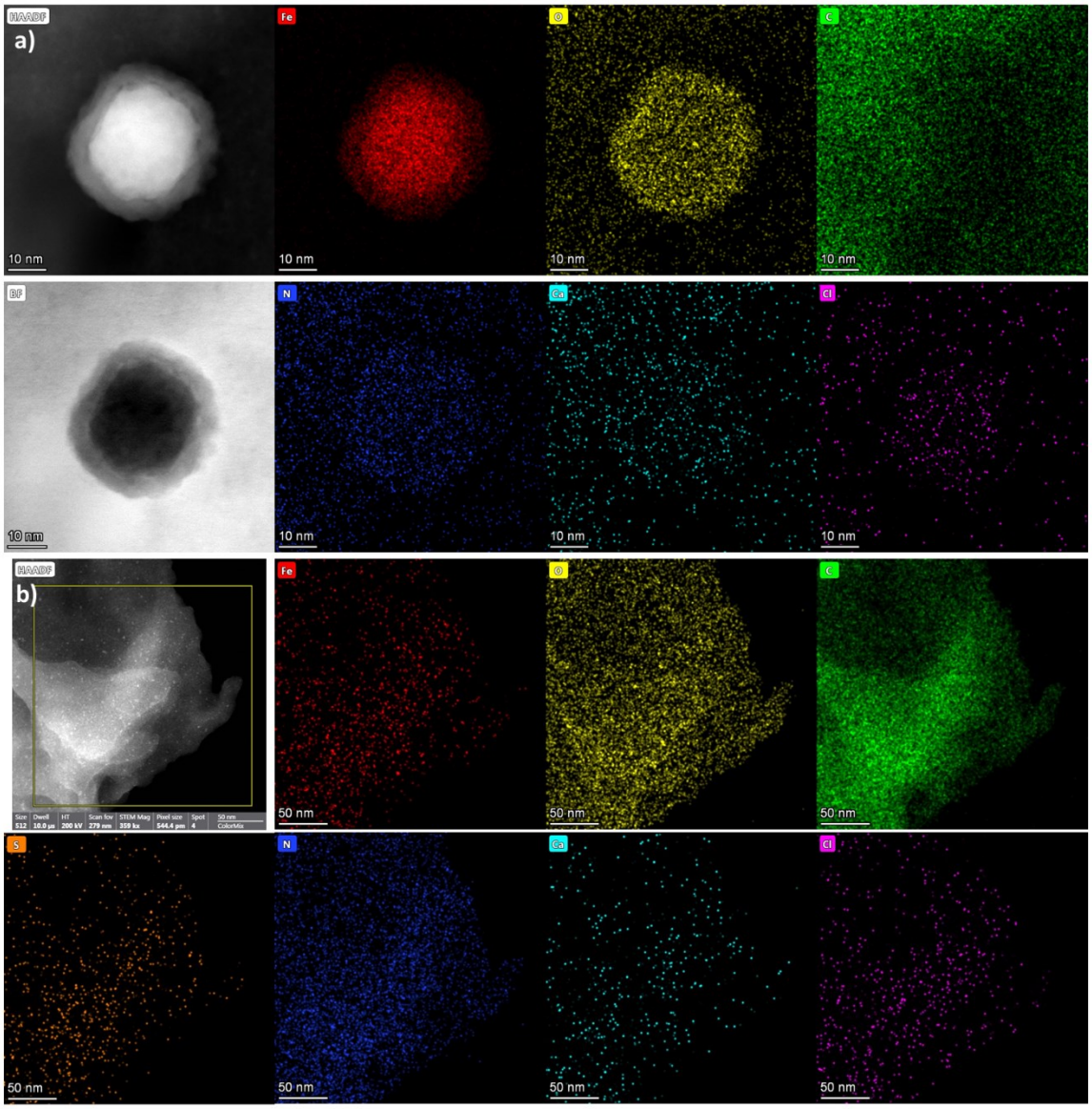


Figure C6. HAADF-STEM and EDX spectroscopy of a.) 40 nm particle b.) nanometric clusters in TAP 900@Fe900.

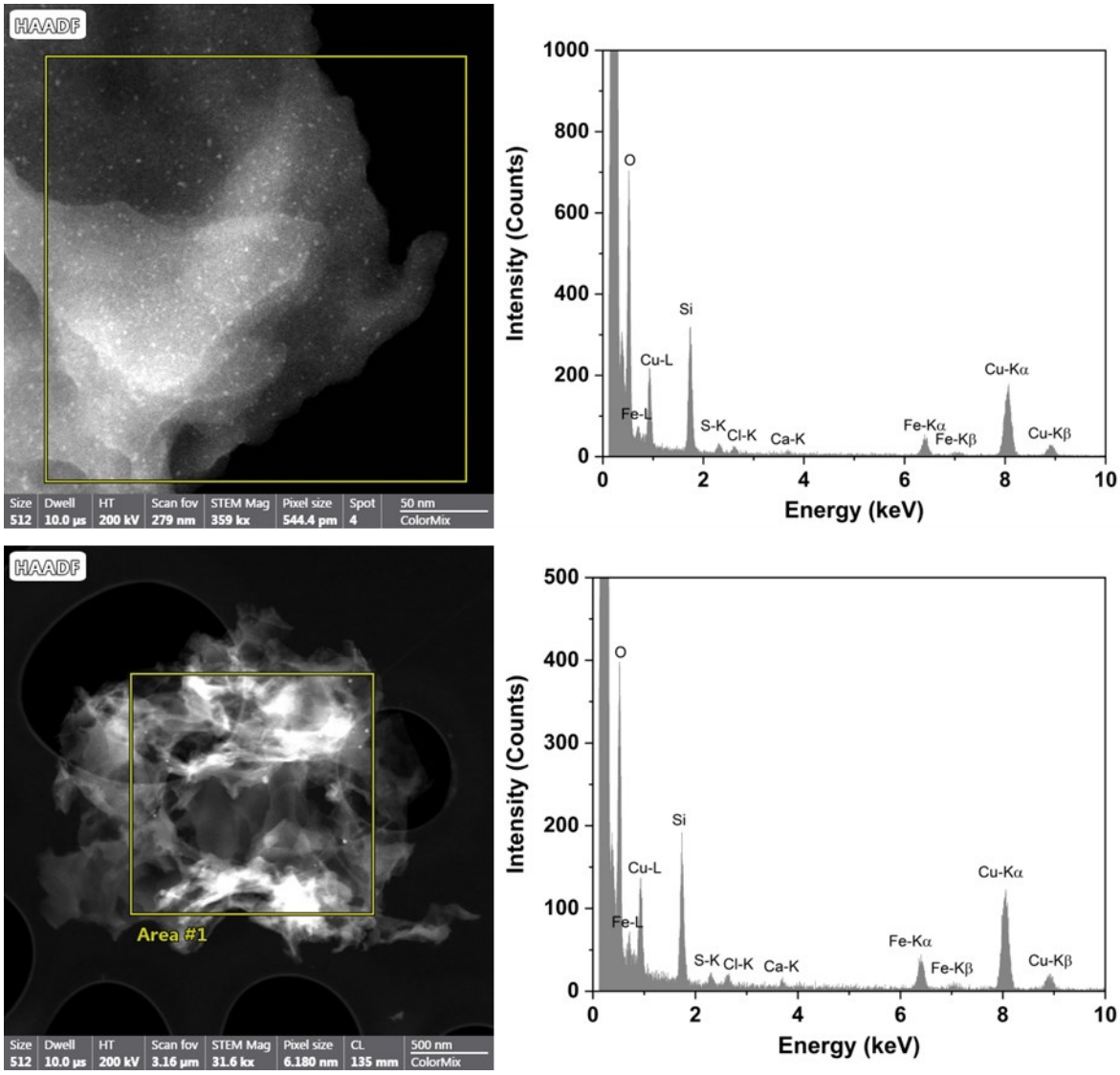


Figure C7. EDX spectroscopy on two areas of TAP 900@Fe900.

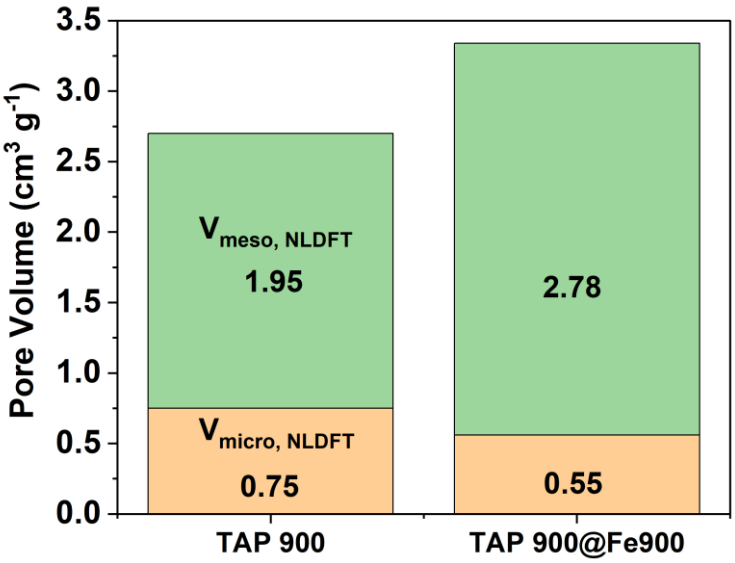


Figure C8. Pore volume of TAP-derived materials. TAP 900 value from Chapter 4.

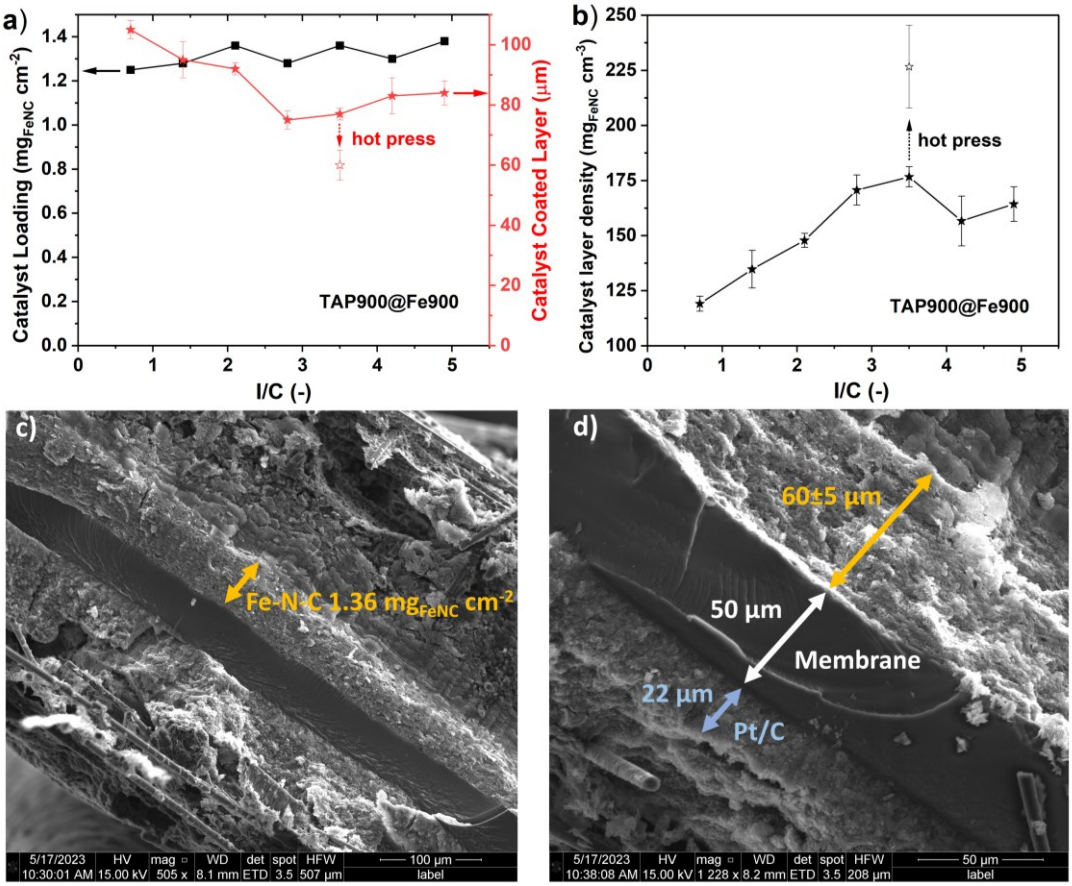


Figure C9. Effect of I/C on a.) CCL thickness and corresponding b.) calculated catalyst layer density prior to hot pressing measured by micrometer. Empty star represents of thickness and consequent catalyst layer density measured by cross-sectional SEM. Cross-section SEM of MEA with d.) 100 µm scale bar e.) 50 µm scale bar. I/C = 3.5 with FeNC loading of 1.36 mg_{FeNC} cm^{-2}. Distances measured using ImageJ software.

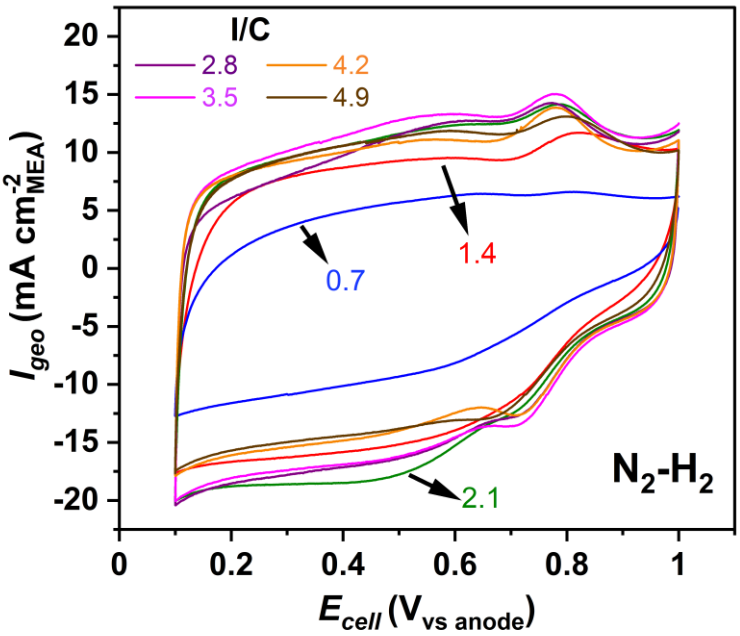


Figure C10. Cyclic voltammetry of TAP 900@Fe900 under N_2-H_2 (0.3 sccm flowrate) at 50 mV s^{-1} for varying I/C ratios.

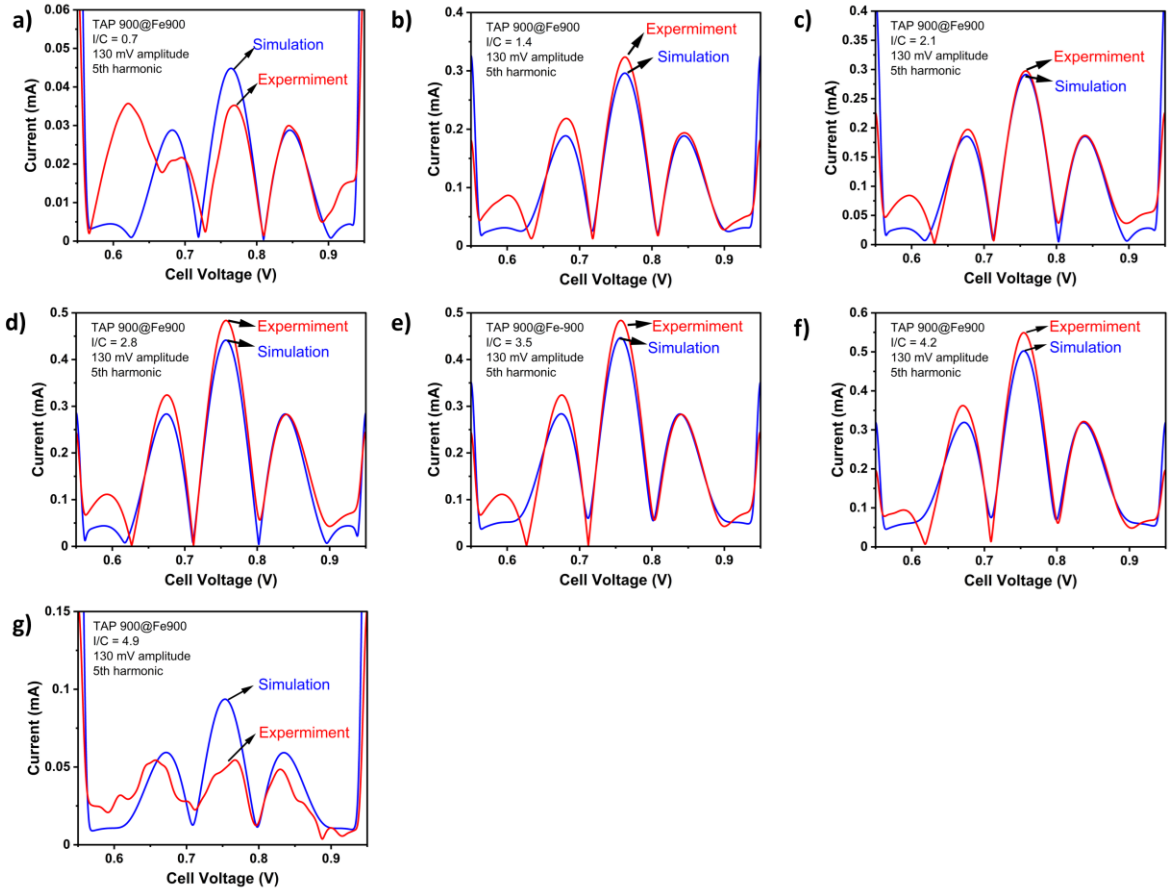


Figure C11. FTacV experiment and simulation results for varying I/C ratios of TAP 900@Fe900. FTacV of 5th harmonic with 130 mV amplitude.

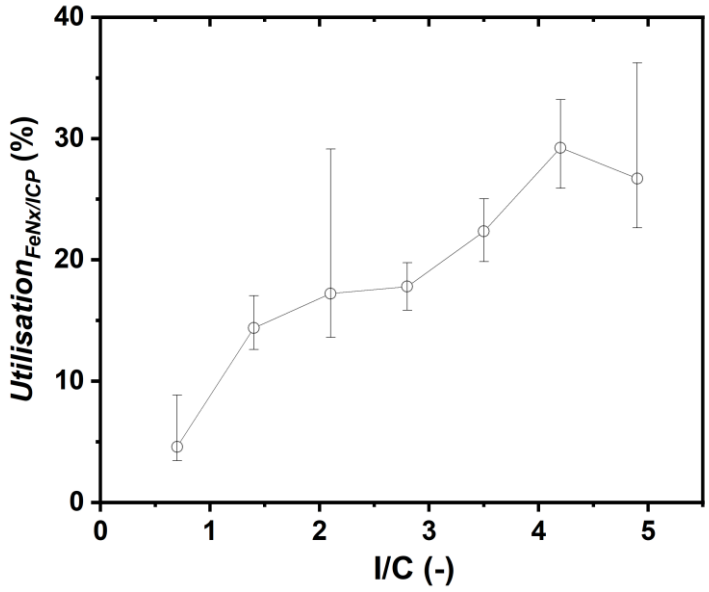


Figure C12. Active site utilisation relative to the total Fe content for I/C ratios of TAP 900Fe900.

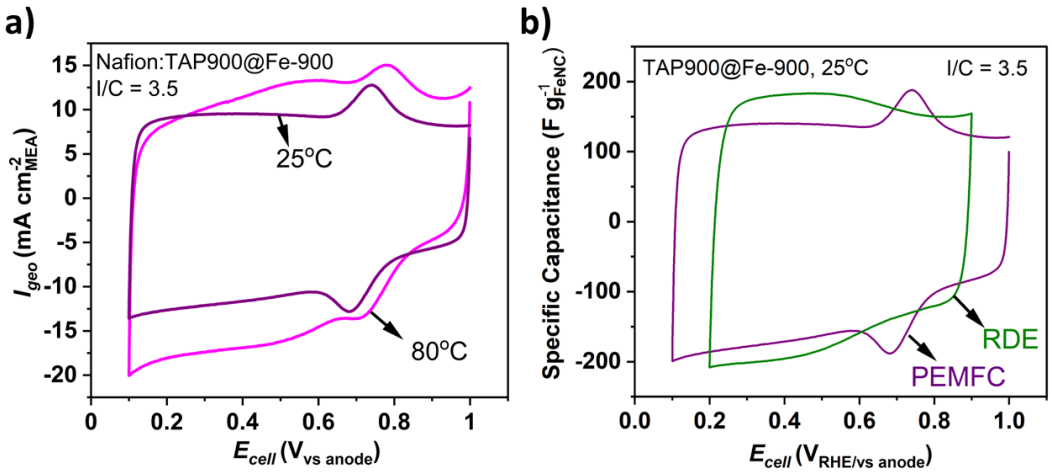


Figure C13. TAP 900@Fe900 a.) CV in PEMFC at 25°C and 80°C (under N_2-H_2). b.) Comparison of specific capacitance for CV in RDE and PEMFC at 25°C. Scan rates of 50 mV s^{-1}, with RDE in N_2-saturated 0.1 M $HClO_4$.

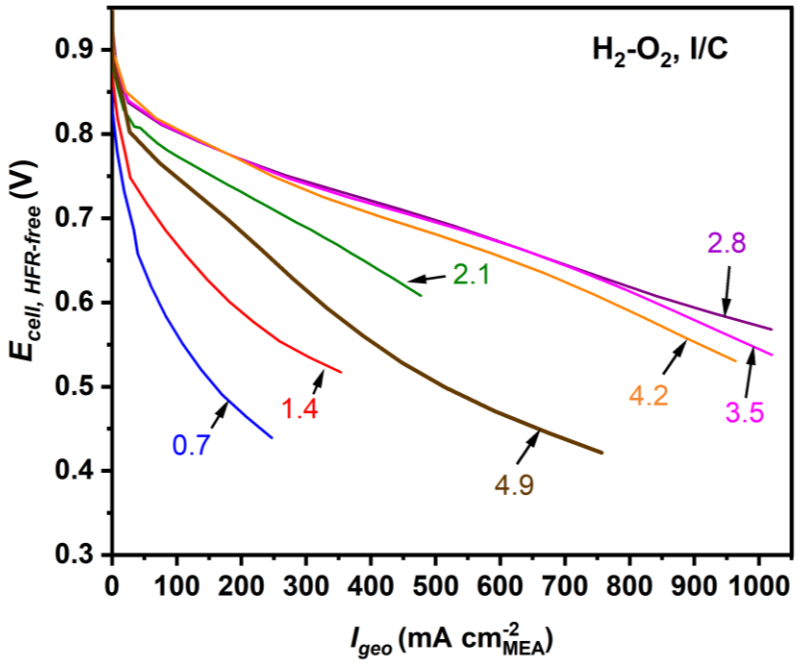


Figure C 14. Initial HFR-free H_2/O_2 performance.

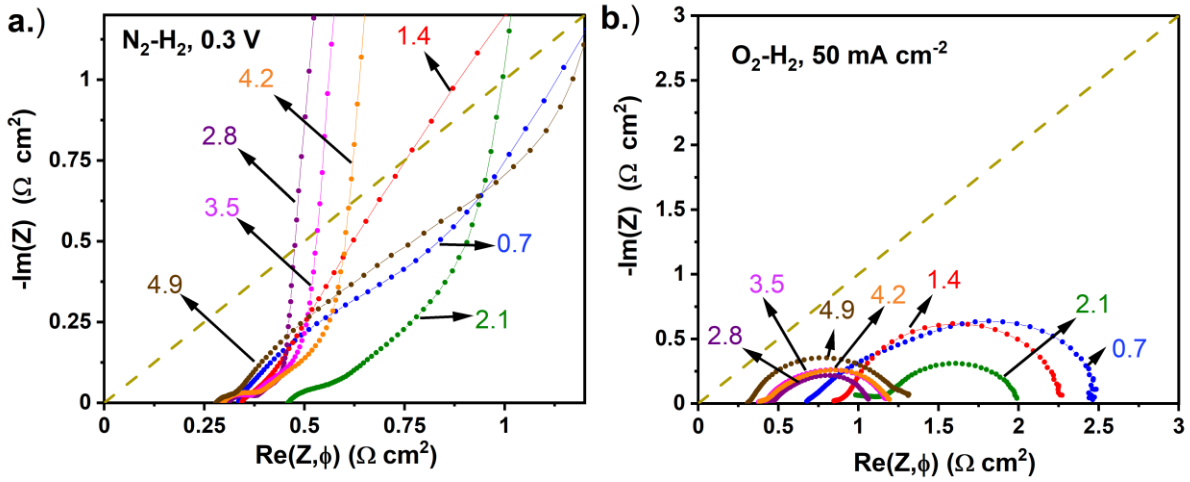


Figure C15. Nyquist plot without high frequency resistance compensation under a.) N_2-H_2 at 0.3 $V_{vs\ anode}$ b.) O_2-H_2 at 50 mA cm^{-2}. Dashed line represents 45°.

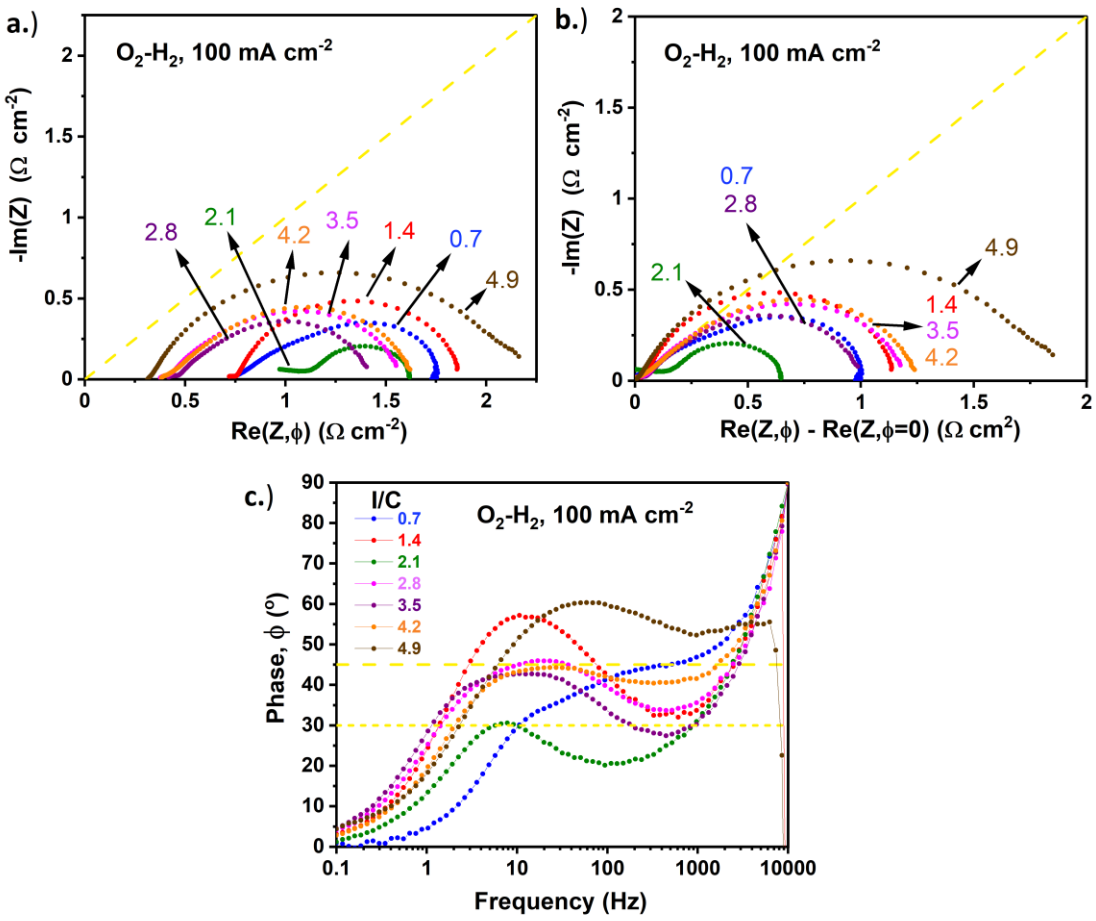


Figure C 16. O_2-H_2 at 100 mA cm^{-2} a.) Nyquist plot. b.) Nyquist plot with removal of Re(Z,ϕ=0). c.) Bode phase angle plot.

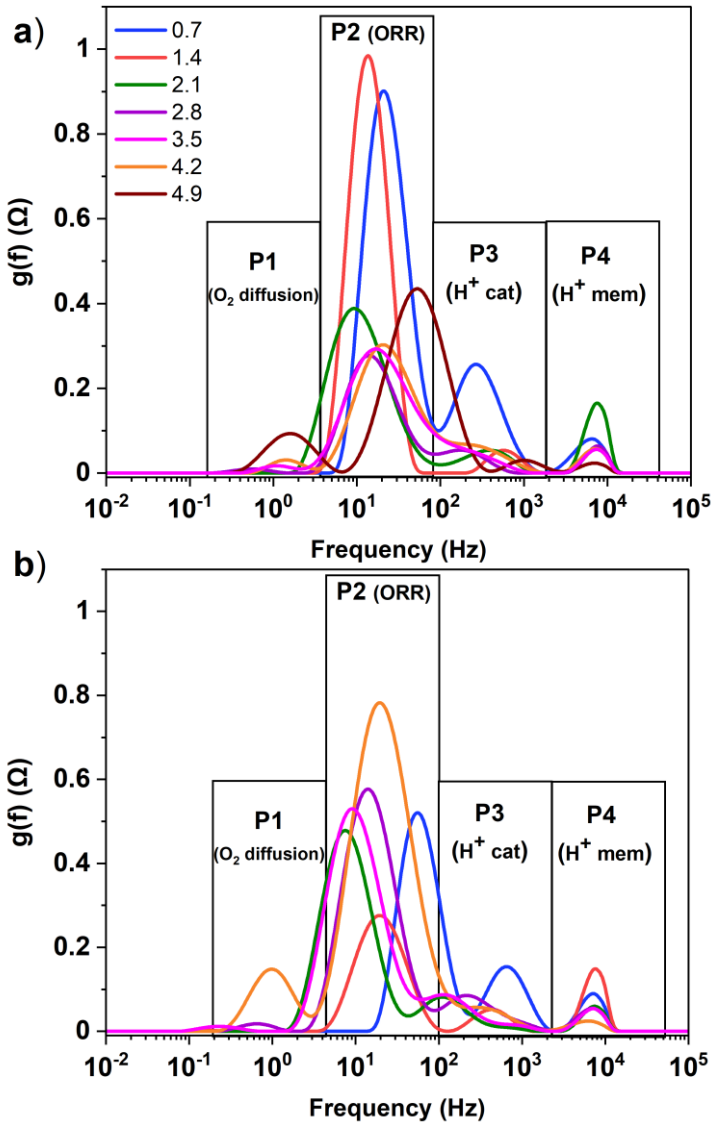


Figure C17. DRT analysis at varying I/C ratios at a.) 50 mA cm^{-2} and b.) 100 mA cm^{-2}.

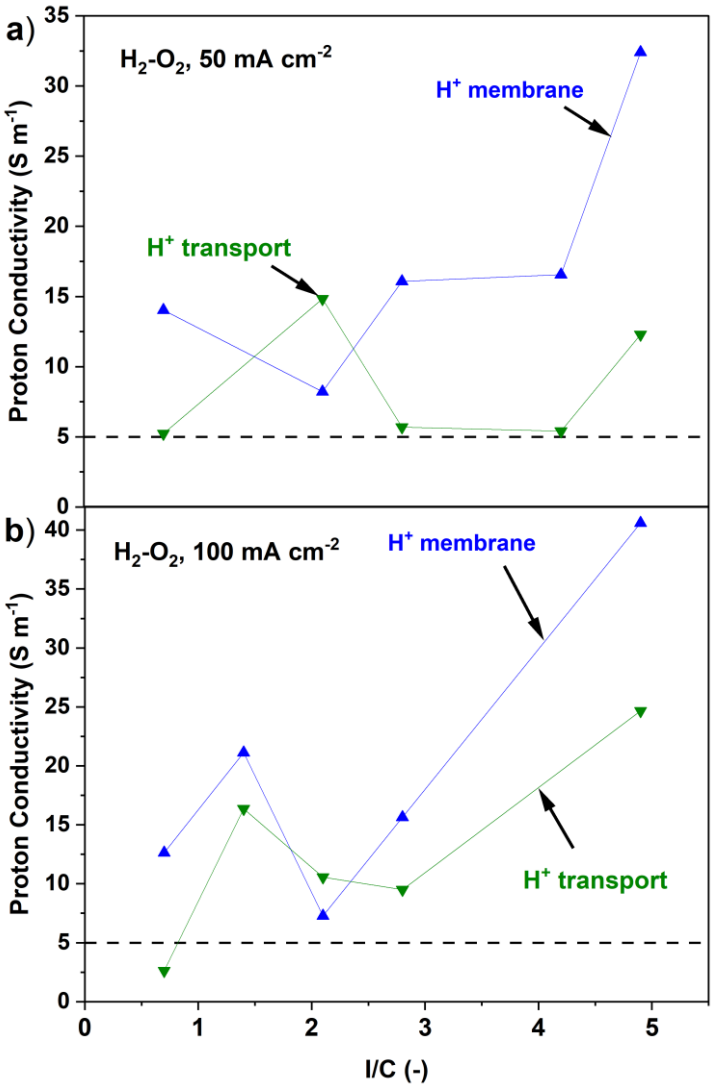


Figure C18. Calculated proton conductivity derived from DRT analysis and catalyst layer thickness values (Figure S9) at a.) 50 mA cm^{-2} and b.) 100 mA cm^{-2}. Horizontal dashed line at 5 S m^{-1} represents minimum proton conductivity required at high current density, as determined by Jaouen *et al*.[3]

References

1 O. Marciano, S. Gonen, N. Levy, E. Teblum, R. Yemini, G. D. Nessim, S. Ruthstein and L. Elbaz, *Langmuir*, 2016, **32**, 11672–11680.

2 L. Elbaz, C. R. Kreller, N. J. Henson and E. L. Brosha, *J. Electroanal. Chem.*, 2014, **720–721**, 34–40.

3 F. Jaouen, E. Proietti, M. Lefèvre, R. Chenitz, J.-P. Dodelet, G. Wu, H. Taek Chung, C. Marie Johnston and P. Zelenay, *Energy Environ. Sci.*, 2011, **4**, 114–130.

Appendix D (Chapter 7): Comparative techno-economic and life-cycle analysis of Pt/C versus Fe-N-C

Pt/C loading Calculation

For the baseline scenario the required amount of catalyst was calculated as follows:

Number of cells used were 380 with an active area of 185 cm^2 per cell.

The area to be coated is calculated by:

$$Total\ area\ coated\ with\ catalyst = 380\ \times\ 185 cm^2 = 70{,}300\ cm^2$$

With a loading of 0.125 mg cm^{-2} of Pt this gives total amount of Pt loading of:

$$70{,}300\ cm^2 \times 0.125 \frac{mg_{Pt}}{cm^2} = 8.79\ g_{Pt}$$

The Pt/C catalyst is made up of 46 wt.% Pt, therefore Pt/C:

$$\frac{8.79\ g}{0.46\ wt.\%} \approx 20\ g_{Pt/C}$$

Fe-N-C loading Calculation

The total required Fe-N-C for 80 kW PEMFC is based on power density of 290 mW cm^{-2} at 0.657 V with loading of 2.5 mg_{FeNC} cm^{-2}:

$$\frac{80{,}000\ W \times 0.0025\ g\ cm^{-2}}{0.290\ W\ cm^{-2}} = 690\ g_{FeNC}$$

Pt/C Manufacturing Calculation

Chloroplatinic acid (CPA) calculations were based on the molar ratios shown below:

$$\boldsymbol{Pt + 4\ HNO_3 + 6\ HCl\ \rightarrow\ H_2PtCl_6 + 4\ NO_2 + 4H_2O} \qquad \textit{Equation D 1}$$

Molecular weights were used to calculate the amount of mass required to produce 1.23 kg of CPA.

Table D 1. Chloroplatinic acid production inputs. Reproduced from ref [1] under Creative Commons CC BY 3.0.

Inputs			
Flow	Amount	Unit	Provider/Category
Hydrochloric acid, without water, in 30% solution state	0.66	kg	Market for Hydrocholoric acid, APOS, U - RER
Nitric acid, without water, in 50% solution state	0.76	kg	Market for nitric acid, APOS, U - RER
Platinum	0.64	kg	Market for platinum, APOS, U - GLO
Outputs			
Chloroplatinic acid	1.23	kg	
Nitrogen dioxide	0.55	kg	
Wastewater, average	216	mL	

Table D2. Pt/C production inputs and outputs for 20 g baseline scenario with provider of LCA data. Reproduced from ref [1] under Creative Commons CC BY 3.0.

Inputs			
Flow	Amount	Unit	Provider
Acetone	768	g	Market for acetone, APOS, U - RER
Carbon black	10	g	Market for carbon black, APOS, U - GLO
Chloroplatinic acid	17.7	g	Table S1
Electricity	4.43	MJ	Market group for electricity, medium voltage, APOS, U - GLO
Ethylene glycol	2.05	kg	Market for ethylene glycol, APOS, U - GLO
Hydrochloric acid, without water, in 30% solution state	255	g	Market for hydrochloric acid, APOS, U - RER
Sodium hydroxide	23	g	Market for sodium hydroxide, APOS, U - RER
Water, deionised	39.7	kg	Market for water, deionised, APOS, U - Europe without Switzerland
Outputs			
Acetone, emission to waste	768	g	
Hydrochloric acid, emission to water	255	g	
Pt/C catalyst	20	g	This Table.
Sodium hydroxide, emission to air	23.3	g	
Wastewater, average	39.7	kg	
Ethylene glycol, waste	2.05	kg	

Table D3. Modelled process inputs and outputs for Iron Nitrite nonahydrate. Reproduced from ref [1] under Creative Commons CC BY 3.0.

Inputs			
Flow	Amount	Unit	Provider
Iron ore	0.14	g	Market for iron ore, APOS U - GLO
Sodium nitrate	0.46	g	Market for sodium nitrate, APOS U - GLO
Water deionised	0.40	g	Market for deionised water, APOS U - RoW
Outputs			
Iron nitrate nonahydrate	1	g	

Table D 4. Modelled process inputs and outputs for Nicarbazin production. Reproduced from ref [1] under Creative Commons CC BY 3.0.

Inputs			
Flow	Amount	Unit	Provider
2-nitroaniline	317	g	Market for 2-nitroaniline, APOS, U - GLO
2-pyridinol	109	g	Market for 2-pyridinol, APOS, U - GLO
Outputs			
Nicarbazin	426	g	

Reaction of HF with Silica:

$$4HF + SiO_2 \rightarrow SiF_4 + 2H_2O \qquad \textit{Equation D 2}$$

Table D5. Energy inputs for synthesising 25 g Fe-N-C. Reproduced from ref [1] under Creative Commons CC BY 3.0.

Equipment	Power Consumption (kW)	Duration of usage (h)	Energy (kWh)
Planetary ball mill	2.2	1	2.2
Tube furnace	7	3	21
Filtration pump	0.5	4	2
Dry Oven	1	8	8
Tube furnace	7	3	21

Table D6. Production process inputs and outputs for 691 g Fe-N-C baseline scenario, with provider of LCA data. Reproduced from ref [1] under Creative Commons CC BY 3.0.

Inputs			
Flow	Amount	Unit	Provider/Category
Silica	1.38	kg	Market for activated silica, APOS, U - GLO
Electricity	5,393	MJ	Market group for electricity, medium voltage, APOS, U - GLO
Hydrogen fluoride	2.21	kg	Market for hydrogen fluoride, APOS, U - RER
Iron nitrate nonahydrate	0.45	kg	Table S3
Nicarbazin	3.46	kg	Table S4
Water deionised	111	kg	market for water, deionised, APOS, U - Europe without Switzerland
Outputs			
Silica	1.38	kg	Market for activated silica, APOS, U - GLO
Fe-N-C Catalyst	691	g	This Table
Hydrogen Fluoride	2.21	kg	Emission to air
Nicarbazin	2.76	kg	Table S4
Wastewater, average	111	kg	Sewerage

Table D7. Monetary valuation factors for the endpoint impacts. Factors for human health and ecosystem quality were obtained from Dong et al.[2] Conversion of 2017 USD to 2023 USD values were based on inflation over that period. Reproduced from ref [1] under Creative Commons CC BY 3.0.

Endpoint Impact	Unit	Equivalent Monetary Value Factor (USD 2017 / Unit)	Conversion factor from 2017 to 2023
Human health	DALY	108,836	
Ecosystem quality	Species·Year	13,964,286	1.22
Resources	USD 2013	1.05	

Table D8. Cost of production for baseline 20 g Pt/C at 500,000 stacks. Reproduced from ref [1] under Creative Commons CC BY 3.0.

PRODUCTION COST SUMMARY						**USD $kg_{Pt/C}^{-1}$**
RAW MATERIALS	Chloroplatinic Acid					13,275
	Acetone					38.4
	Carbon Black					0.75
	Ethylene glycol					136.53
	HCl					2.85
	Sodium Hydroxide					1.40
	Water, deionised					97.31
TOTAL RAW MATERIALS						13552.23
TOTAL UTILITIES	Power					23.46
NET RAW MATERIALS & UTILITIES						13575.69
	Supervisors	1	Employee	29953	USD	1.50
DIRECT FIXED COSTS	Maintenance, Material & Labour		4.0	% of ISBL		7.79
	Direct Overhead		100	% Labour & Supervision		1.50
TOTAL DIRECT FIXED COSTS						10.79
ALLOCATED FIXED	General Plant Overhead		50.0	% Direct Fixed Costs		5.39
COSTS	Insurance, Property Tax		0.8	% Total Plant Capital		2.10
TOTAL ALLOCATED FIXED COSTS						7.50
TOTAL FIXED COSTS						18.28
TOTAL CASH COST						13593.97
Depreciation		0.10	for ISBL & OPC	0.05	for OSBL	29.46
COST OF PRODUCTION PER kg						13623.43
						USD kW^{-1}
COST OF PRODUCTION PER kW						3.41

[a] Inside battery limits

[b] Other project costs

[c] Outside battery limits

Table D9. Cost of production for baseline 691 g Fe-N-C at 1,000 PEMFC stacks. Reproduced from ref [1] under Creative Commons CC BY 3.0.

							USD
PRODUCTION COST SUMMARY							**$kg_{Fe\text{-}N\text{-}C}^{-1}$**
RAW MATERIALS	Iron Nitrate Nonahydrate						0.42
	Nicarbazin						37.00
	Silica						2.00
	Hydrogen fluoride						3.20
	Water, deionised						8.02
TOTAL RAW MATERIALS							50.64
TOTAL UTILITIES	Power						229.81
NET RAW MATERIALS & UTILITIES							280.45
	Supervisors	1	Employee		29,953	U.S. $	1.50
	Maintenance, Material & Labour			4.0	% of ISBL[a]		9.58
DIRECT FIXED COSTS	Direct Overhead			100	% Labour & Supervision		1.50
TOTAL DIRECT FIXED COSTS							12.58
ALLOCATED FIXED	General Plant Overhead			50.0	% Direct Fixed Costs		6.29
COSTS	Insurance, Property Tax			0.8	% Total Plant Capital		2.54
TOTAL ALLOCATED FIXED COSTS							8.83
TOTAL FIXED COSTS							21.41
TOTAL CASH COST							130.22
Depreciation		0.10	ISBL & OPC [b]		0.05	OSBL [c]	35.80
COST OF PRODUCTION PER kg							337.66
							USD kW^{-1}
COST OF PRODUCTION PER kW							2.92

Table D10. Cost of 80 kW PEMFC components for F = 86.4% learning curve of Pt/C cathode system, with calculated r and *A* values. Reproduced from ref [1] under Creative Commons CC BY 3.0.

Production Rate	Cathode Catalyst	Membrane + GDL	Bipolar Plates	Gaskets	Stack + Conditioning	Anode Catalyst	Total Cost
Stacks year^{-1}	USD kW^{-1}						USD kW^{-1}
1,000	12.61	33.05	15.65	14.23	3.61	2.55	81.70
10,000	7.76	15.75	5.76	6.78	3.05	1.57	40.66
20,000	6.70	12.60	4.26	5.42	2.89	1.36	33.23
50,000	5.53	9.38	2.86	4.04	2.70	1.12	25.63
100,000	4.77	7.50	2.12	3.23	2.57	0.97	21.16
500,000	3.40	4.47	1.05	1.92	2.28	0.69	13.81
F (%)	86.4	80.0	74.0	80.0	95.0	86.4	-
-*r* (-)	-0.21	-0.32	-0.43	-0.32	-0.07	-0.21	-
A (-)	4330	24437	25166	10518	482	876	-

Table D11. Cost of 80 kW PEMFC components for learning curve of PtCo/C cathode system, with calculated *r* and *A* values. Reproduced from ref [1] under Creative Commons CC BY 3.0.

Production Rate	Cathode Catalyst	Membrane + GDL	Bipolar Plates	Gaskets	Stack + Conditioning	Anode Catalyst	Total Cost
Stacks year^{-1}	USD kW^{-1}						USD kW^{-1}
1,000	14.58	33.05	15.65	14.23	3.61	2.55	83.66
10,000	8.97	15.75	5.76	6.78	3.05	1.57	41.87
20,000	7.75	12.60	4.26	5.42	2.89	1.36	34.28
50,000	6.39	9.38	2.86	4.04	2.70	1.12	26.49
100,000	5.52	7.50	2.12	3.23	2.57	0.97	21.90
500,000	3.93	4.47	1.05	1.92	2.28	0.69	14.34
F (%)	86.4	80.0	74.0	80.0	95.0	86.4	-
-*r* (-)	-0.21	-0.32	-0.43	-0.32	-0.07	-0.21	-
A (-)	5005	24437	25166	10518	482	876	-

Table D12. Cost of 80 kW PEMFC components for F = 86.4% learning curve of Fe-N-C cathode system, with calculated r and A values. Reproduced from ref [1] under Creative Commons CC BY 3.0.

Production Rate	Cathode Catalyst	Membrane + GDL	Bipolar Plates	Gaskets	Stack + Conditioning	Anode Catalyst	Total Cost
Stacks year^{-1}	USD kW^{-1}						USD kW^{-1}
1,000	2.92	129.69	61.41	55.82	14.18	9.91	273.93
10,000	1.79	61.80	22.59	26.60	11.95	6.10	130.83
20,000	1.55	49.44	16.71	21.28	11.36	5.27	105.61
50,000	1.28	36.81	11.23	15.84	10.61	4.34	80.11
100,000	1.10	29.45	8.31	12.67	10.08	3.75	65.37
500,000	0.786	17.54	4.13	7.55	8.95	2.67	41.63
F (%)	86.4	80.0	74.0	80.0	95.0	86.4	-
-r (-)	-0.21	-0.32	-0.43	-0.32	-0.07	-0.21	-
A (-)	1001	95892	98753	41273	1891	3404	-

Global Sensitivity Analysis

Table D13. Total Sobol sensitivity indices for midpoint global sensitivity analysis of Pt/C baseline. Reproduced from ref [1] under Creative Commons CC BY 3.0.

Midpoint Impact Method	Acetone	Carbon black	CPA	Electricity	Ethylene glycol	HCl	NaOH	H_2O
Global warming (kg CO_2-Eq)	0.0001	0	0.6346	0.3651	0.0001	0.0001	0	0
Acidification potential (kg SO_2-Eq)	0	0	0.9972	0.0027	0	0.0001	0	0
Marine eutrophication (kg N-Eq)	0	0	0.7673	0.2326	0	0.0001	0	0
Freshwater eutrophication (kg P-Eq)	0	0	0.9169	0.083	0	0.0001	0	0
Human toxicity potential (kg 1,4-DCB-Eq)	0	0	0.9793	0.0206	0	0.0001	0	0
Fossil resource scarcity (kg oil-Eq)	0.0002	0	0.7458	0.2537	0.0002	0.0001	0	0
Mineral resource scarcity (kg Cu-Eq)	0	0	0.9998	0.0001	0	0.0001	0	0

Table D 14. Total Sobol sensitivity indices of midpoint global sensitivity analysis of Fe-N-C baseline. Reproduced from ref [1] under Creative Commons CC BY 3.0.

Midpoint Impact Method	Activated Silica	Electricity	HF	Iron Nitrate Nonahydrate	Nicarbazin	H_2O
Global warming (kg CO_2-Eq)	0	0.9994	0.0001	0	0.0001	0
Acidification Potential (kg SO_2-Eq)	0.0089	0.6135	0.3668	0	0	0
Marine eutrophication (kg N-Eq)	0	0.4086	0	0.0001	0.5912	0
Freshwater eutrophication (kg P-Eq)	0	0.9998	0.0001	0	0.0001	0
Human toxicity potential (kg 1,4-DCB-Eq)	0	0.0064	0.9936	0	0	0
Fossil resource scarcity (kg oil-Eq)	0	0.9987	0.0002	0	0.0011	0
Mineral resource scarcity (kg Cu-Eq)	0.0002	0.964	0.0244	0.0001	0.0103	0

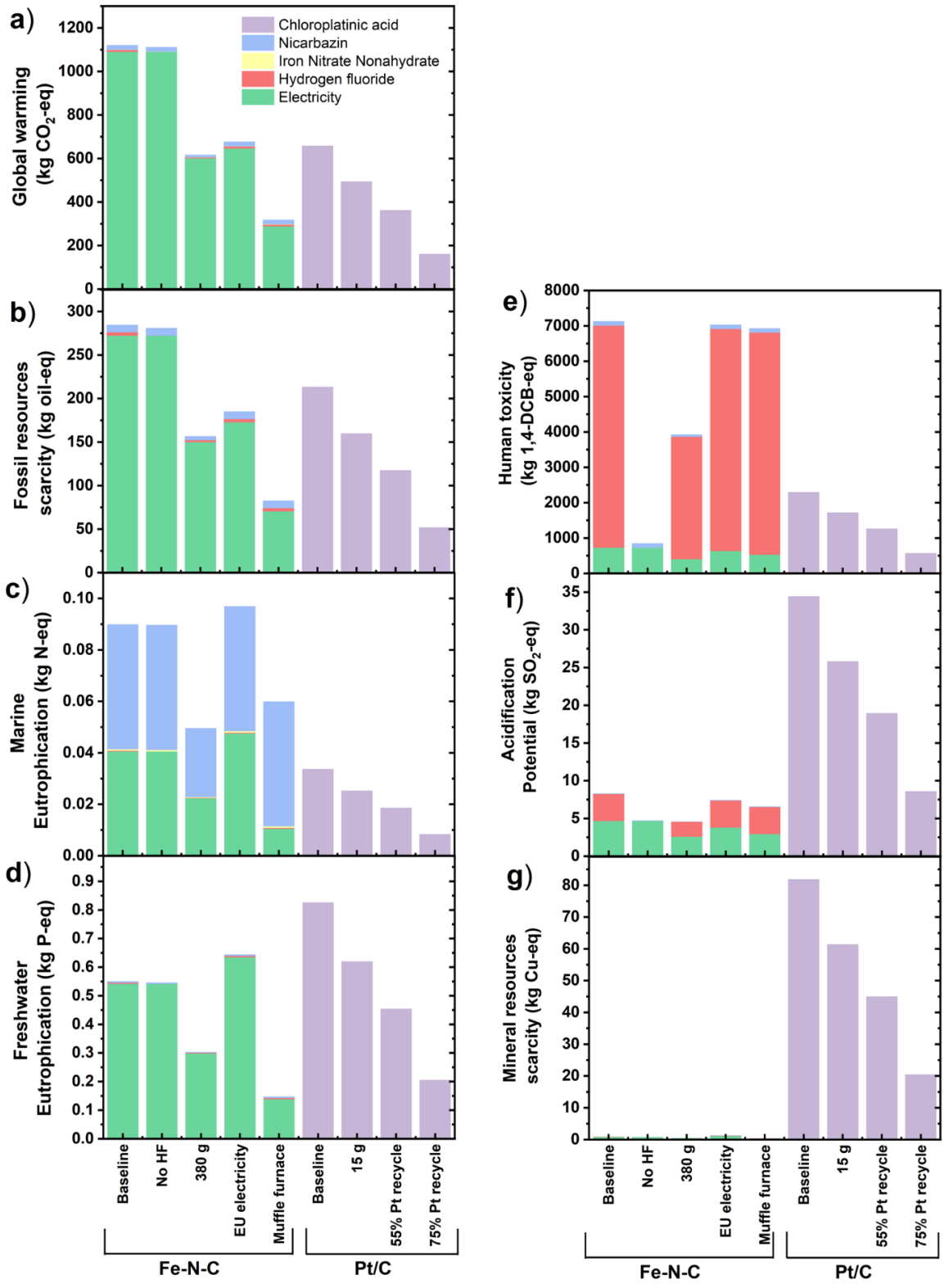


Figure D1. Scenarios of Fe-N-C (baseline, no HF, 380 g, EU electricity) and Pt/C (baseline, 15 g, 55% and 75% Pt recycling for midpoints categories: (a) Global warming (kg CO_2-eq). (b) Fossil resource scarcity. (c) Marine Eutrophication (kg N-eq). (d) Freshwater eutrophication (kg P-eq) (e) Human Toxicity (kg 1,4-DCB-eq). (f) Acidification potential (kg SO_2-eq). (g) Mineral resource scarcity (kg Cu-eq). Reproduced from ref [1] under Creative Commons CC BY 3.0.

Table D15. Midpoint impact results for baseline and varying scenarios. Reproduced from ref [1] under Creative Commons CC BY 3.0.

	Fe-N-C					Pt/C			
Midpoint Impact Method	Baseline	No HF	380 g	EU electricity	Muffle furnace	Baseline	75% Pt recycling	55% Pt recycling	15 g
Global warming (kg CO_2-Eq)	1,130	1,120	623	677	319	659	162	363	494
Fossil resource scarcity (kg oil-Eq)	286	282	157	185	83	213	52	118	160
Marine eutrophication (kg N-Eq)	0.09	0.09	0.05	0.10	0.06	0.03	0.01	0.02	0.03
Freshwater eutrophication (kg P-Eq)	0.55	0.55	0.30	0.64	0.15	0.83	0.21	0.46	0.62
Human toxicity potential (kg 1,4-DCB-Eq)	7,140	856	3,930	7,030	7,138	2,300	571	1,260	1,720
Acidification Potential (kg SO_2-Eq)	8.36	3.79	4.60	7.44	6.58	34.4	8.6	18.9	25.8
Mineral resource scarcity (kg Cu-Eq)	1.01	0.90	0.56	1.28	0.45	81.9	20.5	45.0	61.4

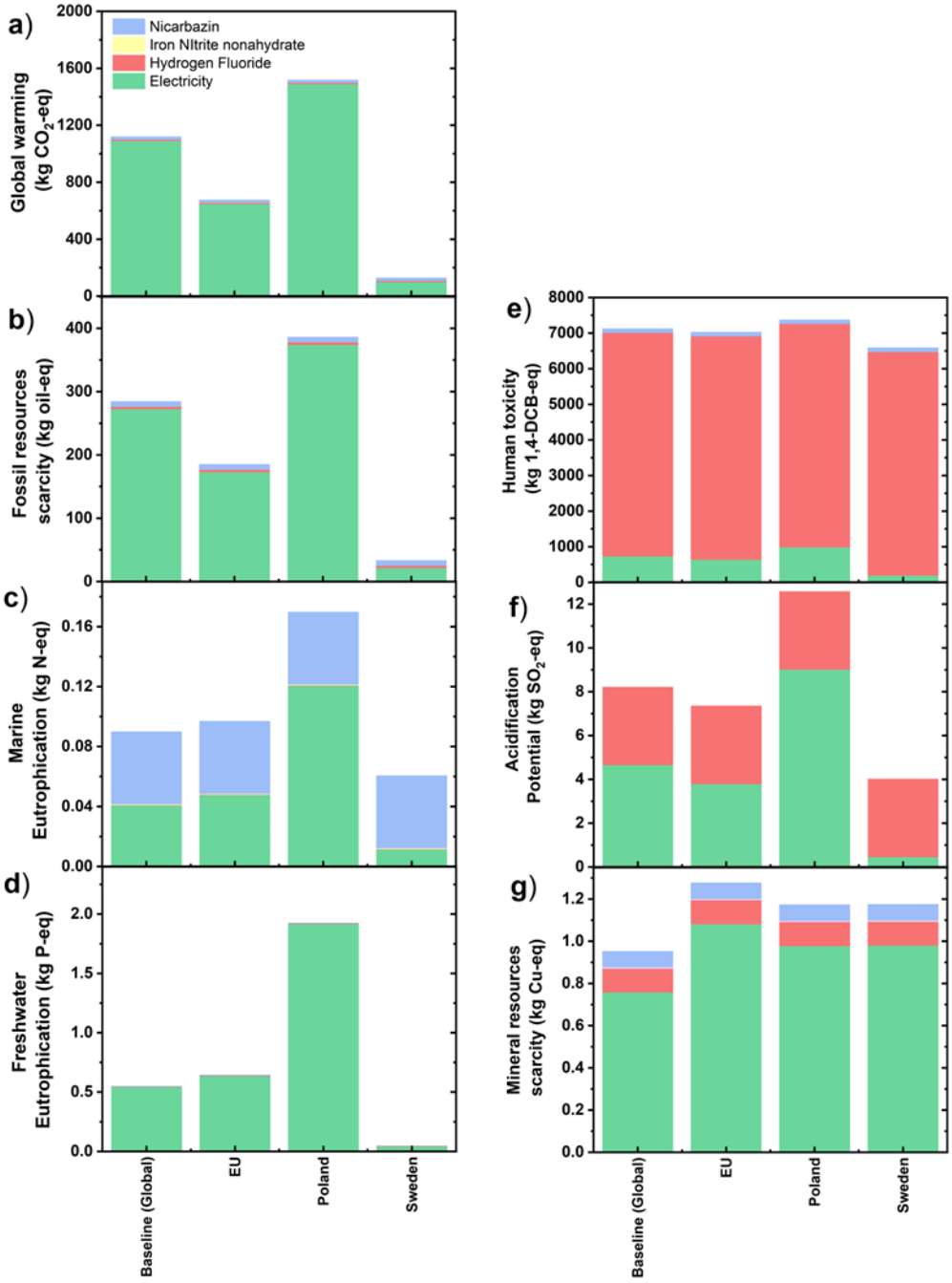


Figure D2. Midpoint impacts for Fe-N-C for different electricity mix scenarios. Reproduced from ref [1] under Creative Commons CC BY 3.0.

Table D16. Midpoint impact results for baseline (global electricity) and EU, Poland, and Sweden electricity mix for Fe-N-C. Reproduced from ref [1] under Creative Commons CC BY 3.0.

	Fe-N-C			
Midpoint Impact Method	Baseline (Global electricity)	EU electricity	Poland electricity	Sweden electricity
Global warming (kg CO_2-Eq)	1130	677	1520	129
Fossil resource scarcity (kg oil-Eq)	286	185	387	34
Marine eutrophication (kg N-Eq)	0.09	0.10	0.17	0.06
Freshwater eutrophication (kg P-Eq)	0.55	0.64	1.93	0.05
Human toxicity potential (kg 1,4-DCB-Eq)	7140	7030	7380	6590
Acidification Potential (kg SO_2-Eq)	8.36	7.44	12.7	4.11
Mineral resource scarcity (kg Cu-Eq)	1.01	1.28	1.17	1.17

Table D17. Midpoint contribution to endpoints for baseline scenario. Reproduced from ref [1] under Creative Commons CC BY 3.0.

Impact Method Contribution	Fe-N-C	Pt/C
Human Health (10^{-3} DALY)	2.01	3.16
Climate Change	1.04	0.62
Human Toxicity	0.47	1.16
Ionising Radiation	0.00	0.00
Ozone Depletion	0.00	0.00
Particulate Matter Formation	0.50	1.38
Photochemical Oxidant Formation	0.00	0.00
Resources (USD 2013)	54.66	59.41
Fossil resources scarcity	54.43	40.47
Mineral resources scarcity	0.23	18.94
Ecosystem Quality (10^{-5} Species·Year)	0.61	5.65
Freshwater ecotoxicity	0.00	0.02
Freshwater eutrophication	0.04	0.06
Global warming, freshwater ecosystem	0.00	0.00
Global warming, terrestrial ecosystem	0.32	0.18
Land use	0.12	4.56
Marine ecotoxicity	0.00	0.00
Marine eutrophication	0.00	0.00
Ozone formation, terrestrial ecosystem	0.03	0.12
Acidification potential	0.08	0.69
Terrestrial ecotoxicity	0.00	0.00
Water consumption, aquatic ecosystem	0.00	0.00
Water consumption, terrestrial ecosystem	0.01	0.01

Table D18. Total Sobol sensitivity indexes for endpoint global sensitivity analysis of Pt/C baseline. Reproduced from ref [1] under Creative Commons CC BY 3.0.

Endpoint Impact Method	Acetone	Carbon black	CPA	Electricity	Ethylene glycol	HCl	NaOH	H_2O
Human health (DALY)	0	0	0.9829	0.0170	0	0.0001	0	0
Ecosystem quality (species·Year)	0.0008	0	0.7615	0.2370	0.0007	0.0001	0	0
Resources (USD 2013)	0.0004	0	0.8714	0.1277	0.0004	0.0001	0	0

Table D19. Total Sobol sensitivity indexes for endpoint global sensitivity analysis of Fe-N-C baseline. Reproduced from ref [1] under Creative Commons CC BY 3.0.

Endpoint Impact Method	Activated Silica	Electricity	HF	Iron Nitrate Nonahydrate	Nicarbazin	H_2O
Human health (DALY)	0.0011	0.9428	0.0561	0	0.0034	0
Ecosystem quality (species·year)	0	0.9954	0.0007	0	0.0039	0
Resources (USD 2013)	0	0.9955	0.0006	0	0.0039	0

Table D20. Endpoint impact results for baseline and different scenarios. Reproduced from ref [1] under Creative Commons CC BY 3.0.

	Fe-N-C					Pt/C			
Midpoint Impact Method	Baseline	No HF	380 g	EU electricity	Muffle furnace	Baseline	75% Pt recycling	55% Pt recycling	15 g
Human health (10^{-3} DALY)	2.01	1.68	1.10	1.49	1.04	3.16	2.37	1.74	0.79
Ecosystem quality (10^{-5} species·year)	0.61	0.60	0.34	0.46	0.18	5.65	4.24	3.11	1.41
Resources (USD 2013)	54.7	53.4	30.1	35.3	17.4	59.4	44.6	32.8	14.4

Table D21. Endpoint impact results for baseline and scenarios considering different production location electricity mix for Fe-N-C. Reproduced from ref [1] under Creative Commons CC BY 3.0.

Endpoint Impact Method	Fe-N-C			
	Baseline (Global electricity)	EU electricity	Poland electricity	Sweden electricity
Human health (10^{-3} DALY)	2.01	1.49	2.72	0.48
Ecosystem quality (10^{-5} species·year)	0.61	0.46	1.03	0.17
Resources (USD 2013)	54.7	35.3	34.7	10.5

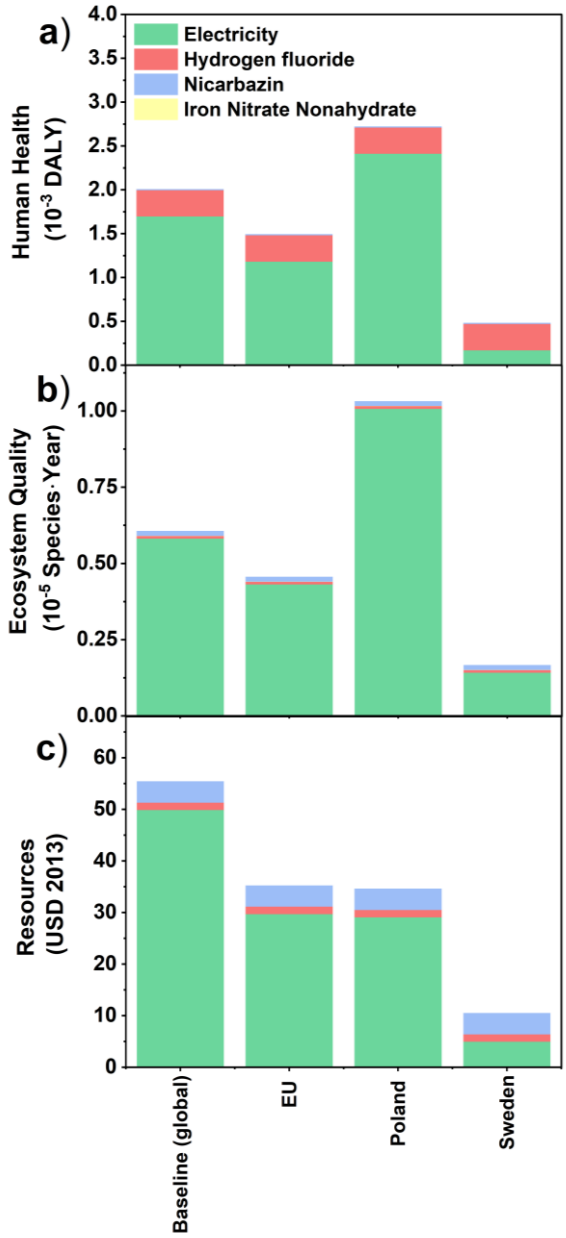


Figure D3. Endpoint scenarios for Fe-N-C for different electricity mix supplies. Reproduced from ref [1] under Creative Commons CC BY 3.0.

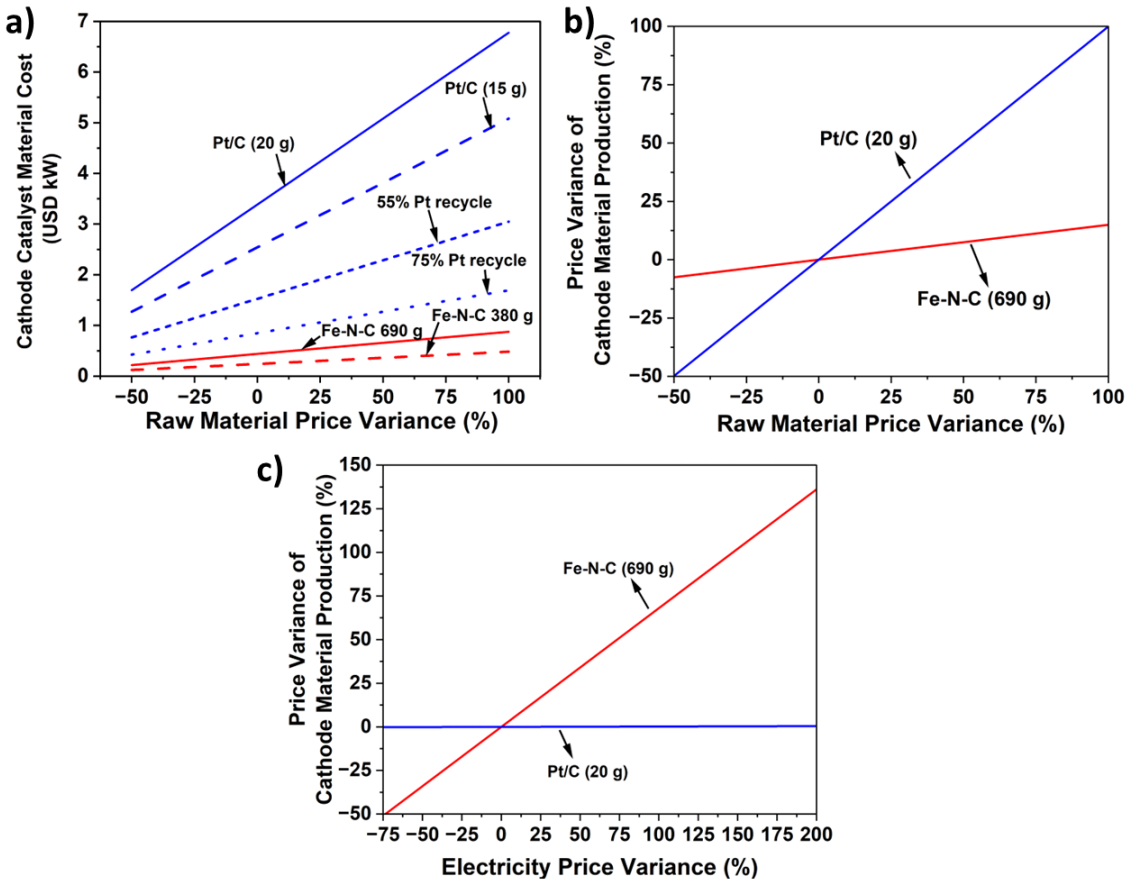


Figure D4. Sensitivity analysis on catalyst material feedstock price variance for a.) cathode catalyst material costs for baseline and varying catalyst scenarios and b.) catalyst production cost variance. c.) Electricity price variance on catalyst production cost variance. Reproduced from ref [1] under Creative Commons CC BY 3.0.

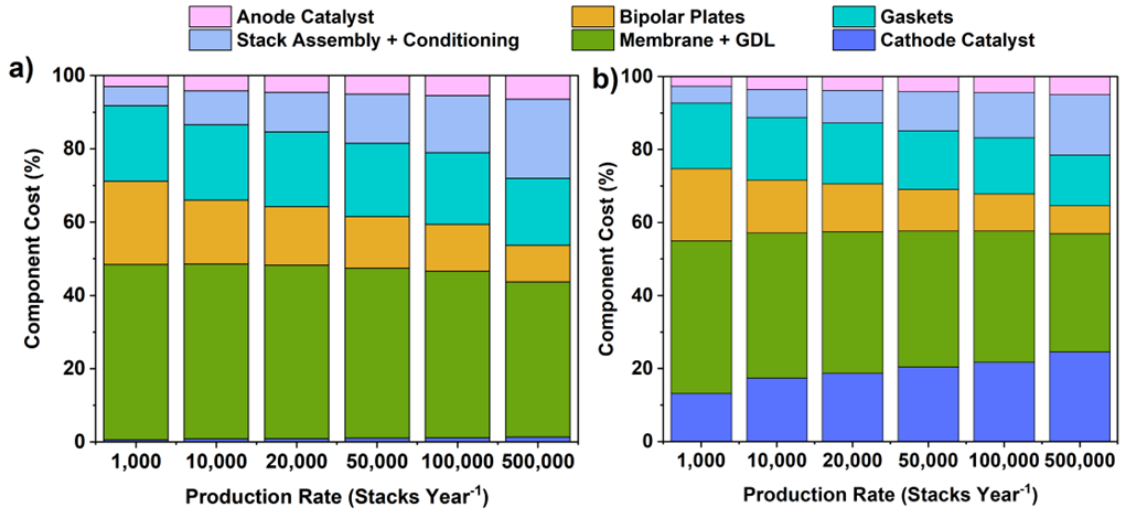


Figure D5. Percentage breakdown of 80 kW PEMFC component costs with cathode (a) Fe-N-C. (b) Pt/C. Reproduced from ref [1] under Creative Commons CC BY 3.0.

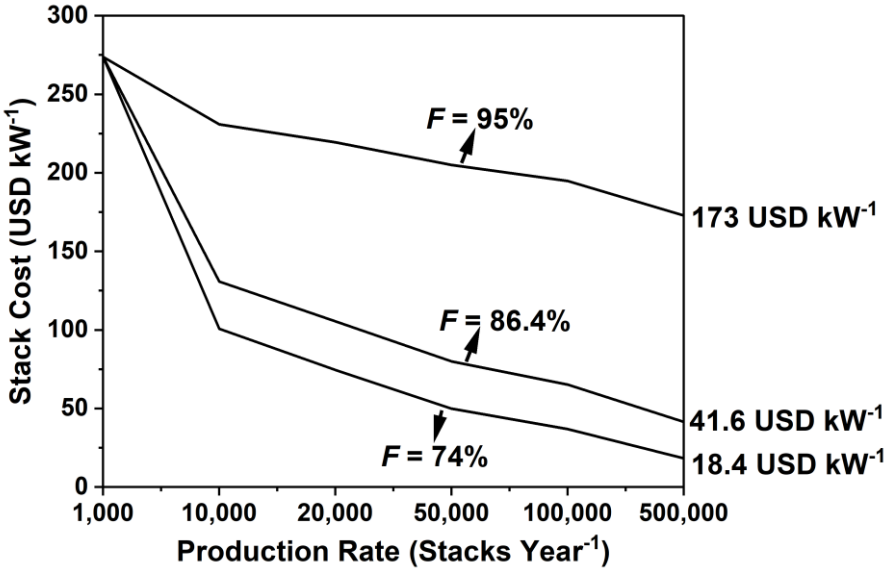


Figure D6. Different F values applied for baseline Fe-N-C based 80 kW PEMFC stack. For F = 74 and 95%, this F value is applied to all PEMFC components. F = 86.4% is only applied to the catalysts, with other values found in Table S20. Reproduced from ref [1] under Creative Commons CC BY 3.0.

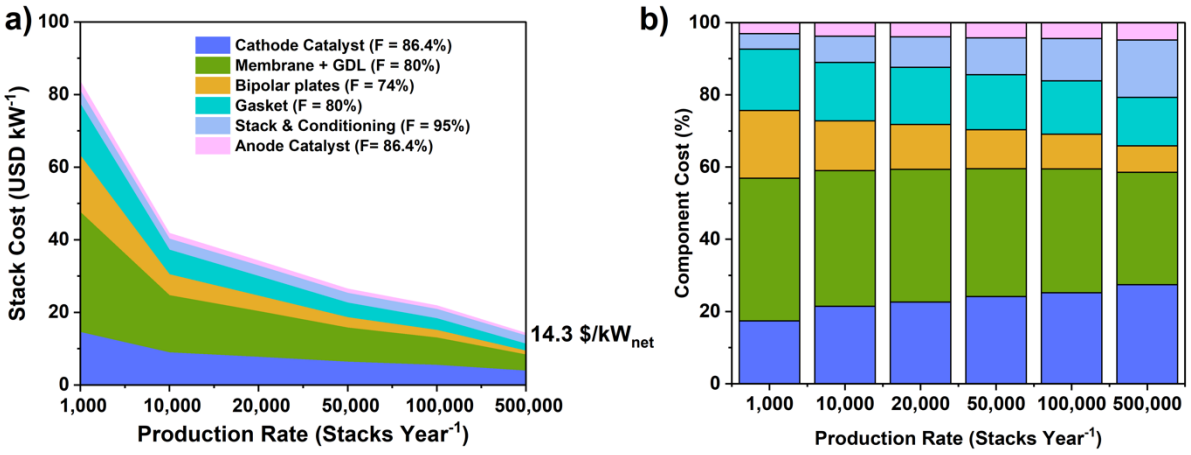


Figure D7. a.) Learning curve of 80 kW PEMFC stack containing cathode PtCo/C. b.) Corresponding percentage breakdown of component costs. Reproduced from ref [1] under Creative Commons CC BY 3.0.

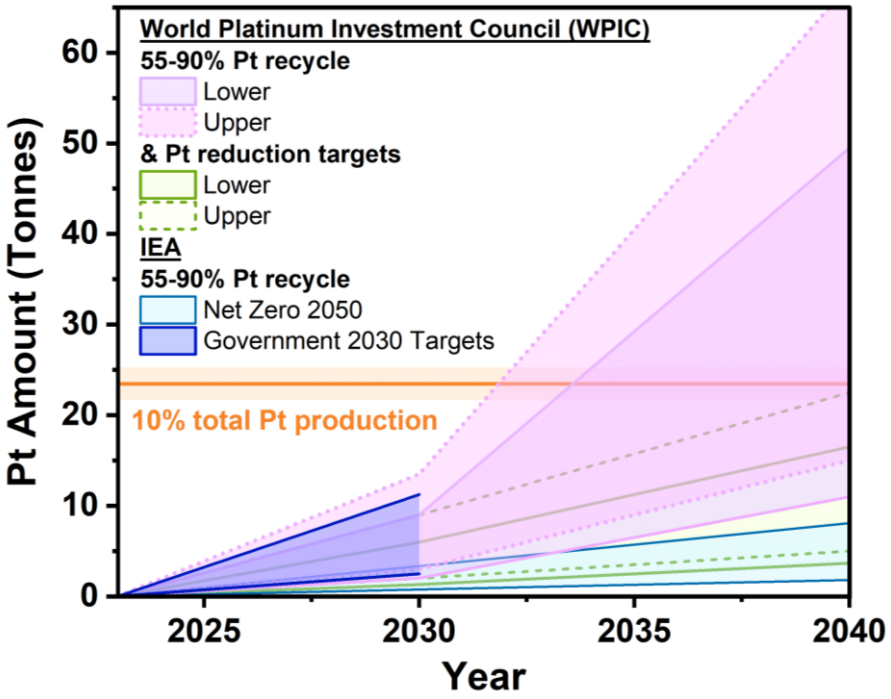


Figure D8. Different scenarios of Pt consumption over time based on PEMFC electric vehicle (FCEV) production from World Platinum Investment Council (WPIC)[3] of lower (11 million FCEV) and upper (15 million FCEV) by 2040. Also, IEA 2050 net zero scenario (equivalent to 2.85 million FCEV)[4] and 2030 government targets (2.5 million FCEV).[5] 10% annual Pt consumption limit for deployment of new technology based on ref,[6] with error representing variation in Pt production between 2017-2023.[7] Reproduced from ref [1] under Creative Commons CC BY 3.0.

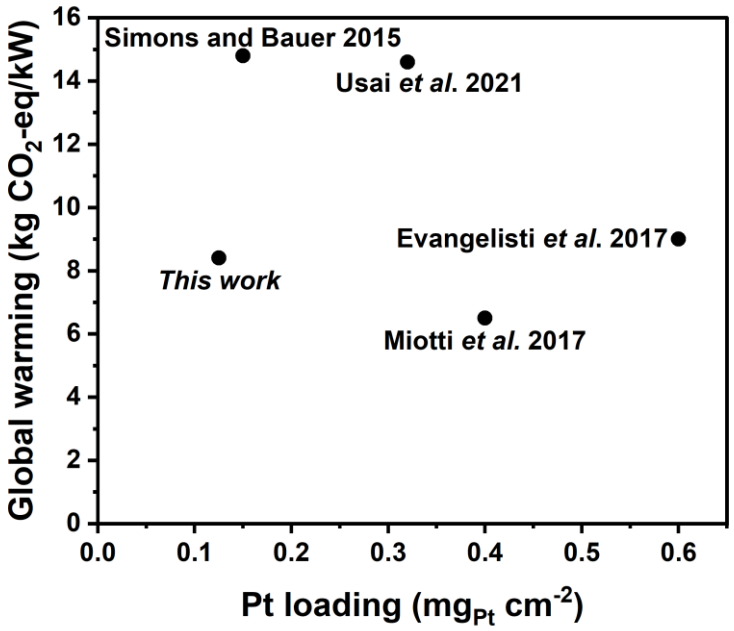


Figure D9. Calculated Global warming impact per kW for assumed Pt loadings in references (Usai et al. 2021,[8] Evangelisti et al. 2017,[9] Miotti et al. 2017,[10] Simons and Bauer 2015[11]) and this work. Reproduced from ref [1] under Creative Commons CC BY 3.0.

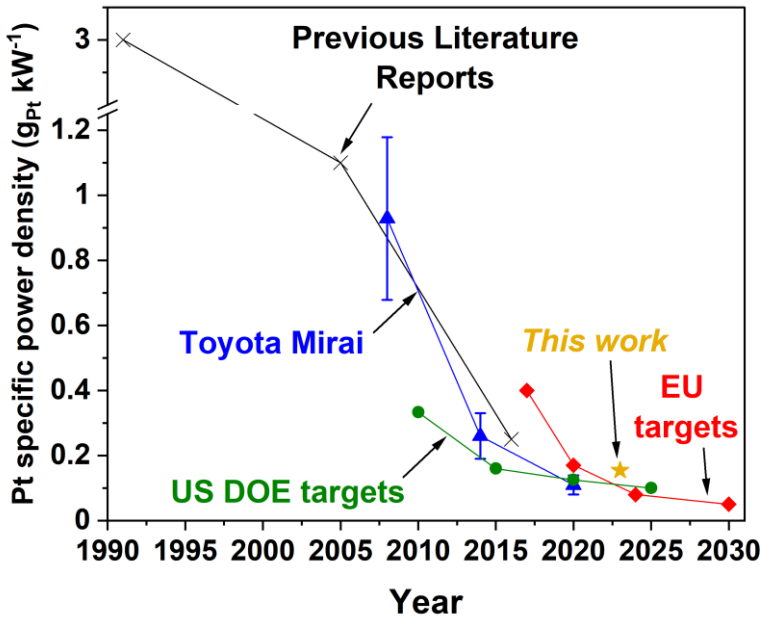


Figure D10. Reported Pt specific power density and targets over time. Toyota Mirai based on reported reductions,[12] with g_{Pt} kW^{-1} based on calculations from Gröger et al.[13] Targets reported for EU[14] and US DOE.[15,16] Previous literature reports from 1991,[17] 2005,[18] and 2016.[19] The reported values and targets are based on different operation conditions. Reproduced from ref [1] under Creative Commons CC BY 3.0.

References

1 A. Pedersen, J. Pandya, G. Leonzio, A. Serov, A. Bernardi, I. Stephens, M.-M. Titirici, C. Petit and B. Chachuat, *Green Chem.*, 2023, **25**, 10458–10471.

2 Y. Dong, M. Hauschild, H. Sørup, R. Rousselet and P. Fantke, *J. Clean. Prod.*, 2019, **209**, 538–549.

3 T. Raymond, E. Sterck and B. Clifford, *PLATINUM ESSENTIALS Fuel cell electric vehicles are forecast to drive material long-term demand growth for platinum*, 2022.

4 International Energy Agency, *World Energy Outlook*, 2022.

5 International Energy Agency, *The Future of Hydrogen*, 2019.

6 A. B. Laursen, J. Sehested, I. Chorkendorff and P. C. K. Vesborg, *Chin. J. Catal.*, 2018, **39**, 16–26.

7 Johnson Matthey, *PGM market report, May*, 2022.

8 L. Usai, C. R. Hung, F. Vásquez, M. Windsheimer, O. S. Burheim and A. H. Strømman, *J. Clean. Prod.*, 2021, **280**, 125086.

9 S. Evangelisti, C. Tagliaferri, D. J. L. Brett and P. Lettieri, *J. Clean. Prod.*, 2017, **142**, 4339–4355.

10 M. Miotti, J. Hofer and C. Bauer, *Int. J. Life Cycle Assess.*, 2017, **22**, 94–110.

11 A. Simons and C. Bauer, *Appl. Energy*, 2015, **157**, 884–896.

12 T. Yoshizumi, H. Kubo and M. Okumura, *SAE Tech. Pap.*, 2021, **2021-01–0740**, 1–6.

13 O. Gröger, H. A. Gasteiger and J.-P. Suchsland, *J. Electrochem. Soc.*, 2015, **162**, A2605–A2622.

14 *Fuel Cells and Hydrogen 2 Joint Undertaking Key Performance Indicators*, 2021.

15 US DOE - Hydrogen and Fuel Cell Technologies Office, *Hydrogen and Fuel Cell Technologies Office Multi-Year Research, Development, and Demonstration Plan. Section 3.4: Fuel Cells*, 2017.

16 B. D. James, J. M. Huya-Kouadio, C. Houchins and D. A. DeSantis, *Mass Production Cost Estimation of Direct H2 PEM Fuel Cell Systems for Transportation Applications: 2018 Update*, 2018.

17 D. H. Swan, O. A. Velev, I. J. Kakwan, A. C. Ferreira, S. Srinivasan and A. J. Appleby, in *Project Hydrogen'91, Technical Proceedings, American Academy of Science*, Independence, USA, 1991.

18 H. A. Gasteiger, S. S. Kocha, B. Sompalli and F. T. Wagner, *Appl. Catal. B Environ.*, 2005, **56**, 9–35.

19 A. Kongkanand and M. F. Mathias, *J. Phys. Chem. Lett.*, 2016, **7**, 1127–1137.